CORONAL TEMPERATURE DIAGNOSTICS DERIVED FROM MULTILAYER OBSERVATIONS WITH THE MULTI-SPECTRAL SOLAR TELESCOPE ARRAY

A DISSERTATION

SUBMITTED TO THE DEPARTMENT OF PHYSICS

AND THE COMMITTEE ON GRADUATE STUDIES

OF STANFORD UNIVERSITY

IN PARTIAL FULFILLMENT OF THE REQUIREMENTS

FOR THE DEGREE OF

DOCTOR OF PHILOSOPHY

Paul Boerner

July 2004

I certify that I have read this dissertation and that, in my opinion, it is fully adequate in scope and quality as a dissertation for the degree of Doctor of Philosophy.

Philip Scherrer

Principal Adviser

I certify that I have read this dissertation and that, in my opinion, it is fully adequate in scope and quality as a dissertation for the degree of Doctor of Philosophy.

Sarah Church

I certify that I have read this dissertation and that, in my opinion, it is fully adequate in scope and quality as a dissertation for the degree of Doctor of Philosophy.

Vahé Petrosian

Approved for the University Committee on Graduate Studies:

ABSTRACT

In recent years, satellite-based extreme ultraviolet multilayer telescopes observing the solar corona have provided some of the most beautiful and fascinating images ever seen. However, our ability to extract quantitative information about the thermodynamic state of the solar atmosphere from these images has been limited by their broad temperature response, uncertain calibration status, and the limited number of bandpasses available. In this dissertation, I present a unique dataset and novel analysis techniques designed to provide rigorous constraints on conditions in the corona with the high spatial and temporal resolution of multilayer images. The data were obtained during the third flight of the Multi-Spectral Solar Telescope Array, a sounding rocket payload which was launched on April 30, 2002. The MSSTA imaged the solar atmosphere in seven different ultraviolet bandpasses, centered on strong emission lines at 150 Å, 171 Å, 180 Å, 195 Å, 211 Å, 1216 Å and 1550 Å. These images, along with satellite observations, can be used to constrain the differential emission measure of the corona in the temperature range of 300,000 to 3,000,000 K; however, uncertainty in the data and fundamental limitations in the emission processes impose strict limits on the range and accuracy of the results. I present spatially-resolved differential emission measure functions obtained from the MSSTA data, and discuss the potential applications of these results, along with an analysis of the limitations of the current data set and of the DEM reconstruction technique.

ACKNOWLEDGEMENTS

Much of the work described here was the collaborative effort of a number of people, and in recognition of this fact I have generally used the plural "we" to describe the activity and deliberation of the MSSTA team throughout the text. However, a number of vital contributions are not mentioned in the body of the dissertation, or were so integral to the MSSTA project or my own ability to proceed that they demand explicit recognition.

Arthur B. C. Walker conceived and created the MSSTA payload, so any work derived from that instrument owes him a tremendous debt. Even more importantly, for me, Art was a mentor and a friend. He kept me from giving up on science altogether and sparked my interest in solar physics; taught me to plan and test scientific instruments with a critical eye; and gave me the confidence to pursue my own path. His passing in April of 2001 was devastating for all who knew him. The breadth of his accomplishments, and his brilliance, kindness and courage, have been mourned by many people with more eloquence than I feel I can provide. I will always feel blessed to have known him and learned from him, and owe all the satisfaction I derive from thinking of myself as a solar physicist to him. I am also grateful to Victoria Walker for her compassion, for sharing some part of her admiration and love for Art with me.

Philip Scherrer has been my thesis advisor since 2001, and has been wonderfully supportive, patient and good to me in that time. His guidance ensured that the only obstacles I faced in continuing to work on the MSSTA mission were scientific, and enabled me to continue at Stanford. He has also helped me understand the place of my work in the larger solar physics community, and helped me to connect to other members of that community. I am grateful to the members of Phil's research group who provided helpful suggestions on the analysis of the MSSTA data, especially Sasha Kosovichev and Rasmus Larsen.

Dennis Martínez-Galarce has managed to be a scientific colleague, an advisor, a beer-drinking comrade, and a supervisor to me, frequently playing all these roles in series within the same 24 hour period, and all without any officially-sanctioned status. He took over the direction of the

MSSTA project in 2001 and demonstrated extraordinary tenacity and ingenuity in ensuring the payload's success. I owe a great deal to his intelligence, experience, and willingness to develop an extremely productive and relaxed working relationship with me.

I'd like to think that T. J. Bay and I worked similarly well together. Certainly T. J. managed to accomplish a tremendous amount despite joining the MSSTA team as launch time approached; he made himself an expert on the payload in less than a year and made invaluable contributions to the calibration experiments, alignment, assembly and pre-flight testing of the telescopes. Ramesh Kumar and AmirAli Talasaz took over the arcane payload electronics and software, and transformed them into a sophisticated camera-control computer through long hours and divine inspiration. Naseem Hakim, Felicia Tam and Dave Robertson all helped keep the payload work moving forward and solved some of the innumerable little problems that make experimental physics interesting. Hakeem Oluseyi and Craig DeForest shared generously of their own experiences on past MSSTA flights and the wisdom they have gained since the completion of their graduate work.

The NASROC team at White Sands Missile Range, lead by Carlos Martínez and Bill Payne, probably worked harder on our payload than on any three other missions, but they never complained, and were never anything but cheerful, professional and skillful. It was difficult not to feel that they could have built and flown the whole experiment in a month if only we members of the science team would get out of their way. Their supreme competence earned my gratitude and awe.

Troy Barbee and Phil Baker were collaborators who were happy to act as teachers when it became clear that I needed more from them than just the work that the original proposal called for. Eric Gullikson and the staff at the ALS, and Hal Tompkins and the staff at SSRL, were similarly helpful and understanding. My dissertation committee – Sarah Church, Vahé Petrosian, Blas Cabrera, and Umran Inan – provided patience and useful feedback.

It goes without saying that I would have failed in a thousand ways over the past seven years without the ceaseless support of my family and friends. To all of you, thank you.

AUTHORSHIP

By its nature, a dissertation requires at least some account of how much of the described work was performed by the individual author, and to satisfy this requirement as well as to absolve the innocent of any blame for my own mistakes of commission or omission, I will attempt to make explicit the extent of my own role in the project here described.

The text of the dissertation is entirely my own writing. With the exception of Section 5.4, which is adapted from (Boerner, Martínez-Galarce et al. 2004), none of the text has been previously published elsewhere. The material in Chapter 1 is essentially a restatement of a large body of existing knowledge, which I have taken pains to cite appropriately; while this is mostly background, with little that is truly new, some of the formalism and all of the arguments presented in Chapter 1 are my own.

The experimental work described in Chapters 2 and 3 was mostly performed between 2000 and 2002. During this time, I was the senior graduate student of the MSSTA team. The planning of the experiment and the day-to-day labor in the lab were truly a team effort involving Dennis, myself, our collaborators and the other students in the group. I take full responsibility for those parts of Chapters 2 and 3 that give the impression that the MSSTA experiment was characterized by somewhat more frequent delays and errors than might be expected from an experienced scientist, and partial responsibility for the rest. I do not describe any of the experimental efforts (such as revision of the flight software) that were predominantly carried out by another member of the team.

The analysis techniques presented in Chapter 4 are my own work; I have cited the results of other authors who have performed similar analyses, but did not work directly with anyone else, outside of brief discussions, in developing these techniques.

TABLE OF CONTENTS

LIST OF TABLES

LIST OF FIGURES

1 Introduction

1.1 Overview

The primary goal of this work is to describe the results of the third flight of the Multi-Spectral Solar Telescope Array, a sounding-rocket-borne observatory that imaged the solar atmosphere at a variety of extreme-ultraviolet and far-ultraviolet wavelengths. I will begin by discussing the context of the mission, explaining what the solar corona is, what we want to know about it, and why. By section 1.3, I will make the definition of the problem more quantitative by presenting a detailed derivation of the Differential Emission Measure function, which describes the temperature structure of the solar atmosphere. I will also describe how multilayer observations such as those obtained by the MSSTA can be used to constrain the DEM.

Chapter 2 contains an exhaustive account of the calibration of the MSSTA instrument. Each component – multilayer mirrors, filters, and photographic film – is treated individually. Since accurate calibration is critical to interpretation of the results from the MSSTA, I will attempt to make any uncertainties in the instrument calibration as clear as possible. Chapter 2 concludes with the presentation of the instrument temperature kernels, which define how the MSSTA telescopes respond to the coronal DEM.

Chapter 3 is an account of the integration and launch of the MSSTA. Representative images from the dataset are presented, and the resolution and calibration of the data are examined in comparison with similar data from other instruments.

Chapter 4 contains my numerical analysis of the MSSTA data. It begins with the testing of various techniques for DEM reconstruction using simulated data. The stability and uniqueness of these techniques are evaluated. I then apply a forward modeling approach to the MSSTA images

and obtain DEMs representing the full solar disk and selected sub-regions. Finally, I discuss the reliability of these results.

In Chapter 5, the implications of the DEM reconstruction analysis are summarized. Suggestions for additional applications of the MSSTA data, and for improvements to future missions now in the planning stages, are presented. I finish by describing the design of a new sounding-rocket mission based on the MSSTA truss, and scheduled for launch in 2006.

1.2 Background

1.2.1 THE CORONA

It is a minor miracle that the moon appears almost exactly the same size as the sun when viewed from Earth. There is no obvious reason why things should have worked out that way, but the result is that occasionally creatures on the Earth are treated to full solar eclipses, when the moon just blocks the disk of the sun. Early observers generally understood the occurrence of eclipses as evidence of divine displeasure. A more modern reading is that eclipses are evidence of a divine mandate to humanity to study the solar corona.

The corona is a diffuse halo of material that surrounds the sun. As seen during eclipses, it is a faintly opalescent glow, dynamic, structured, and tenuous, that streams out to several times the diameter of the solar disk. We now know that the corona links the sun to interplanetary space; indeed, it can be said that the Earth floats through the extended corona. Certainly the storms and surges of the sun's atmosphere are important components in any understanding our own planet's environment, and as we grow as a species and come to rely on satellites operating above most of the earth's atmosphere, or to venture beyond the protection of that atmosphere ourselves, understanding the corona will become increasingly vital to our future.

Observing the corona from earth is extremely challenging because it is so faint compared to the solar disk. It was a long time before respectable scientists believed that the corona was anything but an optical illusion. Once it became possible to make quantitative measurements of its properties, observers were confronted with a mystery: the presence of spectral lines unlike any seen in an earthly lab. Most attributed these to the presence of a novel element called coronium, but this material appeared to behave in bizarre, unphysical ways. Eventually, Bengt Edlén (Edlén 1945) was able to reconcile the extent and behavior of the corona with its observed spectral features: he discovered that the corona was many times hotter than the surface of the sun, up to

several million degrees Kelvin (the surface is ~6000 K). The mysterious lines come from a diffuse, highly ionized plasma of ordinary elements.

This explanation is almost more confounding than the mystery it solved. How can the corona be hotter than the solar surface? It is as if you held your hand over a stove burner, and found that the air above the burner grew hotter rather than cooler as you pulled your hand away (Golub and Pasachoff 2001). The source of the coronal heating remains something of a puzzle to this day. It is clear that energy is stored in the sun's twisted magnetic field, and that this energy is deposited in the solar atmosphere, but the mechanism that releases that heat and produces the structures and motions that we see is not understood in any amount of detail.

However, the discovery that the corona is hot did open up a new avenue for measuring the corona. At 6000 K, the photosphere emits most of its radiation in the visible and infrared range of the spectrum. Because it is so much hotter than the photosphere, the corona emits vastly more ultraviolet and x-ray light, despite the fact that it is not very dense. By pointing an x-ray telescope at the solar disk, we can black out the photosphere and see the corona without waiting for an eclipse or building an occulting disk. Extreme ultraviolet and x-ray astronomy quickly became the primary techniques for studying the solar atmosphere.

1.2.2 X-RAY SOLAR PHYSICS

Of course, trying to observe in x-rays is a challenging problem on its own. First of all, there is the unfortunate fact (unfortunate, that is, for solar physicists; fortunate as far as most living things are concerned) that the earth's atmosphere absorbs essentially all energetic radiation. Instruments must be carried above the atmosphere. In the 1940s and '50s, scientists began mounting solar x-ray detectors on rockets – first on captured German V-2s, then later on dedicated scientific sounding rockets like the Aerobee – and launching them, taking data during the brief period of the rocket's flight when it was above the absorbing layers of the Earth's atmosphere. As technology progressed to the point where it became possible to put instruments on satellites positioned for continuous monitoring of the sun over many years, the amount of solar data grew

exponentially. Still, the sounding rocket program remains an important test bed for new instrumentation, and has produced invaluable data along the way.

The instruments carried on the first rockets were fairly simple proportional counters, with only enough spatial resolution to verify that their signal was coming from the sun. Actually imaging energetic radiation is much more difficult; it tends to penetrate optics, and bending x-rays enough to focus them is not easy. The classical solution is to use grazing-incidence optics like the Wolter telescope, a thin curved shell that deflects incoming radiation by about a degree to form a focus well behind the mirror. Grazing-incidence telescopes are inefficient due to their extremely small collecting area; furthermore, they are quite sensitive to surface errors, and thus are difficult to construct in such a way that they are capable of producing high-resolution images.

The MSSTA

A breakthrough came with the development of multilayer structures capable of reflecting energetic radiation at high angles of incidence. The advantages of multilayer telescopes over grazing incidence optics are legion. Their effective area is orders of magnitude greater, since conventional telescope optics can be used. They are intrinsically wavelength-selective, producing spectroheliograms rather than broadband intensity maps. (A spectroheliogram is an image of the sun in a narrow range of wavelengths.) And they offer the diffraction-limited resolving power of easy-to-fabricate normal incidence optics. The operation of multilayers is discussed in Section 2.2.1.

Depositing a multilayer structure on a Cassegrain mirror enabled A. B. C. Walker's consortium of Stanford University, Lawrence Livermore National Laboratory and the Marshall Space Flight Center to obtain the first high-resolution normal-incidence EUV image of the solar atmosphere (Walker, Lindblom et al. 1988). Within three years, the Walker group had constructed a sounding rocket payload that carried a suite of 14 multilayer telescopes: Multi-Spectral Solar Telescope Array (Walker, Lindblom et al. 1990). The MSSTA flew successfully in 1991 and 1994, imaging the solar atmosphere in a variety of bandpasses. The success of the MSSTA program and the parallel efforts of the NIXT team (Golub 1989) caught the attention of solar physicists

everywhere, and led directly to a series of satellite missions using similar techniques. In 1995, the Extreme Ultraviolet Imaging Telescope (EIT) was launched on board the Solar and Heliospheric Observatory (SOHO); it soon began imaging the solar disk with an array of four multilayer telescopes. In 1998, it was followed by the Transition Region and Coronal Explorer (TRACE), which obtains stunning high-resolution images and movies in similar bandpasses.

1.3 Measuring the Solar Atmosphere

1.3.1 STATEMENT OF THE PROBLEM

Today, TRACE and SOHO are part of a fleet of spacecraft probing all aspects of the solar atmosphere. Extreme ultraviolet observations of the sun have produced some of the most exciting and beautiful images the world has seen in the last decade. Thanks to a fortunate convergence of advances in materials technology and advances in our physical understanding of the corona, we have been treated to pictures showing vast, elegant plumes of superheated plasma arcing over the solar surface; movies depicting the flash of intense energy released during solar flares and the formation of immense arcades of loops in their wake; and measurements of the ceaseless outflow of the solar wind from the coronal holes near the solar pole. These observations have been part of a revolution in solar physics, a quantum leap forward in our understanding of how the solar atmosphere works. Gone are the models of the chromosphere, transition region and corona as spherical shells sitting on top of each other with energy flowing downward to the solar surface; now we recognize the corona as a forest of ever-shifting, interconnected structures spanning spatial scales from meters to hundreds of Megameters.

However, in spite of the qualitative change in our understanding of the solar atmosphere, quantitative analysis of these results has proven extremely challenging. The most basic properties of the plasma that we see in narrowband spectroheliograms – How hot is it? How dense? How are these structures related to each other? What is the source of their energy? – remain elusive. Attempts to measure such quantities often report inconclusive or contradictory results, depending on the assumptions of the investigator and the technique used to analyze the data. The true potential of multilayer telescopes – their unique ability, not only to discern the fine structures of the corona, but to thoroughly diagnose their energetic state – has not yet been achieved. How much detailed, specific, quantitative information about the state of the coronal plasma can be obtained from a set of calibrated, high-resolution extreme-ultraviolet spectroheliograms? It is the goal of this work to answer that question, both in theory and in practice.

1.3.2 DEM

The data set of an instrument like the MSSTA consists of a large number of pixel values $p_i(\mathbf{x})$, where the index i refers to one of the telescopes in the array and $\mathbf{x}$ refers to a particular point in the image plane. These pixel values consist of measurements of the solar irradiance integrated over the solid angle subtended by the pixel and the wavelength bandpass of the telescope:

(Equation 1) $$p_i(\mathbf{x}) = \int_0^\infty \eta_i(\lambda)\mathrm{d}\lambda \int_{pixel\ \mathbf{x}} I(\lambda,\boldsymbol{\theta})\mathrm{d}\boldsymbol{\theta} \qquad [\text{counts s}^{-1}]$$

Here η_i is the efficiency function of the telescope (its bandpass, in units of pixel counts per unit flux at the aperture).

It is not immediately clear how to invert such measurements to obtain a meaningful description of the state of the emitting plasma. A few limitations are obvious: because all its data are obtained from the same vantage point at nearly the same instant of time, the MSSTA can do little to unfold the distribution of plasma along the line of sight or within the pixel, so all measurements will describe a volume integral of some quantity. Furthermore, because it lacks the spectral resolution to measure the shape of emission lines, the MSSTA is essentially limited to measuring some combination of emission line intensities within that volume. That is, as far as the MSSTA is concerned, the intensity of radiation from any volume element of plasma can be treated as a combination of continuum emission and line emission:

(Equation 2) $$I(\lambda) = I_{cont}(\lambda) + \sum_{X,m,j,k} I(\lambda_{jk}^{X+m})\delta(\lambda - \lambda_{jk}^{X+m}) \qquad [\text{ergs cm}^{-2}\ \text{s}^{-1}\ \text{sr}^{-1}\ \text{Å}^{-1}]$$

The symbol λ_{jk}^{X+m} refers to the wavelength of the transition from excited state k to lower state j by an ion of element X in ionization state m.

We can see that any attempt to use MSSTA data to draw inferences about the physics of the corona will rely on understanding how the conditions in the emitting plasma determine the intensities of the various EUV emission lines (as noted in section 2.4.1, the intensity of the EUV

continuum is negligible for our purposes). This problem is discussed in detail in the astrophysical literature [*e.g.* (Pottasch 1963), (Withbroe 1975), (Sylwester, Schrijver et al. 1980), (Judge, Hubeny et al. 1997)], but it will be helpful to explicitly present the derivation of the basic theory of interpreting line intensities, in order to highlight the assumptions on which it rests.

The line-of-sight integrated intensity of an emission line from an optically thin plasma is

(Equation 3) $$I(\lambda_{jk}^{X^{+m}}) = \frac{hc}{4\pi\lambda_{jk}^{X^{+m}}} \int_{z=0}^{1AU} N_k^{X^{+m}} A_{kj} \mathrm{d}z \qquad [\text{ergs cm}^{-2}\ \text{s}^{-1}\ \text{sr}^{-1}\ \text{Å}^{-1}]$$

where A_{ij} is the spontaneous transition probability and N_j is the number density of the upper level j. The integral is taken along the line of sight z through the corona to the MSSTA aperture. Here we have already begun making simplifying assumptions:

- **Assumption 1:** The plasma is optically thin everywhere above the photosphere, which is treated as a uniform spherical layer at $z(\boldsymbol{\theta}) = 0$, so we can ignore opacity.

We can write the excited-state population as the electron density times a number of ratios:

$$N_k^{X^{+m}} = \frac{N_k^{X^{+m}}}{N^{X^{+m}}} \frac{N^{X^{+m}}}{N^X} \frac{N^X}{N^H} \frac{N^H}{N_e} N_e$$

Treating each of these factors in turn requires a series of assumptions, which are detailed below.

- **Assumption 2:** The elemental abundance $Ab^X = N^X / N^H$ is constant at all points in the corona, and its value is known. We use the coronal abundances measured by [(Feldman 1992), (Landi, Feldman et al. 2002), (Grevesse and Sauval 1998)].
- **Assumption 3:** The fraction of atoms of element X that are in ionization state $+m$ (the ionization fraction $Ion^{X^{+m}}(T) = N^{X^{+m}} / N^X$) is a known function of temperature. We use the ionization equilibrium calculations of [(Arnaud and Rothenflug 1985), (Arnaud and Raymond 1992), (Landini and Fossi 1991)].
- **Assumption 4:** The fraction of ions X^{+m} occupying state j $Pop_k^{X^{+m}}(T, N_e) = N_k^{X^{+m}} / N^{X^{+m}}$ is constant in time, and is a function only of plasma temperature and density. This is equivalent

to stating that the plasma is in local thermodynamic equilibrium, so that the population of the energy levels can be found by solving a system of linear equations for each ion.

Now we can rewrite the emission line intensity (Equation 3) as

(Equation 4) $$I(\lambda_{jk}^{X+m}) = \int_0^{1AU} G_{jk}^{X+m}(T, N_e) N_e N^H \mathrm{d}z \qquad [\text{ergs cm}^{-2}\ \text{s}^{-1}\ \text{sr}^{-1}\ \text{Å}^{-1}]$$

where we have defined the *contribution function* for the $k \rightarrow j$ transition of the ion X^{+m} as

$$G_{ij}^{X+m}(T, N_e) = \frac{hc}{4\pi\lambda_{jk}^{X+m}} \frac{A_{kj}}{N_e} Pop_k^{X+m}(T, N_e) Ion^{X+m}(T) Ab^X$$

The contribution function contains all of the detailed atomic physics parameters that go into determining line strengths – all the complex calculations that we'd like to avoid worrying about and treat as known quantities. To do so, we need to make still more approximations.

- **Assumption 5:** We assume that the processes affecting the ionization state of an element are separable from the processes affecting the level populations of the ions. This is generally the case if the plasma has sufficiently low density, such that collisional excitation is dominant over ionization and recombination in populating the energy levels. Thus, the level populations are determined entirely by electron and proton excitation rates, and the radiative decay rate A_{jk}.

With this assumption, the rate balance equations that will determine the contribution function depend on knowledge of the statistical weights of the levels of each ion, and the radiative decay rate and electron and proton collision rates for each transition. These values are contained in the CHIANTI database (Dere, Landi et al. 1997), along with the abundance and ionization equilibrium tables cited above and a set of routines that perform the calculation of line contribution functions.

While the line contribution functions depend on both temperature and density, their temperature dependence is much stronger. Indeed, Judge *et al.* (Judge, Hubeny et al. 1997) showed that the density dependences of coronal line contribution functions are so weak that it is nearly impossible to derive reliable information about the density of an emitting plasma from even a large number

of observed line intensities. Therefore, we will approximate the contribution function as a univariate function of temperature by making a final assumption.

- **Assumption 6:** The pressure is constant everywhere in the corona. We use a value of $p = 10^{15}$ K cm^{-3}, thereby eliminating the density dependence of the line contribution functions. In fact, pressure probably varies by a factor of 2-4 over the range of plasma imaged by the MSSTA, but the weak density dependence of the contribution function means that this error should not substantially contaminate the interpretation of the contribution function.

With all the atomic physics now contained in constant-pressure contribution functions $G_{jk}^{X^{+m}}(T)$, which can be calculated with CHIANTI, we can change Equation 4 from an integral along the line of sight to an integral over temperature by defining the *differential emission measure* (DEM):

$$DEM(T) = N_e N^H \frac{\mathrm{d}z}{\mathrm{d}T} \qquad [\mathrm{cm}^{-5}\ \mathrm{K}^{-1}]$$

Note that the DEM is sometimes defined as $n_e^{\,2}\, dz/dT$ by setting N^H/N_e, the hydrogen density relative to the free electron density, to 0.83. This is generally valid for coronal plasmas where hydrogen and helium are completely ionized.

The line intensity now becomes

(Equation 5) $$I(\lambda_{jk}^{X^{+m}}) = \int_0^\infty G_{jk}^{X^{+m}}(T) DEM(T) \mathrm{d}T \qquad [\mathrm{ergs\ cm}^{-2}\ \mathrm{s}^{-1}\ \mathrm{sr}^{-1}\ \text{Å}^{-1}]$$

The DEM describes the temperature distribution of the emitting plasma (it can be interpreted as describing the amount of plasma along the line of sight that is emitting the observed radiation and that has a temperature between T and T+dT). Because this function is the only way in which information about the distribution and state of the solar atmosphere enters into the determination of the emission line intensity, the DEM contains all the information about the corona that it is possible to derive from a set of measured line intensities (subject to the above assumptions).

This is an essential point to keep in mind during any analysis of multilayer images. It implies two very important limitations on such an analysis. First, even if we accept that the 6 assumptions

listed above are valid and, therefore, that the DEM tells us everything we can learn from the observations, simply measuring the function DEM(T) does not tell us everything we might *want* to know about the plasma. It does not explicitly describe the spatial distribution of plasma along the line of sight (though we can draw inferences about how structured the plasma is by examining the DEM); this is a fundamental problem in observations of optically thin plasmas. Nor does the DEM contain diagnostic information about energetic processes like magnetic reconnection, since defining a DEM requires assuming that the plasma is in equilibrium and at constant pressure.

Second, we cannot be sure that the assumptions are valid, or that we have assumed accurate values for those quantities that cannot be measured. Of the above assumptions, number 2 is the most troubling. While we have simply chosen a characteristic abundance value and decreed that it is constant everywhere, Feldman *et al.* (Feldman, Doschek et al. 1999), (Feldman 1992) found that absolute abundances can vary by an order of magnitude throughout the solar atmosphere. Our results are quite sensitive to such disparity, since line intensity is essentially proportional to abundance. The situation isn't quite as bad as it looks: the MSSTA instruments do not probe the full temperature range of the solar atmosphere, and thus will see only a fraction of the total abundance variation. Furthermore, most of the strong emission lines seen by the MSSTA (and essentially all those seen by EIT, TRACE and the AIA) are from ionized iron; therefore, the distortion caused by relative abundance errors is limited. Still, the possibility that abundances vary substantially (conceivably as a function of temperature) along all lines of sight appears to be a substantial source of uncertainty in our analysis. The assumed ionization equilibrium values (assumption 3) may also contain uncertainties as large as a factor of 2, and even the assumption that the plasma ionization states and level populations reflect local thermodynamic equilibrium is questionable in light of the possibility of nanoflare heating of the corona (Parker 1988).

Nevertheless, in spite of all the limitations associated with defining and interpreting the line-of-sight DEM, it remains an essential tool for studying the corona. It is particularly useful as an interface between observation and theory. A theoretical model of a particular structure or region or condition in the corona can be made to specify a temperature distribution; this DEM is then used in Equation 5 to predict emission line intensities, which can be compared with observed line intensities to check the model. Observations of emission line intensities can only distinguish between different models to the extent that those models produce different DEMs, and to the

extent that the data set has sufficient accuracy and temperature coverage to constrain the DEM itself.

Thus, measuring the coronal DEM observationally has been a primary goal of numerous solar physics experiments over several decades. The principal technique for obtaining a DEM is to use a spectrograph to measure a large set of emission line intensities $I(\lambda_{ij}^{X^{+m}})$ – at least 20 lines, and as many several hundred. Then, forward modeling is used to find the function DEM(T) that best reproduces the observations [*e.g.* (Brosius, Davila et al. 1996), (Dupree 1972), (Schmelz, Saba et al. 1999)]. A characteristic result of this technique, using observations by the SERTS rocket (Thomas and Neupert 1994), is shown in Figure 1. The best-fit DEM reproduces the intensity of about half of the observed lines to within the experimental errors (although it is worth noting that the error bars indicate relative errors only. The absolute calibration of the SERTS instrument, and thus the overall normalization of the resulting DEM, is uncertain by a factor of two (Brosius, Davila et al. 1998)). There is an RMS scatter of roughly 20-30%

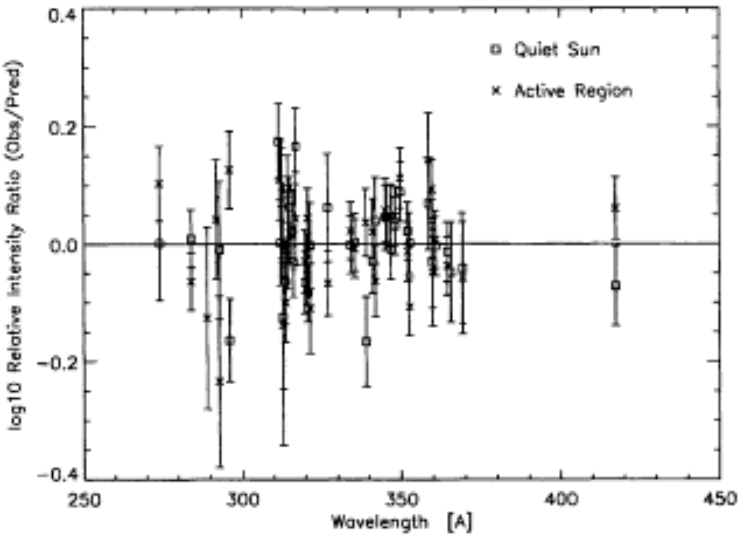

Figure 1. The ratio of intensity predicted by the best-fit DEM to the observed intensity for each of the 26 strong lines used to constrain the DEM. This level of agreement is typical of attempts to extract DEMs from observed spectra. (Figure taken directly from (Brosius, Davila et al. 1996)).

While the scatter is not insignificant, it is small enough to suggest that the assumptions that go into using a DEM are not wildly inconsistent with the reality of the solar atmosphere. Therefore DEMs derived in this way are considered fairly reliable descriptions of the state of the corona

along the observed line of sight. However, there are a number of serious drawbacks to using a spectrograph to measure DEM:

- Field of view: a slit spectrograph has an extremely narrow field of view (only one pixel wide). This can be increased by widening the slit or rastering the spectrograph, but only at the cost of spatial resolution and time resolution;

- Spatial resolution: The best solar EUV spectrographs today – SUMER (Wilhelm, Curdt et al. 1995) and CDS (Harrison, Sawyer et al. 1995) on SOHO, and the SERTS rocket (Thomas and Neupert 1994) – have nominal spatial resolution of 1-10 arc seconds; however, obtaining enough counts in enough lines to measure a DEM generally requires averaging over a much larger area;

- Time resolution: The cadence of these spectrographs is generally on the order of minutes for each pointing; rastering the slit increases the time required substantially;

- Computation time: Finding the DEM that optimizes the fit between predicted and observed line intensities generally takes less than a minute on a fast computer – trivial if only a single DEM is desired, but prohibitive if the DEM is to be found point-by-point over a large field of view with high spatial resolution and time cadence.

In short, spectrographic observations are best suited to measuring a single DEM that describes representative conditions in an average field of view, rather than characterizing particular structures or events. This vagueness, combined with the difficulty of obtaining well-calibrated spectrograms, means that very few temperature-broad, reliable DEMs have ever been measured (the CHIANTI database still makes use of standard “active region” and “quiet sun” DEM functions, which are defined based on averages of spectra taken by (Vernazza and Reeves 1978) in 1973; the well-calibrated observations by the SERTS rocket (Neupert, Epstein et al. 1992) produced single representative active-region DEMs from its flights in 1991 and 1993, which are also widely used).

While deriving DEM in this way is certainly no mean feat, such average DEMs are of limited use. First, averaging emission over a large area increases the likelihood that one or more of the assumptions involved in using a DEM to model that emission will break down. Second, as pointed out in (Aschwanden 2002), observations with a spatial resolution worse than 1 arc second cannot reliably isolate individual coronal loops. Therefore, broadly-averaged DEMs obtained by spectrographs with a resolution of 10-20 arc seconds will never be able to answer fundamental questions about the basic building blocks of the solar atmosphere.

Every time technology has advanced in order to allow us to see the corona with higher resolution, we have found more fine structure and more dynamic phenomena. Clearly the formation and heating of the corona is governed by highly localized processes that take place very quickly; it is impossible to understand the corona without studying it at small spatial scales and with fast cadence. At the same time, a large field of view is also necessary, as the solar atmosphere is both unpredictable and capable of supporting enormous structures spanning hundreds of megameters. Currently, multilayer telescopes are the only instruments that can offer any hope of seeing small details over the full solar disk with a high time cadence.

1.3.3 DEM AND MULTILAYER OBSERVATIONS

Unfortunately, multilayer telescopes, unlike spectrographs, do not return data that can easily be reduced to a tabulated set of emission line intensities. Therefore, it is not trivial to extract a DEM from multilayer observations; quantitative analysis of multilayer images is generally far more limited in scope. However, because the pixel values in a multilayer image (Equation 1) are essentially determined by line emission (Equation 2), and thus by the DEM of the observed plasma (Equation 5), we can attempt to recover a DEM from a set of multilayer observations. The following section describes how multilayer observations depend on DEM.

The Instrument Temperature Kernel

We begin by substituting Equation 2 into Equation 1, setting the continuum intensity $I_{cont}(\lambda)$ to 0, and integrating over all lines of sight that are directed to a particular pixel by the telescope:

$$p_i(\mathbf{x}) = \int_0^\infty \eta_i(\lambda) \sum_{X,m,j,k} I(\lambda_{jk}^{X+m}, \mathbf{x}) \delta(\lambda - \lambda_{jk}^{X+m}) \mathrm{d}\lambda \qquad [\text{counts s}^{-1}]$$

where $I(\lambda_{jk}^{X+m}, \mathbf{x})$ is now the line-of-sight emission line intensity averaged over the pixel. The delta function is an approximation, acceptable here because the widths of the emission lines are smaller by a factor of ~100 than the bandwidths of EUV multilayers; it allows us to write

(Equation 6) $$p_i(\mathbf{x}) = \sum_{X,m,j,k} \eta_i(\lambda_{jk}^{X+m}) I(\lambda_{jk}^{X+m}, \mathbf{x}) \qquad [\text{counts s}^{-1}]$$

That is, the pixel value is just the sum of the intensity of all the coronal emission lines, weighted by the efficiency function of the telescope at the wavelength of the line.

We now substitute the definition of line intensity from Equation 5 into Equation 6, and pull the sum over all lines inside the integral over temperature to write

$$p_i(\mathbf{x}) = \int_0^\infty \sum_{X,m,j,k} \eta_i(\lambda_{jk}^{X+m}) G_{jk}^{X+m}(T) DEM(T, \mathbf{x}) \mathrm{d}T$$

This equation is identical in form to Equation 5 (although here the fact that the variation of intensity along different lines of sight is entirely due to spatial variations in the DEM is made explicit). We can take advantage of the similarity to define a *temperature kernel* function for the instrument:

$$K_i(T) = \sum_{X,m,j,k} \eta_i(\lambda_{jk}^{X+m}) G_{jk}^{X+m}(T)$$

The temperature kernel is simply the sum of the contribution functions of all the lines in the telescope bandpass, weighted by the efficiency of the telescope at the wavelength of each line. With the temperature kernel acting as a sort of multi-line contribution function, we can see that the quantity measured by a multilayer telescope – pixel value – is determined by combining basic

atomic physics with a description of the global state of the plasma in exactly the same way that emission line intensities are determined. That is, we can write

(Equation 7) $$p_i(\mathbf{x}) = \int_0^\infty K_i(T) DEM(T, \mathbf{x}) \mathrm{d}T \qquad [\text{counts s}^{-1}]$$

This suggests that a set of multilayer observations can be used to measure DEM in exactly the same way that spectrograms have been.

The temperature kernel defined above is exactly the same as the instrument response function $R(T)$ described in (Aschwanden, Schrijver et al. 2001), among other places. The function is sometimes calculated by discretizing temperature and sampling at a number of different temperatures T_j, rather than by performing the weighted sum of the line contribution functions. First, a set of spectra $I(\lambda, T_j)$ are generated using discrete isothermal DEMs:

$$DEM_j(T) = D_0 \delta(T - T_j)$$

Then the isothermal spectra are folded through the instrument bandpass to find the instrument's response to plasma at a particular temperature, i.e.

$$K_i(T_j) = \frac{1}{D_0} \int_0^\infty \eta_i(\lambda) I(\lambda, T_j) d\lambda$$

This is the method used by (Weber, DeLuca et al. 2004), among others. It has the advantage of including the effect of the continuum in the isothermal spectra (the continuum is set to 0 in the weighted-sum method). However, the contribution of the continuum is insignificant at EUV wavelengths, and the weighted-sum method is more intuitive and provides more insight into the importance of the various components of an instrument's response.

Chromospheric Instruments

Note that some of the narrowband telescopes carried by EIT, TRACE and the MSSTA probe the chromosphere and lower transition region, rather than the upper transition region or corona. These instruments are not susceptible to temperature kernel analysis because the processes responsible for the bulk of the emission in their bandpasses do not obey the 6 assumptions of

section 1.3.2 (not even in the approximate fashion that we consider acceptable for the coronal bandpasses).

For one thing, chromospheric plasma is not necessarily in LTE (due to ambipolar diffusion, among other effects). More importantly, the opacity of the solar atmosphere is much higher at FUV wavelengths, and at the 304 Å He II line imaged by EIT, than it is at most EUV wavelengths. Therefore, the assumption that the emitting plasma is optically thin is much more likely to break down. Because the line of sight integral for pixels in 1600 Å, 1216 Å, or 304 Å images is more complicated than for other multilayer bandpasses, these chromospheric instruments do not see the same plasma that the other telescopes see, and combining their measurements with those of the coronal telescopes is not straightforward. Furthermore, the far ultraviolet (FUV) emission imaged by the 1216 Å and 1600 Å telescopes on MSSTA and TRACE contains a substantial continuum component. The different observational constraints involved in analyzing FUV and EUV emission are detailed further in section 2.4.1

Observation and analysis of the connection between chromospheric and coronal plasmas has always been a primary goal of the MSSTA (Boerner, Walker et al. 1999); the quality of the chromospheric images obtained in flight ensures that the MSSTA dataset can potentially provide some insight into that connection. However, such analysis is essentially outside the scope of this work.

Requirements for Using Temperature Kernels

It is clear from Equation 7 that multilayer images can provide insight into the coronal DEM at every point on the solar disk in much the same way that spectrographic observations currently do for broadly-averaged regions, provided an adequate set of instrument temperature kernels $K_i(T)$. Of primary importance is the accuracy of these temperature kernels. In the EUV, where a useable instrument temperature kernel can be defined, its accuracy depends on the accuracy of its two ingredients: the bandpass efficiency function of the instrument, and the contribution functions of the relevant emission lines. Obtaining a good measurement of the bandpass efficiency requires detailed knowledge of every component of the instrument. Meanwhile, the line contribution

functions depend on the accuracy of various measured and calculated parameters of the emitting ions, and the validity of the 6 assumptions described in the previous section that go into the definition of the contribution function itself.

Thus, the basic requirements – knowledge of the instrument and of the underlying atomic physics – and the fundamental uncertainties involved in quantitative analysis of line-of-sight emission from an optically thin plasma are the same for both spectrographs and narrowband telescopes. However, using a suite of instruments is a little more complicated than measuring multiple lines from a single instrument. Since each bandpass in a multilayer dataset essentially plays the role of a single emission line, an assortment of bandpasses with accurate temperature kernels is essential to constrain the DEM over a range of temperatures. Maximizing the diagnostic capability of multilayer telescopes demands a dataset consisting of high-resolution images from a large number of separate, well-calibrated bandpasses.

1.3.4 APPLICATIONS OF TEMPERATURE KERNELS

Unfortunately, such a dataset did not exist prior to the flight of the MSSTA III. The most comprehensive narrowband images came from EIT and TRACE, each of which carries three coronal telescopes with bandpasses centered at 171 Å, 195 Å and 284 Å. Images and movies from those satellites have yielded great advances in our understanding of the solar atmosphere; but with only three separate bandpasses, their ability to yield quantitative information about the thermal structure of the corona is severely limited.

Nevertheless, the literature is full of investigations into the temperature of the corona based on multilayer images from TRACE and EIT. The most common approach is the filter ratio method (e.g. (Wheatland, Sturrock et al. 1997), using soft x-ray observations from Yohkoh; (Neupert, Newmark et al. 1998), using EIT 171 and 195 Å images; (Testa, Peres et al. 2002), who combined TRACE 171 and 195 Å data with forward modeling; and [(Aschwanden, Newmark et al. 1999), (Aschwanden, Alexander et al. 2000)], which used all three EIT bandpasses, though never all three at the same time). This technique requires the assumption that the line of sight to a given pixel passes through plasma at a single temperature; in that case, then the ratio of pixel

values $R_{ij}(T)$ in each of two narrowband images i and j is simply a function of that temperature, found by taking the ratio of the instrument temperature kernels:

$$R_{ij}(T(\mathbf{x})) = p_i(\mathbf{x}) \Big/ p_j(\mathbf{x}) = K_i(T) \Big/ K_j(T)$$

For a set of three narrowband observations of a pixel, two independent filter ratios can be measured; the filter ratios for EIT's 171, 195 and 284 telescopes are shown in Figure 1. The filter ratio temperature T_j^i of a pixel is found by inverting $R_{ij}(T)$.

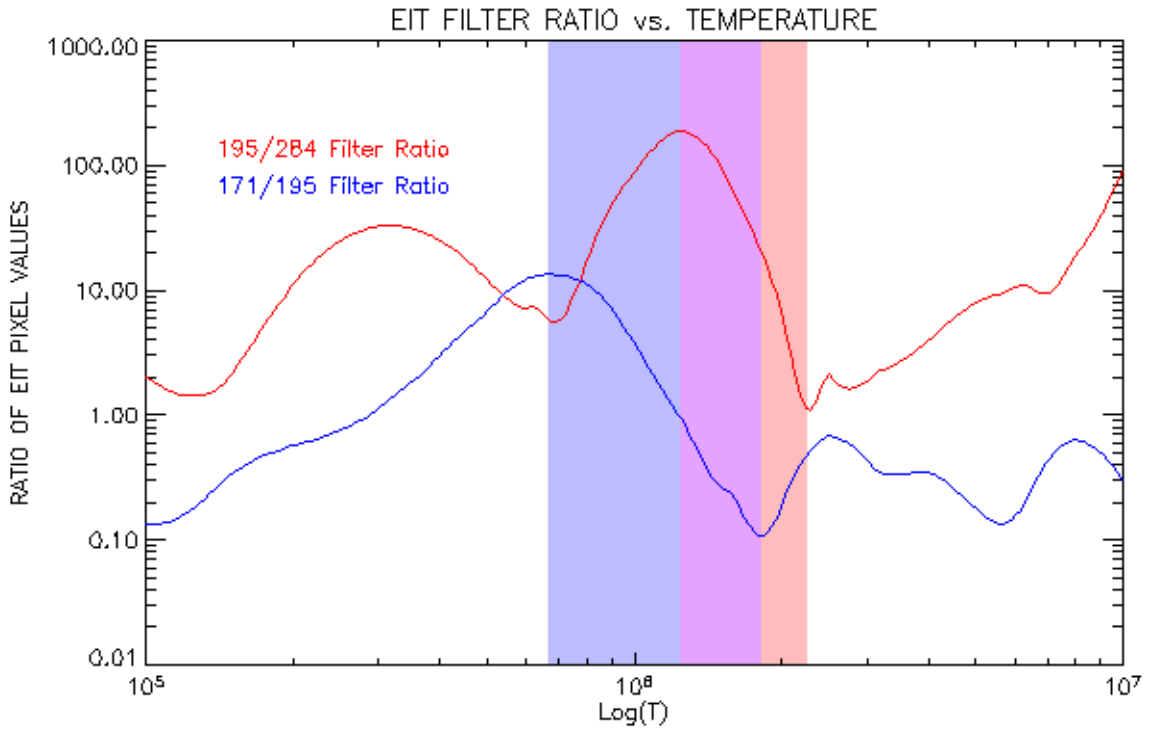

Figure 2. Filter ratios used to measure temperature from EIT observations. The shaded regions indicate the range over which each of the two filter ratios is considered valid (in that the ratio is unique, and each bandpass reasonably responsive). Only in the purple region from T ~ 1.2 MK – 1.8 MK is it possible to obtain two independent measures of plasma temperature.

The numerous drawbacks to the filter ratio method are obvious. First, as illustrated in Figure 1, $R_{ij}(T)$ is seldom a unique function of temperature, so there is generally confusion about the temperature implied by a given filter ratio. Of course, the sensitivity of narrowband telescopes is rather strongly peaked in temperature, so they are unlikely to see substantial contributions from

plasma at a very different temperature from the peak of their bandpass, but still, the difficulty in inverting $R_{ij}(T)$ is inconvenient.

Much more problematic is the assumption of isothermality that must be made before even attempting to measure temperature from a filter ratio. Because the solar atmosphere is highly structured and optically thin at EUV wavelengths, a given line of sight will generally pass through a large number of different plasma elements which are unlikely to be at the same temperature, all of which will contribute to the observed emission. It may be possible, by undertaking painstaking searches for well-isolated loops extending above the solar limb and carefully subtracting the background (Del Zanna and Mason 2003), to find a few pixels whose emission is dominated by a single structure. Even then, however, there is no guarantee that all the plasma along the column-of-sight to that pixel is at the same temperature. As noted in (Martens, Cirtain et al. 2002), the mean free path of electrons in the corona is ~300 km along magnetic field lines, and on the order of centimeters transverse to field lines. Therefore, it must be acknowledged that, even with the best resolution available today – about 1 arc-second, or ~750 km, from TRACE – a particular pixel can contain many separate, thin loop fibrils at different temperatures.

Yet the filter ratio method will always report a single temperature for each pixel. In fact, a given filter ratio always seems to report the same temperature, which is generally midway between the peak response temperatures of the two filters. For example, measurements of the 171/195 Å filter ratio consistently produce temperatures T_{195}^{171} ~ 1.3 MK in a wide variety of structures, and at all points along those structures (e.g. (Lenz, DeLuca et al. 1999) measured four coronal loops at four points each with TRACE's 171 and 195 Å bandpasses; all 16 measurements found the same temperature to within a fraction of the error bars). In the few instances where multiple separate filter ratios have been measured for the same pixel, they do not agree. In (Schmelz, Beene et al. 2003), both EIT filter ratios were measured simultaneously along a number of loops. In all measurements, T_{195}^{171} was ~1.3 MK and T_{284}^{195} was ~1.9 MK for the same pixel.

Assuming that a pixel images isothermal plasma is not only an oversimplification; it will, in general, destroy our ability to extract information about the true temperature structure of the

plasma along that column-of-sight. The DEM of a given pixel contains full information about the distribution of temperatures in that pixel, and can in general be expected to be a broad, complicated function. Requiring the pixel to be isothermal and using a filter ratio to measure a single temperature is not a useful approximation in cases where the pixel actually contains a broad range of temperatures; it does not, say, give insight into the temperature at which the pixel's DEM peaks, or the weighted mean of the DEM. As demonstrated by (Martens, Cirtain et al. 2002), a broad DEM will always produce constant filter ratio temperatures, whose values have more to do with the instruments themselves than with the plasma.

With three bandpasses to choose from, it is not necessary to assume isothermality. Making an isothermal approximation requires two observations to constrain its two variables – temperature, and emission measure at that temperature. With three observations, we can add in more variables, and thereby capture more of the subtlety of the temperature structure. For example, (Zhang, White et al. 1999) constructed a two-component model of the solar atmosphere using four variables – the temperatures and emission measures of the hot and cool components – which they constrained with the three EIT bandpasses and a set of (rather broad) assumptions. While this approach is intriguing, it is badly underconstrained; the technique has difficulty reproducing even conservative (*i.e.* relatively smooth) artificial DEMs, and is highly sensitive to noise. The model results of (Zhang, White et al. 1999) do not constitute a substantially better estimate of the DEM than those obtained from filter ratios.

Indeed, any attempt to measure the temperature structure of even a very well-resolved (half arc-second) pixel by inverting observations in three independent bandpasses is doomed to fail amid non-uniqueness and invalid assumptions. An alternative approach is to use forward modeling to attempt to reproduce the pixel values seen in multilayer images. In this case, rather than try to extract the DEM from the observations, an artificial set of observations is generated from a model of the physical state of the plasma, and compared to the true observations. Then the parameters of the model are adjusted to optimize the correlation between observed and expected pixel values. This technique can be very powerful, and has the advantage that it goes straight to the underlying physics. Rather than attempting to parameterize the DEM in terms of the observations, it allows the investigator to directly tune the actual conditions in the corona – the reconnection rate, say, or the plasma density, or whatever variables allowed by the model – in order to match the data.

For example, (Aschwanden, Schrijver et al. 2001) calculated hydrostatic loop models that were able to reproduce a set of TRACE 171 Å and 195 Å observations. They found that only models of essentially isothermal loops in which the heating of the coronal plasma took place at the base of the loops were able to match the data; loops heated uniformly along their length, or near their tops, produced intensity profiles that were inconsistent with those seen by TRACE. These findings constitute some of the strongest observational evidence to date for the location of coronal heating, and demonstrate how forward modeling can extend the utility of the limited observations currently available.

However, the fundamental limitations that apply to inverting a set of observations are not erased by taking a forward approach to the problem. Forward models must be fairly simple, if they are being compared to a small data set. In particular, loop models generally assume that only one, or perhaps a few, structures contribute to the flux seen by a given pixel; otherwise, the model complexity grows to the point where it has enough flexibility to trivially reproduce any observations. Yet the corona is not simple, and most pixels contain huge numbers of structures. Background subtraction remains essential, but background subtraction is difficult off the limb and nearly impossible at the center of the solar disc. There is no reason to believe that a simple model can accurately describe the flux seen in the vast majority of pixels in a multilayer image.

Furthermore, even in cases where a simple model might reasonably apply, the fact that a particular model reproduces a limited set of observations is not entirely compelling. While the inability of a class of models to reproduce the observations is telling, there is no guarantee that a successful forward model is a unique solution. Even if the optimized parameters of the model satisfy the most rigorous tests of uniqueness, perhaps the model itself is flawed. If another, entirely different model is able to reproduce the same observations equally well, there is no way to distinguish between the two without more observations. Thus the conclusions obtained from forward models must be viewed with caution.

In the case of the loop models of (Aschwanden, Schrijver et al. 2001), it may be premature to conclude that their ability to match TRACE observations only with loops heated at their bases proves that the corona is heated near its interface with the chromosphere. Alternative models,

such as the nanoflare picture of (Cargill and Klimchuk 2004), predict stochastic heating all along the loop; this model leads to multithermal loops whose broad DEM has a roughly power-law slope. The nanoflare model has not yet been tested as rigorously as the base-heated isothermal models (Aschwanden, Schrijver et al. 2001). However, as noted by (Schmelz, Beene et al. 2003), broad DEMs such as those predicted by assuming multi-threaded, uniform-heated loops can produce the constant filter ratios just like those used to constrain the models of (Aschwanden, Schrijver et al. 2001).

Thus some of the central questions in solar physics – are individual coronal loops isothermal or not? Where does the heating of the corona take place? – remain unanswered. What is most frustrating is not simply that they are unanswered, but that different datasets seem to be providing different, but equally clear, answers at the same time. Spectral observations consistently find a broad DEM, implying multithermal loops (probably heated along their length) at even the smallest spatial scales they can see, while highly-resolved narrowband images suggest that loops are isothermal (and thus most likely heated at their footpoints). Proponents of spectral observations suggest, quite correctly, that a set of three narrowband images is insufficient to prove that a given plasma element is isothermal. Proponents of multilayer observations counter, equally correctly, that the poor spatial resolution of the current generation of spectrographs is responsible for the broad temperature distributions they find, while the fundamental loops are only resolved by narrowband imagers.

Clearly, what is needed is a way to obtain detailed temperature information about the corona – much more detailed than what is available from the three EUV bands of TRACE and EIT – at very small spatial and temporal scales – much smaller than those probed by CDS or SUMER. We have already specified that a suite of high-resolution, temperature-separated multilayer bandpasses is desirable. More specifically, though, we now see that we need enough bandpasses that their temperature kernels allow for an accurate measurement of the coronal DEM. The data must be sufficient to constrain the DEM over a broad temperature range, without making any additional assumptions beyond those that go into defining the DEM.

For it is crucial to point out that most forward models of the corona do not get around the uncomfortable necessity of using the DEM and all the dangerous assumptions described in

Section 1.3.2. Generating a set of theoretical observations to compare with the data means asking the physical model to produce a DEM, and using that DEM to predict line fluxes with Equation 5. Therefore, if a technique can be developed to extract an optimized DEM from a set of observations, it can be still be used to constrain forward models. If the DEM extraction technique itself is reliable, flexible, unique and robust to noise, it is the best of all possible worlds: the resulting function contains all the information about the temperature structure of the plasma along a line of sight that can possibly be extracted from a set of observations with temperature-kernel type instruments.

Extracting spatially-resolved DEMs from high-resolution multilayer images is the holy grail of solar EUV observations; it is similar to the pursuit of other holy grails (Malory and Cooper 1998) in that even failure to achieve the final goal can be illuminating. And failure is a possibility: even if we can develop a technique that should be able to recover the DEM from a set of observations, a technique that consistently reproduces artificial data under realistic conditions, we may find that this technique is incapable of recovering a DEM from actual data. There may not be a DEM function that reproduces all the observations of a given pixel to within their experimental errors. In that case, we will have demonstrated (and, indirectly, measured) inaccuracies in either the instrument calibration or the assumptions and parameters underlying our line flux calculations.

The possibility of failure, and the corresponding ability to identify the limits of the data and analysis technique, is the one of the central advantages of using a DEM-extraction approach before attempting any modeling. If a forward model fails to reproduce observations, its failure is generally taken as proof that the physical model itself is invalid. However, since most models rely on producing DEMs to simulate observations, knowing whether there exists a DEM that can reproduce the data is vital to interpreting the results of a modeling effort. If a DEM can be found, the model output can be compared with that DEM before it is checked against the observations. If not, then negative results from forward models can be disregarded, and new observations or assumptions are necessary.

Previous analyses of multilayer observations have been restricted by the limited number of bandpasses to making approximate and rather dubious estimates of the temperature structure of the emitting plasma. Ultimately, their results tend to be either internally inconsistent (as when

multiple filter ratios report different temperatures for the same pixel) or trivial (as when a single filter ratio finds isothermal plasma everywhere). Such findings say more about the assumptions that go into the analysis than they do about the data themselves. Only by extracting a full DEM spanning the range to which the instruments are sensitive, or determining that there is no such DEM capable of reproducing the observations, can we fully realize the temperature diagnostic capability of narrowband instruments.

1.4 Summary

A cartoon summarizing the proposed approach to analysis of multilayer observations is shown in Figure 3. Beginning with raw images of the solar corona, we create a set of calibrated images. Currently, that is where the processing of data from multilayer instruments stops; it is up to each investigator to create a model of the solar atmosphere visible in those images, use that model to predict a DEM, and fold that DEM through the instrument temperature kernels for comparison with the observations (following the red arrows). Instead, we propose to take the path indicated by the blue arrows, and use the calibrated images and knowledge of the instrument temperature kernels to derive a unique DEM that fully describes the state of the coronal plasma. The essential difference between the two approaches is that our proposed path will answer the question of whether any DEM is observable; if it is, it will provide an estimate of how well-constrained that DEM is. The majority of the work conducted with multilayer images has proceeded without this knowledge, and the success or failure of this work to reproduce the observations has lead to conclusions that, upon closer examination, the data do not fully support.

The items in circular icons in Figure 3 all correspond to potential sources of error – statistical noise in the raw images, uncertainties in the calibration measurements on the film, mirrors and filters, and breakdowns in the assumptions or the accuracy of the atomic physics. Whatever path is followed, these errors must be monitored, understood and minimized. In the following chapter, I will explicitly describe my efforts to measure and reduce the calibration errors of the MSSTA III.

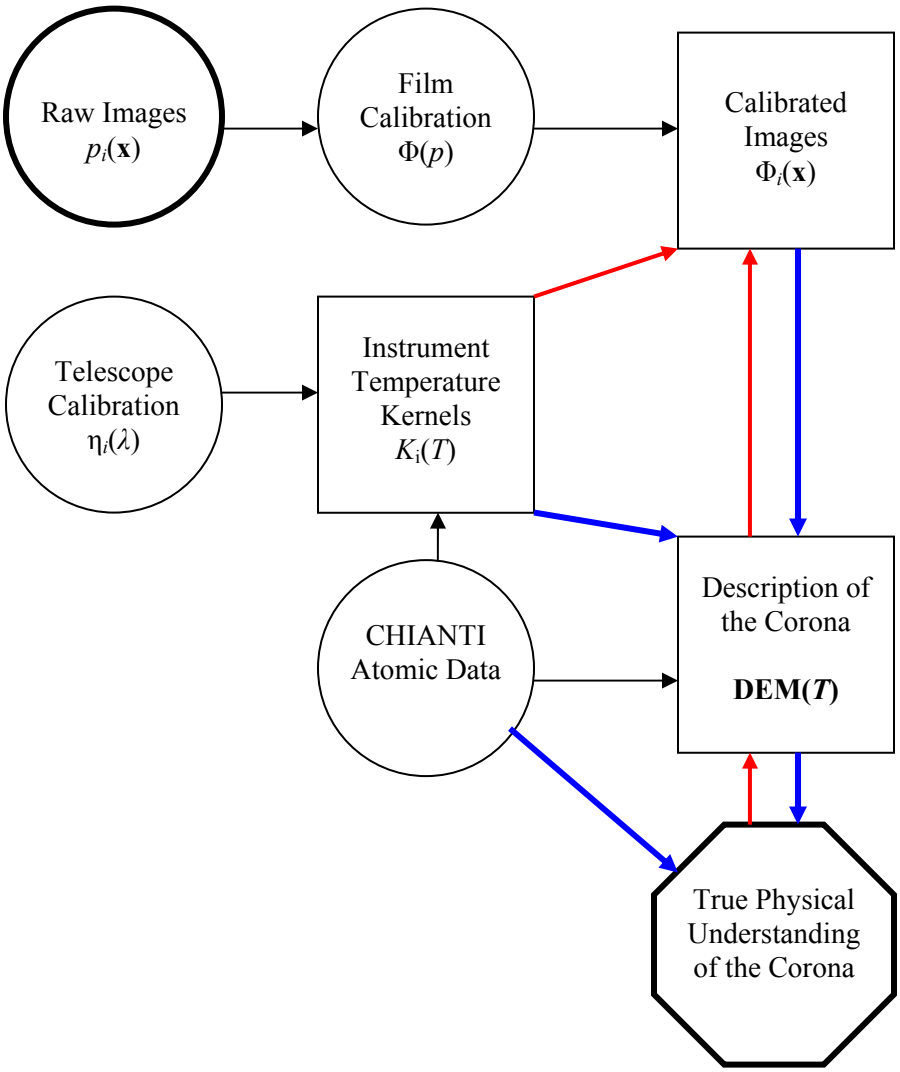

Figure 3. Schematic depiction of how EUV spectroheliograms can lead to a better understanding of the solar atmosphere. Conventional analysis follows the red arrows; we hope to create a more rigorous and streamlined approach following the blue arrows.

2 Design and Pre-Flight Calibration

2.1 Overview

2.1.1 INTRODUCTION

The essential approach of the MSSTA in all its incarnations has been to obtain simultaneous images of the solar disk in as many different UV bandpasses as possible, sometimes at the expense of producing a single image with extremely high spatial resolution, signal-to-noise, or accurate calibration. The current generation of EUV observatories, including EIT and TRACE, have improved on the MSSTA's performance in a number of areas: they deliver high-resolution, high-cadence images, and have enabled exciting studies of coronal dynamics and energy flows [e.g. (De Pontieu, Berger et al. 1999), (Schrijver, Aschwanden et al. 2002)]. But they are limited to three or fewer coronal bandpasses, and (in the case of TRACE) cannot take simultaneous images at different wavelengths or see the full disk at once. The truly multi-spectral philosophy of the MSSTA means that it is uniquely capable of diagnosing the state of the corona over a broad temperature range and at numerous locations on the disk at one instant of time.

As discussed in the previous chapter, taking advantage of this capability to generate spatially-resolved coronal DEMs imposes two requirements:

- Bandpass selection: the payload must produce images in enough different EUV bandpasses to constrain the DEM over a broad temperature range. Ideally, the bandpasses should produce temperature kernels that are narrow and well-spaced in temperature; however, double-peaked or redundant temperature kernels provide useful consistency checks and are helpful in dealing with noise.
- Calibration: The instruments must be accurately calibrated, as the inversion problem is extremely sensitive to error.

These considerations were central to the planning of the MSSTA III.

In this chapter, I will discuss the design of the payload, focusing on the selection of telescope bandpasses for optimal coverage of coronal temperatures. I will then give a detailed step-by-step account of the calibration of the MSSTA telescope mirrors, filters and film. Understanding the calibration, and knowing to what extent and in what ways its accuracy may be limited, is essential to interpreting MSSTA data. Finally, I will present the temperature kernels of the MSSTA telescopes, along with an assessment of the uncertainty associated with each.

2.1.2 DESIGN OF THE MSSTA III

The MSSTA payload is, by design, modular and reconfigurable. The truss is essentially an open support structure with enough mounting surfaces to attach 20 or more instruments. Indeed, the MSSTA II attempted to make full use of the truss's flexibility by incorporating 19 different telescopes (Figure 4). Unfortunately, only 5 of these telescopes produced high-quality images. A discussion of the failure of the other instruments can be found in (Martínez-Galarce), but the complexity of the payload clearly made it difficult to ensure that each instrument would function properly. In particular, the small Herschelian telescopes (those with apertures of 25-30 mm) generally shared cameras and filters with each other, greatly increasing the difficulty of payload integration while offering limited scientific return. Early in the design of the MSSTA III, we decided to limit the instrument suite to 11 telescopes, all with apertures of 60 mm or larger.[1]

Originally, two of these telescopes were to feed grating spectrographs to probe the 170-180 Å region and the 2800 Å Mg II complex with high spectral resolution. The EUV spectrograph design used a Herschelian primary and a multilayer-coated grating in a Wadsworth configuration, and would have been the first instrument of its kind used for solar research (Boerner, Walker et

[1] A single small Herschelian from the MSSTA II payload, centered at 94 Å, was added to the MSSTA III during final integration; this is briefly discussed in section 3.1.1.

al. 1999). However, time pressure and manpower shortages led us to scrap both spectrographs, and to replace them with more straightforward imaging telescopes. This was a disappointing compromise; imaging spectroscopy of the solar atmosphere is badly needed, and the MSSTA has potential as a platform for testing such instruments. Nevertheless, the decision to fly 11 telescopes of moderate aperture, and to avoid the inclusion of smaller telescopes or more complicated spectrographs, resulted in a payload that was well-focused on addressing the questions raised in Chapter 1.

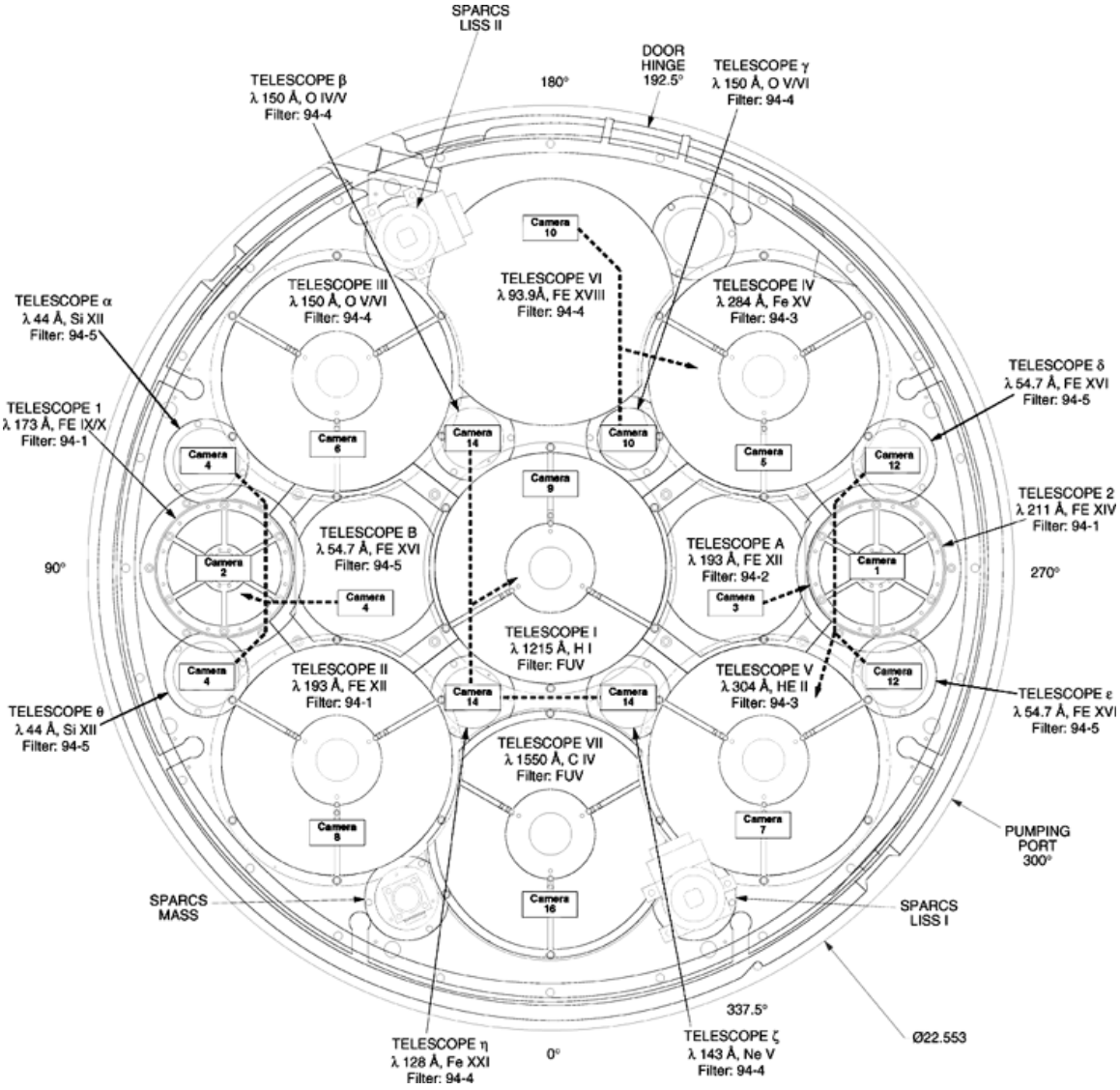

Figure 4. Front aperture view of the MSSTA II, showing the placement of the 19 telescopes it pointed at the sun during its flight in 1994. For the MSSTA III, all of the small (aperture < 60mm) telescopes were abandoned in order to focus on the 11 large telescopes. Drawing taken from (Hoover, Walker et al. 1992).

Bandpass Selection

The only remaining question was what bandpasses should be used for the 11 telescopes. Two slots were reserved for the 127 mm-aperture FUV telescopes that had flown on both previous MSSTA missions (centered at 1216 Å H Ly α and 1550 Å C IV). These instruments had delivered excellent data on both flights. The 1216 Å image had proven particularly valuable in the analysis of x-ray bright points identified from the MSSTA I data [(Kankelborg, Walker et al. 1996), (Kankelborg, Walker et al. 1997)], and there is no other source of well-filtered Lyman α spectroheliographs. Of course, the FUV telescopes pose a number of challenges; they are not directly useful in DEM analysis, as the solar FUV radiation violates many of the underlying assumptions developed in Chapter 1; and they require entirely separate calibration and alignment techniques from the EUV telescopes, as described later in section 2.6. In fact, neither FUV instrument was fully calibrated; nevertheless, they were seen as indispensable to the mission.

While FUV optics are robust, so that the age of the 1550 Å and 1216 Å telescopes was not a source of concern, advances in multilayer technology and the frailty of thin-film filters made it inadvisable to re-fly any of the EUV telescopes from previous MSSTA missions. Thus we had to choose 9 EUV bandpasses, and design multilayer telescopes for each, in order to maximize our ability to diagnose the state of the coronal plasma.

A similar exercise was carried out for the design of the MSSTA II (Plummer, DeForest et al. 1994), relying heavily on the investigators' experience and knowledge of the solar EUV spectrum. While we had less experience to call on in choosing instruments for the MSSTA III, we did have access to the CHIANTI database, which can be used to generate temperature kernels from an assumed instrument bandpass given any of a variety of assumptions. A suite of IDL procedures was written to implement a "brute force" approach to bandpass selection. First, a set of idealized bandpass candidates was generated. These took the form of Gaussians centered at all wavelengths from 50 – 300 Å, in 1 Å steps. The amplitude (peak reflectivity) of the Gaussian and FWHM were made to be functions of wavelength, based on a few rules of thumb about multilayer performance:

- Multilayer reflectivity peaks at around 60% for 131 Å (an important wavelength in EUV lithography), declining sharply on the high-energy side. We modeled this by setting peak

reflectivity for a bandpass centered at λ to $R_{max}(\lambda) = 0.6 \times (131\ Å / \lambda)^k$, where k = 1 for λ ≥ 131 Å and k = -2 for λ < 131 Å.

- The FWHM of a multilayer bandpass is ~7 Å at 171 Å; it gets much narrower at short wavelengths, as the energetic photons penetrate deep into the multilayer stack. We modeled this by setting the bandpass FWHM = λ/25.

These assumptions gave reasonable approximations to the expected parameters of the multilayers.

Then, a temperature kernel for each of the bandpass candidates was generated, and the set of temperature kernel candidates was examined. We looked for kernels that featured strong, narrow peaks in temperature (indicating telescopes that produced unambiguous, almost isothermal images); we also required that the instrument's response at its peak be strong enough to ensure a usable image from at least a solar active region. While there was no shortage of candidate lines offering strong peaks in the Log(T) = 6.0 – 6.2 range, we struggled to find wavelengths that could probe the UTR at temperatures from 5.5 – 6.0 without contamination (and with sufficient sensitivity to guarantee results, given that the UTR emission is not as strongly enhanced in active regions as coronal emission).

The final selection was, inevitably, somewhat subjective. We left out some very strong coronal lines in hopes of broadening the temperature coverage of the payload into the UTR. Some secondary issues also factored into the bandpass selection – for example, the Mg X line at 58 Å was chosen for study even though it essentially duplicated the temperature response of Fe X 180 Å. It was decided that such redundancy offered a valuable cross-check, and could be useful in assessing the validity of assumptions about relative abundances. Also, the relatively short wavelength represented a challenge to the ability of multilayers to operate in the x-ray regime, offering an excellent opportunity to demonstrate the advantages of new multilayer deposition techniques.

The nine candidate bandpasses chosen for flight are plotted against a synthetic active region spectrum from CHIANTI in Figure 5. In Figure 6, the temperature kernels of these bandpasses are displayed. The actual temperature kernels for the EUV instruments based on these bandpasses are derived and plotted in section 2.6.1.

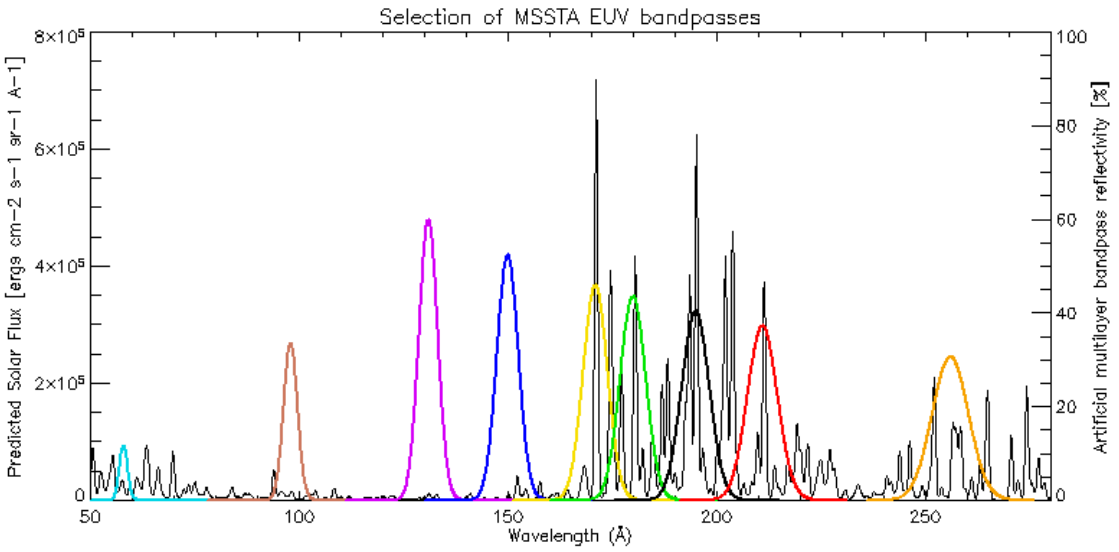

Figure 5. Synthetic spectrum of a solar active region generated with CHIANTI; plotted in red are the idealized Gaussian bandpasses used to select the 9 EUV telescopes of the MSSTA III.

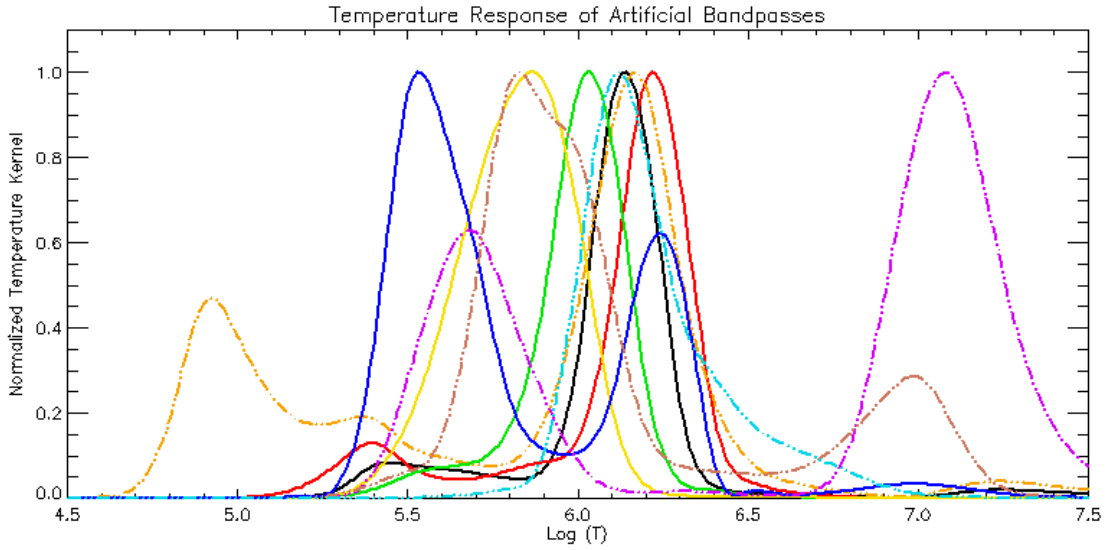

Figure 6. Approximate relative temperature kernels of the MSSTA III EUV telescopes, generated using artificial Gaussian bandpasses. These curves are useful only as a quick look at the bandpass; actual temperature kernels based on measurements of the flight instruments are presented in section 2.6.1.

The technique of discretizing the temperature kernels into an instrument response matrix and analyzing the singular value decomposition of that matrix was not employed, but probably would have been helpful. As discussed in section 4.1.2, the SVD is an excellent way to discover how much information can be extracted from a set of observations based on knowledge of the

instrument used to obtain those observations. It can also provide insight into, for example, what temperatures are well-constrained by a particular set of candidate instruments. The diagnostic ability of the MSSTA instrument package, and some supplements and alternatives, are discussed quantitatively in section 4.2.3.

Instrument Assignment

The front aperture of the MSSTA has slots for 7 telescopes of 127 mm aperture, two of ~100 mm aperture, and two more of 63.5 mm. The truss is configured to use single-reflection Herschelian telescopes, with primary mirrors mounted on the rear bulkhead and back-facing cameras in the middle of the payload, for the 100 mm and one of the 127 mm slots; the other instruments are all two-reflection Ritchey-Chrétien telescopes in self-contained tubes. We divided up the 9 chosen EUV bandpasses among these optical configurations as follows:

- The FUV telescopes are already assembled using 127 mm Ritchey-Chrétien layouts. The 150 Å instrument uses the standard 1000 mm-long, f/28 optics set employed by most of the large Ritchey-Chrétien, while the 1216 Å instrument is built in a slightly shorter, faster tube (800 mm, f/20) designed to mount in the center slot on the payload.

- Solar emission at our short wavelength lines (58 Å, 98 Å, and 131 Å) is fairly weak, and the multilayers are relatively inefficient below 100 Å. Therefore, these three lines were assigned to the Herschelian systems, which offer much faster focal ratios (f/8 – f/15, rather than f/28 or more) than the Ritchey-Chrétiens, along with relatively high efficiency (because they use only a single reflection). The 131 Å bandpass was designated as the highest priority of these 3, and was therefore assigned to the lone 127 mm Herschelian, leaving the 58 Å and 98 Å telescopes on the two 100 mm Herschelians.

- High-resolution images in the 171 Å bandpass were not seen as a high priority, as they are widely available from EIT and TRACE. Rather, the MSSTA 171 Å telescope was primarily chosen to make cross-calibration with those instruments possible. Therefore, it was assigned

to one of the small 63.5 mm f/31 Ritchey-Chrétien telescopes. The 180 Å bandpass was chosen to complement the 171 Å, and was assigned to the other small Ritchey-Chrétien.

- The remaining bandpasses (150 Å, 195 Å, 211 Å and 256 Å) were assigned to 127 mm f/28 Ritchey-Chrétien telescopes. These were generally the highest priority instruments on the MSSTA, as they offer the best combination of photographic speed and resolution capability.[2]

A summary of the 11 telescopes selected and flown on the MSSTA III is presented in Table 1.

All the EUV optics were fabricated from Zerodur, figured and flow-polished by Phil Baker of Baker consulting in 2000-2001. They were cleaned and the multilayer coatings deposited by Troy Barbee of Lawrence Livermore National Laboratory. Appropriate thin-film filters and photographic film for each telescope were selected after the multilayers had been deposited. The calibration and assembly of the instruments, and their final temperature kernels, are described in the following sections.

[2] In fact, the 256 Å telescope was not originally chosen, and was not considered a high priority; rather, it was added to the payload to replace the Mg II spectrograph instrument.

Central Wavelength (Ångstroms)	Target Ion	Telescope Design		Goals
		Aperture (mm)	F/Ratio	
58	Mg X	Herschelian		Short wavelength;
		100	15	Coronal (1 MK) material
98	Ne VIII	Herschelian		Transition region
		100	15	(0.7 MK) material
131	Fe VIII	Herschelian		Transition region
		127	8	(and flares, if lucky)
150	O VI	Ritchey-Chrétien		Transition region
		127	28	and coronal material
171	Fe IX	Ritchey-Chrétien		Coronal (1 MK)
		65	31	TRACE/EIT cross-cal
180	Fe X	Ritchey-Chrétien		Coronal (1.1 MK)
		65	31	
195	Fe XII	Ritchey-Chrétien		Coronal (1.5 MK)
		127	28	TRACE/EIT cross-cal
211	Fe XIV	Ritchey-Chrétien		Coronal (2 MK)
		127	28	
256	He II	Ritchey-Chrétien		Chromospheric/LTR
		127	28	EIT 304 comparison
1216	H I	Ritchey-Chrétien		Chromospheric/LTR
		127	16	TRACE cross-cal
1550	C IV / Cont	Ritchey-Chrétien		Chromosphere/TR
		127	28	TRACE cross-cal

Table 1. The instruments of the MSSTA III.

2.2 Mirrors

2.2.1 INTRODUCTION

The innovation that made the MSSTA and other solar observatories like it possible was the development of multilayer structures capable of reflecting EUV light with high efficiency at near-normal incidence[(Barbee and Keith 1978), (Spiller 1972)**]**. A multilayer is a regularly-spaced stack of alternating materials that acts as an artificial Bragg crystal, reflecting energetic photons at an angle determined by the layer spacing,

$$n\lambda = 2d\sin(\theta),$$

as illustrated in Figure 7**.** Multilayers can be deposited on curved substrates, such as the hyperboloidal mirrors of a Ritchey-Chrétien telescope, resulting in narrowband reflectors with an efficiency of better than 50% and a resolution ($\lambda/\Delta\lambda$) of 30 or more at wavelengths of around 150 Å.

In 1987, Walker et al. obtained the first high-resolution image of the solar atmosphere using multilayer-coated normal incidence optics (Walker, Lindblom et al. 1988). The multilayers were made by Troy Barbee of Lawrence Livermore National Laboratory, who also produced the multilayers for the MSSTA missions. Since then, this technique has become the standard for observations of the solar transition region and corona. The TRACE satellite (Handy, Acton et al. 1999), launched in 1998, represents the current state of the art. It is capable of obtaining high-resolution (1 arc-second) images of the corona in three EUV wavebands using multilayer mirrors made by Troy Barbee. TRACE observations (particularly high-cadence movies of active-region dynamics) have greatly enhanced our understanding of the solar atmosphere.

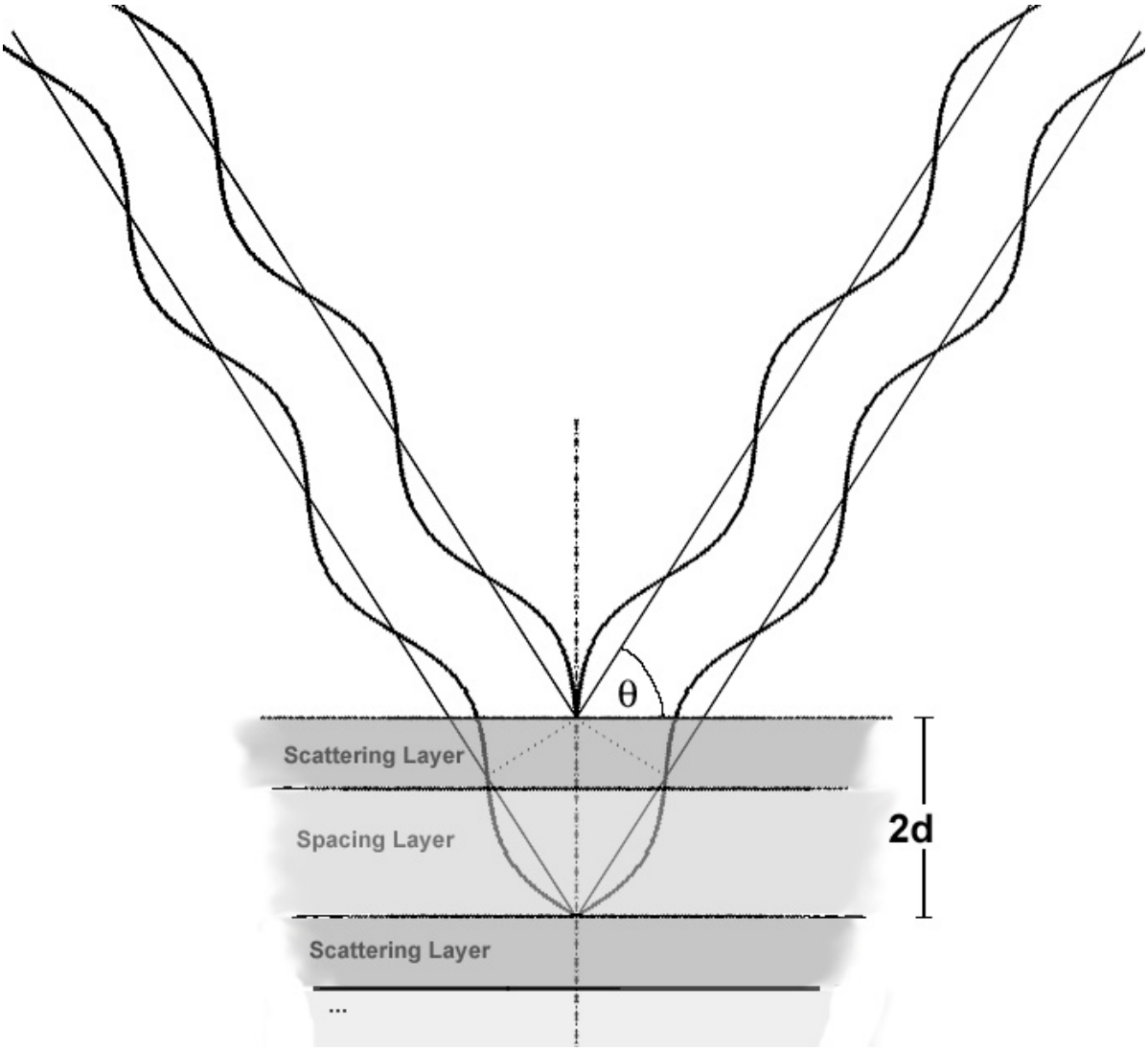

Figure 7. High-energy photons are reflected by a multilayer stack of layer spacing 2d if their wavelength and angle of incidence satisfy the Bragg condition (resulting in constructive interference of the reflections from different layers).

Making a multilayer structure with layers as small as the wavelength of EUV or soft x-ray light is extremely challenging, and places strict demands on the smoothness of the substrate and the control of the deposition process. Scattering by irregularities in the layer interfaces becomes increasingly problematic as the layers grow thinner, and at present limits the utility of multilayers for normal-incidence reflection to wavelengths longer than ~40 Å. On the long-wavelength side, the short penetration depth of less-energetic EUV photons makes multilayers relatively inefficient for wavelengths longer than about 300 Å (such photons are almost all scattered or absorbed by

the top few layers in the stack; the more layers sampled by the incident beam, the narrower the bandwidth and the higher the reflection efficiency).

The MSSTA III used multilayer-coated mirrors centered on solar emission lines ranging from 57.9 Å to 256 Å. The multilayers consist of 25-100 bilayer pairs Mo_2C and Si or W/C multilayers, and were fabricated by Troy Barbee. Improvements in multilayer fabrication – new materials, smoother substrates, more precise control of the deposition process – have lead to corresponding improvements in mirror performance. New multilayers offer higher reflectivity, narrower bandwidths, and better stability than those produced just a few years ago. At the time of their launch, the multilayers on the MSSTA III telescopes were the most advanced suite of EUV imaging optics yet used for solar observations. In this section, I will discuss the calibration of the MSSTA mirrors.

2.2.2 CALIBRATION OF THE MSSTA III MULTILAYER MIRRORS

The early successes of EUV-reflective multilayers, including those used on the first MSSTA flight, have opened up a broad and exciting field of research. Multilayers are being developed for applications ranging from lithography for microfabrication to high-energy laser optics to high-resolution microscopy. The drive to improve multilayer technology has lead to the creation of facilities optimized for testing and characterization of multilayers. Beamline 6.3.2 at the Advanced Light Source synchrotron of Lawrence Berkeley National Laboratory (http://www-cxro.lbl.gov/als6.3.2/; (Underwood, Gullikson et al. 1996))is one such facility. On line since 1995, beamline 6.3.2 is ideally suited to measuring reflectivity of multilayer optics like the MSSTA telescope mirrors. Figure 8 shows the layout of the beamline.

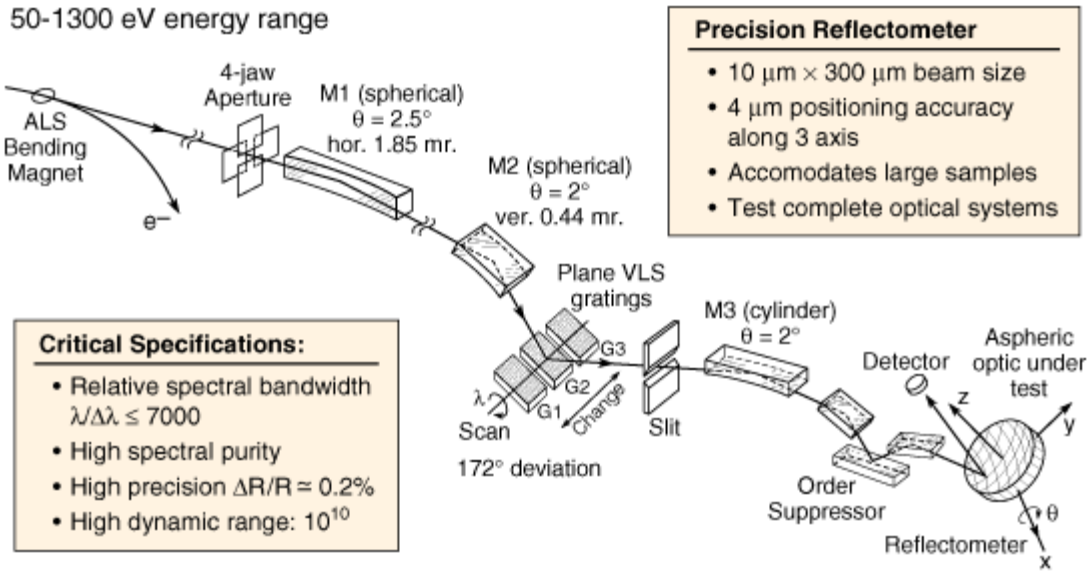

Figure 8. Beamline 6.3.2 (taken from (Gullikson, Mrowka et al. 2001)). Key features include the tunable three-reflection order suppressor, which can limit higher-order contamination to 0.25% by selection of appropriate materials and grazing angles; the selectable variable line spacing gratings, which enable the monochromator to cover the wavelength range from ~10 – 250 Å; and the reflectometer end station, which allows for easy and precise positioning of the optic and the detector.

We obtained 10 shifts of beam time over a four-day period in December 2001, and in this time were able to measure the primary mirrors of all 9 EUV telescopes, and several of the telescope secondary mirrors as well. Thanks to the excellent spectral purity, brightness and mechanical design of beamline 6.3.2, the data we obtained have a higher signal-to-noise ratio and lower systematic errors than those gathered in previous MSSTA calibration experiments at other synchrotrons, experiments that generally took several weeks to complete.

The procedure used in the calibration measurements is summarized below, with particular attention to issues that may impact the accuracy of the final reflectivity values.

The optic to be tested was mounted in the reflectometer vacuum chamber. The mounting stage allows three-axis positioning of the optic, and two-axis rotation (to vary angle of incidence with the test beam, and azimuthal position of the beam on the optic). We designed an adapter plate that would allow the on-axis Ritchey-Chrétien mirrors to be mounted in their cells with their centers on the rotation axis of the stage. Thus, azimuthal rotation of the optic allowed us to sample different points on the mirror surface without having to realign the beam and detector.

Each time the optic was changed, several steps were taken to ensure accurate wavelength calibration of the monochromator. First, a silicon prefilter was placed in front of the detector, and the monochromator scanned over 123.8 – 124.8 Å. The resulting transmission scan showed the L-absorption edge of the Si; if the wavelength scale of the edge appeared substantially different from its known value, an offset was entered into the monochromator motors. This process could be iterated to increase the calibration accuracy; in general, once calibrated the monochromator wavelength remained accurate to better than 0.01 Å. Then, if the Si prefilter was not appropriate for the wavelength being tested, it was exchanged for another prefilter (Al, Be, B, or C), and the order suppressor was adjusted for the wavelength region of interest. Since higher orders are less efficiently reflected at large grazing angles, the combination of the prefilter and the three-reflection order sorter strongly attenuates high-order contamination, to as little as 0.25% of the total beam flux. (Past MSSTA calibration runs have been plagued by higher order contamination as large as 30%, so this was a substantial improvement.)

For reflectivity measurements, the optic was positioned at an 85° angle to the incident beam. (In practice, because the position and angle at which the beam reaches the surface of the optic is not fixed by the reflectometer, this involved positioning the detector to receive a beam directed deflected by 170° from the incident beam, which is as close to normal incidence as the reflectometer geometry allows, without having the detector block the beam. The position and tilt of the optic are then adjusted in order to maximize the signal, indicating the full beam is reaching the detector. There was a large “sweet spot” in this adjustment over which the signal was constant and maximum, suggesting that misalignment was not a problem in these measurements).

With the beam, optic and detector aligned, the angle of the grating was scanned to scan the wavelength of the monochromator over the bandpass of the optic. Three samples were taken at each wavelength step, with a 30 msec integration time, and averaged. The data acquisition system reported the detector signal and current in the synchrotron ring for each point. After the full wavelength scan, the optic was rotated in azimuth so that the beam found a new point on the optic; the alignment was re-optimized, and the wavelength scan repeated. On the Ritchey-Chrétien systems, re-optimization was trivial, as the angle of reflection was essentially unchanged by azimuthal rotation around the optical axis of the mirror. For the primaries, 6-12 surface points

were measured; for the secondaries, only one. The Herschelian mirrors are off-axis, and thus lacked the symmetry that made sampling different points on the Ritchey-Chrétien mirrors so simple. Each different point on a Herschelian mirror required complete realignment of the optic and detector, and thus these mirrors were only sampled at 1-3 points each.

Before and after scanning the bandpass at all the points on an optic, several scans were taken to aid in calibrating the results. First a "direct beam" scan, with the optic pulled aside and the synchrotron beam directly incident on the detector, was taken, to establish the intensity of the beam itself as a function of wavelength. Then dark current in the detector (and the background light in the chamber) was measured by blocking the synchrotron beam and measuring the detector signal while the monochromator scanned (of course, the action of the monochromator was irrelevant while the beam was blocked). After the optic was moved into place, another dark current scan was taken in case the position of the optic changed the amount of background light that reached the detector. Table 2 summarizes the data acquired at the ALS for each mirror.

Central Wavelength	Optic Tested	Number of Points Measured	Number of Repeat Measurements	Number of Angles Measured
58	Herschelian	2	1	8
98	Herschelian	2	2	9
131	Herschelian	1	2	1
150	R.-C. Primary	6	2	1
171	R.-C. Primary	6	2	1
180	R.-C. Secondary	1	2	1
195	R.-C. Primary	12	3	1
211	R.-C. Primary	8	3	1
256	R.-C. Primary	12	2	1

Table 2. Summary of the measurements made at the ALS. Most optics were measured at different points on their surface (in order to estimate the uniformity of the multilayer bandpass), and measured repeatedly at the same point (to measure the repeatability of our calibration technique). Certain mirrors were also measured at a range of angles of incidence to test the validity of correcting for the measurement angle. For the two-mirror systems, only one mirror was measured (generally the primary), and the bandpass on the second mirror was assumed to be the same.

2.2.3 ANALYSIS OF THE MULTILAYER CALIBRATION DATA

The following quantities were measured for each mirror:

$$S_{(R/D)}(\lambda;\theta,\mathbf{x})$$
$$D_{(R/D)}$$
$$C_{(R/D)}(\lambda;\theta,\mathbf{x})$$

where S is the strength of the signal from the photodiode, measuring either the direct beam (S_D) or the beam reflected at angle θ from point $\mathbf{x}$ on the mirror surface (S_R); D is the strength of the dark current, measured before or after a given reflected or direct beam scan and averaged over wavelength (it can be attributed to thermal noise in the photodiode or background light in the experimental chamber); and C is the ring current at the time when each value of S was measured. The ring current determines the strength of the synchrotron beam; it decays over time as the electrons in the accelerator radiate away their kinetic energy (the electrons are dumped and a new packet is injected into the ring once a day). Ring current was used as an overall normalization factor for the beam strength at each sample point. Note that C is not actually dependent on λ, θ or $\mathbf{x}$; however, a different value of C is reported by the beamline data acquisition system simultaneously with each value of S, and the appropriate samples must be matched up. S and D have units of counts/sec, and must be adjusted for the gain of the photodiode.

Dividing the reflected intensity spectrum by the direct beam intensity spectrum effectively corrects for any λ dependence in the response of the photodiode or in the output of the synchrotron, and gives us the reflectivity of the multilayer:

(Equation 8)
$$R(\lambda,\theta,\mathbf{x}) = \frac{\left(S_R(\lambda,\theta,\mathbf{x}) - D_R\right) \Big/ C_R(\lambda,\theta,\mathbf{x})}{\left(S_D(\lambda) - D_D\right) \Big/ C_D(\lambda)}$$

Generally, θ was fixed at 85° during the measurements. Since the effective spacing (the induced phase shift) of the multilayer stack is sin(θ) times the actual layer spacing, the measured results were converted to normal incidence (90°) reflectivities by multiplying the measurement wavelengths by sin(85°) (the validity of this correction procedure is discussed in section 2.2.5**)**. Finally, the measurements at different points **x** on the mirror surface were cross-checked for consistency and averaged, producing an effective normal-incidence reflectivity $R_{eff}(\lambda)$:

$$R_{eff}(\lambda) = \left[R(\lambda \sin(85°), 85°, \mathbf{x})\right]_{\mathbf{x}}$$

Except as noted below, all the sampled points were included in the average and weighted equally. The effect of sampling different points on the optic is discussed in section 2.2.4.

Figure 9 presents the calibrated reflectivities of the 9 MSSTA III EUV multilayer telescopes.

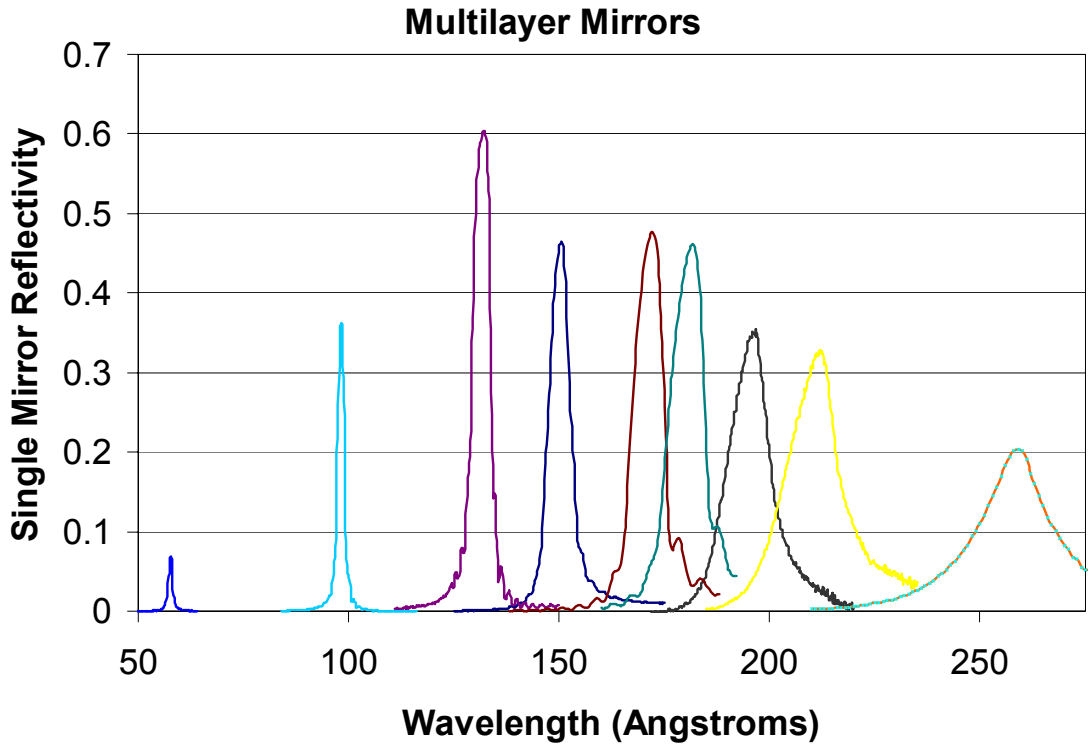

Figure 9. Reflectivity of the multilayer mirrors used in the MSSTA III EUV telescopes. Note that these are all single-mirror reflectivities; the efficiency of the two-mirror Ritchey-Chrétien systems is found by squaring the single-mirror bandpass.

2.2.4 NOISE AND ERROR

Because ALS beamline 6.3.2 is so well optimized for EUV multilayer reflectometry, we were able to obtain substantially more and better mirror data than has been available from previous MSSTA calibration efforts. In particular, by measuring each optic multiple times at different points, we are able to estimate the error in the final bandpass and identify the source of this uncertainty.

In the center of the synchrotron's wavelength range, the brightness of the beam is extremely high, resulting in smooth curves with an excellent signal-to-noise ratio (see, for example, the measurements of the 131 Å Herschelian in Figure 16). The beamline's output begins to drop off at wavelengths longer than ~200 Å, and is quite low above 250 Å, so the bandpass measurements of the longer-wavelength optics like the 211 Å and 256 Å Ritchey-Chrétiens (Figures 10 and 11) are noticeably noisy. However, photon statistics are not the largest error source for any of the instrument bandpasses.

There are two significant sources of systematic error in the measured reflectivity curves. The first is measurement error introduced by our experimental procedure. Because each reflectivity curve requires four synchrotron scans to produce (signal and dark current scans for the direct and reflected beams; Equation 8), any uncontrolled variation that affects one of these scans but not the others will throw off the resulting reflectivity. In particular, the dark current measurements showed some tendency to drift with time as the diode's temperature varied.

In order to estimate the effect of this systematic measurement error, we sampled the same point on each optic twice, using two completely separate sets of four synchrotron scans. The results are plotted in the upper panels of Figures 10 – 18. In most cases, the agreement was quite good, with differences of roughly the same order as the statistical noise (<1% at wavelengths up to 180 Å; ±1-5% at longer wavelengths).

The second major source of error is the fact that we only sample a few points on the optic; if the multilayer bandpass varies substantially over the surface, we can only construct an average

bandpass that may not represent the mirror's overall properties. The lower left panels of Figures 10 – 18 show the result of sampling different points on the optic (generally 6-12 points for the Ritchey-Chrétien primaries; only 1 or 2 for the Herschelians). Evidently, point-to-point variation over large optics is a factor; for the small Ritchey-Chrétien 171 Å mirror (Figure 14), there is very little deviation in the bandpass at different points, but the 5" primary on the 150 Å Ritchey-Chrétien (Figure 15) shows substantial variation that dominates the uncertainty in the average bandpass. (As discussed in section 2.6.2, this uncertainty complicates the interpretation of the 150 Å telescope's images.)

The results and estimated errors of the MSSTA III EUV mirror bandpass measurements are presented in Table 3.

Wavelength of Measured Peak (Å)	Measured Peak Reflectivity (%)	FWHM (Å)	% Error at peak	RMS % Error Over Bandpass
58.0	9.2	0.8	5	7
98.6	36.2	1.9	2	15
132.5	60.4	4.8	*0*	*0*
151.2	46.5	6.0	7	24
172.7	47.7	8.3	1	4
182.5	46.1	9.5	*0*	*1*
197.6	37.5	12.0	11	17
212.8	32.9	14.0	10	16
260.0	20.4	18.3	20	25

Table 3. Results of the bandpass measurements of the MSSTA III multilayers. The error estimates are dominated by point-to-point variations in the reflectivity over the surface of the optic. Because the 131 Å and 180 Å telescopes were only measured at a single point, we cannot confidently estimate the error of these bandpasses.

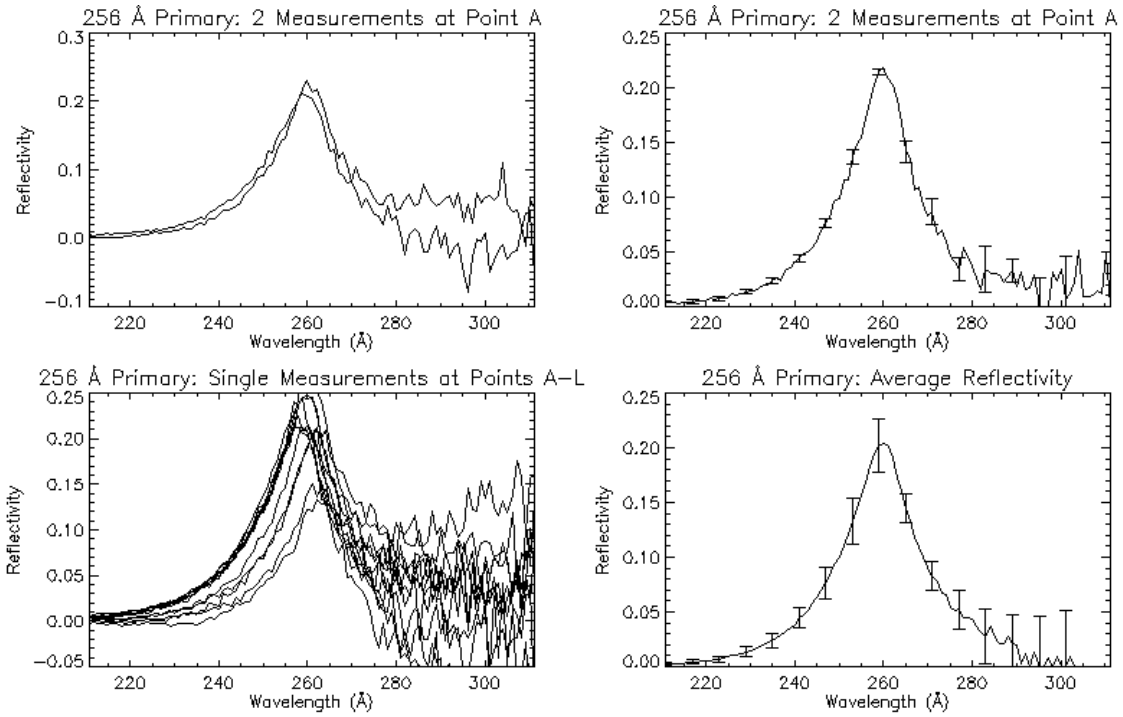

Figure 10. Measurements of the 256 Å Ritchey-Chrétien primary mirror. Wavelengths longer than 250 Å are outside the synchrotron's nominal range, so the throughput is low and the data is extremely noisy.

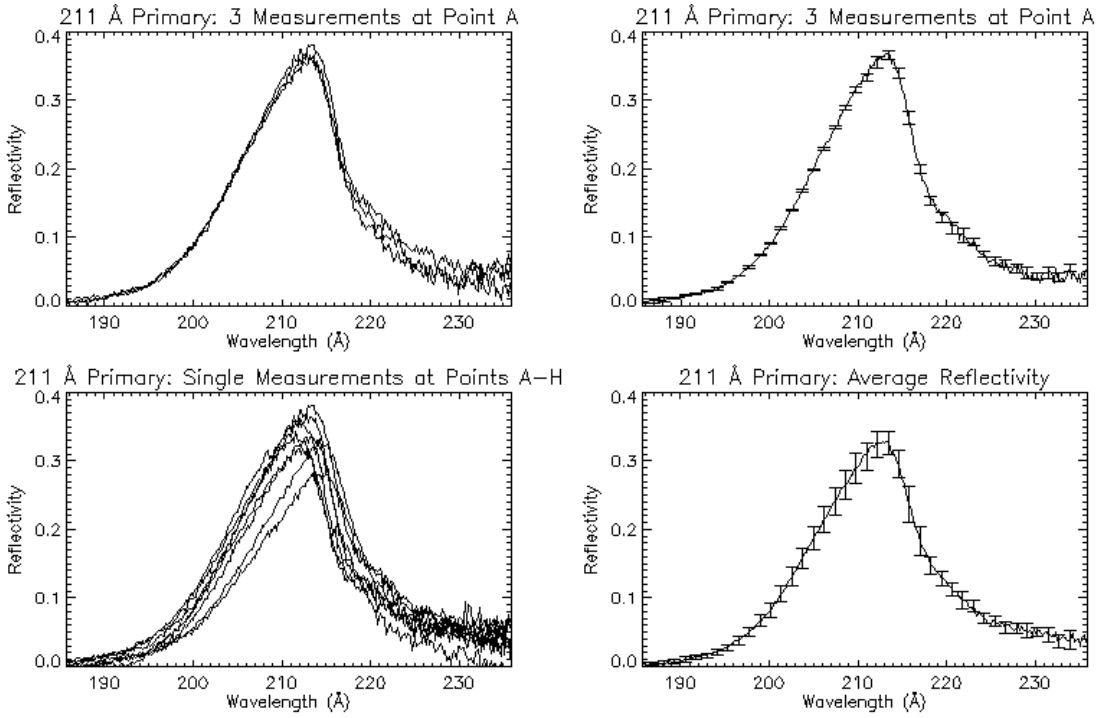

Figure 11. Measurements of the 211 Å Ritchey-Chrétien primary.

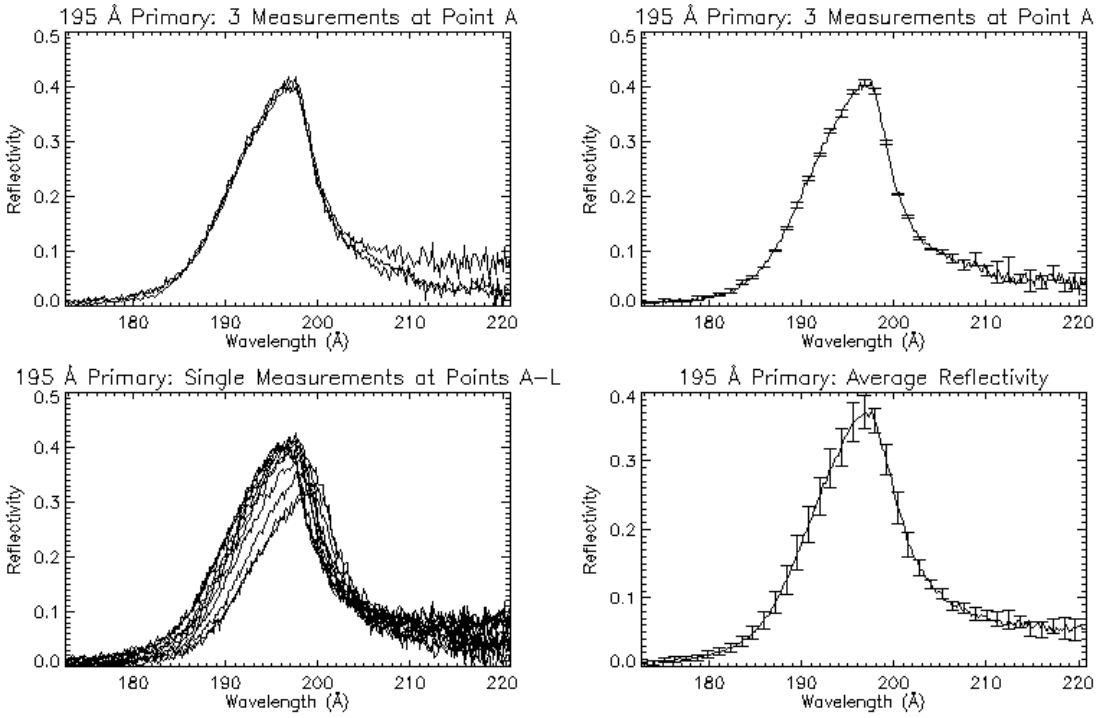

Figure 12. Measurements of the 195 Å Ritchey-Chrétien primary.

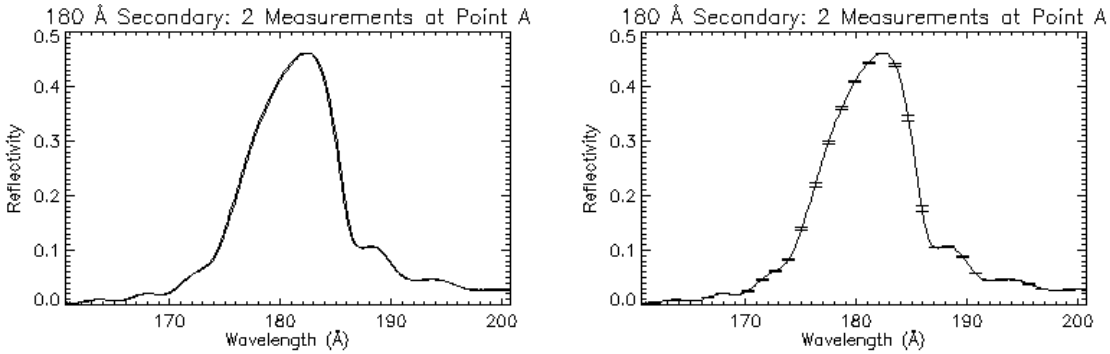

Figure 13. Measurements of the 180 Å Ritchey-Chrétien secondary. Because of the secondary's small size, the mirror was only measured at one point.

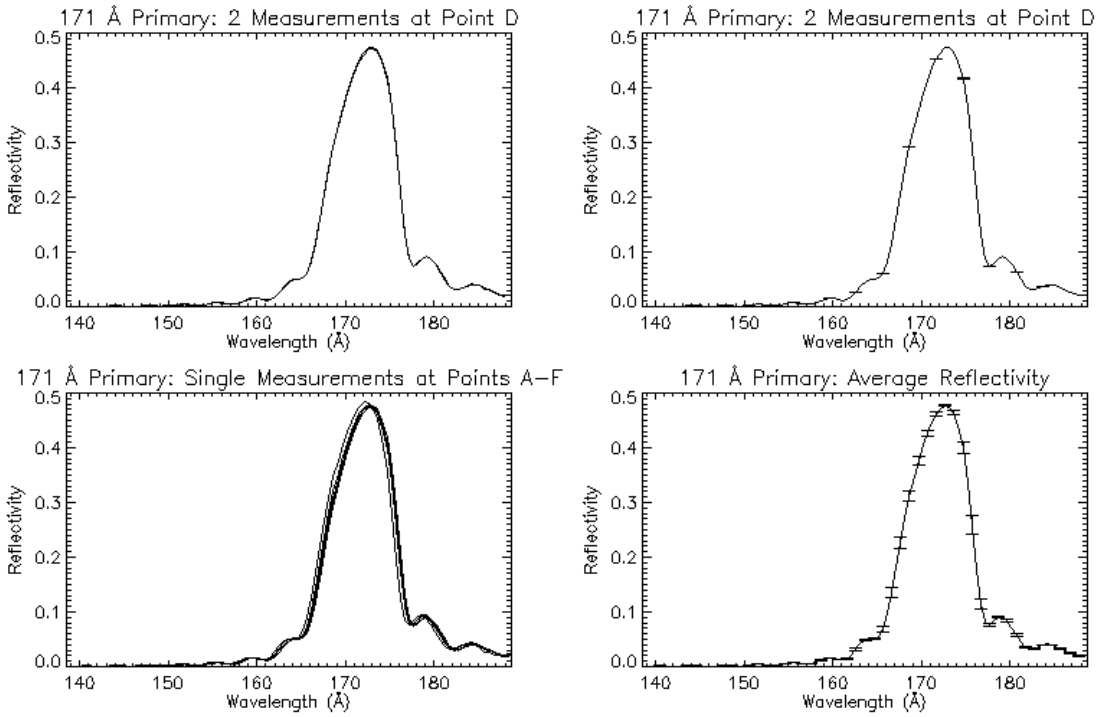

Figure 14. Measurements of the 171 Å Ritchey-Chrétien primary.

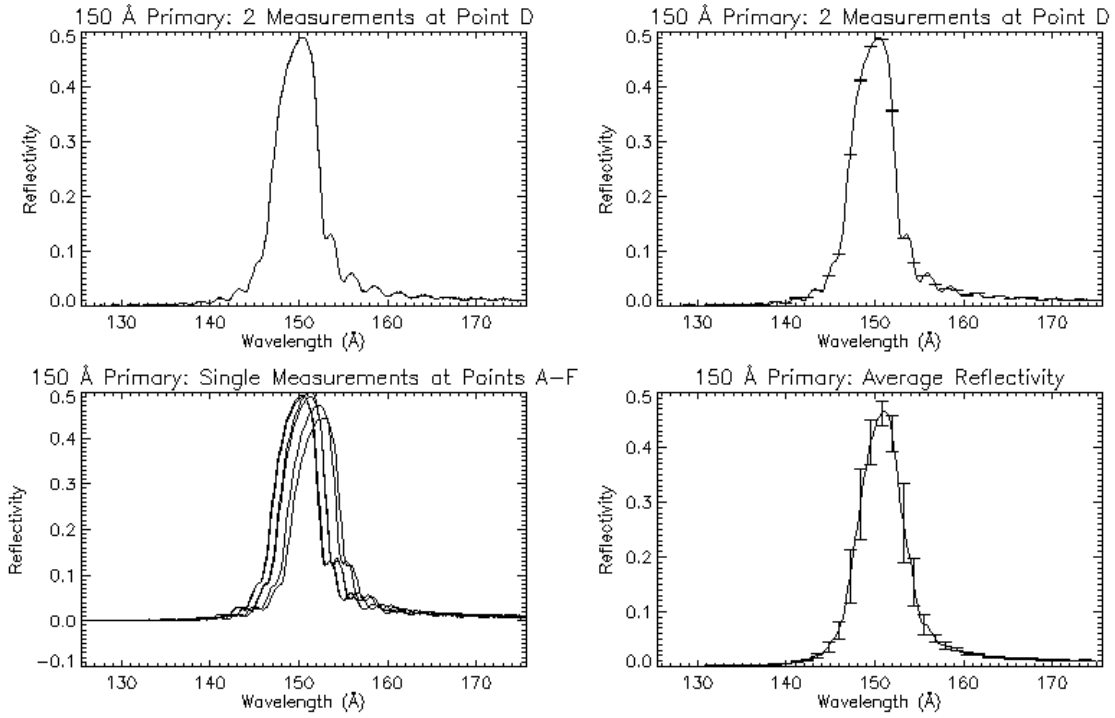

Figure 15. Measurements of the 150 Å Ritchey-Chrétien primary, showing substantial point-to-point variations over the optic.

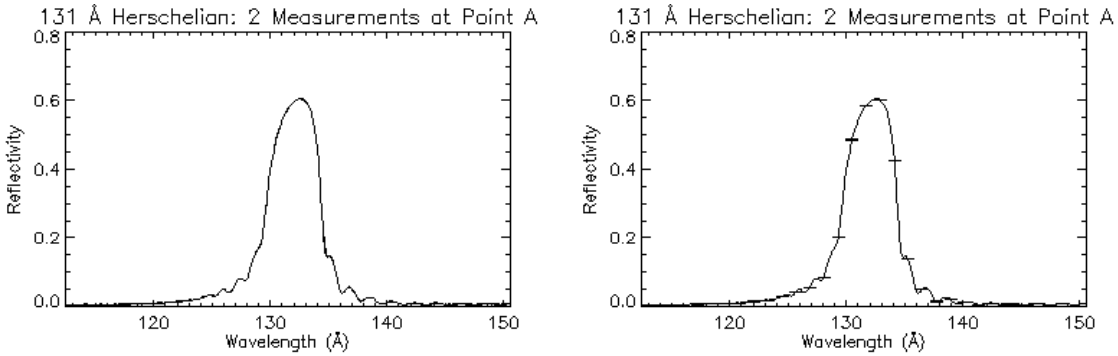

Figure 16. Measurements of the 131 Å Herschelian. The multilayer was only sampled at a single point.

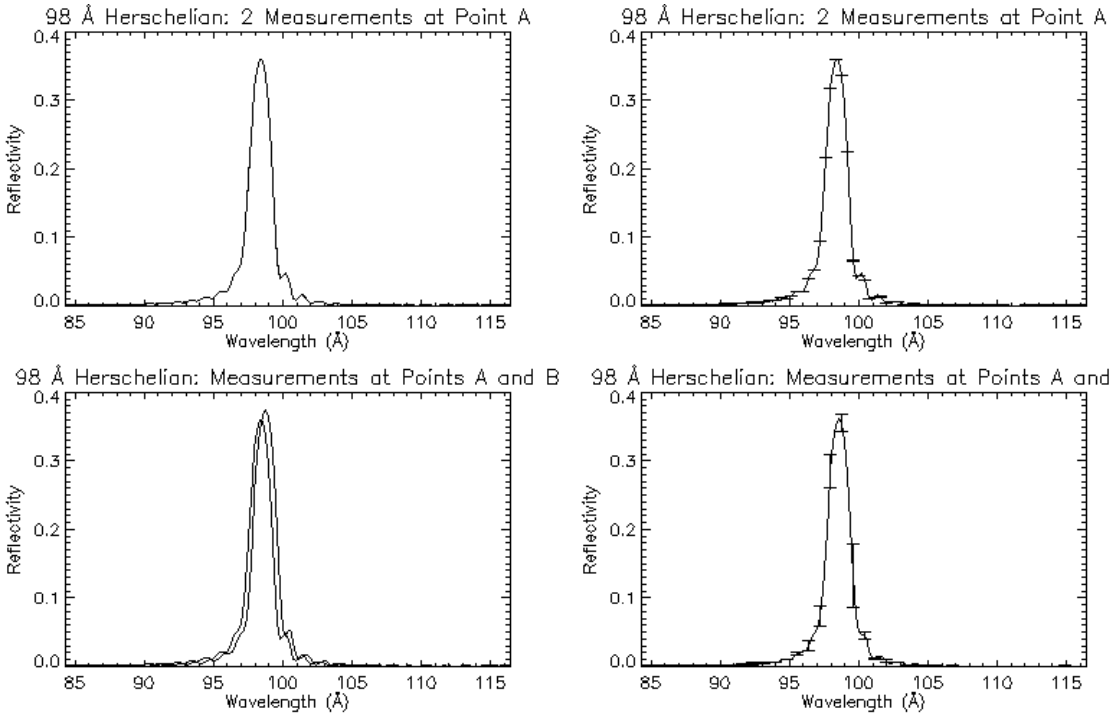

Figure 17. Measurements of the 98 Å Herschelian.

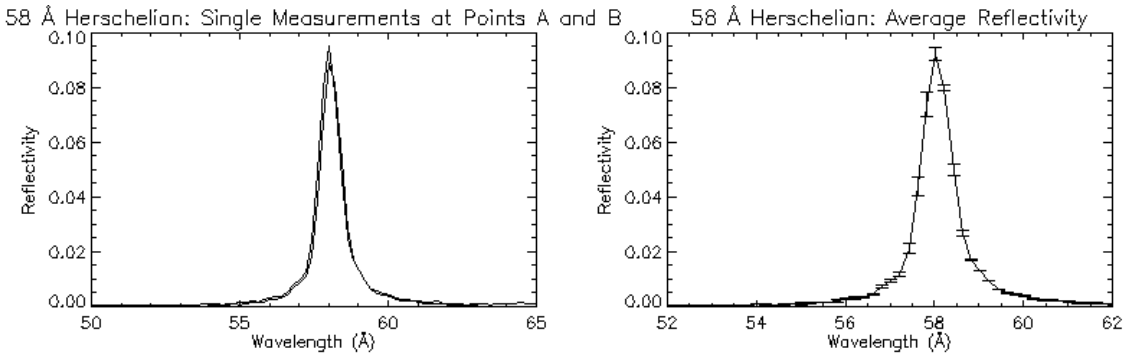

Figure 18. Measurements of the 58 Å Herschelian. Repeat measurements at a single point were not taken.

2.2.5 ANGLE OF INCIDENCE VARIATION

In flight, the MSSTA III telescopes focus light by reflecting at angles that vary from 80.0° (for the farthest off-axis point on the 131 Å Herschelian) to 89.8° (for points near the center of the large Ritchey-Chrétien secondaries). Since the effective spacing of the multilayer stack is sin(θ) times the actual layer spacing, this variation in angle of incidence, and the difference between the angle at which the multilayers were measured and at which they operate, will have a small but noticeable effect, of order $(\theta/90°)^2$, on the instrument's bandpass. The multilayer measurements have been corrected to give reflectivity at normal (90°) incidence (shifting the peak reflectivity to longer wavelengths).

In order to test the validity of this correction, we measured two of the Herschelian mirrors (the 98 Å and 58 Å Herschelians) at a range of angles, as noted in Table 2. The results are shown in Figure 20 and Figure 21. The bandpass shifts agree reasonably well with the sin(θ) prediction (represented by the curve through the 87° data point). In the case of the 98 Å Herschelian, the total reflectivity is seen to decrease at shallower angles of incidence, evidently as a result of scattering or absorption within the multilayer. This effect was not compensated for in generating the instrument bandpass used for analysis.

It is possible to generate a bandpass that accurately accounts for the variation in angle of incidence over the surface of an optic and at the image plane (i.e. the fact that the edges of the on-axis Ritchey-Chrétien primary mirrors reflect incident light at a different angle than points near

the center). Figure 19 shows the effective bandpass of the 131 Å Herschelian telescope for a point at the center of the image plane. It is slightly broadened, and slightly shifted to lower wavelengths, by the fact that various rays are reflected at angles slightly less than normal. Because this effect is fairly subtle (especially for on-axis mirrors), and because the computation is complex and the result varies for every point in the image, this effect was ignored in our bandpasses, but in the case of the short-wavelength Herschelian mirrors (which feature narrow reflectivity curves and substantial angle-of-incidence variation) it can become significant.

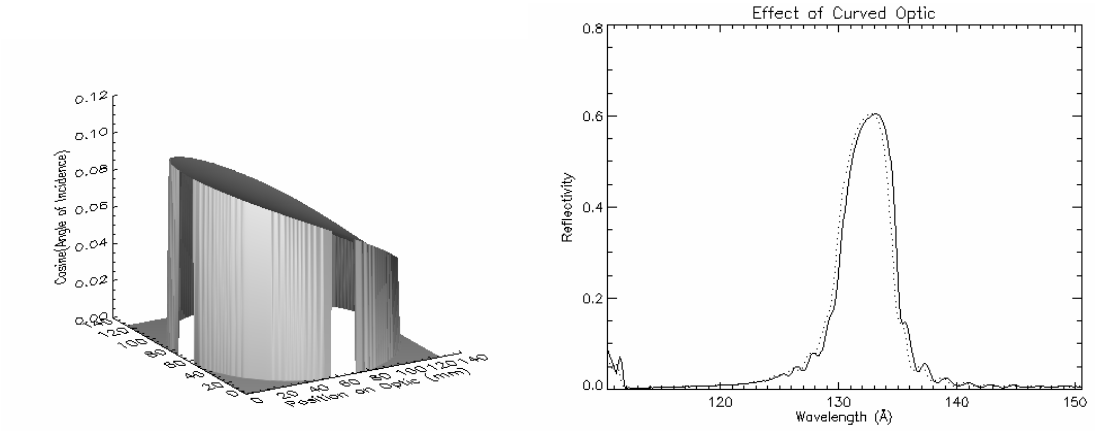

Figure 19. Because the effective bandpass of the multilayer depends on the angle of incidence of light, a curved optic behaves slightly differently than a flat optic at normal incidence. On the left, the cosine of the angle of incidence of rays destined for the center of the image plane of the MSSTA III large Herschelian telescope is shown; at right, the effect of this variation on the effective bandpass of the optic is plotted, showing a slight broadening and a slight shift to lower wavelengths. This subtle effect can become more dramatic with steeply curved optics or narrow, short-wavelength multilayer bandpasses.

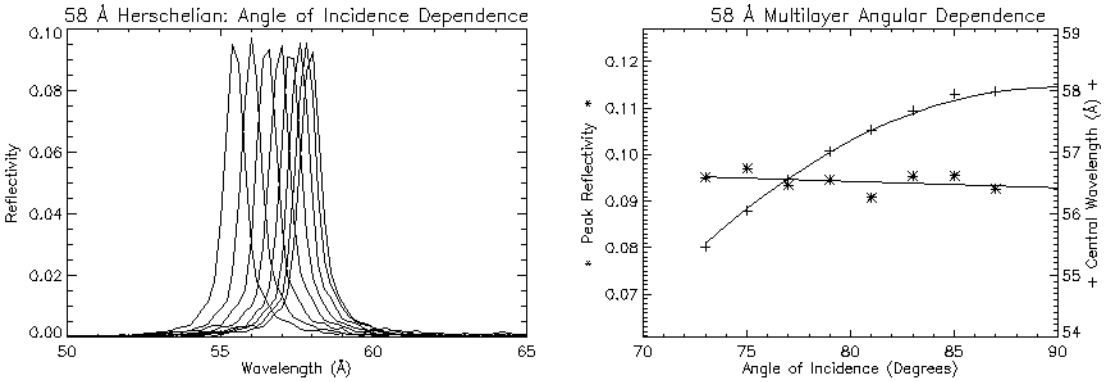

Figure 20. Varying the angle of incidence on the 58 Å Herschelian. The curves on the left show measurements taken at angles ranging from 73° to 87°. At right, it can be seen that the bandpass shifts to longer wavelengths with increasing angle of incidence, as predicted by simple geometry. The peak reflectivity is not affected noticeably by changing angle.

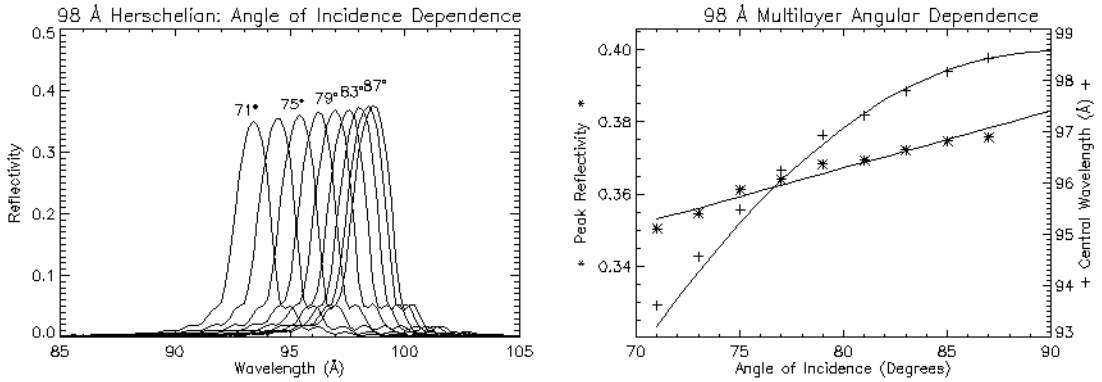

Figure 21. Varying the angle of incidence on the 98 Å Herschelian mirror. The bandpass shift matches the prediction reasonably well. There is a more significant decline in the peak reflectivity at shallower angles than what is seen with the 58 Å mirror, as the light path through the material lengthens. This seems to indicate that the peak reflectivity at 90° is ~38%, rather than the 36% we measured at 85°. This effect was not compensated for.

2.2.6 MIRROR POTTING

Holding the mirrors securely enough to maintain critical telescope alignment through the rocket launch, without exerting enough stress to deform the mirror surfaces and degrade their performance, is quite challenging. The Herschelian and Ritchey-Chrétien primary mirrors were mounted in aluminum cells as follows: the outside edge of the zerodur mirror blanks and the inside edge of the aluminum mirror cells were coated in primer. The mirrors were placed face-up on a set of standoffs. Then the aluminum mirror cells were lowered over them (the cells were designed to offer ~⅛" clearance all the way around the OD of the mirror). We then injected ~5 cc of Dow-Corning Silastic RTV through each of a series of 6-12 evenly-spaced cutouts in the mirror cell. The RTV formed pads around the mirror that bound the mirror to the cell; when cured, it is extremely strong, but (in principle) offers enough flexibility to allow the mirror to stabilize without being strained. A set of three aluminum détentes were attached to each mirror cell and overhung the front of the mirror, to prevent the mirror from flying loose in the payload in case it broke free from the RTV. These did not contact the mirror surface.

The Ritchey-Chrétien secondary mirrors were held in their cells less gently: a nylon retaining ring was inserted in the cell; then the mirror was lowered into place, and a pressure plate was attached

to the cell behind the mirror. Nylon-tipped set screws in the pressure plate pushed on the back of the secondary mirror, while the front of the mirror rested on the retaining ring. The small Ritchey-Chrétien secondaries (171 and 180 Å) were a particularly tight fit in their cells, and the performance of these telescopes suffered as a result.

During the application of the primer to the Herschelian mirrors, droplets of primer were inadvertently splashed on the front surface of the 58 Å, 98 Å and 131 Å telescopes. Gentle washing removed some of this contamination, but dried primer spots remained on these mirrors. They covered much less than 1% of the surface area of all of the affected mirrors. The effect of the primer on EUV reflectivity was measured (see Figure 22), but no further action was taken to account for these minor blemishes on the multilayers.

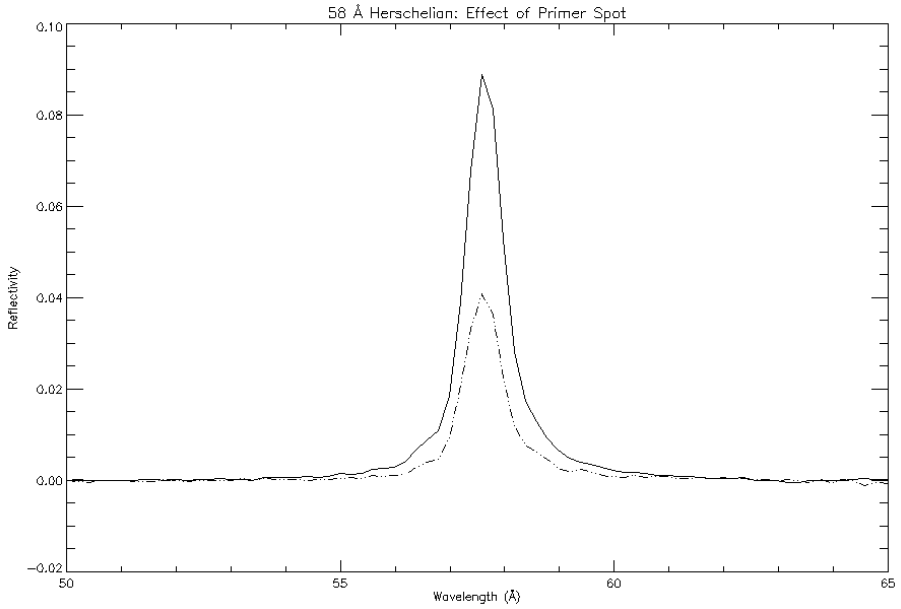

Figure 22. The surface of the 58 Å Herschelian was splattered with spots of primer during mirror potting. Shown here is the effect of the primer on the mirror reflectivity (a uniform decrease of ~60%); because of the small area covered by the primer, this effect was largely ignored.

2.3 Filters

2.3.1 INTRODUCTION

While the multilayer mirrors of the MSSTA telescopes are efficient, narrowband reflectors in the extreme ultraviolet, they are also ~50% reflective (via simple specular reflectivity) at visible and near-infrared wavelengths. Because the integrated solar blackbody irradiance at visible wavelengths can be eight or more orders of magnitude stronger than the flux from a single EUV emission line, filtering out the longer-wavelength solar radiation while allowing the EUV photons through the telescope is an important design challenge.

The MSSTA telescopes use a variety of thin metallic foils, composed of aluminum, zirconium, or niobium and mounted just in front of the focal plane of each telescope, to reject the visible light. The filters typically consist of a 1500-4500 Å thick metal film deposited on a mesh of nickel wires, spread over a 2" diameter frame. Such thin foils are extremely vulnerable to damage from differential pressure or heating, and require special precautions in their manufacture and use. These filters were manufactured by Luxel Corporation.

In addition to their primary function of blocking visible/IR light, the filters accomplish a number of secondary tasks, including:

- blocking photons from out-of-band EUV and FUV emission lines (particularly He II 304 Å), whose wavelengths are long enough that they experience some specular reflectivity from the multilayer mirrors;

- narrowing the EUV bandpass with carefully chosen absorption edges (particularly the 171 Å bandpass, where the absorption edge of the aluminum filter sharpens the high-energy cutoff of the bandpass);

- reducing higher-order contamination by EUV emission lines with wavelengths roughly half that of the line of interest.

These tasks must, of course, be accomplished while minimizing the attenuation of the target wavelength.

2.3.2 SINGLE VS. DOUBLE FILTERS

The primary failure mode of the thin-foil filters is the development of pinholes. Mechanical stress and heating by concentrated solar flux can produce thin spots or tiny punctures in the foil, and even microscopic holes in the filter can cause it to be out of specification. Because the filters are close to the focal plane, the effect of a small pinhole on the final image is localized; however, a large enough flaw could let in sufficient visible light to ruin an entire exposure (or even damage the detector).

In order to reduce the risk of total instrument failure from the formation of pinholes, the MSSTA I and TRACE missions used double filters – two focal plane filters, each slightly thinner than what would be required of a single filter. The rationale was that a pinhole that developed in one filter would be unlikely to coincide with a pinhole in the second filter, so no part of the detector would be exposed to completely unfiltered solar radiation. However, because the robustness of a filter is dependent on its thickness, double filtering has two important drawbacks: first, the two filters must be made more than half as thick as an optimized single filter, and thus the total thickness of the filter stack is greater than optimal, resulting in a reduction below optimal levels of the in-band flux; second, because each of the double filters is thinner than an optimized single filter, each is more vulnerable to damage from vibration or pressure differentials created during the rocket launch, and thus the risk of catastrophic filter failure is not necessarily decreased over

using a single filter. After consultation with Forbes Powell of Luxel, it was decided that single filters offered better overall stability and performance.

2.3.3 FILTER MATERIALS

Light is attenuated exponentially as it passes through any material; the transmission of light at wavelength λ in passing through a filter of material Z and thickness d can be written:

(Equation 9) $$T_Z(\lambda, d) = e^{-d\mu_Z(\lambda)}$$

where the function $\mu_z(\lambda)$ describes the absorption spectrum of the material. Luxel Corporation has manufactured filters for a number of soft x-ray applications, and has compiled a large database of absorption coefficients for different materials from a variety of sources[(Henke, Gullikson et al. 1993), (Palik 1985; Palik 1991)]. These include "practical" visible light absorption coefficients, a single number for each material that can be used to generate conservative estimates of the visible light rejection of a filter of that material (Powell and Fox 1994).

Typically, materials used in filters have μ_z values around $10^{-2} - 10^{-3}$ $Å^{-1}$ at visible wavelengths, and μ_z of a few 10^{-4} at EUV wavelengths, and thus can attenuate visible light by many order of magnitude without reducing EUV throughput by even a factor of ten. Of these materials, aluminum is preferred; it offers a very high relative attenuation of visible light, and has been used extensively, so that its mechanical robustness and ability to withstand the heat load of concentrated visible light are well known. Wherever possible, aluminum filters were used for the MSSTA telescopes. However, aluminum has two drawbacks:

- it has a sharp absorption edge at 170 Å, and EUV wavelengths shorter than this are strongly attenuated;
- it does not attenuate longer-wavelength EUV lines, particularly 304 Å He II.

Therefore, the MSSTA telescopes centered on lines below 170 Å cannot use aluminum filters, and those above 170 Å must supplement their aluminum filters with a thinner coating of some material that will attenuate the 304 Å flux.

Finding a material that strongly attenuates 304 Å while passing photons within the MSSTA bandpasses from 171 – 256 Å is challenging. Zirconium was chosen for the supplemental coating on the aluminum filters, for its relatively high absorption at 304 Å and its good stability. Pure zirconium filters were produced for the 150 Å, 131 Å, and 98 Å telescopes, which fall below the aluminum absorption edge. Because the 58 Å line falls below the absorption edge of zirconium, niobium was used to make a filter for the 58 Å Mg X telescope. Figure 23 shows the absorption spectra of the materials used for the MSSTA filters, along with the bandpasses of the MSSTA instruments.

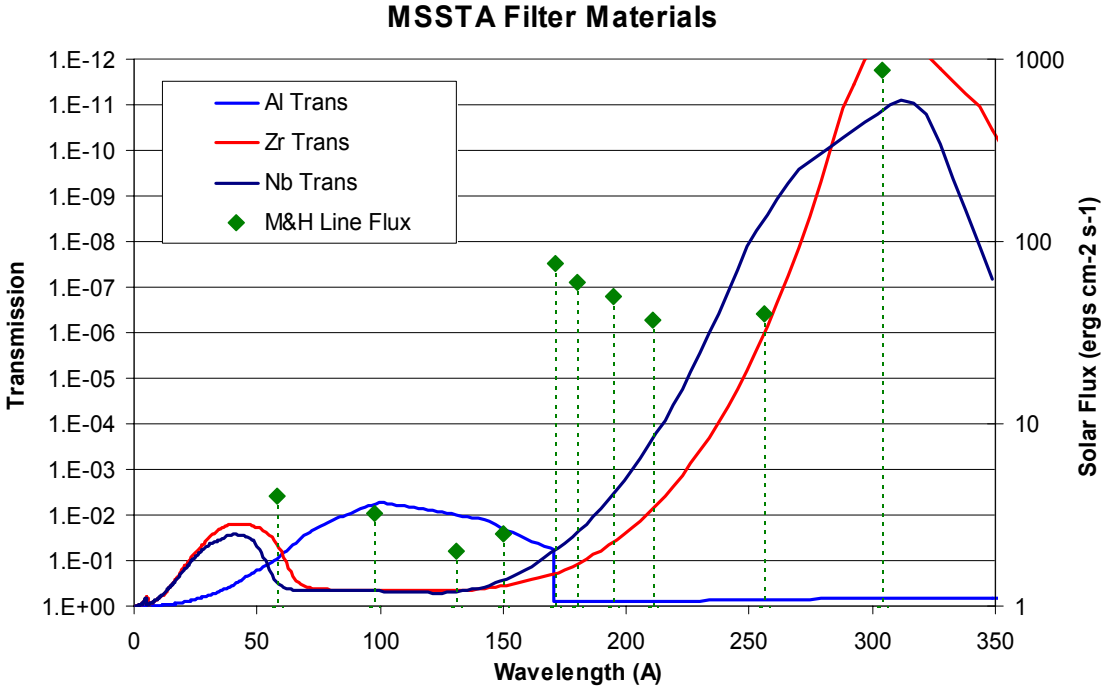

Figure 23. Absorption spectra of the materials used in the MSSTA III filters. The thickness of each material plotted here was chosen to achieve a visible-light attenuation of 10^{-12}. Aluminum is reliable and very effective at attenuating visible light while passing EUV; it was used wherever possible. Zirconium was used to supplement the aluminum filters to reject 304 Å light, and to filter three of the telescopes below the aluminum edge. Niobium was used to filter the 58 Å telescope, since Zr attenuates 58 Å. Superimposed on the filter spectra are the strengths of the central lines in the MSSTA bandpasses, and of the 304 Å line that can contaminate some multilayer images if not filtered.

2.3.4 ANALYTICAL METHOD FOR MSSTA FILTER DESIGN

Given the materials, designing the filters is a matter of optimizing the in-band transmission while satisfying constraints on the exclusion of out-of-band light. These constraints can be expressed as the filter's required relative density:

(Equation 10) $$D_{Vis} = \log\left(\frac{T_{EUV}}{T_{Vis}}\right) = \log\left(\frac{\Phi_{EUV}}{\Phi_{Vis}}\right) + \log\left(\frac{R_{EUV}}{R_{Vis}}\right) + \log\left(\frac{f_{EUV}}{f_{Vis}}\right) - \log\left(\frac{\varepsilon_{EUV}}{\varepsilon_{Vis}}\right)$$

where T is the transmission of the filter, Φ is the total solar flux, R is the reflectivity of the multilayer mirror (squared for two-mirror systems), f is the relative efficiency of the film, and ε is the relative exposure desired in the final image. The *Vis* subscript denotes an effective value of the quantity in question at visible wavelengths, and can be thought of as an integral or average over visible wavelengths as appropriate. A similar expression can be written for D_{304}, the requirement that the filter exclude He II 304 Å radiation, by substituting 304 Å for visible light in the denominator of each factor.

	Flux in Central Line		Reflectivity		Film Response	Exposure Ratio	Relative Density	
Central λ	$\log\left(\frac{\Phi_{EUV}}{\Phi_{Vis}}\right)$	$\log\left(\frac{\Phi_{EUV}}{\Phi_{304}}\right)$	$\log\left(\frac{R_{EUV}}{R_{Vis}}\right)$	$\log\left(\frac{R_{EUV}}{R_{304}}\right)$	$\log\left(\frac{f_{EUV}}{f_{Vis}}\right)$	$\log\left(\frac{\varepsilon_{EUV}}{\varepsilon_{Vis\,/\,304}}\right)$	D_{Vis}	D304
58 Å	-8.5	-2.3	-1.7	0.3			-15.2	-4.0
98 Å	-8.7	-2.5	-0.3	1.7			-13.9	-2.7
131 Å	-8.8	-2.6	0.2	2.2			-13.7	-2.5
150 Å	-8.7	-2.5	-0.1	1.9			-13.7	-2.5
171 Å	-7.4	-1.2	0.0	2.0	-3	2	-12.5	-1.3
180 Å	-7.4	-1.2	-0.1	1.9			-12.4	-1.2
195 Å	-7.4	-1.2	-0.3	1.7			-12.8	-1.6
211 Å	-7.6	-1.4	-0.4	1.6			-12.9	-1.7
256 Å	-7.5	-1.3	-0.8	1.2			-13.3	-2.1

Table 4. Relative density specifications for the MSSTA III filters (see Equation 10). Note that the film response factor is only used to find visible light relative density.

We can deal with each of these factors in turn, as summarized in Table 4. The flux values for the EUV lines in the MSSTA bandpasses are drawn from Malinovsky and Heroux (Malinovsky and Heroux 1973); only the single strongest line in each bandpass is used, leading to conservative underestimates (by a factor of 2-3 in most cases) of the EUV flux. The 304 Å flux is from Judge *et al.* (Judge, McMullin et al. 1999). Reflectivity is the measured value for each multilayer for the EUV lines; visible light reflectivity is assumed to be ~50% from each multilayer, and 304 Å reflectivity is taken to be 5% (based on synchrotron measurements of the MSSTA II telescopes by Allen *et al*. (Allen, Willis et al. 1991)). Film response is treated in more detail later; for the purpose of this calculation we compared the exposure (in ergs/cm^2) required to produce a unit density above the fog (i.e. a spot that transmits 10% as much light as a clear portion of the film) at EUV and visible wavelengths. Hoover *et al.* (Hoover, Walker et al. 1990) found that ~100 ergs/cm^{-2} of EUV light are required, while Kodak (Dancy and Buckley 1987) found that T-Max 100, which has similar visible-light responsivity to XUV-100, reaches the specified density under only 0.1 ergs/cm^{-2} of exposure to visible light. Film response is not included in the 304 Å calculation.

The value of relative exposure ε indicates that the filters are designed to ensure that EUV light accounts for ~100 times as much exposure in the final image as visible light. In practice, the value is higher, as all the values used in Equation 10 are conservative and err on the side of excluding more out-of-band light (at the cost of reduced in-band throughput). Typical values of these factors are as follows:

$$\log\left(\frac{\Phi_{EUV}}{\Phi_{Vis}}\right) \sim -8;$$

$$\log\left(\frac{R_{EUV}}{R_{Vis}}\right) \sim 0;$$

$$\log\left(\frac{f_{EUV}}{f_{Vis}}\right) \sim -3$$

$$\log\left(\frac{\varepsilon_{EUV}}{\varepsilon_{Vis}}\right) = 2$$

Once D_{vis} and D_{304} have been specified for each filter, the thickness of the filters can be found. For the single-material filters (pure Zr on the 98, 131 and 150 Å telescopes, and pure Nb on the 58 Å telescope) this is a simple matter; substituting Equation 9 into Equation 10, we have

$$D_{Vis} = \log\left(\frac{T_{EUV}}{T_{Vis}}\right) = \log\left(\frac{e^{-d\mu(EUV)}}{e^{-d\mu(Vis)}}\right) = \log\left(e^{-d(\mu(EUV)-\mu(Vis))}\right)$$
$$= -d\ln(10)\left(\mu(EUV) - \mu(Vis)\right)$$

The difference in the absorption coefficient μ [$Å^{-1}$] of the material in- and out-of-band is divided into the required relative density to give the required filter thickness in Å. The thicknesses required to achieve the necessary D_{vis} and D_{304} specifications are found, and the greater thickness is used (because Zr and Nb strongly reject 304 Å light, the visible light rejection limited the thickness of all the single-valued filters).

For the aluminum/zirconium filters used on all the telescopes centered at wavelengths over 170 Å, it is a slightly more complicated constrained optimization problem: the two parameters (Zr thickness and Al thickness) are varied to satisfy the two constraints (D_{vis} and D_{304}) while maximizing the in-band transmission. This problem can be solved numerically; the calculations were performed by Jordan Alexander of Luxel.

From a practical standpoint, filter thicknesses can be manufactured to within 10% error, and the specified relative densities are conservative and imprecise; therefore, they were rounded to produce target thicknesses for each filter. After manufacture, Luxel reports the thickness of each filter to a tolerance of ±50 Å. Using these values, and the known absorption coefficients of the materials, combined with the transmission of the 70 lpi nickel mesh supporting each filter (a geometrical factor ranging from 79.0% - 84.0%), we can calculate the predicted transmission of each filter as a function of wavelength in the EUV bandpass, as well as the relative density at 304 Å and to visible light.

The thickness and in-band transmission of the filter used on each of the MSSTA III telescopes are presented in Table 5. The bandpasses of these filters are presented in Figure 24.

Central Wavelength	Filter	Transmission at Central Wavelength
58 Å	4306 Å Nb	0.09
98 Å	3880 Å Zr	0.28
131 Å	3880 Å Zr	0.29
150 Å	4100 Å Zr	0.18
171 Å	1811 Å Al + 634 Å Zr	0.43
180 Å	1811 Å Al + 634 Å Zr	0.40
195 Å	2050 Å Al + 718 Å Zr	0.31
211 Å	2050 Å Al + 718 Å Zr	0.21
256 Å	2050 Å Al + 718 Å Zr	0.03

Table 5. Description of the filters used on the MSSTA III EUV telescopes.

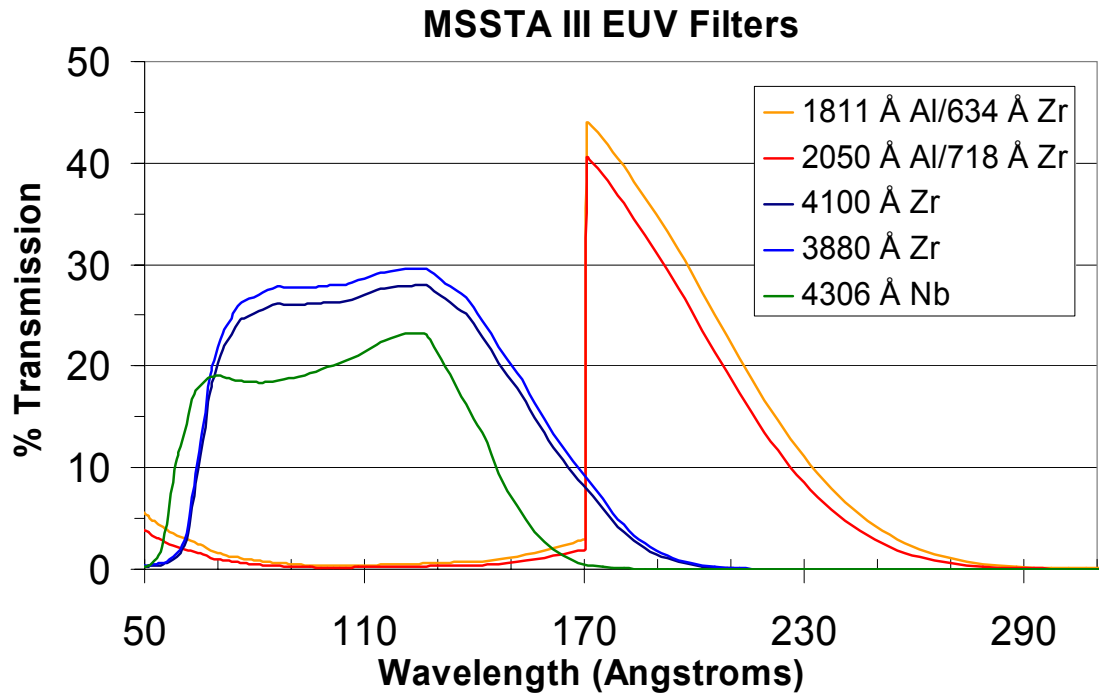

Figure 24. Transmission of the filters used on the MSSTA III. These are values calculated based on the material properties measured by Henke *et al.*, and are the values that were used to generate the temperature kernels for the MSSTA telescopes.

2.3.5 CALIBRATION OF EUV FILTERS

Unlike the multilayer mirrors, the filters were not measured at a synchrotron source to verify their in-band transmission characteristics prior to flight. While single-point transmission measurements are quite straightforward on ALS beamline 6.3.2, there were several reasons why the MSSTA III filters were not tested:

- The filters are extremely thin and delicate, and can be destroyed by any kind of rough handling (despite reasonable precautions, one backup filter was found to have developed pinholes, and, during the process of mounting the filters in the telescopes before flight, two flight filters were destroyed). Therefore, we wanted to minimize their exposure to damage.
- The integrity of the filter is a major variable in determining its performance; the presence of minute pinholes or thickness variations over the surface of an individual filter can be expected to affect its overall transmission more than deviation from quoted average thickness during production. Therefore, measuring a single filter at a single point would not be substantially more accurate than simply accepting the calculated values of the filter transmission. It would be necessary to measure the transmission of each filter over its whole area, which is impractical.

In generating the instrument bandpasses, we used the predicted filter transmission values presented in Figure 24 above.

The accuracy of these values can be compromised by deviations in average filter thickness from specified values (though Luxel gives a tolerance of ±50 Å, or about 2%, on the filter thickness after manufacture), oxidation or impurities in the filter materials, or the development of pinholes. We can estimate the accuracy of our filter transmission values by looking at the results of previous efforts to calibrate Luxel thin-foil filters.

The filters for the MSSTA I flight were measured at SSRL beamline 1-2 by Allen et al (Allen, Willis et al. 1991), 1-2 years after the flight. They found transmission values scattered widely around the predicted values (±50% RMS error). Similar results were obtained when Plummer et al. measured the filters for the MSSTA II flight (Plummer, DeForest et al. 1994). While these

large errors are discouraging, both sets of measurements were plagued by complications. In addition to the challenges mentioned above (the risk of damage to the filters, and the sensitivity of synchrotron measurements to pinholes or local variations in the filter thickness), the synchrotron beamline used was contaminated by up to 30% higher-order light, and the experimental chamber was not optimized for transmission measurements and had to be reconfigured in the middle of each run. Therefore, it is not unreasonable to suggest that the measured values are less trustworthy than the calculated values.

An elegant filter calibration was performed in flight by the TRACE instrument on its two Luxel-made thin-foil aluminum focal plane filters (Handy, Acton et al. 1999). By observing a given solar structure through both filters, then through only one, then the other, they were able to measure the average transmission over the TRACE multilayer bandpasses of each filter. The transmissions measured in this way at 171 Å and 195 Å agreed to ~8% with the predicted values. Based on this agreement, we conservatively estimate that the predicted filter transmission values used to generate the MSSTA III instrument bandpasses are accurate to 10%.

2.3.6 FILTER FAILURE

An issue that was not adequately addressed during the design of the MSSTA III filters was their ability to withstand the concentrated solar flux. Because of the success of past MSSTA flights using similar filters, and the experience of the Luxel Corporation in filter manufacture, a detailed analysis of the heat load deposited on the filters was not carried out prior to flight, despite the fact that neither Zr nor Nb had been used for solar observations before. This was a critical oversight, and proved quite costly: three of the filters were melted as soon as they were exposed to concentrated sunlight.

Table 6 shows the approximate heat load on each filter, and summarizes their performance in flight. The danger of using focal-plane filters placed <10 cm in front of the film, rather than entrance filters, is evident, as is the risk of using untested materials. Figure 25 shows one of the destroyed filters. The filter failure occurred almost instantaneously upon the payload acquiring

the sun; all the frames of film shot through damaged filters, including the first, very short exposures, are fully exposed and have roughly sun-sized holes burned through them.

Central Wavelength	Telescope Aperture and Design	Approx. Solar Flux Density at Filter (Solar Constants)	Filter Type	Result
58 Å	100mm f/15 Herschelian	27	Nb	Melted
98 Å	100mm f/15 Herschelian	27	Zr	Melted
131 Å	127mm f/8 Herschelian	95	Zr	Melted
150 Å	127mm f/28 Ritchey-Chrétien	4	Zr	OK
171 Å	63.5mm f/31 Ritchey-Chrétien	3	Al/Zr	OK
180 Å	63.5mm f/31 Ritchey-Chrétien	3	Al/Zr	OK
195 Å	127mm f/28 Ritchey-Chrétien	4	Al/Zr	OK
211 Å	127mm f/28 Ritchey-Chrétien	4	Al/Zr	OK
256 Å	127mm f/28 Ritchey-Chrétien	4	Al/Zr	OK

Table 6. Concentration of solar flux on the MSSTA III EUV filters, and the result

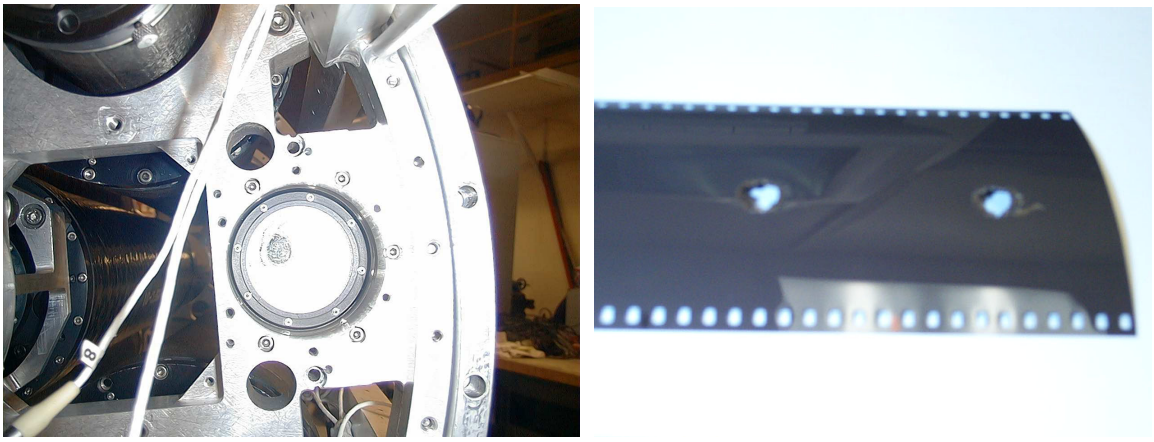

Figure 25. a) The 131 Å Zr filter after the flight; b) two frames of film from the 131 Å camera after the flight, showing very overexposed solar images

A few points are noteworthy:

- All of the relatively fast Herschelian telescopes (f/15 or faster) destroyed their filters, while none of the Ritchey-Chrétien telescopes (slower than f/25) did. However, the MSSTA has obtained EUV images with f/8 Herschelians in the past, using Al filters. Evidently, Al, with its superior reflectivity and thermal conductivity, is better able to handle the concentrated solar flux than Zr or Nb.

- While two of the pure Zr filters did fail rather spectacularly, the one on the much slower 150 Å Ritchey-Chrétien telescope performed well. Therefore, Zr has potential as a filter material, but must be used either as a prefilter or with a slow optic.

2.4 FUV optics

2.4.1 INTRODUCTION

Two of the 11 bandpasses studied by the MSSTA III – the 1216 Å Lyman α and 1550 Å C IV Ritchey-Chrétiens – lie in the wavelength regime generally referred to as far ultraviolet or FUV; the other nine are in the extreme ultraviolet (EUV). The distinction between EUV and FUV is important both in terms of how data are gathered in these regimes, and what they can tell us. The sun's FUV output is qualitatively and quantitatively quite different from both its EUV and its visible light output. While the solar EUV flux consists entirely of well-spaced emission lines from highly-ionized plasma at temperatures around 1,000,000 K, the solar FUV spectrum is characterized by numerous strong emission lines from neutral or barely-ionized atoms in the temperature range of 10,000 – 100,000 K. In addition to being much stronger than most EUV lines, these FUV lines are superimposed on continuum radiation from a variety of mechanisms, and therefore cannot be isolated without extremely narrowband (R ~ 1000) instruments. Table 7 describes some of the important observational and physical characteristics of the wavelength regimes explored by the MSSTA.

Like EUV, FUV is absorbed by the Earth's atmosphere, and must be observed from space. However, it behaves very differently in interactions with most materials. FUV photons are not energetic enough to penetrate the thin-foil filters or reflective multilayer stacks used by the MSSTA EUV telescopes, and thus imaging the sun in the FUV requires entirely different technologies. Fortunately, high-resolution FUV telescopes are a relatively well-developed technology; a number of techniques for constructing narrowband mirrors and filters in this regime have been proven effective, and have a longer history than the EUV telescopes that make up the bulk of the MSSTA payload (Foing, Bonnet et al. 1986).

		Visible	Far Ultraviolet (FUV)	Extreme Ultraviolet (EUV)	Soft X-Ray
Wavelength (Å)		3500-7500	1200-2000	50-300	1-50
Temperature of plasma responsible for solar emission		6000	10,000-100,000	100,000-5,000,000	5,000,000-30,000,000
"Layer" of the solar atmosphere where emitting plasma lies		Photosphere	Chromosphere/ Lower Transition Region	Upper Transition Region/Corona	Corona
Typical strength of emission lines (Log10, ergs cm-2 s-1 at the Earth's atmosphere)		N/A (continuum/ absorption lines)	-0.5	-2.0	-4.0
Typical strength of continuum (Log10, ergs cm-2 s-1 Å-1 at the Earth's atmosphere)		2.5	-1.5	-7.0	-6.5
Radiation can penetrate…	Earth's atmosphere?	Yes	No	No	No
	FUV filter substrate (4 mm MgF2)?	Yes	Yes	No	No
	EUV thin-foil filter (2000 Å aluminum)?	No	No	Yes	Yes

Table 7. Comparison of the ultraviolet wavelength regimes of the solar spectrum. Various definitions for all of these regimes can be found; no effort has been made here to be comprehensive or authoritative, though the definitions given in this table are used throughout this work. Radiation between 300-1000 Å is also generally called EUV, but because it is not efficiently reflected by EUV multilayers or transmitted by thin-foil filters, from an experimental standpoint it constitutes a different wavelength regime from either the EUV or FUV as defined above.

The MSSTA I included a pair of FUV telescopes, their bandpasses centered on 1216 Å (H Ly α) and 1550 Å (C IV) emission lines. Narrowband FUV reflective filter coatings were applied to the same zerodur Ritchey-Chrétien mirror substrates, figured and flow-polished by Baker Consulting, that were used for the MSSTA I EUV telescopes (see section 2.1.2). These were supplemented by two transmission filters each, consisting of 2" diameter MgF_2 windows with narrowband FUV

metal-dielectric coatings deposited on the front face. Both the mirrors and filters were coated by Acton Research Corporation of Acton, Massachusetts.

For the MSSTA II, the 1550 Å telescope was re-flown, and another 1216 Å telescope with the same aperture but slightly shorter tube and faster mirrors was used. This short Ritchey-Chrétien Lyman α telescope used only one of the two 1216 Å filters, in order to allow faster exposure times.

The MSSTA III payload used the 1550 Å telescope and the short 1216 Å telescope (reconfigured to hold both transmission filters). Both sets of optics were originally fabricated in 1989 and had been flown successfully on previous MSSTA experiments. In February of 2001, we attempted to re-calibrate the FUV optics at beamline 8.1 at SSRL. However, this bending magnet beamline is designed for higher-energy radiation (10-200 eV, or ~60-1200 Å, according to its specifications). The beamline output in the FUV is quite low, and 50% or more of what flux there is consists of higher-order radiation. Efforts to attenuate the higher-order light with MgF_2 filters proved unsatisfactory, and eventually we abandoned the project and returned the optics to Acton research for measurement on their vacuum spectrophotometer system (Callahan and Flint 1999).

Because of the cost, risk and inconvenience of disassembling the FUV telescopes and sending their mirrors to Acton for measurement, we only had the transmission filters measured. For the mirrors, we have only the reflectivity measurement that was supplied in 1989 when the mirrors were originally coated for the MSSTA I flight. While the reflective coatings are somewhat soft and vulnerable to damage, there is no reason to believe that they should degrade spontaneously if kept in a clean environment and not exposed to energetic radiation for prolonged periods. The MSSTA FUV telescope mirrors are relatively old, but they have lived fairly sheltered lives; the surfaces have never been cleaned, and they were stored in shrink-wrap in between flights. Their only exposure to UV has come during flight (when the vacuum of space should have prevented them from accumulating contaminants). Therefore, the 1989 measurements should provide a reasonable estimate of the mirrors' performance. A summary of the calibration measurements used to generate the instrument bandpasses is provided in Table 8.

Optic	Peak Efficiency (%)	FWHM (Å)	Date Measured
1216 Å mirror coating	51	200	5/2/1989
1550 Å mirror coating	79	340	5/2/1989
1216 Å filter 1	8	50	4/18/2001
1216 Å filter 2	15	120	4/18/2001
1550 Å filter 1	16	290	4/18/2001
1550 Å filter 2	16	240	4/18/2001
1550 Å filter 3	13	200	4/18/2001
1216 Å Composite Bandpass	0.26	50	
1550 Å Composite Bandpass	1.53	150	

Table 8. Summary of the efficiency (reflectivity or transmission) measurements of the MSSTA III FUV optics. The 1550 Å filter 3 was not used in flight. The narrowband reflective coatings on the two Ritchey-Chrétien mirrors of each telescope were last measured prior to the MSSTA I flight. It is possible that their FUV performance has degraded over time; this uncertainty dominates the error in the final composite bandpasses.

The efficiency of the mirrors and filters at visible wavelengths was not measured. However, Acton supplies typical reflectivity curves for the mirrors which show efficiency ranging from 2-10% across the visible portion of the spectrum. Alignment tests of the telescopes using visible light qualitatively confirm this estimate, as the mirrors produce only a faint, deep red image of a white-light target. The filter specifications include visible light transmission of 10^{-4}; this was not confirmed experimentally. If the coatings were damaged and pinholes formed, their visible light rejection could have been compromised. However, even allowing for some degradation, using the specified values for the mirrors and filters gives a visible light relative density (see section 2.3.4) that is more than adequate to ensure that the image is free of white-light contamination.

The contribution of various types of radiation (primary emission line, FUV continuum, and visible light) to the image produced by the FUV telescopes is discussed in detail in section 2.6.3. The telescope bandpasses used for this analysis, based on the measurements taken by Acton research as described above, are presented in Figure 26.

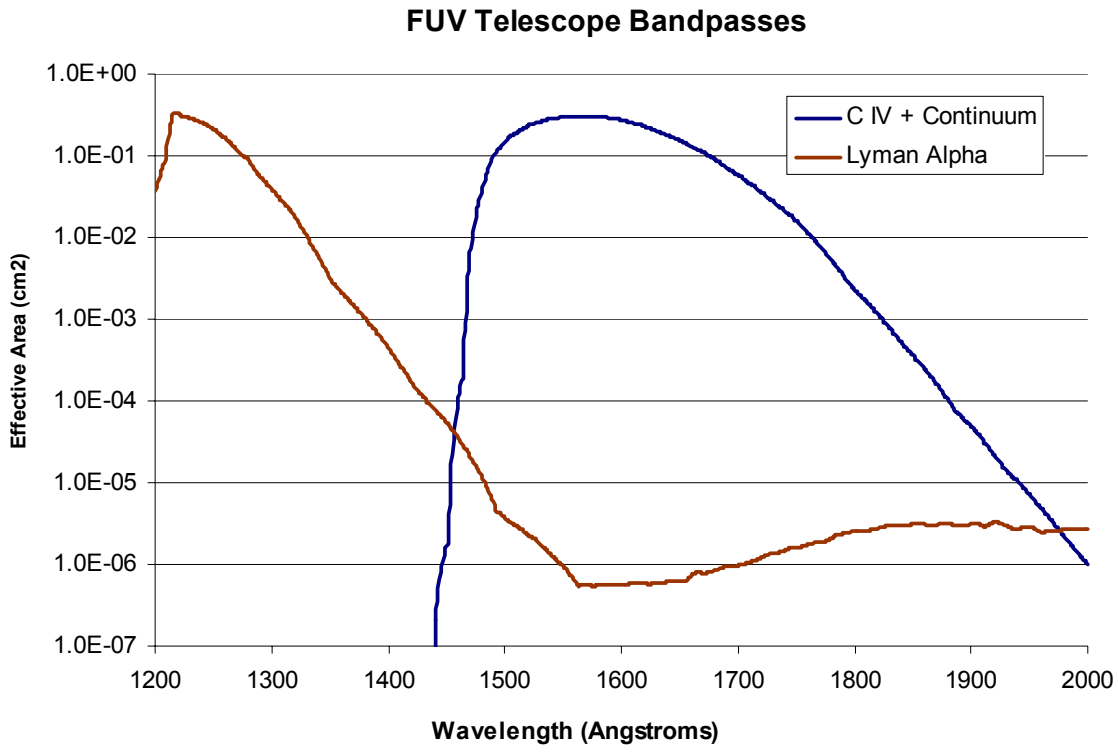

Figure 26. Effective area of the MSSTA III FUV telescopes (geometrical collecting area times efficiency of the two mirrors and two filters). Visible light rejection was not measured, but manufacturer's specifications on the mirrors and filters suggest that each telescope has a visible-light effective area less than 10^{-8} cm^2.

2.4.2 ERROR ESTIMATES

All mirror and filter calibrations were conducted by making a single measurement at a single point on the optic in question, so we do not have sufficient data to estimate the errors of those calibrations. However, measuring optics with a vacuum spectrophotometer is relatively straightforward and measurement error is generally quite small. Because of the less-stringent demands on surface smoothness and layer spacing, point-to-point variation on the optics is also

less likely to be an issue with FUV optics than with the EUV multilayers. The main uncertainty comes from the possibility of degradation in the mirror coatings since they were last measured. Based on the stability of the filter bandpasses over this same interval, we can estimate that the mirror bandpasses did not change by more than ~10%. Therefore, we can draw the following conclusions about the accuracy of the FUV mirror and filter calibration:

- For the purpose of deriving absolute fluxes from MSSTA III FUV images, the errors in the FUV mirror and filter calibration are small enough to be insignificant compared to the uncertainties involved in the energy calibration of the photographic film. Indeed, as discussed in section 2.5.3, the film was entirely uncalibrated at FUV wavelengths. Cross-calibration using known total irradiance values is possible; however, the error associated with fluences derived with this technique is entirely dominated by the uncertainty of the comparison, without any additional contribution from the mirror and filter efficiencies.

- For the purpose of estimating the contribution of various sources of solar emission to the final FUV image, the uncertainty in the shape of the bandpass derived from the mirror and filter measurements is sufficiently small that the conclusions drawn from the bandpass analysis in section 2.6.3 will be qualitatively correct.

2.5 Film

2.5.1 INTRODUCTION

The MSSTA III may represent the last time that photographic emulsions were used for a space-based astronomical imaging application. As such, it represents the end of an era of productive and exciting research. The emulsions it carried – XUV-100 and Spectroscopic 649, both manufactured by Kodak – are extremely advanced compared to the films used by early space missions, and offer superior sensitivity, spatial resolution, and exposure latitude. Only the availability of these films made it possible to fly 11 fully independent telescopes, each capable of imaging the solar disk and lower corona with arc-second scale resolution.

However, the end of the film era is welcome in many ways. CCDs now provide substantially better response to light across the x-ray and ultraviolet spectrum, and are much easier to characterize and use. Photometric calibration of the MSSTA III film required extensive experimental effort, and the uncertainties and complications resulting from the process remain the largest source of error in the interpretation of the MSSTA images. In this section, the film calibration is described, and the resulting errors are analyzed.

Photography in the EUV

Photographic film consists of a flexible backing covered with an emulsion in which silver halide grains are suspended (Figure 27). When these grains absorb sufficient energy from incident photons, they become "activated" (partially ionized). The development process then renders the activated grains to metallic silver, darkening the film. The optical density of an area of the developed film is proportional to the amount of light that reached that area (the time-integrated flux, or fluence: $\Phi = \int \phi \mathrm{d}t$, generally in ergs cm^{-2}).

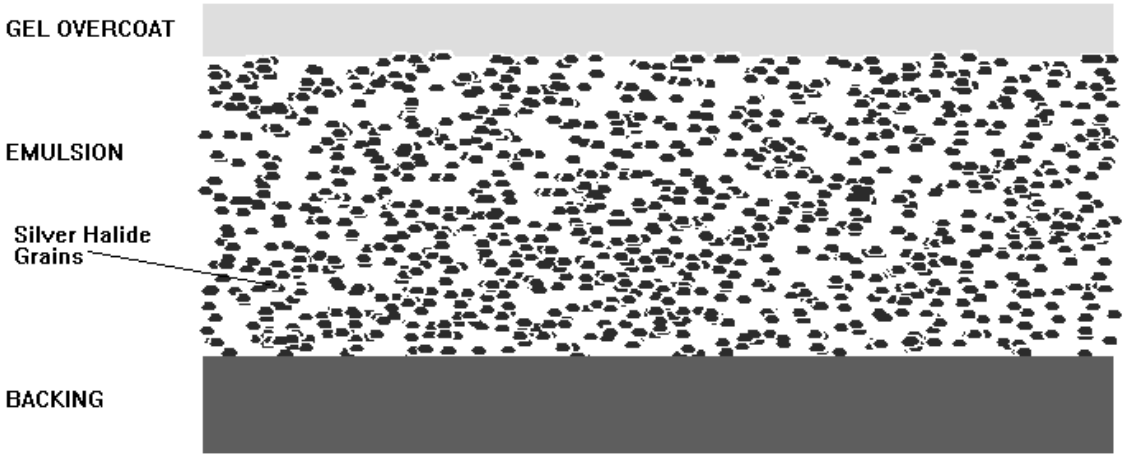

Figure 27. Photographic film consists of light-sensitive silver halide crystals embedded in an emulsion, protected by a gelatin overcoat.

Because the density on the negative is due to the pattern of discrete silver grains, there is a fundamental trade-off between spatial resolution and sensitivity to low light levels. Choosing a film requires making a compromise between very fast film with large grains and poor spatial resolution, or a slower film with finer imaging capabilities.

The basic description given above is sufficient to understand how conventional film operates in everyday use, but it glosses over a number of complications that become significant when the film is used as the detector for an EUV telescope:

- **Absorption in the Overcoat:** Over the emulsion is a gelatin coating which protects the emulsion from scratches and prevents it from drying out. The gel overcoat also tends to prevent UV photons from reaching the emulsion, which is why most films are insensitive to the wavelengths studied by the MSSTA III.

- **Drying/Sparking in Vacuum:** When transported through the camera in vacuum, the emulsion dries out rapidly despite the gel overcoat. The dry emulsion is susceptible to cracks

that appear as long lines across the negative, and to static discharge that partially exposes the film and produces a background fog.

- **Energetic Photons:** At visible wavelengths, each grain can absorb a large number of photons before becoming fully activated. Light is attenuated as it passes through the emulsion, and the film acts like an energy detector. However, when the incident photons are energetic enough to fully activate a grain individually, the film response is qualitatively different. It acts like a photon counter, and the signal is dominated by scattering statistics. The EUV wavelengths studied by the MSSTA III lie on the border of these two regimes.

An additional set of complications is raised by the fact that the intensity of the radiation reaching the film plane of the MSSTA telescopes is much lower than what conventional film is designed to image:

- **Reciprocity Failure:** Partially-activated silver halide grains can be spontaneously neutralized by electrons in the crystal if their activation is not quickly reinforced by more photons. Thus, at very low incident intensity levels, the activation process is highly inefficient. The reciprocity law, which holds that film density is determined simply by the total fluence, independent of the intensity (the rate at which that fluence is deposited), is not entirely valid under these conditions.

- **Harsh Developer:** The aggressive developing processes demanded by the low exposure values of the MSSTA images result in increased granularity on the negative, dramatically lowering the film's signal-to-noise ratio at small spatial scales.

These considerations dictate our choice of film and developing procedures. Previous MSSTA teams have conducted extensive studies on the suitability of various films for flight [(Hoover, Walker et al. 1991), (Hoover, Walker et al. 1991)], settling on two specialized emulsions from Kodak. XUV-100 is a tabular grain film similar to Kodak's consumer T-Max 100. It uses a specially-formulated overcoating that makes it orders of magnitude more sensitive to EUV light than conventional black-and-white film. Spectroscopic 649 (S-649), which was developed for

scientific applications, is an extremely high-resolution emulsion; it has a relatively thin coating that does not substantially reduce its efficiency in the EUV. Both films use a conductive ESTAR base that reduces static discharge under vacuum.

The properties of these films are summarized in Table 9. Alternative emulsions from Kodak and Agfa were studied, but none offered compelling advantages over these two. Both have been used in previous MSSTA flights, with good results.

Film	Resolution (lp/mm)	Visible speed (ASA)	Base
XUV-100	200	100	Conductive ESTAR
Spectroscopic 649	2000	0.002	Conductive ESTAR
Technical Pan	320	64	ESTAR-AH
SO-253	1250	1	ESTAR-AS

Table 9. Properties of the two photographic films used by the MSSTA, Kodak XUV-100 and Spectroscopic 649. Also included for comparison purposes is Kodak Technical Pan, a consumer film that is widely used for astronomical photography, and SO-253, the holographic film that was used for alignment testing.

The resolution listed in Table 9 for each emulsion is an approximate value based on MTF curves supplied by Kodak. Resolution is strongly affected by the developing process (and may depend on the wavelength of the exposing photons as well), and the harsh developers used by the MSSTA generally do not allow the emulsions to achieve the specified resolution. This effect is discussed further in section 2.5.4.

With scientific photography falling out of favor, the specialized emulsions used for high-resolution x-ray imaging are no longer manufactured. We were forced to rely on the remaining stock of XUV-100 and S-649 left over from the earlier MSSTA flights. These batches were originally produced in 1991; though they had been sealed and stored in a freezer since then, an overall increase in granularity and base fog density, and a decrease in sensitivity, should be expected as a result of this long storage.

The shortage of XUV-100 and S-649 was so severe that we became concerned we might not have enough for all the payload telescopes. To reduce the risk of running out of flight film, we refrained from using them for pre-flight resolution testing of the telescopes. Instead, a fine-grained holographic SO-253 film was used. Furthermore, we decided to use commercially-available Kodak Technical Pan emulsion on the 256 Å telescope, after that instrument was added to the payload, in order to save the specialized flight film for the other telescopes (this decision is described in more detail below).

Film Calibration

In order to conduct quantitative study using a MSSTA spectroheliograms, it is necessary to convert film density to physical units describing the absolute intensity of the radiation from the imaged plasma. This means performing experiments where the film is exposed with a known fluence at the wavelength of interest, then developed in a carefully-controlled process identical to the one used on the flight film. The resulting density is measured and a transfer function (fluence as a function of density) can be derived by inverting the results. Such experiments were performed prior to past MSSTA launches (Hoover, Walker et al. 1994).

However, despite the wealth of calibration data and the quality of the images obtained in these flights, the utility of the data has always been limited by uncertainty in the film calibration. The primary source of this uncertainty has been the inconsistent developing practice used on the flight film. For the first two flights, each camera carried a variety of different emulsions, spliced together in several places. The flight negatives were developed using a wide variety of processes, most of which were different from the ones used on the calibration film (and which, in the worst cases, were not even recorded, making it impossible to calibrate the process after the flight).

Using uncalibrated processes was deemed necessary because the ability of the telescopes to record high-contrast images was unproven; it was thought that employing a wide variety of processes would ensure at least some usable data. However, when the flight negatives were being reduced, it was discovered that the calibration was either entirely unknown, or was obviously

faulty (because it resulted in flux measurements that differed by orders of magnitude from accepted mean values) (Kankelborg 1996). Cross-calibrating the images with each other or with data from other instruments made some quantitative analysis possible [(Allen, Oluseyi et al. 1997), (Kankelborg, Walker et al. 1997)]. Still, reliance on cross-calibration defeats the purpose of the carefully measuring the optics, and undermines one of the primary goals of the MSSTA mission.

In order to avoid these inconsistencies, we decided that each MSSTA III telescope would carry only a single type of film, and that all film of a given type would be developed with the same process. Previous film measurements provided invaluable guidelines for choosing the appropriate film for each telescope, and the appropriate development process for each film. However, the film calibration work described in (Hoover, Walker et al. 1991) and elsewhere could not be completely relied upon. The degradation in the film response after eight years in a freezer had to be accounted for; also, some of the earlier calibration results were called into question when their application to flight images resulted in unphysical solar flux values. Finally, it is evident from MSSTA I and II flight film that the granularity of the XUV-100 in any of the tested development processes is substantially worse than the specified value of 200 lp/mm, and limits the telescope's image quality. This led to the conclusion that better data could be obtained by using a new, gentler process, or using the S-649 emulsion in place of the XUV-100. Therefore, in order to identify the optimal emulsion and process for each telescope, and to obtain accurate quantitative measurements from the resulting data, it was necessary to perform a new set of film calibration experiments.

2.5.2 CALIBRATION MEASUREMENTS

The EUV film calibration experiments were performed between February 7 and March 20 of 2000 on Beamline 8-1 at the Stanford Synchrotron Radiation Laboratory (SSRL). This is a bending magnet beamline using a toroidal grating monochromator to deliver ultraviolet light between 10 – 200 eV (60 – 1200 Å) (Tirsell and Karpenko 1990). Because of the wide variety of experiments carried out on this beamline, there is no permanent experimental end station; instead, we supplied our own vacuum chamber, configured for testing the response of photographic emulsions.

The test chamber is shown schematically in Figure 28. It was designed to use the standard Pentax 645 cameras that are flown on the MSSTA. These cameras are fundamentally incompatible with the demands of a UHV beamline. While they were cleaned and lubricated with vacuum grease, they still contain countless virtual leaks and outgassing materials; indeed, the photographic emulsion itself outgases considerably. Despite the high-capacity cryopump attached to the chamber and the use of auxiliary turbopumps, pressure in the camera chamber never got below 10^{-5} torr, while the upstream segments of the beamline require pressure below 10^{-9} torr. SSRL supplied us with a differential pumping station (Warburton and Pianetta 1990) which helped support this pressure gradient. Still, the calibration measurements were fraught with difficulties stemming from the chamber and beamline vacuum systems. However, vacuum-related issues did not hamper the accuracy of the measurements, so these problems and their solutions will not be discussed here. The procedure used in the calibration measurements is summarized below.

The camera was loaded with a batch of 70mm film for testing, and the chamber was sealed and evacuated. Once the pressure dropped below 5×10^{-5} torr, the gate valve to the differential pump was opened, allowing the synchrotron beam into the chamber. With the monochromator set to pass 0-order (white) light, the beam was roughly aligned with the experimental apparatus. Then the monochromator was set for the desired EUV wavelength, and the appropriate order-suppressing pre-filter (generally aluminum on a nickel mesh for wavelengths > 171 Å; silicon or boron for shorter wavelengths) was inserted into the beamline.

The intensity of the EUV beam was measured using an absolutely-calibrated x-ray photodiode. The reading was corrected for dark current and background light by taking another reading with the beam shuttered. The photodiode was then pulled out of the path of the beam, allowing it to reach the camera.

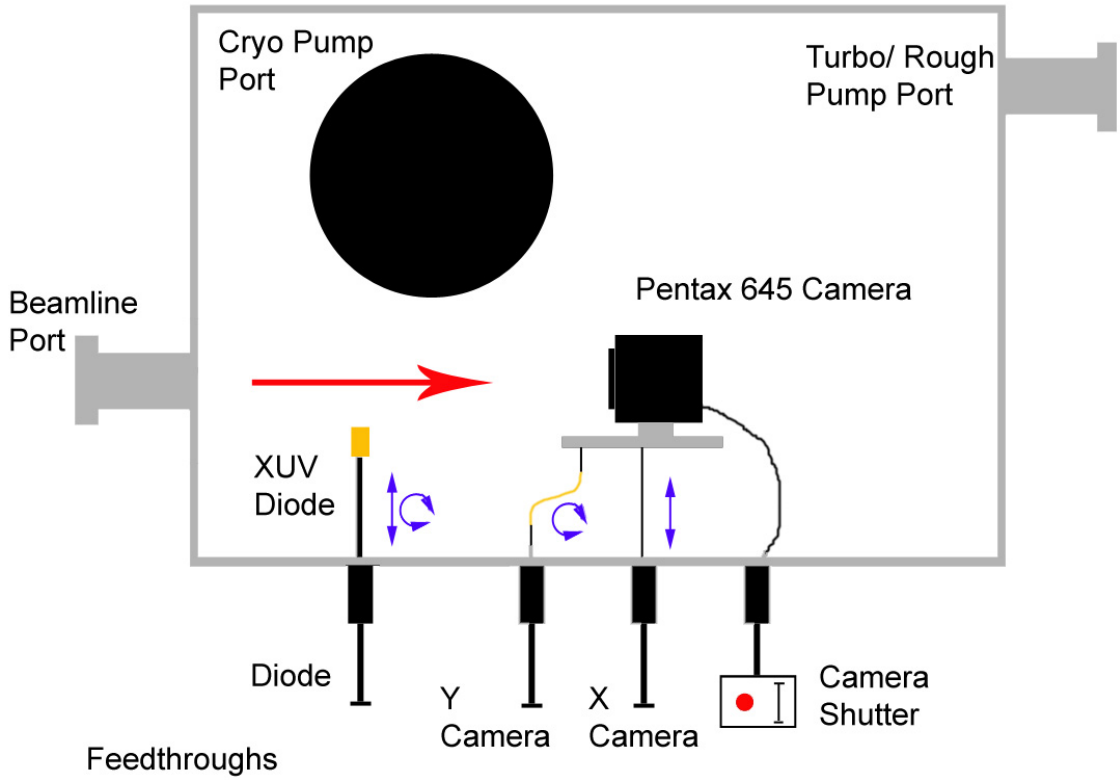

Figure 28. Schematic top view of the experimental chamber used for film calibration measurements at SSRL.

The camera was operated through a set of vacuum feedthroughs that enabled us to position it in two axes perpendicular to the synchrotron beam. The shutter was controlled by an BNC feedthrough connected to a circuit that commanded exposures from 1/64 s to 4096 s. The camera's film advance mechanism was disabled via another feed-through, so that, by moving the camera in between exposures, were able to obtain up to nine exposures of different duration on a single negative before advancing the frame.

Generally, two frames (~18 exposures) would be taken at a given EUV wavelength, providing a sufficient variation in fluence to characterize the film's response at that wavelength. We then reinserted the photodiode to the beam path and took another calibrated measurement of the incident intensity. The average of the "before" and "after" intensity measurements was used in the analysis of the negatives. It would have been preferable to be able to sample the beam intensity simultaneously with exposing the film; unfortunately, no convenient mechanism for doing so was available. In general, the beam intensity varied by less than 5% between the before

and after measurements (primarily due to the exponential decay of the current in the synchrotron). This variation was ignored in the analysis.

After re-measuring the intensity, the monochromator was set to a new wavelength, and the "before" intensity of this wavelength was measured with the photodiode still in place. Then the diode was pulled aside and the exposure sequence was repeated. Up to 5 different wavelengths could be measured in this way on a single roll of film without breaking vacuum. Then chamber was vented, the film was removed from the camera and immediately developed in the SSRL darkroom.

A variety of chemical developers and development times were tested; however, we made an effort to hold all other parameters of the development process constant. Development was done in a JOBO film processor, which maintained the temperature of the negatives and all the chemistry at 20° C. It also agitated the negatives during development in order to ensure uniform processing. All negatives were fixed for 4-5 minutes using Kodak Rapid Film Fixer, rinsed with hypo-clearing agent, washed, and treated with Kodak photo-flo to prevent water spotting.

FILM	DEVELOPER	DEVELOPMENT TIME [minutes]	Number of Exposures at each Wavelength					
			58	98	150	173	193	211
Tech Pan	D-19	20	12					
Tech Pan	HC-110-1:9	8				14		
XUV-100	D-19	20				29		21
XUV-100	HC-110-1:9	15	9	18	18	18	17	
S-649	D-19	10	8	9	5	6	9	
S-649	Dektol	12	13	12	12	12	12	
S-649	HC-110-1:9	15	8	9	11	10	12	
S-649	HC-110-1:6	15		11	11	11	10	
S-649	HC-110-1:4	15	6	2	10	13	12	

Table 10. Films and processes calibrated at SSRL.

Table 10 lists the emulsions, development processes and wavelengths which were tested during this experiment. The data taken on Tech Pan were not analyzed in detail after our tests revealed a number of undesirable characteristics, including a tendency to fog heavily under vacuum. Qualitatively examining the negatives suggests that Tech Pan is slightly less sensitive than XUV-100 to EUV. Thus, it could be used as a backup to XUV-100, but is not the best choice for any of the MSSTA instruments.

Some of the choices concerning which films and developers to test turned out to be less than optimal. In particular, we emphasized testing of the S-649 film, at the expense of examining XUV-100's wavelength response more extensively. This proved to be a costly mistake when we determined that S-649 is unsuitable for use with the MSSTA telescopes at EUV wavelengths. Unfortunately, because the analysis of the measurements was performed after our synchrotron run had ended, we did not recognize this limitation in time to change our program. Furthermore, the challenges associated with getting a usable vacuum inside the experimental chamber consumed much of the time originally allocated to the experiment. Still, the data we did gather represents the best set of EUV measurements of high-resolution emulsions ever obtained.

We also attempted to use the beamline to test the film's response to FUV wavelengths studied by the MSSTA (1216 Å and 1550 Å). Unfortunately, the beamline's output in this regime is so low that higher order contamination completely dominates. Even when we attempted to exclude the higher orders by filtering the beam with MgF_2 windows, the flux of FUV photons was insufficient to expose the film or measure with the photodiode. We were unable to find an alternate FUV light source for film calibration. Therefore, the MSSTA FUV telescopes are essentially uncalibrated. It may be possible to cross-calibrate the images after flight, given accurate measurements of their bandpasses.

2.5.3 ANALYSIS OF CALIBRATION FILM

In general, photometric calibration of film aims to produce a "characteristic curve" such as the one shown in Figure 29. The characteristic curve gives film density, defined as defined as the Log_{10} of the transmission of the photographic negative, as a function of exposure (typically

measured in lux seconds). For a given type of film, this curve is sensitive to changes in the developing process, but certain qualitative features are common to the characteristic curves of most films. At low exposures, the film is unresponsive; there is a toe region where it "turns on" and begins to show the effect of increasing exposure, and a linear region over which density increases proportionally with exposure until the shoulder is reached and the film begins to saturate.

Once the characteristic curve has been measured, it can be inverted and modeled with a transfer function such as the one described by Green and McPeters (Green and Mcpeters 1975):

(Equation 11)
$$\Phi(D) = \Phi_0 \left\{ \frac{10^{(D-D_{\min})} - 1}{1 - 10^{\beta(D-D_{\max})}} \right\}^{\gamma} \quad [\text{ergs cm}^{-2}]$$

Here Φ is the fluence on an area of the film (in ergs cm^{-2}) and D is the density produced in that area. The best-fit parameters Φ_0, $D_{\min}$, $D_{\max}$, γ and β and can be found, and the transfer function is then applied to solar images whose density has been measured at each point. This procedure results in a calibrated solar image.

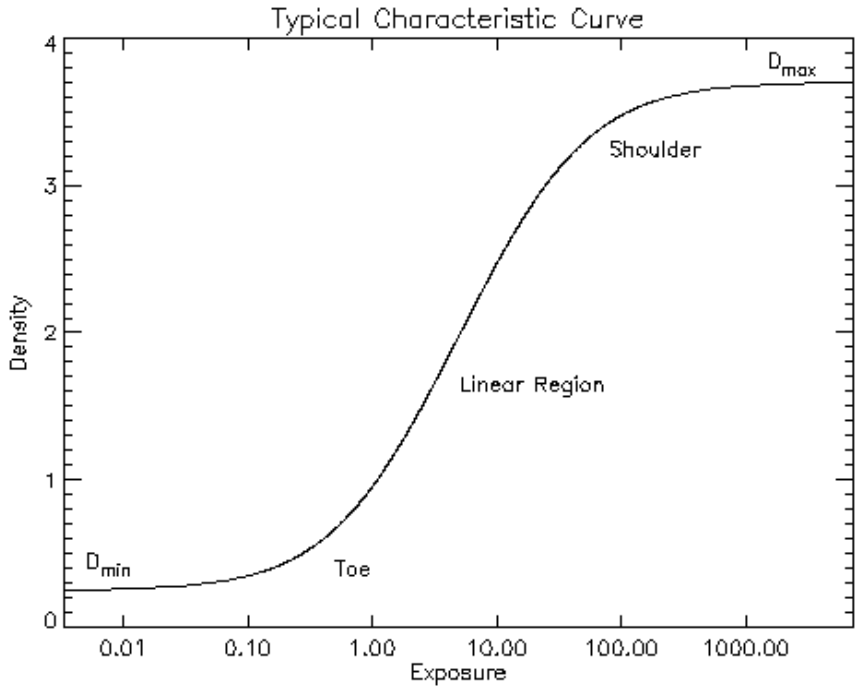

Figure 29. A typical characteristic curve describing the response of a given film and developing process.

Characteristic curves are generally provided by the film's manufacturer as a guideline for photographers. Indeed, Kodak has published curves for S-649 film (Dancy and Buckley 1987), though these measurements were made at visible light with development processes that are less extreme than those used for the MSSTA images, and thus are not usable by us. Previous solar rocket observatories, including the MSSTA, have measured and published characteristic curves for a variety of EUV films [(Hoover, Walker et al. 1994), (Golub, Nystrom et al. 1990)], and used their measurements to present calibrated data.

Unfortunately, constructing and interpreting characteristic curves is not as straightforward as it appears. Simply measuring a single point on the curve requires exposing an area of film to a reasonably uniform light of known intensity, so that the density in the area can be measured and plotted against the exposure. Calibration at EUV wavelengths requires illuminating the film with a synchrotron beam; the energetic beam generally cannot be shaped or diffused with conventional optics, and produces a spot that is highly non-uniform (see Figure 30). It is possible to measure the average density of the entire spot and plot this against the total energy contained in the beam. However, because the film is non-linear (particularly in the toe of its response curve), averaging the density in the spot is a rough approximation at best.

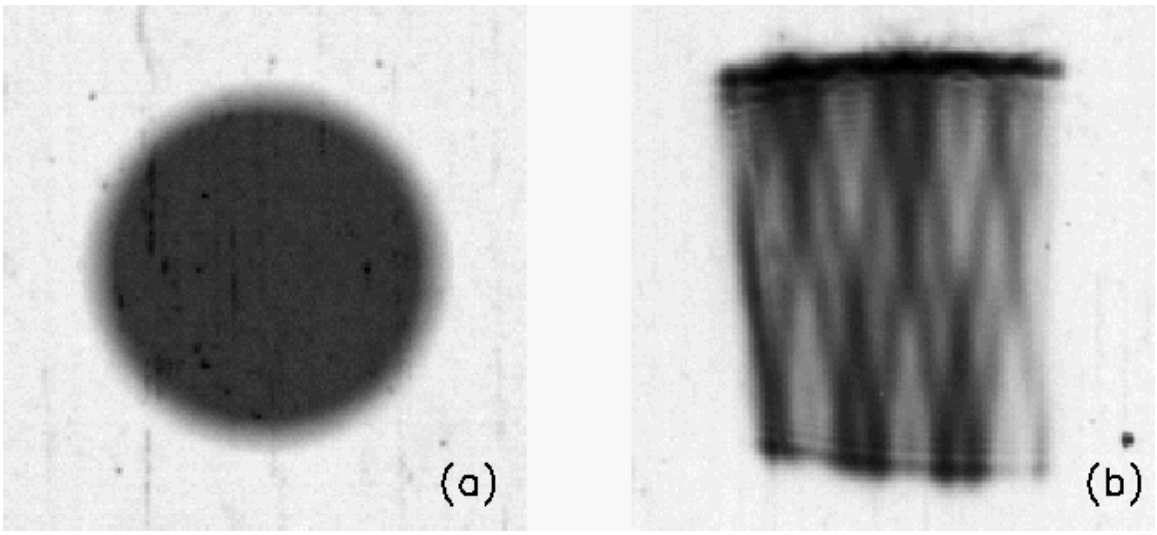

Figure 30. Generating a characteristic curve means exposing spots on the film with a known fluence and measuring the resulting density on the negative. At visible wavelengths (a), this is straightforward, as conventional optics can be used to smooth the beam cross-section and produce a uniform spot. However, at EUV wavelengths, the spot is produced by a synchrotron beam, and contains nonuniformities (especially the shadow of the order-suppressing filter) which are difficult to correct for (b). The spot in (a) is a synthetic image; b is a sample of actual data taken at SSRL.

An even more basic problem lies in the definition of film density. In order to apply a transfer function to a solar image, it is necessary to digitize the negative – that is, to generate an array of numbers $D(x, y)$ describing the density at each point on the negative. By convention, this is done with a scanning microdensitometer, which measures diffuse density at each point on the negative as shown in Figure 31. However, such systems are generally expensive and slow, and produce images with a lower spatial resolution and signal-to-noise ratio compared to conventional CCD-array-based film scanners. Film scanners, such as those used to digitize the MSSTA III negatives, assign pixel values to each point in the image by measuring a type of specular transmission (Figure 31). Converting scanner pixel values to diffuse density is not simply a matter of accounting for nonlinearities in the response of the scanner CCD; the scanner is measuring a fundamentally different quantity from diffuse density. The two measurements are strongly correlated, of course, but digitizing the same negative with a scanner and a microdensitometer (or even with two different scanners) and cross-correlating the results can produce considerable scatter, even if the signal-to-noise of each scan is quite high. Therefore, converting scanner pixel values to diffuse density before applying the transfer function effectively adds noise to the calibrated image.

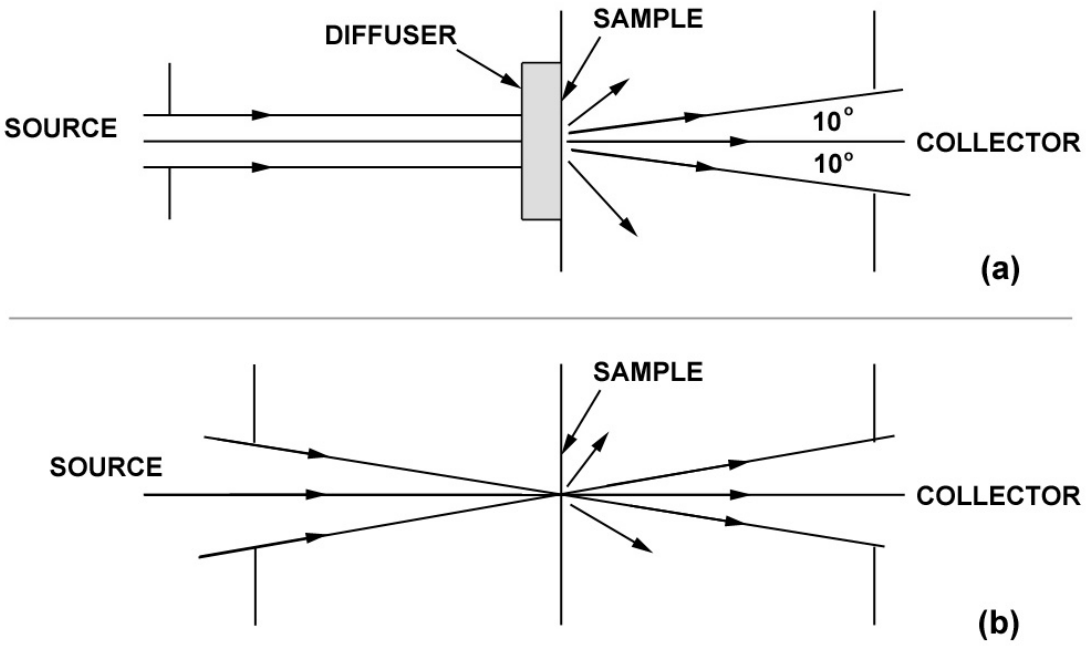

Figure 31. Density of a point in the image depends on how the negative is measured. Most calibration curves provide diffuse density, which must be measured as shown in (a). However, better image quality is obtained with a film scanner that measures some type of specular density, such as the one shown in (b). Adapted from (Dancy and Buckley 1987).

The solution is to implement a forward-fitting procedure that bypasses the step of converting a scanned spot image into a point on the diffuse density vs. fluence curve. In this procedure, a transfer function $\Phi(p)$ that converts pixel values to fluence is assumed. This function is then applied to all the pixels in a scanned image of a beam spot, and the resulting fluence values are summed to give the total energy deposited on the film in generating that spot. This energy can be compared with the known energy of the spot (determined from the photodiode measurements), and the parameters of the transfer function $\Phi(p)$ are varied to minimize the difference between the known and calculated energies of all the spots.

There are a few drawbacks to this approach, compared with the conventional technique of using the spots as points on a $D(\Phi)$ curve and then fitting to the inverted curve to find a transfer function $\Phi(D)$. The forward-fitting approach is considerably more computationally intensive, as the transfer function has to be applied to the entire digitized image at each iteration of the fit. It is also less intuitive; because the error at each point is determined after summing over thousands of pixels, it is not possible to say what effect changing the parameters will have on the error at a given point. Finally, the resulting transfer function will be specific to the scanner used in the calibration measurement, whereas diffuse density is a standardized quantity.

Nevertheless, the forward-fitting technique rests on fewer questionable assumptions than the conventional approach, and is more accurate and reliable. It is also easier to implement in the case where the same scanner is used for calibration and flight data. In the following section, the process is described in detail, and the final results of the film calibration are presented.

Fitting the Transfer Function

The calibration measurements taken at SSRL consist of a set of negatives exposed with images of the synchrotron beam. For a given type of film and development process f, a total of i spots were recorded at each of a number of different wavelengths λ. These spot images are digitized with a Umax PowerLook film scanner and saved as an array of pixel values. The photodiode readings taken before and after the exposure sequence are used to determine the intensity of the

synchrotron beam during the exposure. Thus, the data can be expressed as a pair of quantities describing each spot:

$p_{i,\lambda,f}$(x,y) – image of the spot (pixel values at position [x,y] in the array)

$E_{i,\lambda,f}$ – the total energy that fell on the film to expose the spot image

The idea of the forward-fitting technique is to define a transfer function $\Phi_{\lambda,f}(p)$ and apply this to all the spot images to generate calibrated spot images $\Phi_{i,\lambda,f}$. The calibrated spot images are integrated over area to give

$$E'_{i,\lambda,f} = \int \Phi_{i,\lambda,f} \mathrm{d}x\mathrm{d}y \qquad \text{[ergs]}$$

the calculated total energy of the spot. The parameters of the transfer function are then varied to minimize the differences between the measured and calculated total energy values (E and E').

The first step is to define the basic form of the transfer function $\Phi(p)$. In addition to providing the ability to match the data, the function should reflect the underlying physics of the photographic process. Ideally, the affect of varying its parameters should be intuitively clear as well. The basic form of the Green and McPeters film model (Equation 11) can be adapted to give a pixel-to-fluence transfer function by realizing that density is related to the $-\log_{10}$ of the transmission of a point on the negative, and the pixel values are roughly proportional to transmission (and, therefore, high pixel values correspond to clear spots on the negative, or areas of relatively low fluence):

$$\Phi(p) = \Phi_0 \left\{ \frac{p_{\max}/p - 1}{1 - \left(p_{\min}/p\right)^{\beta}} \right\}^{\gamma} \qquad \text{[ergs cm}^{-2}\text{]}$$

It is generally best to take advantage of the linear region of the film's response; however, the MSSTA images are all recorded with the film operating around the toe of the curve (getting into the linear region would require either faster telescopes or faster film, both of which tend to decrease the spatial resolution of the images). Therefore, the parameters β (and $p_{\min}$), which describe the shoulder of the characteristic curve, can be set to arbitrarily high (low) values, and the model becomes:

(Equation 12) $$\Phi(p) = \Phi_0 \left(\frac{p_{\max}}{p} - 1 \right)^{\gamma} \quad [\text{ergs cm}^{-2}]$$

Negative values of the quantity in parentheses are replaced with 0. This function is elegant and intuitive, and provides a reasonable fit to the data. The parameters are easily understood:

- $p_{\max}$ is the maximum pixel value, corresponding to the base fog density in unexposed areas of the film;
- γ is the exponent describing the contrast; and
- Φ_0 is the scale factor (specifically, the fluence that produces a pixel value of half the maximum).

Applying the transfer function to each spot image gives a calibrated spot image, which is integrated over area as described above to give a total energy value for the spot E_i' . The total energies in each spot derived from the film model are then compared to the known energies E_i as measured with the photodiode, and the fit error χ^2 is computed:

$$\chi^2 = \sum_i \left(\frac{E_i - E_i'}{E_i} \right)^2$$

The χ^2 value describes the goodness of the fit; lower values indicate that the model is accurately representing the film's behavior. The best model is obtained by varying the parameters $p_{\max}$, Φ_0 and γ until the value of χ^2 is minimized. The calculation and optimization was performed in IDL, using the built-in AMOEBA function to minimize χ^2. (A more intuitive measure of the fit quality is the RMS error, which is obtained by dividing χ^2 by the number of spots and taking the square root.)

The set of best-fit parameters identified by the minimization routine should be subjected to a common-sense check to make sure they are self-consistent and physically reasonable. In particular, $p_{\max}$ should be a little less than the highest pixel values in the spot images (i.e. ~60,000), and the exponent γ should be ~1-2. It should be ensured that the optimization converges to the same parameter values from a range of starting points, that it is not driving one or more parameters up against a hard limit, and that the solution is stable to small variations in the best-fit parameters.

This process is repeated for each type of film and development process, and for each test wavelength used; in general, the set of best-fit parameters is different for different films at different photon energies. However, certain parameters should be consistent; for example, $p_{\max}$ for a given film and process should not be a function of incident wavelength. Finally, the residuals of the fit E_i'/E_i should be examined to see specifically where the model fails to reproduce the data. Agreement is most important at the low exposure values that are generally recorded during flight (even at the expense of greater errors on the longer exposures). If the residuals show any obvious systematic error, it is likely that the form of the transfer function is not flexible enough to reproduce the data, and it should be modified accordingly. The residuals also give an indication of the accuracy of the film calibration, which is a crucial component in the photometric calibration of the flight data.

Wavelength Dependence and Accuracy of the Film Model

The forward-fitting technique does not rely on producing a characteristic curve of density vs. fluence for a particular film and development process. However, it is useful to plot the data and results of the calibration in a form that looks like a characteristic curve. Such a plot, showing response of XUV-100 film developed in D-19 for 20 minutes vs. total energy deposited on the film in the form of 173 Å photons, is shown in Figure 32. The total energy in each exposure is shown on the x-axis. The y-axis is an artificial quantity related to the film density; for each spot, it is defined as

$$\text{Approximate Average Density } D^* = -\log_{10}\left(\frac{\text{average pixel value}}{2^{16}}\right)$$

Each digitized beam spot is plotted as a diamond; the red line shows the results of applying the best-fit film model to each spot image.

Note that the red line representing the model transfer function is not a smooth, straight curve. It is worth stressing that this plot is useful only as a rough diagnostic, and is not representative of how the data are actually analyzed. The model must look at each pixel in each spot image, and does

not simply give average density as a function of total energy. As described above, reducing the calibration data to such a curve is an unnecessary compromise and introduces considerable error into the transfer function. In particular, averaging the values of all the pixels in a spot image is not justified given the non-uniformity of the spot and the highly non-linear response of the film in the toe region.

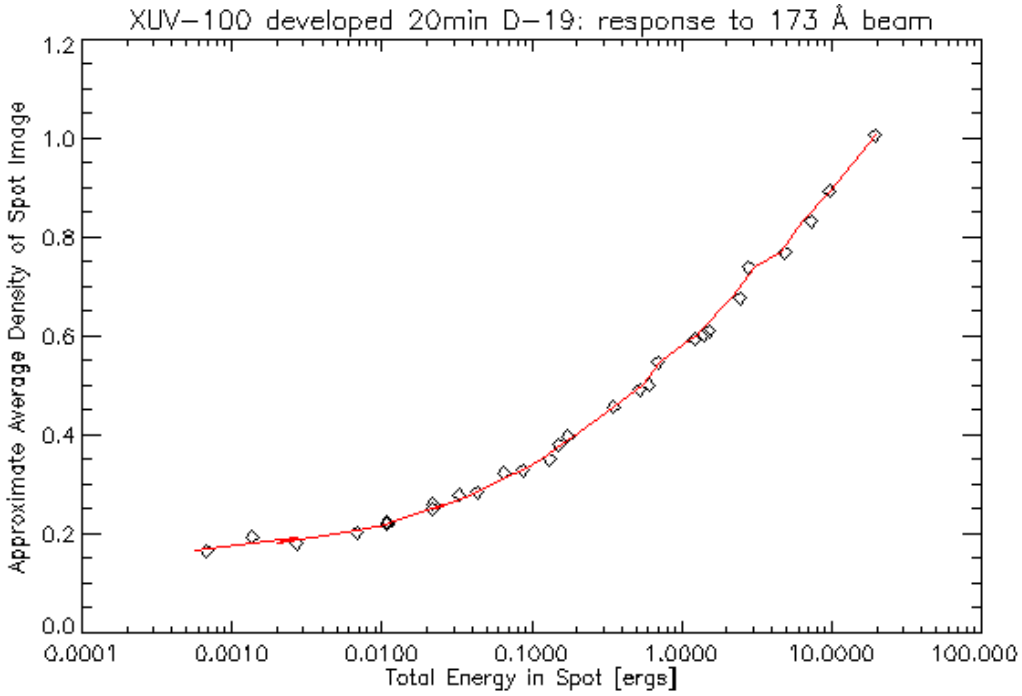

Figure 32. The calibration data for a given film type and development process can be plotted in the form of a characteristic curve. The generation of a characteristic curve is not an inherent part of the data reduction, and only approximately represents its results.

Still, plotting the data in this way does illustrate two important points. First, it is clear that we are indeed operating in the toe of the film's characteristic curve. The lowest-energy exposures are not sufficient to "turn on" the film at all, and most of the spots do not take advantage of the region of linear film response. Second, it appears that the model is doing a reasonable job of reproducing the data.

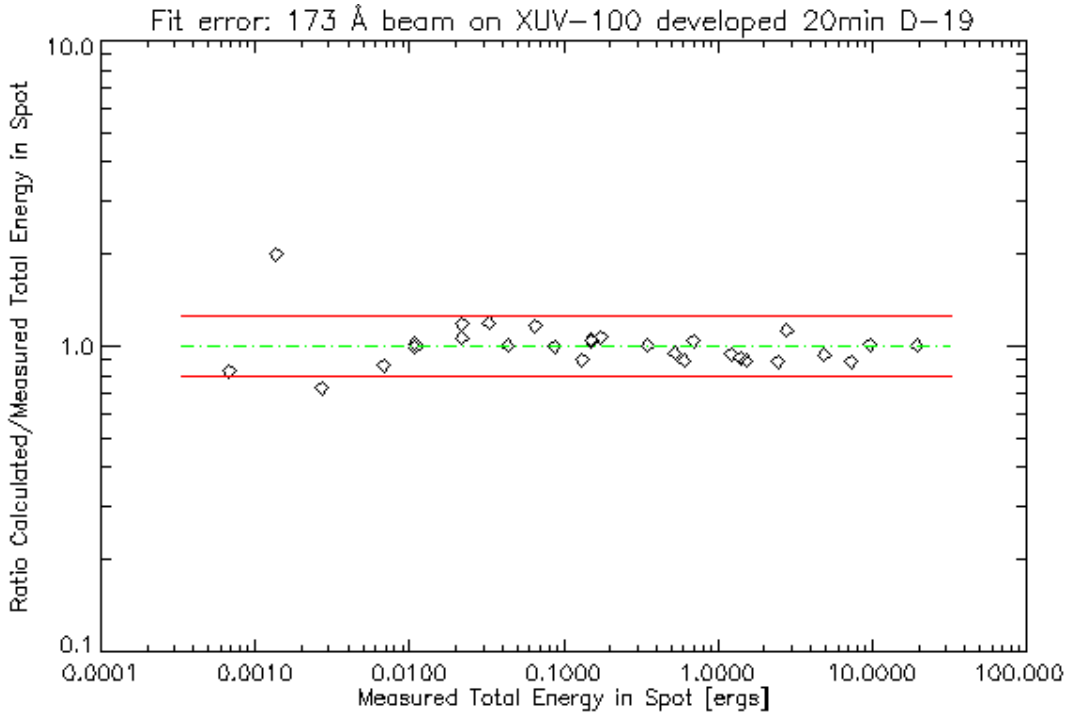

Figure 33. Ratio of total beam energy in each of the spots, calculated using the model (*Ei*′)and measured with the photodiode (*Ei*). The red lines indicate ± 20% error. Similar error plots were examined for each film type and development process studied at SSRL to ensure that the form of the film model was appropriate and to gauge the amount of scatter in the calibration data.

A better idea of the agreement between the model and the data can be obtained by plotting the residuals of the fit, E_i'/E_i vs. E_i, as shown in Figure 33. There is a slight suggestion of an inflection in the residuals around E_i = 0.03 ergs, which supports the finding of Kankelborg (Kankelborg 1996) that the Green and McPeters film model does not adequately capture the sharpness of the turn-on in the toe region. However, overall agreement is good, with an RMS error of 18.7% for the dataset shown. The error is worst at low exposures, where noise, in the form of cracks or opaque particle contaminants on or in the negative, is significant compared to the low-density spot image.

The model described in Equation 12 can consistently fit all the datasets with an error of less than ~25% if the fitting procedure is allowed to optimize each of the three model parameters separately for each different combination of film type, developing procedure and incident wavelength. However, so much flexibility is unphysical, and the model is successful mainly because the data is insufficient to constrain three parameters. A more useful model is obtained by

forcing the p_{max} parameter, which describes the base density of the film, to be a function of film type and development only.

Figure 34 shows all the datasets taken on XUV-100 film, developed for 15 minutes in a 1:9 dilution of Kodak HC-110. Each wavelength has been fit by optimizing γ and Φ_0, but all the models use the same value of p_{max}. The 173 Å and 193 Å datasets were similar enough that they could be fit with a single model. In Figure 35, the error for each of the datasets and best-fit functions is plotted. Here the suggestion that the model of Equation 12 is missing some of the details of the film response is strong: the errors show a consistent shape, and all of the models badly underestimate the fluence of the short-exposure spots. However, the general agreement shown in these figures is acceptable, at around ±20%. Better fits were obtained by using five-parameter empirical models, but the improvement was not sufficient to justify abandoning the elegance and physical basis of Equation 12.

It is encouraging that the film does not appear to distinguish between 173 Å and 193 Å photons. The wavelength dependence of the XUV-100 response seen in Figure 34 is consistent with the finding of Hoover et al. (Hoover, Walker et al. 1994) that the opacity of that film's thin gel overcoat begins to drop quickly at around 150 Å and below. The data show that the film's sensitivity continues to increase with decreasing wavelength, and is almost two orders of magnitude higher for 58 Å soft x-rays than for EUV light at 173 Å, and well into the linear regime for the short-wavelength exposures. Clearly, it will be necessary to use separate film models for each of the MSSTA bandpasses centered below 171 Å.

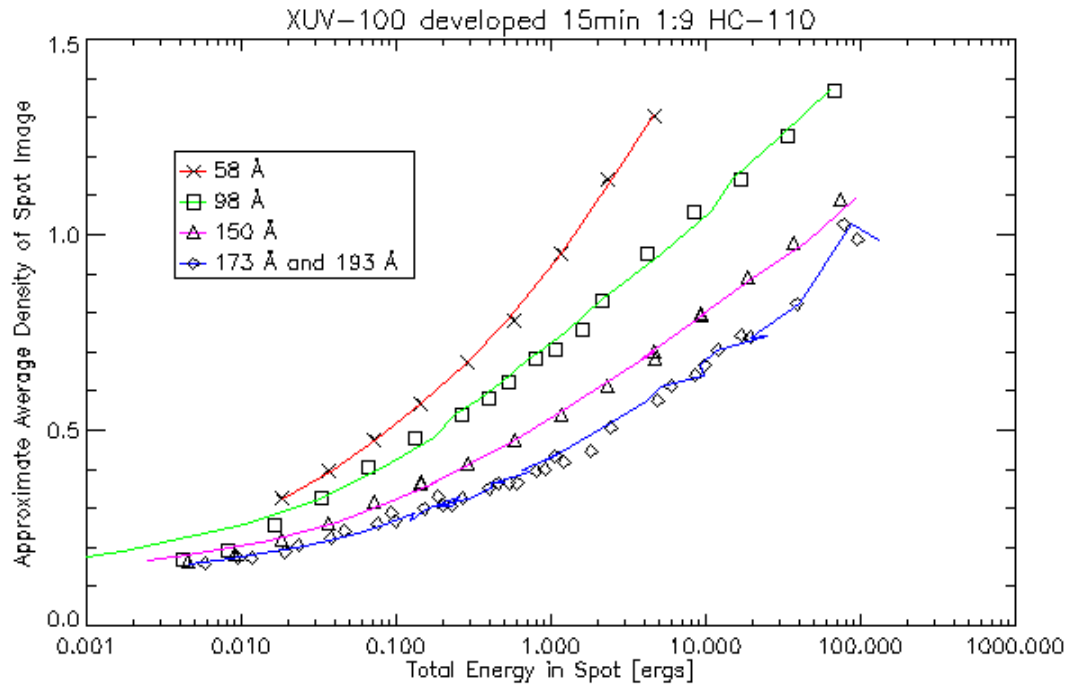

Figure 34. In general, XUV-100 film responds differently to different EUV wavelengths; here γ and E_0 have been chosen separately for each wavelength to give the best fit to the data. However, base density (p_{max}) is a function only of film type and development process, and is fixed for each dataset shown here. The 173 Å and 193 Å datasets overlie each other, and have been fit with a single model.

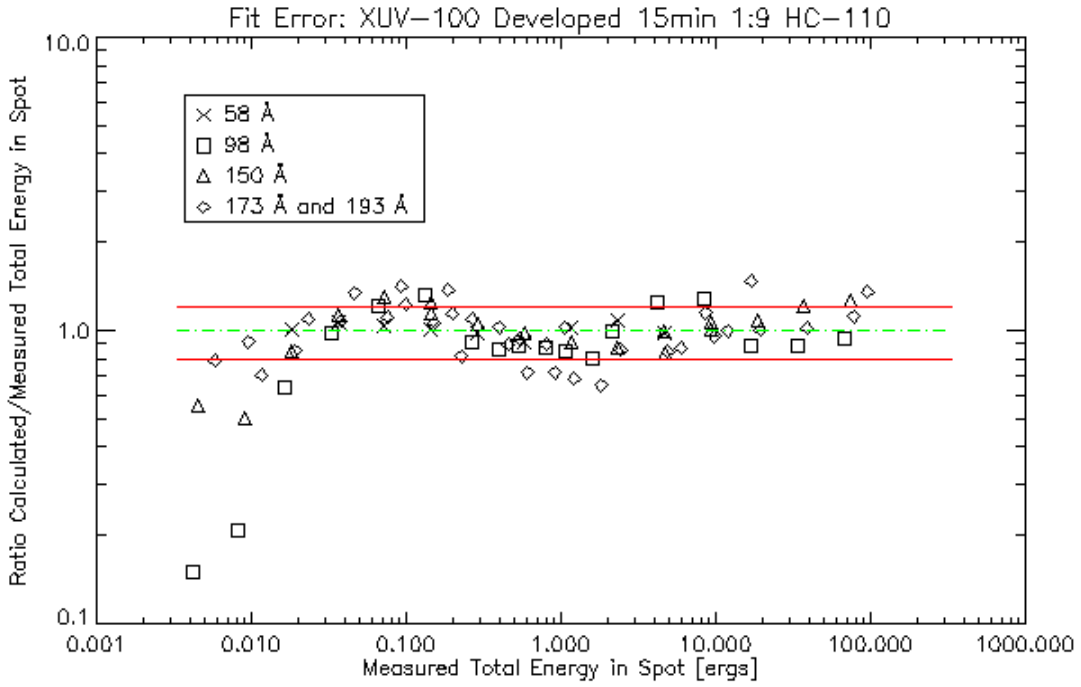

Figure 35. The discrepancy between measured energy and energy calculated from the film model for each of the spots plotted in Figure 34. There is clearly some structure in the error, indicating that the model does not capture all the subtleties of the film's behavior, particularly at low exposures.

Only a handful of other measurements were made at SSRL using XUV-100, as described in Table 10. These are shown in Figure 36 and Figure 37, with a single model being used to match both 173 Å and 211 Å. It is evident that a better fit could be obtained by modeling each wavelength separately; a model optimized for just the 173 Å data is shown in Figure 32 and Figure 33. In particular, it appears that the γ found in the combined model is too high for 173 Å and too low for 211 Å. However, the results are acceptable: the model agrees to an RMS error of ±33% over the full energy range studied, and the error is down to ±18% in the energy interval of .01 to 10 ergs, which is most relevant to the fluences delivered in flight by the MSSTA telescopes. These results confirm the idea of using a single model to describe the film's response to EUV wavelengths between 170 Å and 220 Å, but do not shed additional light on the sensitivity at shorter wavelengths.

The comparatively small amount of data collected at SSRL severely limits our knowledge of, and ability to account for, the wavelength dependence of the film's response. In addition to forcing us to use the same model for the film in different telescopes centered at different wavelengths, this limitation means we have no information about the effect of small differences in incident photon energy ($\lambda/\Delta\lambda \sim 30$), and must therefore make the assumption that the film does not substantially affect the shape of an individual telescope's bandpass. This assumption is particularly risky in the case of the 150 Å telescope, where knowledge of the bandpass is critical to our efforts to identify the source of the emission, and where the film data we do have suggests that the responsivity is undergoing a transition from one regime to another. Still, the mirror reflectivity is changing sharply enough that we will treat the film response as effectively flat over the bandpass when generating temperature kernels for each telescope.

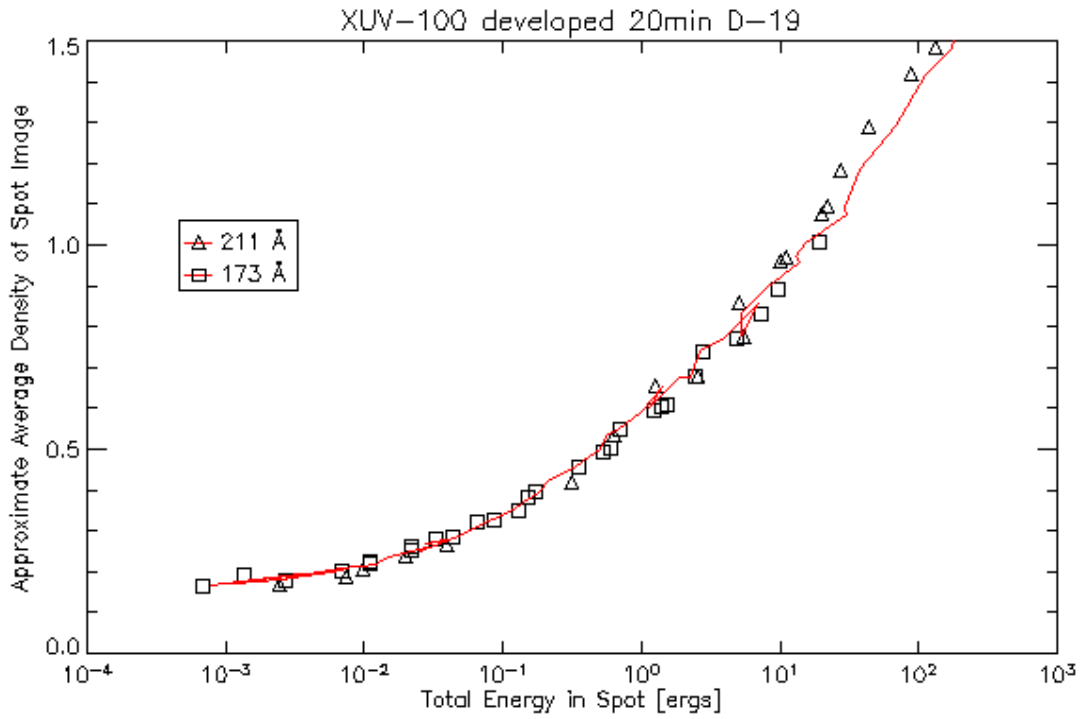

Figure 36. Only two wavelengths were used in studying the D-19 process on XUV-100. Their behavior was sufficiently similar that a single model was used to match both datasets.

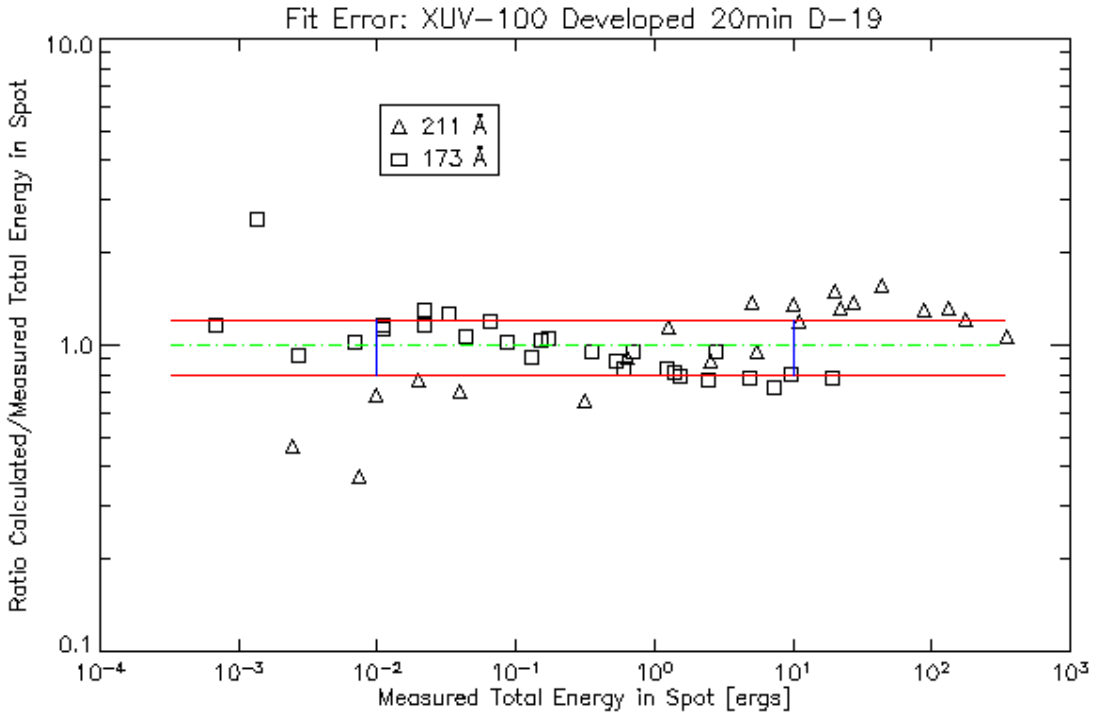

Figure 37. The model used for the two wavelengths is clearly a compromise, as the errors show an upward trend for the 211 Å and a downward trend for 173 Å. However, agreement is acceptable, particularly in the region bounded by the blue lines, which most closely reflects the exposure levels seen in flight.

The S-649 emulsion shows qualitatively different behavior when exposed at different wavelengths. The data taken on S-649 developed in D-19 are shown in Figure 38. (Note, once again, that the red curve describing the modeled energy of each spot is not smooth because the model is not a simple function of density vs. total energy, but must be applied to each pixel in each spot image.) Most of the spots represented on the plot were quite faint, and the data thus only shows the beginning of the toe of the characteristic curve. The model that is fit to all five wavelengths is therefore not terribly well constrained (except for p_{max}); however, it appears to match the data reasonably well. That it reproduces the film's behavior in the below-turn-on part of the characteristic curve is testimony to the fact that the thin, clear S-649 emulsion is much less noisy than is the crack-prone XUV-100.

Figure 39 reveals little wavelength dependence, with the exception of 193 Å, which appears to be following a much lower-γ curve than the model dictates once the exposure is sufficient to move it out of the toe regime. The data on 173 Å and 150 Å are insufficient to support any conclusions about whether the S-649's response changes at around 150 Å, as the XUV-100 appears to; however, it does appear that it responds equally well to 58 Å and 98 Å light. This may indicate that the small grains of S-649 are fully activated by individual photons at either of these wavelengths. Other data taken on S-649 using different developing processes lead to similar conclusions (and similar ambiguity about the film's response in the linear regime).

The model shown in Figure 39 agrees to ±20% or better with the data at each wavelength except 193 Å, where the agreement is only ±38% RMS. While it appears that the data are beginning to diverge from the model at higher fluence values, agreement in the range of total exposure anticipated during flight is generally good.

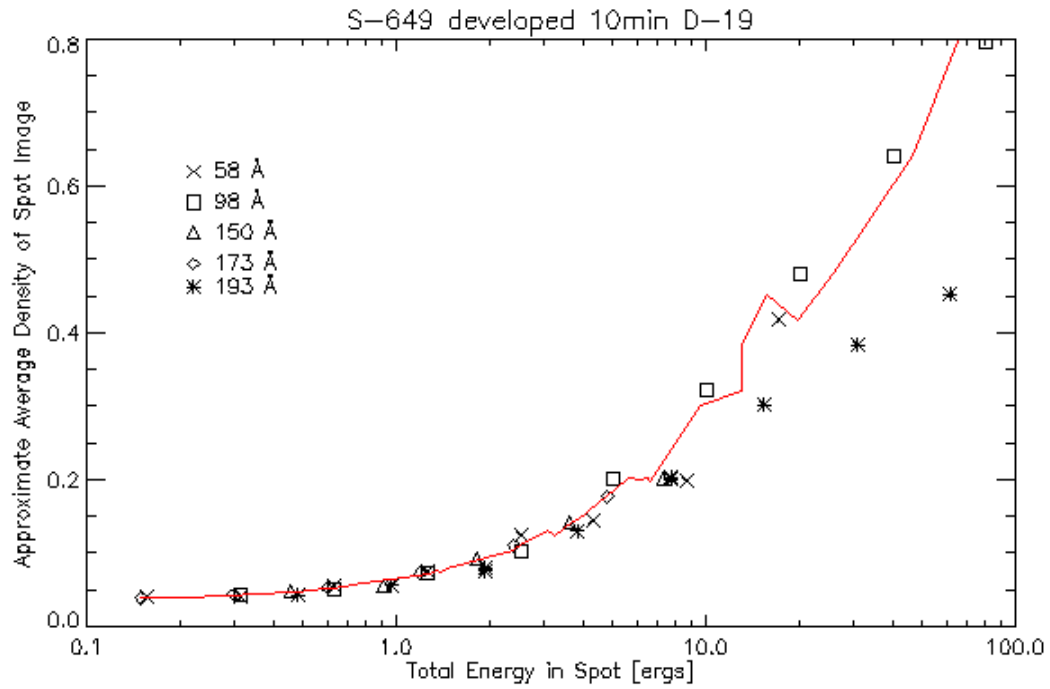

Figure 38. Five wavelengths exposed on S-649 film and fit with a single model. The EUV flux of the synchrotron beam was barely enough to get the film to respond, and most of the data is taken at energies below the point where the film response becomes linear. There is little evidence of wavelength dependence, except in the longer exposures on 193 Å.

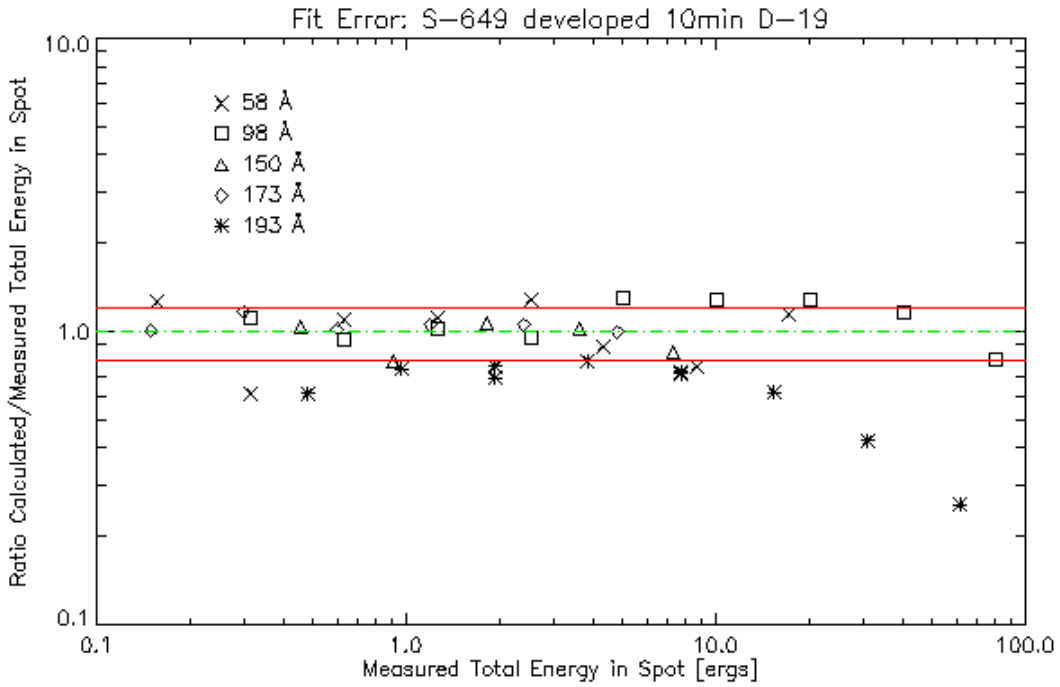

Figure 39. The model gives an RMS error <20% for all wavelengths other than 193 Å. Because the S-649 film is relatively resistant to cracking, signal-to-noise at low exposure values is better than what is seen with the XUV-100. The data appears to be diverging from the model in the long exposures.

In summary, applying the model transfer function of Equation 12 to the calibration film through the forward-fitting approach described above generally resulted in estimates of the total energy deposited on the film that were accurate to ±20%. This figure is not out of line with the target for photometric calibration accuracy of the MSSTA mission (which was ±25%), and is roughly comparable to the accuracy achieved in other phases of the calibration effort. However, a few caveats must be emphasized before accepting that the EUV flight film calibration is accurate to 20%:

- The accuracy of the transfer function has only been evaluated at relatively large spatial scales. The film spots that serve as data points in the plots above occupy as much space on the film as a 3 arc minute section of sun at the focal plane of the large Ritchey-Chrétien MSSTA telescopes. Measuring fluence at smaller spatial scales will result in considerably more scatter, and the calibration is almost completely unreliable at the scale of the film grain (where counting statistics dominate the transfer function).

- There appears to be a break in the characteristic curve of the XUV-100 that is not reproduced by the best-fit transfer function, indicating that the model is not capturing all the physics of the film's response. In general, the model works best over the middle of the fluence range expected from flight; at the higher and lower ends, it is less accurate.

- The data are insufficient to fully characterize the wavelength dependence of the film's response. On the XUV-100, we will use a single model to characterize the film's response to 171 Å, 180 Å, 195 Å and 211 Å; each of the shorter wavelengths will be fit separately. On the S-649, a single model must be used for all wavelengths. For both films, we will have to assume that the film response is essentially flat over the wavelength range of any given telescope's bandpass.

Selection of Film for Flight

With the above cautions in mind, we can use the optimized film models to examine each of the film types and processes studied at SSRL, and select the best combination for use with the flight EUV telescopes. The flight film will be required to provide high signal-to-noise ratio, a large dynamic range, and excellent spatial resolution at the wavelengths and flux levels expected during flight. Thus, the first step in selecting the best film and developer is to anticipate the flux levels each of the MSSTA telescopes will deliver at the film plane.

Doing so requires estimating the intensity of solar radiation over the telescope's bandpass, and folding that through the response of the telescope's mirrors and filters. The product of the predicted solar spectrum with the effective area function of each telescope is integrated over wavelength (and multiplied by the square of the telescope's focal length *fl* to convert steradians of emitting solar material to cm^2 on the film), giving expected flux at the film plane:

$$\phi = fl^2 \int I(\lambda) A_{Eff}(\lambda) \mathrm{d}\lambda \qquad [\text{ergs cm}^{-2}\ \text{s}^{-1}]$$

For a given exposure time Δt, this results in a predicted fluence of

(Equation 13) $$\Phi = \int \phi \mathrm{d}t \approx \phi \cdot \Delta t \qquad [\text{ergs cm}^{-2}]$$

which can be compared with the film calibration results to determine how much contrast will be produced in each film type under consideration.

The effective area function for each telescope is determined by the geometry of the optical system and the results of the mirror and filter calibration:

(Equation 14) $$A_{Eff}(\lambda) = A_{Geom} \varepsilon_f(\lambda) \varepsilon_m^n(\lambda) \qquad [\text{cm}^2]$$

where ε_f is the transmission efficiency of the filter, ε_m is the reflection efficiency of the mirror, n is either 1 (for the single-reflection Herschelian telescopes) or 2 (for the double-reflection Ritchey-Chrétien telescopes), and A_{Geom} is the geometrical collecting area of the telescope,

$$A_{Geom} = \pi(d^2 - o^2) - A_{Spider}\ . \qquad [\text{cm}^2]$$

Here d is the aperture of the telescope and o is the diameter of the central obstruction; the effective area of the Ritchey-Chrétien telescopes is further reduced by the spider vanes.

The predicted intensity of the solar spectrum,

$$I(\lambda) \qquad [\text{ergs cm}^{-2}\ \text{sterrad}^{-1}\ \text{s}^{-1}\ \text{Å}^{-1}]$$

is more difficult to calculate and less reliable. A synthetic spectrum can be generated by using the CHIANTI database and associated IDL routines (Dere, Landi et al. 1997). This process is described in more detail in section 1.3.2; it requires an input differential emission measure function DEM(T) that describes the thermodynamic state of the plasma. In order to examine the full range of intensities the MSSTA could hope to image, synthetic spectra were generated using the previously-measured DEMs of an active region and a coronal hole. The reliability of such calculations in this highly dynamic spectral regime has not been extensively tested; even using the best databases, a theoretical spectrum rests on so many assumptions that it should not be trusted to reproduce the actual solar output over an EUV bandpass with accuracy better than about a factor of 4.

Table 11 shows the predicted fluence on a part of the film imaging an active region and a coronal hole for each of the MSSTA III EUV telescopes. The full dynamic range of the payload is a daunting 5 orders of magnitude, which few films can handle without saturation or underexposure. However, it is clear that, at a minimum, the film should be able to produce a usable density above the base fog at an incident fluence of 0.1 ergs cm^{-2}, and that it not saturate at Φ = 100 ergs cm^{-2}. Most of the images will be taken around the lower end of this fluence range; unfortunately, it is the minimum-fluence criterion that proves much harder to satisfy.

Central λ [Å]	Predicted Solar Flux in Bandpass (λ ±10Å) [ergs cm-2 s-1 sr-1]		A_{Geom} [cm2]	Peak ε_m [%]	Peak ε_f [%]	Focal Length [cm]	Predicted Fluence on Film in 30-sec Exposure [ergs cm-2]	
	Active Region	Coronal Hole					Active Region	Coronal Hole
58	7514	15	314	9	19	150	1.21	0.002
98	1898	15	314	36.1	29.3	150	9.56	0.145
131	828	21	507	60.4	29.6	100	86.50	2.748
150	1620	15	412	46.5	28	350	1.92	0.021
171	20942	498	98	47.7	43.9	200	71.90	2.263
180	27190	492	98	46.1	43.9	200	48.53	0.369
195	31528	104	412	37.3	40.4	350	51.58	0.124
211	21816	46	412	32.9	33.8	350	18.63	0.034
256	11400	51	412	20.4	18.7	350	0.50	0.003

Table 11. Predicted fluence values for the MSSTA telescopes based on measurements of the instrument bandpasses and synthetic spectra calculated with CHIANTI. These predictions served as guidelines in the choice of film and development process. The 256 Å telescope was not added to the payload until after the film calibration experiments were performed.

The best-fit calibration models for each film and process (Equation 12) can be inverted to give the film's response (approximate average density, D^*) as a function of predicted incident fluence. Checking where the predicted fluences of Table 11 fall on the resulting curve is an easy way to estimate the suitability of a film process for observations with a given telescope. Figure 40 shows the inverted models for the XUV-100 calibration. The black curves show the film's response to EUV wavelengths in the 171-211 Å range with two tested development processes; the solid curve for D-19 demonstrates a notably higher sensitivity than is achieved with the HC-110. The solid black curve is linear through most of the fluence range expected from active regions. The green curves illustrate the effect of different wavelengths on the film's response; again, wavelength dependence was not measured on film developed with the D-19 process, but the data in HC-110 suggest that the film grows substantially more responsive at wavelengths of ~150 Å and below. All of the curves show that the film is essentially unresponsive to the very lowest coronal hole fluences anticipated from flight.

The situation is even worse when we examine the results of the S-649 calibration, shown in Figure 41. None of the development processes tested can make that film respond to the fluence levels delivered at coronal hole portions of the MSSTA telescopes' film planes. The S-649 is only suitable for observing the strongest active regions, and even in those cases it is generally not in the linear part of its characteristic curve. Of course, it has one advantage over XUV-100 that is not reflected in Figure 41: its base is much less noisy. Therefore, even though it produces little density in response to very low fluences, the signal-to-noise ratio it produces in its toe region is much better than what XUV-100 delivers. Still, the fact that it does not even begin to respond until the fluence reaches a few ergs cm^{-2} precludes its use with the MSSTA III EUV telescopes.

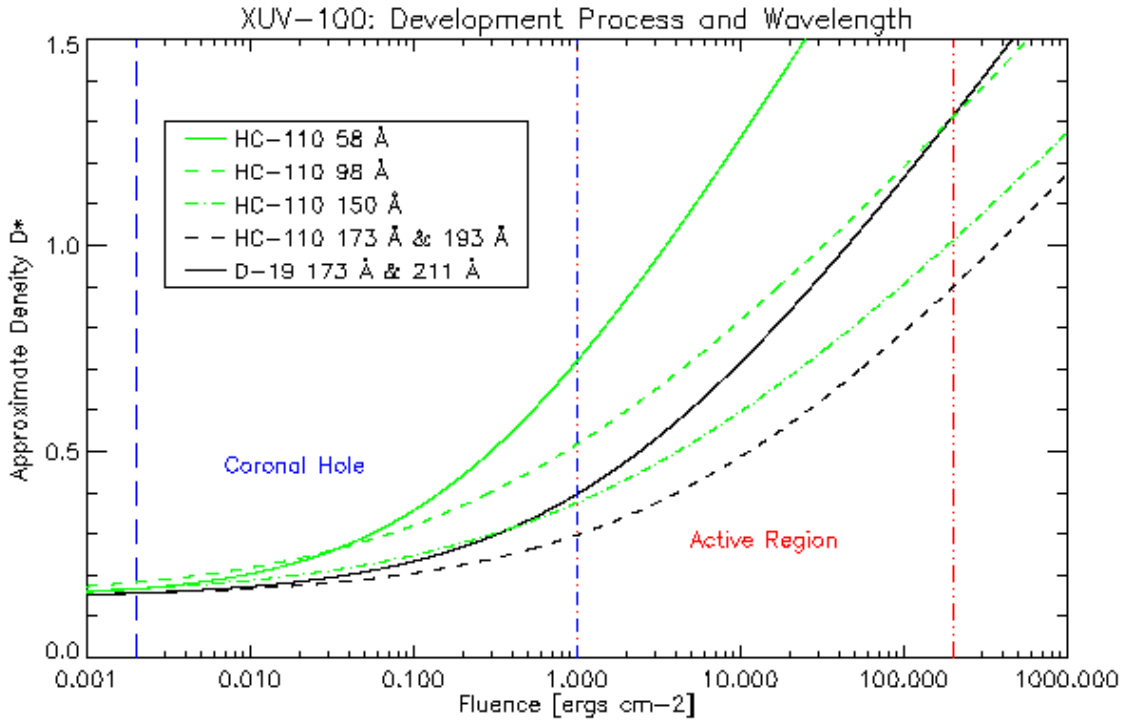

Figure 40. Inverted film models for the calibration of XUV-100. Developing with D-19 results in an enhanced response at wavelengths around 173 Å. Also, it is clear that the film's sensitivity improves at wavelengths below ~150 Å, although the wavelength effect was only measured on film developed in HC-110.

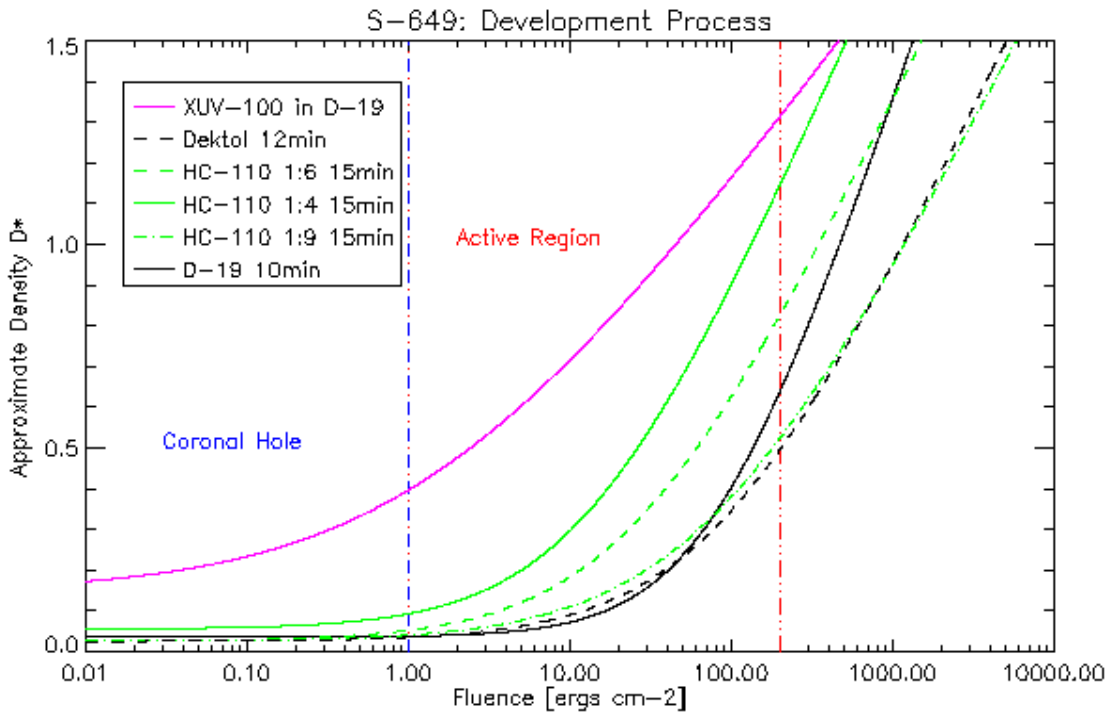

Figure 41. While its sensitivity is noticeably improved by using a concentrated developer, S-649 film (black and green curves) is substantially less responsive than XUV-100 (purple), regardless of the development process, and is unsuitable as a detector for the MSSTA III EUV telescopes. Note that whatever wavelength dependence the 649 film may possess is ignored by these models.

These results agree qualitatively with the observations of past MSSTA missions using XUV-100 and S-649. The S-649 film barely produces a noticeable amount of density when used in fast telescopes centered on strong, active-region lines. The XUV-100 images generally show a widespread (though noisy) low-density response in coronal holes, and strong, almost linear response to bright solar features.

Film in the FUV Telescopes

As described in Section 2.5.2, we were unable to perform any film calibration measurements at FUV wavelengths. Furthermore, the interaction of the various components of a photographic emulsion with FUV radiation is likely to be different enough from their interaction with either visible light or EUV that we cannot draw any quantitative conclusions about the films' FUV

response from our knowledge of their behavior in other regimes. Therefore, the FUV images are essentially uncalibrated.

Given this limitation, we decided to use S-649 film in the two FUV telescopes, centered at 1216 Å Lyman α and 1550 Å C IV. Its superior spatial resolution and noise characteristics, compared to XUV-100, are highly desirable, and, while we lacked detailed knowledge of its response characteristics, past MSSTA missions had proven that S-649 was sufficiently sensitive to record an image from the FUV Ritchey-Chrétien telescopes.

Conclusions

Because we were determined not to splice different films for use in the MSSTA III cameras, we concluded that only XUV-100 offered the necessary sensitivity at the lower end of the expected range of fluences to be produced by the MSSTA telescopes. Therefore, XUV-100 film was chosen as the optimum detector for all of the EUV instruments.

Abandoning the use of S-649 was a difficult decision, as it is in many ways a superior emulsion to XUV-100. Its stated resolution is ten times better, and our experience suggests that the advantage may be even more significant. It is also much less susceptible to cracking, and thus offers a better signal-to-noise ratio in those regimes where the incident fluence is sufficient to activate the film.

An attempt was made to improve the sensitivity of S-649 film by hypersensitization. The film was placed in a vacuum chamber, which was then backfilled with forming gas at a 3 p.s.i. gauge pressure and left for 24 hours. In principle, this process removes moisture from the emulsion and can render it orders of magnitude more sensitive, particularly in low-flux, long-duration exposures (Smith, Schrader et al. 1971). Identical set of exposures were taken on hypered and unhypered film, and developed in an identical process using 1:9 strength HC-110 developer. The results are shown in Figure 42. The hypered film does show a slightly higher density at all energies, but it is not clear that it is any more sensitive than the unhypered S-649; more likely, it is just slightly fogged. The turn-on point in the curve occurs at roughly the same energy. The

uninspiring results, and the difficulty and inconsistency of the hypersensitization process, convinced us to abandon this effort.

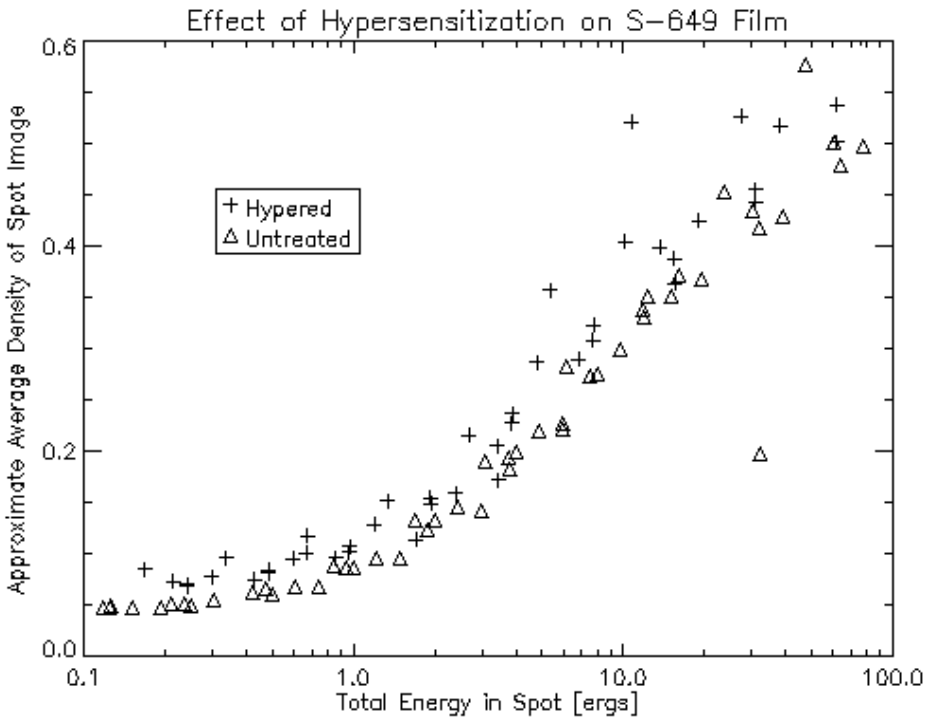

Figure 42. Gas hypersensitization of S-649 film produced a slight overall fogging of the film, with no noticeable change in its sensitivity.

Settling on XUV-100 also meant ignoring the bulk of the calibration data taken at SSRL, since we collected far more data on the response of S-649 than we did on the XUV-100. As a result, only two development processes were tested for XUV-100, and only one of these was examined over a the full range of the payload's wavelengths. However, what data we did gather (Figure 40) suggest that D-19 results in much better sensitivity than HC-110. It has also been used on previous MSSTA flight data, and is therefore more of a known quantity. Thus, D-19 was chosen as the developer for the flight film.

Finally, while the study of the effect of different development processes and wavelengths on EUV-sensitive emulsions is unlikely to be of interest, as film is no longer widely used for astronomical research, a brief examination of our SSRL data allows us to draw some preliminary conclusions about S-649 that bear reporting:

- Its response in the EUV turns on sharply and becomes essentially linear at fluences greater than about 10 ergs cm^{-2};
- In the EUV regime, it does not seem to differentiate based on the exact wavelength of the incident light;
- Using a concentrated developer can significantly enhance its sensitivity (at the expense of some unquantified loss of spatial resolution, though not nearly enough to make it comparable to XUV-100 in that regard);
- Changing development time has a slight effect on the film's responsivity; however, the degradation of spatial resolution as development time is lengthened can be large;
- In contrast to the findings of Hoover *et al.* (Hoover, Walker et al. 1994), Kodak Dektol developer does not produce much better sensitivity in S-649 than D-19 or HC-110 under similar temperature and development-time conditions.

As mentioned above, the one EUV telescope that did not employ XUV-100 was the 256 Å Ritchey-Chrétien, which used commercially-available Technical Pan film. This telescope was a last-minute addition to the payload, settled on after the film calibration experiments had been performed. Because it used a spare thin-foil filter which had not been optimized for 256 Å, its throughput was so low that we considered it marginal for obtaining high-quality data even with XUV-100. While we had very limited data on Tech Pan's EUV performance, it has been used for space-based coronal imaging in the past (Spiller, Barbee et al. 1994). We did not believe that using Tech Pan instead of XUV-100 would improve the quality of the 256 Å images, but felt that using it on this one telescope represented a low-risk, high-reward experiment.

2.5.4 APPLYING FILM CALIBRATION TO FLIGHT DATA

The decision to use XUV-100 and D-19 developer for all of the EUV telescopes meant that we were without calibration data for most of the wavelengths studied by the MSSTA payload. Furthermore, we did not have sufficient data to determine the ideal processing conditions given the choice of chemistry. The only D-19 process we tested called for 20 minutes in the developer at 21° C. This is a rather extreme push process; standard T-Max 100 film is rarely developed for

more than 2-3 minutes. While we do not have reliable data to support this conclusion, there are hints in the literature [(Mouchel 1966), (Dancy and Buckley 1987)] and in our SSRL results that lengthening the development time eventually reaches a point of diminishing returns in terms of contrast enhancement; however, the granularity continues to increase as the film is developed. We decided that cutting the development time for the flight film in half was unlikely to reduce the film's sensitivity by an unacceptable amount, and might offer a small but precious improvement in spatial resolution. Therefore, the flight film was developed in D-19 for 10 minutes.

We originally planned to return to SSRL after the flight in order to calibrate this new process at all of the relevant wavelengths. Unfortunately, the extremely limited supply of XUV-100, and the impossibility of obtaining new emulsion, along with the difficulty of working with the cameras on a UHV beamline, rendered further film calibration experiments impossible. Rather than deriving a new film model for the process used on the flight film, we were forced to use the film model fit to the data taken at SSRL at 173 Å and 211 Å on XUV-100 developed in D-19 for 20 minutes, and introduce a series of ad hoc corrections to account for the discrepancies between the flight and the calibration measurements.

Developing Time Correction

The calibration film was developed for 20 minutes, flight film for only 10 minutes. In order to make this correction, we took two identical sets of visible-light exposures at a range of incident fluences, developing one set in D-19 for 10 minutes and the other for 20 minutes. In order to conserve flight film, we used commercial T-Max 100 film for this cross-calibration experiment. The two sets of developed negatives were scanned, and compared on a pixel-to-pixel basis. A fourth-order polynomial function of the form

(Equation 15) $$\log_{10}(p_2') = \sum_{i=0}^{4} a_i \left(\log_{10}(p_1)\right)^i$$

was fit to the data, with the parameters a_i chosen to minimize the differences between p_2, the pixel values on the negatives developed for 20 minutes, and p_2', the pixel values obtained by applying the transfer function to the raw pixel values in the corresponding part of the negative

developed for 10 minutes (p_1). The converted pixel values p_2' are then entered into the film model to produce a calibrated image.

This step is, of course, a less-than-ideal addition to the calibration process. The transfer function is purely empirical, and allows some scatter into the results. Furthermore, while the properties of T-Max 100 and XUV-100 are quite similar, the fact that we used something other than the flight film, and performed the experiment at visible, rather than EUV, wavelengths, means that the transfer function parameters may not even be the best for correcting the flight data. Nevertheless, the results, shown in Figure 43, indicate that the error introduced by this correction is manageable – the scatter is 20.2%. Much of this can be attributed to alignment errors between the 10-minute and 20-minute exposures; these negatives lacked details that could be used for co-registration, and point-to-point fluctuations in the opacity of the step wedge which was used for this experiment can therefore masquerade as errors in the development time conversion. At worst, half of the error (~10%) seen in Figure 43 is intrinsic to the conversion itself.

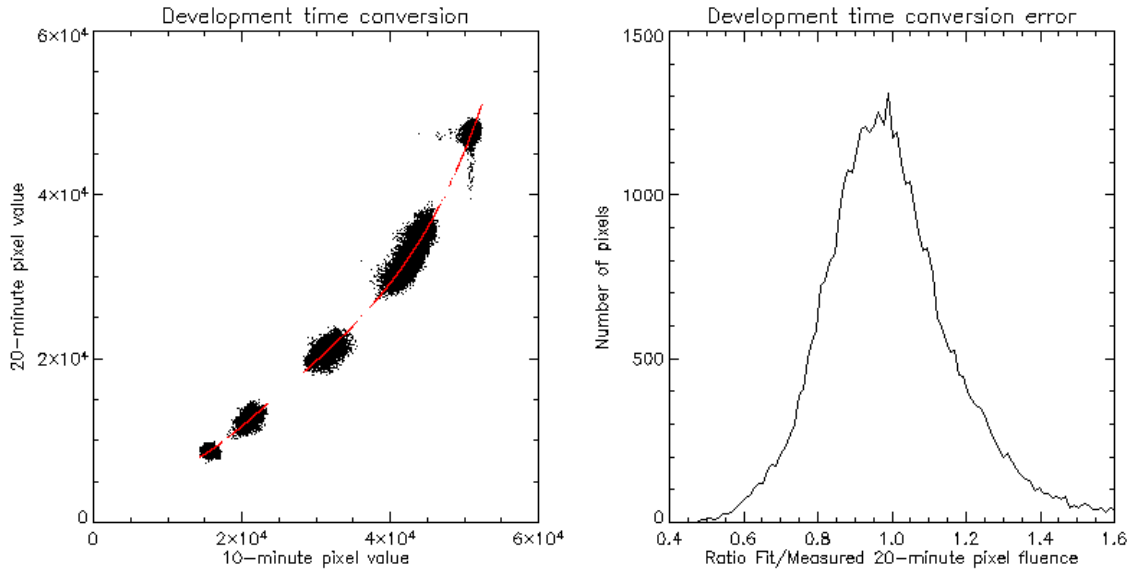

Figure 43. Calibration film was developed for 20 minutes, flight film for only 10 minutes; therefore, before the calibration can be applied, the flight film pixel values are modified to account for this discrepancy. A polynomial transfer function was optimized by comparing a density step strip, developed for 10 and 20 minutes (left). This correction results in an RMS error of about 20% in the extracted fluence values (right). Most of the scatter in these figures is due to imperfect alignment of the step wedge images used in the experiment.

Wavelength Correction

The parameters of the film model were optimized by examining the data taken at 173 Å and 211 Å. They are applicable for the MSSTA telescopes centered at 211 Å, 195 Å, 180 Å and 171 Å; however, our SSRL results indicate that the film response changes significantly at shorter wavelengths. This point was rendered largely moot by the failure of the 58 Å, 98 Å and 131 Å telescopes; however, for the 150 Å telescope, a further correction is applied.

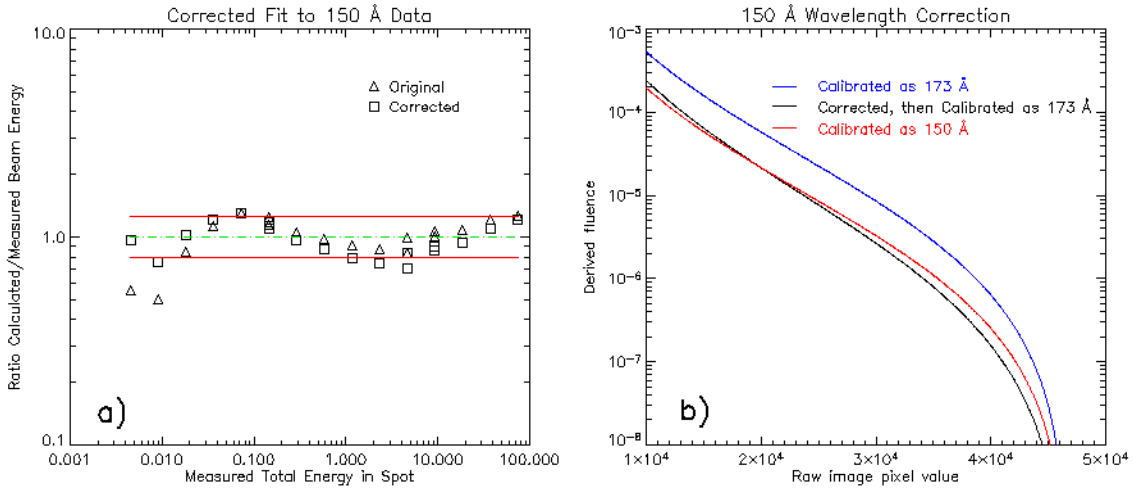

Figure 44. Because the D-19 process used in flight was not tested at different wavelengths, the film's increased response to 150 Å light was accounted for by applying a polynomial correction function to the pixel values in the 150 Å images before applying the film calibration. This additional step actually appears to improve the fit between the film model and the calibration data, as shown in a). In b), the shape of the correction function is shown for comparison with the direct calibration of 150 Å data.

The wavelength correction function is very similar in form to the development time correction (Equation 15); however, the polynomial is only third order, i.e.

(Equation 16) $$\log_{10}(p_{173}') = \sum_{i=0}^{3} b_i \left(\log_{10}(p_{150})\right)^i$$

The parameters b_i were optimized by analyzing the calibration data taken at 150 Å and developed in HC-110 (shown in Figure 34). The pixel values from these spot images p_{150} were converted to the pixel values expected from the same fluence of 173 Å light using the polynomial above, and the resulting "effective 173 Å" pixel values p_{173}' were then converted to fluences (via the film

model, Equation 12) using the film calibration parameters derived from those 173 Å – 211 Å exposures that were developed in the same HC-110 process.

It is assumed that applying the same pixel transformation function to the 150 Å flight data, which was developed in D-19, and then using the film model derived from 173 Å calibration data developed in D-19, will result in correct fluence values. This technique necessarily reduces our confidence in the accuracy of the calibration of the 150 Å data. It requires that we assume that the wavelength response of the emulsion is independent of the developing process used, and thereby opens the door to unquantified systematic errors. However, as Figure 44a demonstrates, the extra step actually gives a slightly better fit to the 150 Å calibration data than simply applying the best film model directly. Thus, to the extent that we can estimate the error, there is no loss of accuracy from the correction.

Scanner Correction

A similar pixel-to-pixel transform allows us to account for the different scanners used on the flight negatives. Most of the images used in the analysis to follow, and all of the calibration data, were digitized on a Umax PowerLook III scanner. The linearity and repeatability of this scanner with flight film was extensively tested. However, it only offers a spatial resolution of ~1200 dpi; in order to take full advantage of the MSSTA telescopes' resolution, we had to use an Imacon Flextight Photo scanner, with a resolution of ~3200 dpi. The Imacon scanner introduced a number of large-scale spatial distortions into the data, so its scans were not used for most analysis. However, in those cases where digitizations with the Imacon scanner were used, the images must be processed by first applying a function of the form

$$p_u'(p_i) = j \times p_i^{\,k} + l$$

to convert the pixel values p_i reported by the Imacon scanner to pixel values comparable to those produced by the Umax scanner under a similar fluence p_u. The parameters j, k and l of this empirical correction function were determined by scanning the same set of flight film with each scanner. The Imacon scan was downsampled to match the lower-resolution Umax scan, and the two were compared pixel by pixel.

As noted in section 2.5.3, different scanners measure density differently, and thus a function mapping pixel values measured with one scanner to pixel values of the other can only ever be an approximation. The scatter in the pixel-to-pixel conversion suggests that images digitized with the Imacon scanner have an additional calibration uncertainty of ~10%. The error is undoubtedly higher when these images are not downsampled, so quantitative work with full-resolution Imacon scans must be approached with caution.

2.5.5 CONCLUSION

The goal of the film calibration effort was threefold: we wished to identify the best film and developing process for use in flight; we needed to characterize this process so that flight data could be reduced to physical units; and we needed to understand the error associated with the calibration process. Based on the results obtained at SSRL, we selected XUV-100, developed in D-19 for 10 minutes, for the EUV telescopes. While we did not test this combination at EUV wavelengths, we developed a two-step method to convert scanned negatives processed in this way to physical units, and can use our calibration experiments to estimate the accuracy of this conversion.

Final Calibration Function

Film calibration takes the form of a function $\Phi(p)$ that converts the pixel values p from a digitized flight negative to fluence delivered to that portion of the film. For flight data digitized with a Umax scanner, the calibration function is

(Equation 17)
$$\Phi(p) = \Phi_0 \left(\frac{p_{\max}}{10^{\sum_{i=0}^{4} a_i (\log_{10} p)^i}} - 1 \right)^{\gamma} \quad [\text{ergs cm}^{-2}]$$

The parameters

$$\Phi_0 = 7.0 \times 10^{-6} \text{ ergs cm}^{-2}$$

$$p_{max} = 46932$$

$$\gamma = 1.85$$

were found by forward fitting to the synchrotron calibration data taken on XUV-100 and developed in D-19. The parameters

$$a_0 = 4274.1392$$

$$a_1 = -3897.6880$$

$$a_2 = 1333.0171$$

$$a_3 = -202.50629$$

$$a_4 = 11.533777$$

were found by comparing two sets of T-Max 100 negatives processed for 10 minutes and 20 minutes in D-19. In general, Φ_0 and γ are functions of wavelength; however, it was found that the values listed above provided acceptable agreement at EUV wavelengths between 171 and 211 Å. For the 150 Å images, the pixel values are subjected to a preliminary wavelength correction (Equation 16), with parameters

$$b_0 = -1.24427$$

$$b_1 = 1.59039$$

$$b_2 = -0.00853001$$

$$b_3 = -0.0130251$$

determined by analysis of synchrotron calibration data taken on XUV-100 and developed in HC-110. The calibration functions for 150 Å and other EUV wavelengths are plotted in Figure 45.

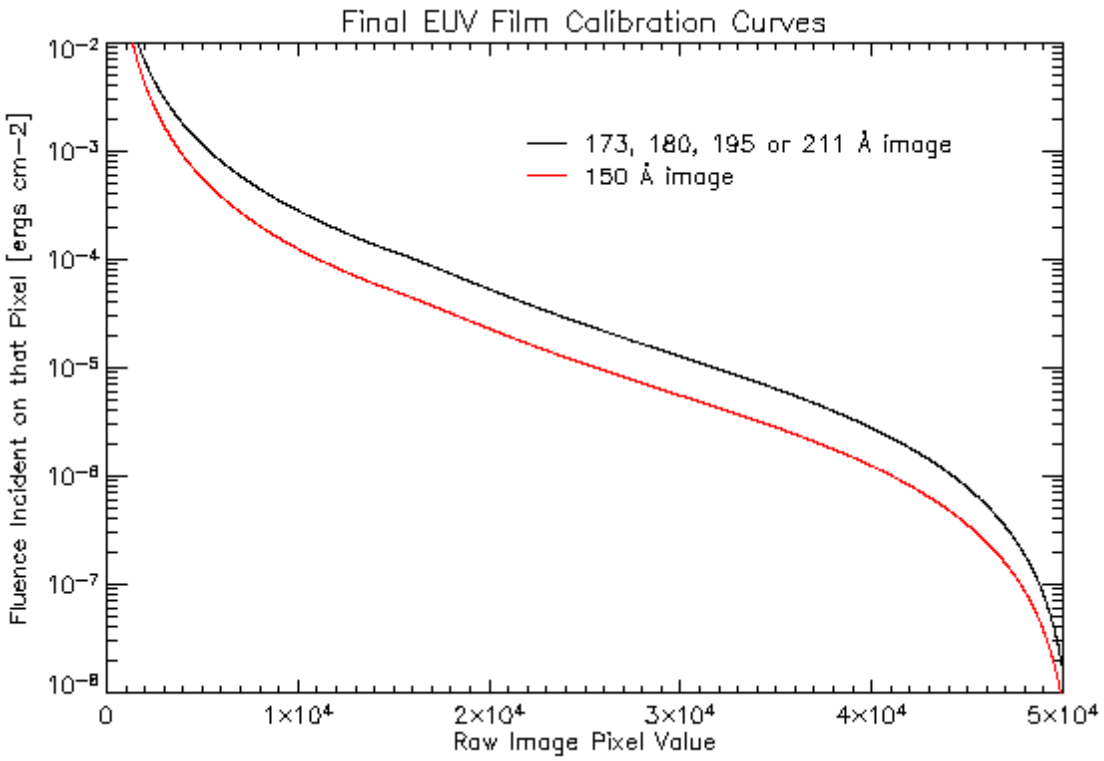

Figure 45. Complete pixel-to-fluence curves used to calibrate the MSSTA III EUV images. For most images, the active region pixel values lie in the linear part of the film's response (~25,000 – 40,000), while the quiet region pixels fall near the toe of the curve (~40,000 – 50,000).

Calibration Error

The film model (the parameters Φ_0, p_{max} and γ) reproduced the results of our synchrotron experiments with an accuracy of better than 20% RMS at all wavelengths. Correcting the film model for the development time discrepancy (with the parameters a_i) adds an additional (uncorrelated) error, whose magnitude we conservatively estimate at 10%. Thus, the measured uncertainty of fluence values obtained with the above function is ~22%.

However, estimating the accuracy of the calibration function when it is applied to flight film is complicated by a number of discrepancies between flight data and calibration measurements. Correcting for these discrepancies requires that we make certain assumptions about the film's behavior, specifically:

- That the effect of cutting the development time from 20 minutes to 10 minutes is the same for XUV-100 and for T-Max 100, and independent of exposure wavelength, since visible light T-Max was used to tune the development-time correction parameters;

- That the wavelength dependence of the emulsion's response is independent of the development process used, since the 150 Å to 173 Å correction was tuned using a different development process than what was used on the calibration and flight film;

- That the batch of XUV-100 emulsion's response characteristics did not change significantly between when the film was calibrated (March 2000) and the time of flight (April 2002);

- That the secondary conditions of the development process, such as chemical temperature, agitation, rinse water hardness, etc. were similar enough on flight film and calibration film that repeatability of the process was not affected.

Quantifying the uncertainty associated with these assumptions would have required an extensive, impractical effort. Therefore, we will proceed as though all of these assumptions are valid, though with the understanding that the unknown systematic errors on our data could be significant.

2.6 Summary

As noted in Section 1.3.3, the calibration of a narrowband EUV telescope does not result in a simple function converting data numbers to physical units of interest, such as coronal temperature. Calibration must proceed in two directions: the film/scanner assembly is measured to allow conversion from arbitrary pixel values to fluence at the focal plane, and the instrument is measured at its operating wavelength to produce a bandpass (effective area as a function of wavelength). In order to obtain a DEM or similar description of the state of the coronal plasma, the bandpass must be used to construct a temperature kernel.

In this section, I will present the temperature kernels generated from the MSSTA bandpass measurements described above. I will then discuss the errors in these temperature kernels, and in the film/scanner calibration. (The implications of these errors for our ability accurately diagnose the state of the corona are presented in Chapter 4).

For the FUV telescopes, the situation is slightly different. First, from a theoretical standpoint, the assumptions that underlie the construction of temperature kernels and DEMs are not generally valid. Furthermore, the calibration of our FUV instruments (and of the film at FUV wavelengths) is far less exhaustive than for our EUV telescopes. I will end this section with a discussion the utility and limitations of our 1216 Å and 1550 Å observations.

2.6.1 TEMPERATURE KERNELS

The process of generating temperature kernels from an EUV instrument bandpass is described in Section 1.3.3. It starts with the instrument bandpass, in the form of an effective area curve $A_{eff}(\lambda)$ based on measurements of the mirror and filter efficiency (see Equation 14). Figure 46 shows the effective area of the 9 MSSTA III EUV telescopes plotted over a model solar active region spectrum. Clearly, the large Herschelian telescope at 131 Å benefits from high-efficiency

multilayers, well-optimized filters and an unobstructed single-reflection system; it is four times more efficient at collecting photons in its bandpass than any of the large Ritchey-Chrétien telescopes. Also, note that the 256 Å Ritchey-Chrétien has an extremely small effective area, primarily due to absorption by the Zr in its visible light-suppression filter. (As described in section 2.3, the filters were designed to reject 304 Å light, and were not optimized for wavelengths longer than ~220 Å). In general, the more efficient telescopes (which also generally used faster focal ratios) were matched to the weaker lines.

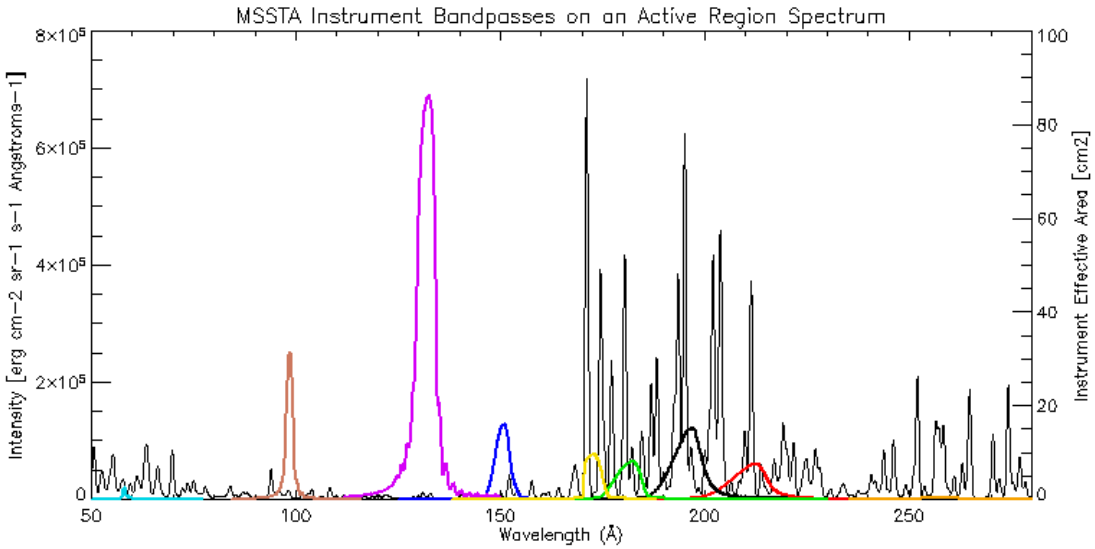

Figure 46. Effective area of the MSSTA III telescopes over a solar active region spectrum.

I then used CHIANTI to generate a list of emission lines from 40 – 300 Å. The contribution function G(T) of each line was calculated using the following assumptions:

- Constant pressure $P = 1.0 \times 10^{15}$ [K/n_e];
- Elemental abundances as specified by CHIANTI's "extended coronal abundances," which relies on the measurements of [(Feldman, Mandelbaum et al. 1992), (Landi, Feldman et al. 2002), (Grevesse and Sauval 1998)];
- Ionization equilibrium states of the elements as specified by CHIANTI's "Arnaud-Raymond_ext", which uses measurements from [(Arnaud and Rothenflug 1985), (Arnaud and Raymond 1992), (Landini and Fossi 1991)];

Then each instrument's temperature kernel was generated by summing all the contribution functions, weighted by the effective area of the telescope at the central wavelength of the emission line. Finally, the temperature kernel was divided by the square of the telescope's focal length:

$$K_i(T) = \sum_j G_j(T) \frac{A_{eff}^i(\lambda_j)}{fl_i^2} \qquad \text{[ergs cm}^{-2}\text{ s}^{-1}\text{ DEM}^{-1}\text{]}$$

Note once again that the units of the temperature kernel are the same as those of the line contribution functions; the telescope simply merges a number of lines, and measures the total flux at its focal plane rather than at its aperture.

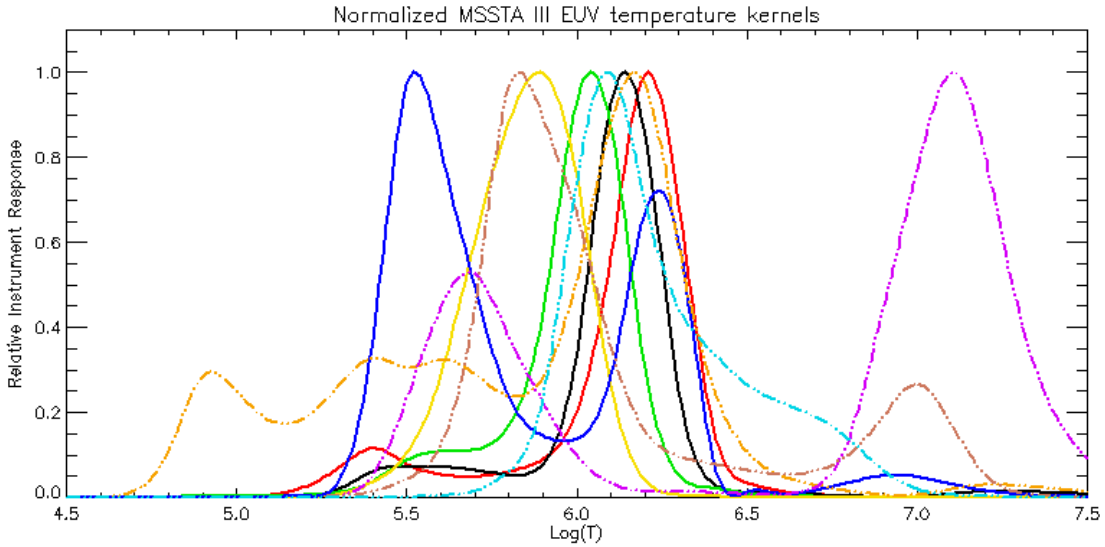

Figure 47. Normalized temperature kernels of the MSSTA III telescopes. The color assignments are those used in Figure 6.

The temperature kernels of the MSSTA III EUV telescopes are plotted in Figure 47. Note that, qualitatively, these are very similar to the predictions of Figure 6, illustrating the insensitivity of the general shape of the temperature kernel to the more subtle aspects of the bandpass curve. As long as the peak of the bandpass falls on the wavelength of a strong line, the telescope's temperature kernel will resemble that of the central line. The contributions from off-peak lines (which are weaker in intensity and less efficiently collected by the bandpass) are generally ten or more times smaller than those of the central line. Such contributions are hard to notice on a linear scale, but, because the DEM varies by orders of magnitude over the temperature range plotted,

they can become significant. Furthermore, it is necessary to look at the absolute (non-normalized) temperature kernels when doing any sort of quantitative analysis. Therefore, the most useful representation of the MSSTA III temperature kernels is that shown in Figure 48.

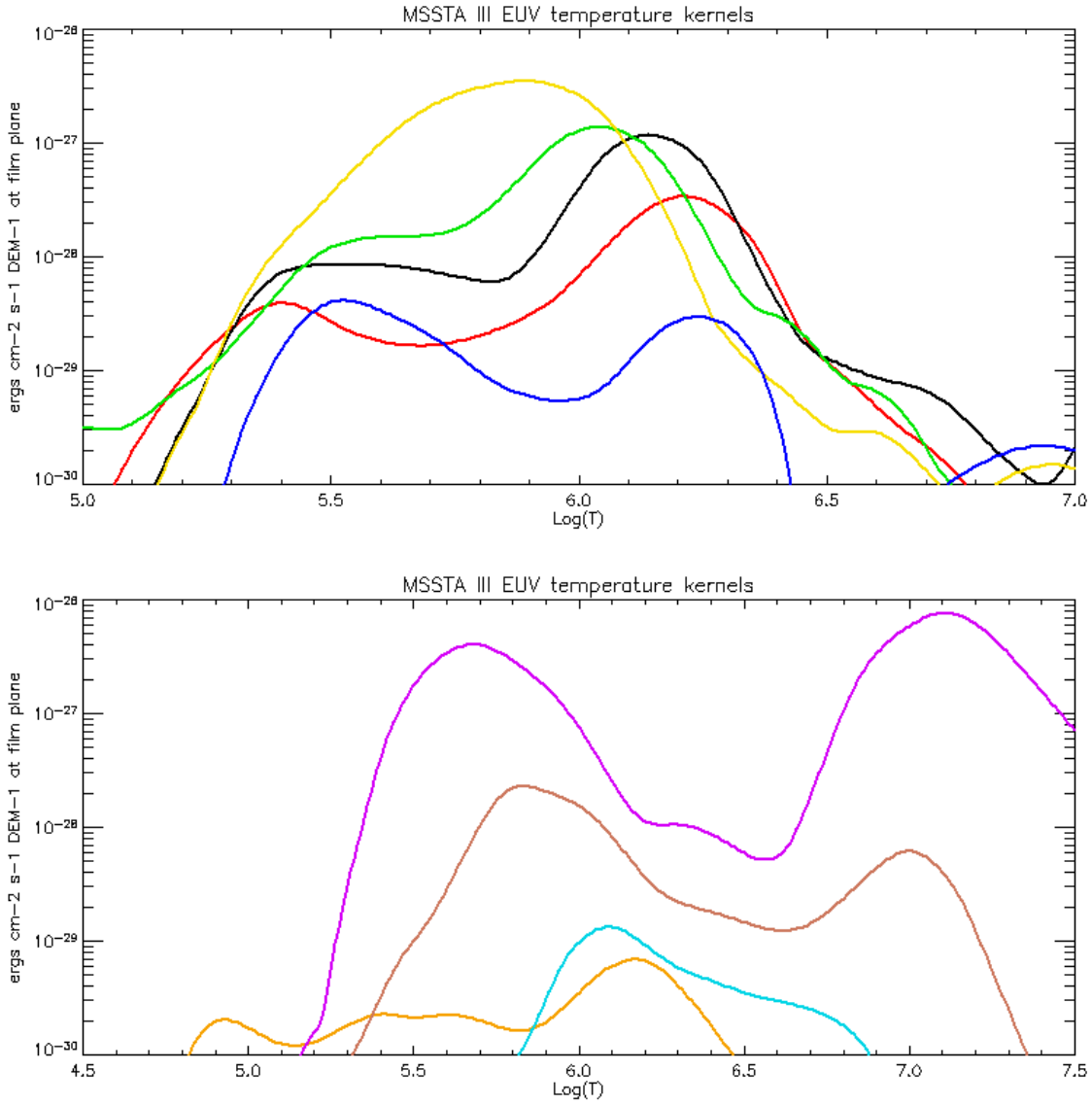

Figure 48. Absolute temperature kernels for the MSSTA III EUV telescopes. On top are the kernels for the 5 telescopes that successfully recorded images; below are the kernels of the four failed telescopes.

2.6.2 ERROR

There are substantial uncertainties in both the temperature kernel matrix $K_i(T)$ – a result of errors in mirror and filter bandpasses, as well as the errors and assumptions inherent in the atomic physics used to define the temperature response of a bandpass – and in the calibrated data (g_i) – arising from uncertain film calibration and, to a much lesser extent, photon statistics. Both contribute to error in the DEM derived from MSSTA observations. However, characterizing the errors in $K_i(T)$ and g_i is more than just a matter of putting limits on the reliability of the results of any analysis. The procedures described in section 4.1 for extracting a DEM are highly sensitive to noise, and require accurate characterization of the error associated with the inputs in order to guarantee that they work stably and produce sensible outputs. Therefore, it is essential that we have a clear understanding of what those errors are.

Effect of error on Temperature Kernels

Mapping the error bars on an instrument's bandpass to error bars on its temperature kernel is not a straightforward process. Errors that are essentially independent of wavelength – such as uncertainty in the filter transmission – are simply handled by assigning the same error to every point in the temperature kernel ($\Delta A_{eff}/A_{eff} = \Delta K/K$). However, the error bars on the mirror reflectivity measurements indicate uncertainty about the wavelength at which the efficiency peaks. The temperature kernel of a bandpass centered at, say, 150 Å looks quite different from one centered at 152 Å (cool O VI lines dominate in the first case, hot Ni XII/XIII lines in the second), and there is no easy way to decide which to use in the case of the MSSTA III EUV telescope, or even to draw meaningful error bars on the temperature kernel that is ultimately chosen.

Part of the problem lies in interpreting the error associated with the mirror calibration. Most of the uncertainty in the shape of the multilayer bandpasses comes from point-to-point variation of the bandpass over the surface of the large Ritchey-Chrétien primary mirrors. It is not clear that treating such measurements as repeat measurements (with individual errors) of a single quantity

is valid. If, as seems likely, each sample adequately represents the performance of some region of the mirror's surface, rather than each representing a random sample of a bandpass that varies constantly over the mirror, then the average of the samples is the true bandpass, and the error is actually fairly small. Furthermore, the secondary mirrors were generally not measured for the large Ritchey-Chrétien telescopes; because of their relatively small surface area, they are unlikely to show a similar variation.

We chose to model the effect of multilayer bandpass error on each instrument's temperature kernel in the following way: first, a range of different bandpasses, each fitting within the composite bandpass error bars, was generated. The temperature kernel of each possible bandpass was generated, and all these temperature kernels were compared to each other qualitatively. In every case except those of the 150 Å and 256 Å Ritchey-Chrétiens, the possible temperature kernels were all quite similar in shape. Either the shape of the bandpass was known well, with only overall magnitude errors expected (as was the case with the 131 Å and 58 Å telescopes), or the solar spectrum in the region was fairly clean and no strong contaminating lines were allowed in even as the bandpass was shifted (as with the 195 Å and 211 Å bandpasses), or both. They can be adequately modeled by treating the bandpass errors as though they were wavelength-independent.

The 150 Å and 256 Å kernels varied so widely when their bandpasses were moved around within the error bars that it is pointless to specify the error on their temperature kernels. It is necessary either to accept that the average bandpass captures the multilayer's point-to-point variation and represents the true performance of these instruments; or to decide that they are not useful for a temperature kernel analysis. Any results obtained from their images should be viewed with caution, and cross-checked if possible.

In those cases where the bandpass error can be treated as wavelength-independent, the error in the resulting temperature kernel is given by

$$\varepsilon_K = \sqrt{(n \times \varepsilon_m)^2 + (\varepsilon_f)^2 + (\varepsilon_t)^2}$$

where ε_m is the uncertainty in the mirror reflectivity at the center of the bandpass (taken from Table 3), n is the number of reflections, ε_f is the filter transmission uncertainty (set at 10%, per

section 2.3.5), and ε_t is the uncertainty associated with the theoretical parameters that go into the CHIANTI database, conservatively set at 10% based on the work (Judge, Hubeny et al. 1997). The resulting errors are listed in Table 12.

Central Wavelength [Angstroms]	% Error in Temperature Kernel	Effective % Error in Observation
58	15.0	26.6
98	14.3	26.2
131	14.1	26.2
150	20.5**	30.1
171	14.2	26.2
180	14.1	26.2
195	25.3	33.5
211	24.8	33.2
256	42.8**	48.1

Table 12. Error on the temperature kernels of the MSSTA III EUV telescopes. The 150 Å and 256 Å temperature kernels are highly suspect, as both are very sensitive to the shape of the bandpass and uncertainties in the mirror calibration are substantial. See the text, as well as the cautions on Table 3.

Absolute flux error

In all but two cases (the 150 Å and 256 Å telescopes), we have concluded that it is sufficient to treat the error on the temperature kernels as a single number, assignable to the overall normalization of the kernel. This error is indistinguishable from the error on the observations Δg_i. The observation error itself is almost entirely due to the uncertain film calibration, shown in section 2.5.5 to be 22%, after appropriate caveats are considered. Therefore, analysis of the MSSTA data can be dramatically simplified by combining all the errors into a single estimate for each telescope, pretending that the kernels are known with absolute certainty and that the only significant error is a composite Δg_i. These results are shown in the final column of Table 12. The following additional considerations, some of which have been previously raised, must be kept in mind:

- The shape of the multilayer bandpasses: Some of the telescopes were not measured enough times to identify point-to-point variations. Where such variations were found, they were

treated as scattered measurements of a single quantity, which may not be valid. Secondary mirrors were not measured, but should demonstrate less variation than primaries. The errors associated with the atomic physics should affect the shape of the bandpass, but are here treated as normalization errors. Similarly, relatively large uncertainty in the wings of the multilayer bandpasses has been ignored.

- Transmission of the filters: The filters were not measured experimentally. Transmission uncertainty was estimated conservatively at 10% based on previous work.
- Film calibration: A number of ad hoc fixes were applied to the film calibration, resting on some untested assumptions. These are listed in section 2.5.5.
- Atmospheric absorption: discussed in more detail in Section 3.3.1. Atmospheric absorption is substantial; the model used to correct for it contains some uncertainties, which can be compensated for but not entirely eliminated.

In summary, the MSSTA III EUV observations are calibrated to ~25-35%.

2.6.3 FUV TELESCOPES

Figure 26 shows the effective area of the two FUV telescopes on the MSSTA III. As described in section 0, these measurements are fairly accurate, although a large uncertainty exists around the stability of the mirror coating. However, our inability to calibrate the S-649 film at FUV wavelengths means that extracting absolute fluence measurements from their images will require that we cross-calibrate the telescopes with other, well-characterized instruments. Furthermore, at FUV wavelengths, good knowledge of the bandpass does not allow the creation of a temperature kernel. It does give us an opportunity to model the output of the FUV telescopes, and thereby determine how to analyze their images. If the images are found to be formed primarily by radiation from a single emission line, they can be cross-calibrated by normalizing the total flux in each image to spectral measurements.

We wish to characterize the response of these instruments to the typical FUV output of the solar atmosphere, in much the same way that Handy et al. characterized the TRACE 1216 Å and 1550 Å bandpasses [(Handy, Bruner et al. 1998), (Handy, Tarbell et al. 1999)]. To do so, we use a

synthetic full-disk solar FUV spectrum (based on the measurements of [(Rottman, Woods et al. 1993), (Curdt, Brekke et al. 2001)] and fold it through the bandpasses shown in Figure 26. The results are shown in Figure 49, which gives expected average flux at the film plane as a function of wavelength.

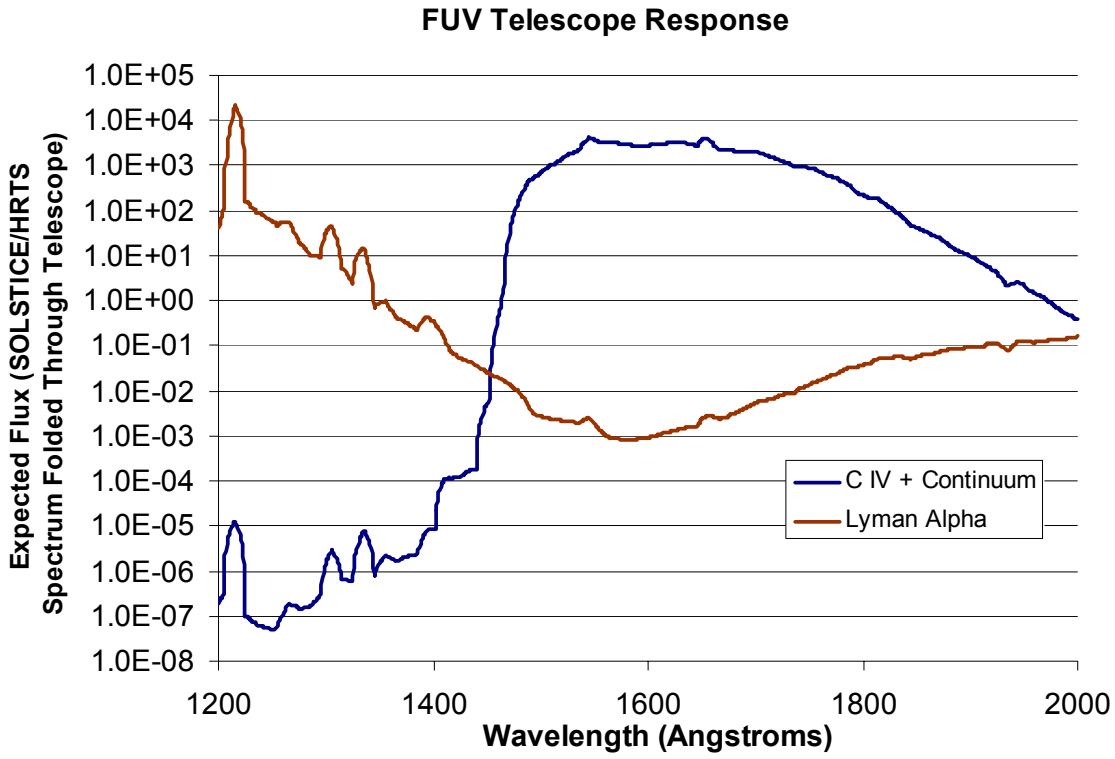

Figure 49. Response of the MSSTA III FUV telescopes showing the spectrum of expected flux at the film plane. The 1216 Å telescope shows a strong peak for Lyman α; in the 1550 Å telescope, the emission lines of C IV are barely visible above the FUV continuum.

The running integrals of the film-plane flux shown in Figure 50 show conclusively that the MSSTA III Lyman α telescope is quite pure spectrally. While these results are based on a full-disk-averaged SOLSTICE spectrum, and thus may be misleading when examining Lyman α-dark cell centers, it is clear that the MSSTA 1216 Å images can be interpreted as essentially uncontaminated maps of Lyman α emission. Contrast this with the running integral shown in (Handy, Tarbell et al. 1999), which indicates strong contamination by FUV continuum in TRACE's 1216 Å images. Their spectral purity makes an approximate cross-calibration of the MSSTA 1216 Å images simple to perform. The full-disk flux of the image can be normalized using the Lyman α line flux measured by SOLSTICE on the day of the MSSTA's flight. This

procedure requires some knowledge of the effect of atmospheric absorption on the MSSTA's throughput, and is discussed further in section 3.3.2.

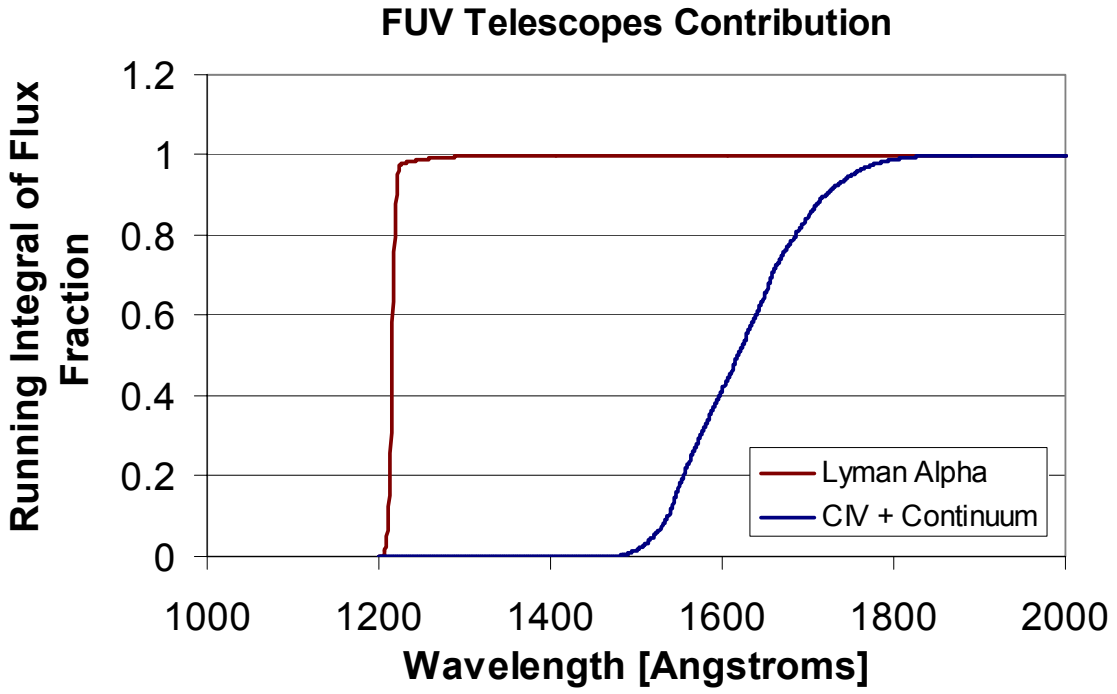

Figure 50. Running integral of the expected flux at the film plane shows that the 1216 Å telescope is completely dominated by Lyman α flux, while the 1550 Å telescope sees emission from a broad range of wavelengths from 1500-1700 Å.

On the other hand, the MSSTA's 1550 Å image is almost entirely FUV continuum, with only a barely-noticeable contribution from the strong C IV and Si II emission lines. Whereas TRACE can increase the contrast between C IV and continuum radiation by subtracting a continuum-only image, our 1550 bandpass is essentially uncalibratable (even cross-calibrating with TRACE's continuum images is unfeasible, as the two instruments have substantially different bandpasses and thus see different chunks of the continuum). Its images are extremely sharp (approximately 1 arc-second resolution), and thus may be useful for studying the morphology of the chromospheric network; but absolute flux measurements cannot be obtained or interpreted for this telescope.

3 Flight of the MSSTA III

3.1 Construction

The MSSTA payload and team arrived at White Sands Missile Range, New Mexico on March 17, 2002. The instrument flew on April 30, more than six weeks later. That interval was filled with more challenges and catastrophes than are typically encountered by half a dozen different payloads in succession, and the fact that the MSSTA was able to fly at all, let alone succeed as well as it did, is a testament to the hard work of my colleagues Dennis Martínez-Galarce, TJ Bay, Ramesh Kumar and AmirAli Talasaz, and the dedication and skill of the NASROC support personnel at White Sands. I will here describe the aspects of payload integration most relevant to understanding the data, and then present the results of the flight itself.

3.1.1 OPTICS

The multilayer-coated mirrors of the Ritchey-Chrétien telescopes were integrated into their optical tube assemblies and bench tested in the MSSTA cleanroom at Stanford after calibration measurements were completed at the ALS (The Herschelian telescopes consist of a single mirror and a camera, and thus cannot be tested as a unit until they have been integrated into the payload itself; they were not aligned until we reached White Sands Missile Range. Because none of these telescopes produced an image, the procedure used to align and test them will not be discussed in detail).

Each Ritchey-Chrétien OTA was tested in two ways: first, immediately after assembly, it was mounted in a Fizeau interferometer in order to sample its wavefront performance. Interferograms were collected using a CCD camera; because the interferometer set-up included two passes through the telescope, the interferograms were twice as sensitive as the Ronchigrams produced by

star-testing telescopes (*i.e.* one fringe corresponds to ¼ wave error). The interferometer system and a representative interferogram are shown in Figure 51. The interferograms were analyzed by eye to give an estimate of the overall level of aberration in the system, and to look for indications of how the performance might be improved. The optics were then tilted in order to minimize coma, rotated in order to optimize matching of the primary and secondary mirrors, and roughly set for focus.

In general, the telescopes performed at roughly the ¼ wave level; that is, they displayed enough aberrations that it is unreasonable to expect them to come close to the theoretical in-band diffraction limit of 0.1 arc-seconds. The interferometer revealed some pinching of the secondary mirrors in their cells on the small Ritchey-Chrétiens (171 Å and 180 Å); we were able to re-mount the 180 Å telescope in a new cell, but the 171 Å secondary was wedged in place and the problem could not be solved. We also discovered some curious distortions around the edge of the primary mirror of the 256 Å telescope, due to either strain from the Silastic putty holding the mirror in place or degradation of the multilayer stack. We constructed an aperture mask for the 256 Å telescope to prevent scattered light from the mirrors edge from contaminating the rest of the image.

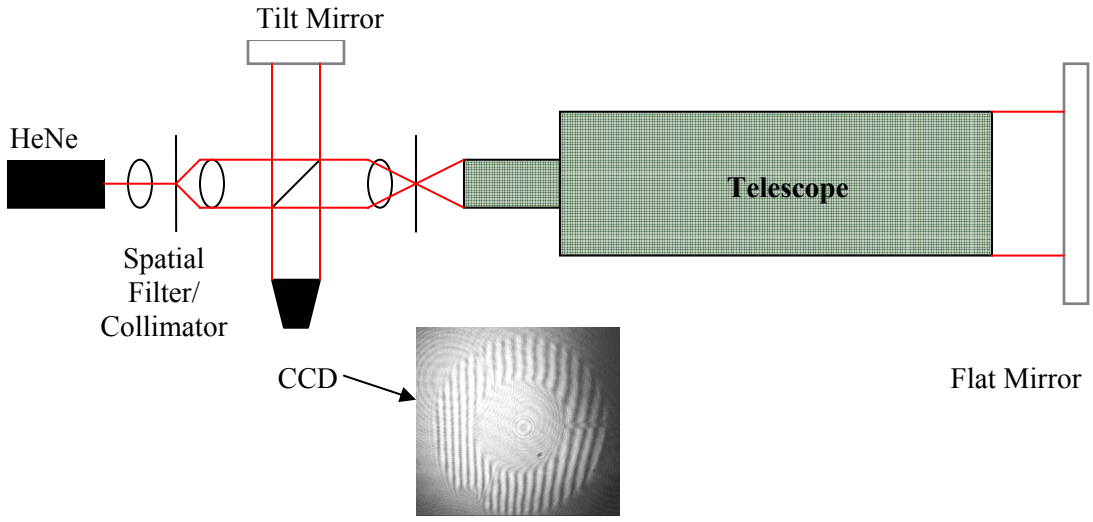

Figure 51. Schematic of the Fizeau interferometer used to assess the wavefront error of the MSSTA Ritchey-Chrétien telescopes. Also shown here is the interferogram of the 211 Å telescope, indicating reasonably smooth optics with some mild coma. This telescope was one of the best performers on the interferometer.

The telescopes were then placed in front of a 12" Cassegrain collimator, which projected a 1951 Air Force resolution test target into the aperture of the Ritchey-Chrétien. The instrument's camera was mounted, and images of the test target were taken on fine-grained SO-253 emulsion (as noted in Section 2.5, the SO-253 is not sensitive enough to EUV radiation for use in flight, but its excellent resolution capabilities ensure that it is not the limiting factor if it is used during alignment). The test target images were used to achieve final focus of the telescope. The OTAs are designed to allow focusing by using adjustment screws to push on the back of the primary mirror in order to affect small changes in its position; unfortunately, we discovered during interferometric testing that these screws stressed the mirrors and distorted the images, so we were forced to focus by shimming the cameras on the back of the telescope. We would set the camera in place, take a picture of the test target, change the shim controlling the focal plane position, and re-shoot the test target. The shim setting giving the best resolution performance was used during flight.

One detail that was not accounted for in past MSSTA flights: while the EUV telescopes use thin-film filters, the FUV telescopes (1550 Å and 1216 Å) use interference filters on 4mm thick MgF_2 substrates. Passing the converging beam of the telescope through a refractive medium results in a backward shift of the focal plane; using Snell's law, we find that a filter of thickness t and index of refraction n_R at the telescope's operating wavelength pushes the focal plane back by

$$s = \left(1 - 1/n_R\right)t$$

The telescopes are focused at visible light; if the effect of the filter is not compensated for, the focal plane will be found >1mm in front of its optimal position for flight, resulting in an increase in the spot size of > 100 μm (about 6 arc-seconds at the focal plane of the Ritchey-Chrétien telescopes). While this may account for some of the blurring seen in earlier MSSTA FUV images, we compensated for it by using CaF_2 blanks (whose visible-light n_R is close to the FUV n_R of MgF_2) during visible-light focus testing. The slight increase in longitudinal spherical aberration due to the presence of the filter is not a significant concern.

Central Wavelength [Å]	Resolution [arc-seconds]
58	15
98	8
131	12
150	8
171	20
180	2.5
195	2.5
211	1.8
256	6
1216	1.5
1550	1.5

Table 13. Pre-flight measurements of telescope resolution. The collimator used to project the test targets was limited to ~1.5 arc-seconds, so the sharper MSSTA telescopes (particularly the FUV instruments, as well as the 211 Å and 195 Å) may have outperformed these estimates.

Some of the alignment was re-done (or done for the first time) at WSMR, and final test-target images were taken with each telescope after shake-testing of the payload. Examining the tests under a microscope gave a pre-flight estimate of the resolving power of each telescope. The results are shown in Table 13. The resolution estimates given there are less optimistic than those given for the MSSTA II telescopes in (Martínez-Galarce, Walker et al. 2000); however, in both cases the resolution of the images is ultimately limited, not by the optical performance of the telescopes, but by the film grain.

3.1.2 ELECTRONICS

The flight electronics were substantially similar to the configuration flown on the MSSTA II (Martínez-Galarce 2000). The design consists of four custom-made circuit boards in isolated housings at the back of the payload truss: the analog board handled the power distribution to the payload, the IMP board contained the main microprocessor and was responsible for control and telemetry, and two camera boards were constructed to relay signals to and from the custom-built control boxes on the Pentax 645 cameras. Several minor updates and IC replacements were made on the electronics boards by AmirAli Talasaz and Ramesh Kumar; the changes are detailed in the Appendix.

The flight software, on the other hand, was almost completely rewritten after a series of bugs and incompatibilities were identified in the latest available version of the software. This was a major undertaking, and was only completed three days prior to launch. The principle revisions consisted of the addition of several layers of redundancy to the camera control system. In addition to the running a pre-loaded exposure sequence, stored in EEPROM on the camera boards, we gave the flight computer the ability to reset individual cameras, and to respond to manual camera firing commands from the ground. All of these capabilities would be required during flight.

3.1.3 PAYLOAD INTEGRATION

Most of the delicacy required in integration of the payload is necessary in order to protect the EUV thin-film filters. They are the reason that the payload must be evacuated during launch, so that vibrations induced by the rocket motors or the explosive decompression of the payload when the shutter door opens do not cause the filters to rupture. In order to minimize the chance of damage to the delicate EUV filters, they were not tested until the day before the payload was buttoned up for flight.

The Ritchey-Chrétien optical tubes were integrated into the payload truss and coaligned with a 16” collimator, using the sun sensor for the SPARCS attitude control system as a reference. Mechanical integration and alignment of the Herschelian telescopes was re-checked with the same collimator.

The full list of instruments included on the MSSTA III is shown in Table 1. A view of the payload from the sun’s perspective just prior to its integration with the telemetry system is shown in Figure 52.

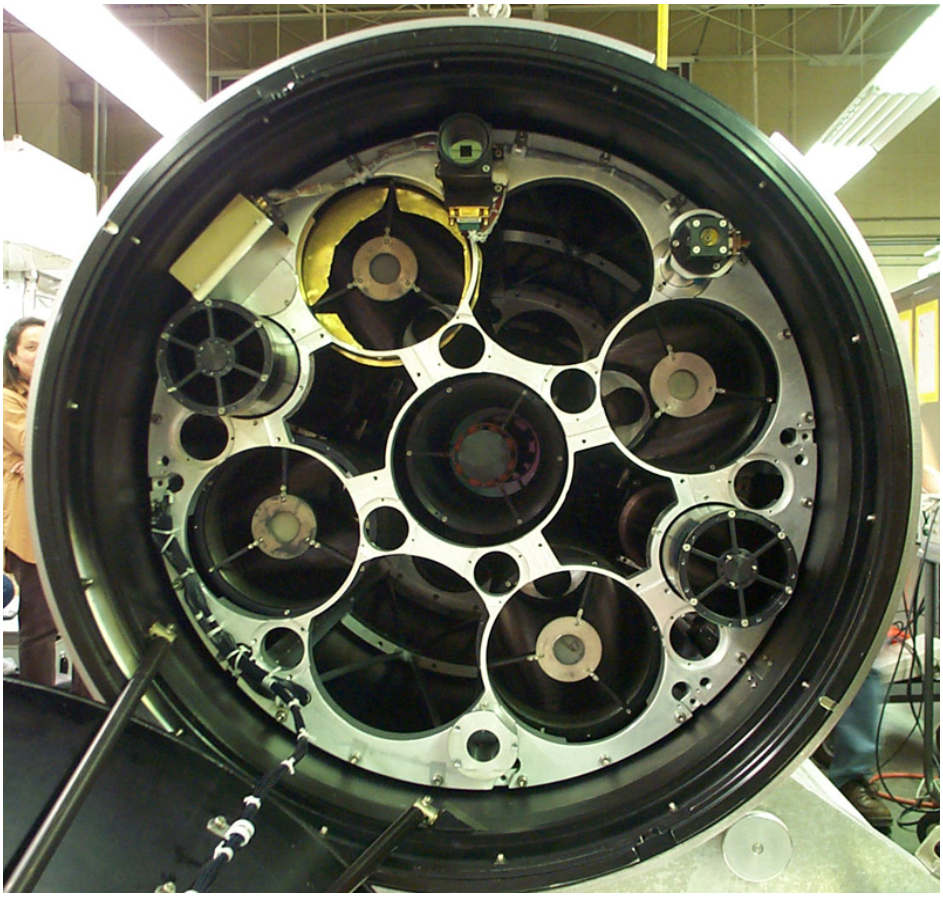

Figure 52. Sun's-eye view of the MSSTA III.

3.1.4 FLIGHT PERFORMANCE

High winds on the day of flight threatened to cause the MSSTA to miss its launch window. We were forced push the launch time back by half an hour (resulting in a lack of simultaneity between the flight and the supporting EIT and TRACE observations) and were on the point of scrubbing the launch when a break in the winds was verified. The payload launched at 12:25 pm MDT (18:25:00 UTC). The two-stage, Terrier-boosted Black Brant launch vehicle gave the payload an apogee of 270.5 km, resulting in more than five minutes of observing time.

Shortly after the start of the exposure sequence, MSSTA telemetry reported that current spikes from the 1550 Å camera had caused the flight electronics to shut that camera off. We were forced to reset the camera board. At that point, we lost reliable telemetry from the instrument altogether

(though telemetry from the power supply and flight guidance systems was not interrupted). We made the decision to activate manual control of the camera firing sequence. Therefore, all the exposures were made in response to me pressing a button in the control room at WSMR. The exposure times of the images were thus not as accurately-defined as they would be had the software-encoded exposure sequence run properly. We reconstructed the exposure times to 0.1-second precision by examining the post-flight log of current flow out of the main battery to the instrument; current spikes indicate the end of each exposure, as the camera advances the film to the next frame.

Nevertheless, the vehicle and the instrument performed well. Upon recovery, the payload showed signs of a rough landing. It had bounced and dragged on its parachute, and the waist vacuum was broken, sucking sand into the payload interior. However, despite the ominous sounds of sand and loose rivets rattling around inside the payload skin, everything was essentially intact.

The log of flight events and a summary of the payload telemetry is included in the appendix. They indicate that the SPARCS ACS performed within its specifications throughout the flight, with the largest excursions occurring during the 100 second exposure. The summary of flight data is based on information supplied by (NASROC 2002).

3.2 The Dataset

After recovery of the payload, the payload skin was opened and the camera backs were unloaded in the darkened alignment room at WSMR. Once we had verified that none of the cameras had broken on landing, the film was transferred to the darkroom of the journalism department of New Mexico State University, where it was developed in the JOBO film processor. Meanwhile, the payload itself was removed from its skins and examined for damage. The failure of the filters on the 58 Å, 98 Å and 131 Å telescopes was immediately noted. However, seven of the other eight telescopes performed well, and recorded multiple images over the course of the flight. These results are presented in the following section.

3.2.1 FILM DEVELOPMENT AND CLEANING

All negatives were developed with the same process based on our film calibration work at SSRL: 10 minutes in Kodak D-19, followed by a stop bath and rinse, then 5 minutes in Kodak Rapid Fixer, and finally a 20 minute rinse in running water. All chemistry was held at 20° C during processing. The negatives were dried overnight. Photo-flo was not used due to concerns about its effect on repeatability; this turned out to be a mistake, as some of the negatives show notable water-spotting.

Worse, the negatives suffer from extensive cracking and clumping in the film grain. As mentioned in Section 2.5, the photographic film used on the MSSTA flight was roughly 10 years old, and showed some signs of degradation in both sensitivity and grain structure. Furthermore, the XUV-100 has always shown a tendency to dry and crack under vacuum, producing heavy dark lines when the negatives are scanned. Software was developed to remove the worst of the damage (see the IDL code for PB_DESCRATCH and PB_DUSTBUSTER in the Appendix). It works by taking the derivative of the image in the direction perpendiculat to the scratches (during descratching) or the Laplacian of the image (during dust removal), thresholding and blurring the result to create a bad pixel mask, and replacing pixels in the mask with pixel values based on the

pixels around the boundary of each excised region. The results are shown in Figure 53; the loss of data cannot be prevented, but the scratches no longer contaminate attempts to measure average pixel values in a given region of the image.

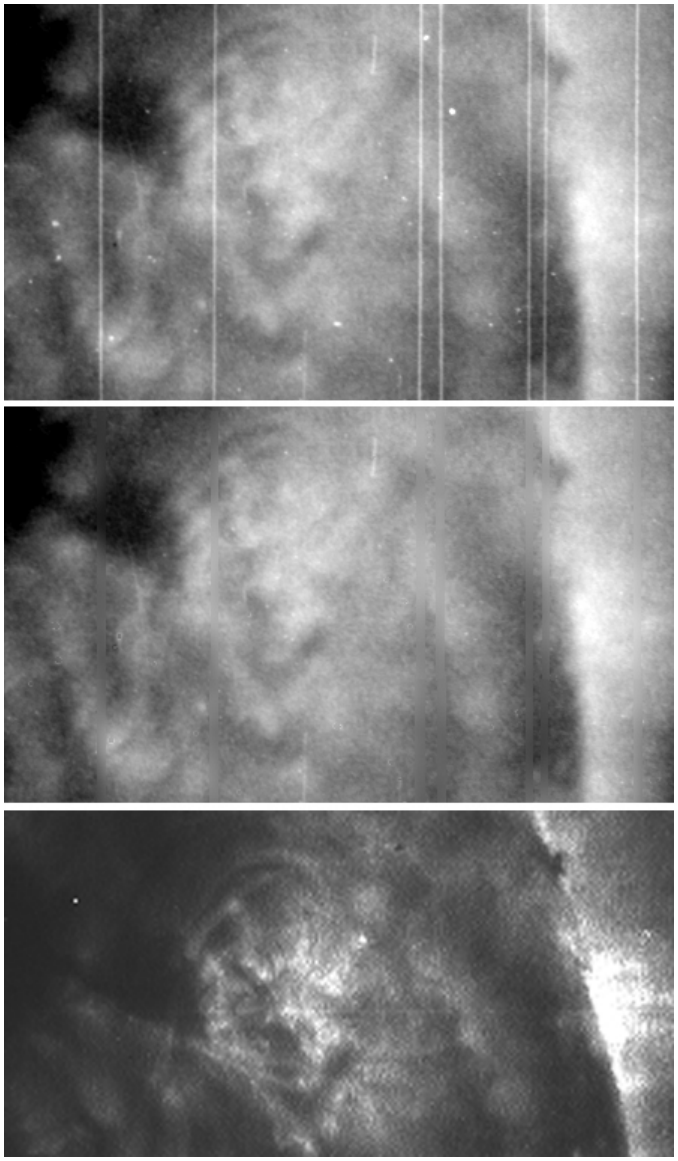

Figure 53. MSSTA images, like the 195 Å 40-second exposure shown here, suffer from film cracking as well as dust and scratches *(top)*. IDL descratching and dustbusting alleviated these problems *(middle)*. Nevertheless, image resolution was comparable to, or slightly worse than, that of EIT's 195 Å telescope *(bottom)*.

The negatives were digitized using a Umax film scanner with 1200 dpi nominal resolution; testing the scanner with a 1951 resolution target suggest its true resolution is close to nominal

perpendicular to the motion of the scanning assembly, and better than ~1000 dpi in the direction of motion. Considerable time was spent digitizing the images with a much more expensive Imacon Flextight Photo Scanner with a nominal resolution of 3200 dpi; unfortunately, while the Imacon scanner performed beautifully over small regions of the image, it was unable to scan a full 4.5 cm negative without introducing unacceptable distortions in the scanning direction. The problem defied several trips to the manufacturer for adjustment, and finally the Imacon scanner was abandoned.

Linearity of the Umax scanners measurements was tested, but is ultimately irrelevant given the film calibration procedure we used, which bypasses pixel value-to-density conversion. As long as the scanner gives repeatable measurements, which it seems to do, linearity is not necessary.

3.2.2 IMAGE COALIGNMENT

Because the MSSTA telescopes are independently mounted in the payload (unlike the TRACE telescope quadrants), and because the digitized images are scanned manually, image coalignment is a significant challenge. The digitized images were coaligned manually by placing green tag markers at ~20 points around the limb of the solar disk in Photoshop. The tagged image was then read in, and an oblate solar disk was fit to the marked limb points. The center coordinates of the resulting disk were used to establish a fiducial point in each scanned negative. The radius of the best-fit limb was not used to correct the image scale of the telescopes, in order to avoid concerns about the varying height of the limb in different bandpasses. The images were then superimposed on a reference EIT image and rotated around their centers in 0.1° increments until the best correlation was found. The resulting image center and rotation angles were stored in the FITS header of each exposure.

3.2.3 RESOLUTION ANALYSIS

On microscopic examination of the flight images, it was immediately apparent that the grain of the XUV-100 film limited the resolution of the EUV images. None of these images came close to

the resolution predicted by their performance on the interferometer or under pre-flight alignment testing with SO-253 film. The grain of the film is quite evident. Quantifying the image degradation caused by the film is simple: a sharp edge between two large regions of uniform density was found by examining the edge of the frame of one of the scanned negatives. The image was summed in the direction parallel to the edge, and the slope of the pixel value curve across the transition indicates the steepness of the film's contrast transfer function. This test indicates that the XUV-100's resolution in flight was roughly 6.5 arc-seconds at the focal plane of the large Ritchey-Chrétien telescopes (and about 11 arc-seconds for the small Ritchey-Chrétien 171 Å and 180 Å instruments). This finding is supported by comparison of the MSSTA images with EIT images in similar bandpasses (see Figure 53). EIT's nominal (pixel-limited) resolution is about 5 arc-seconds.

The FUV images, taken on ultra-fine-grained S-649, fared far better, and essentially reproduced the results of the pre-flight resolution tests. The 1550 Å image displays resolution only slightly worse than TRACE's 1550 Å bandpass, which is pixel-limited at about 1 arc-second.

3.2.4 THE IMAGES

The MSSTA III dataset consists of 84 images in 7 different EUV and FUV bandpasses. An image from each of these bandpasses is presented below, along with a discussion of the important characteristics of each telescope's performance. In all cases, solar North is up; for the EUV images, the results presented here are all 40-second exposures taken near apogee. They have been thresholded and downsized, decreasing their dynamic range and (in some cases) resolution.

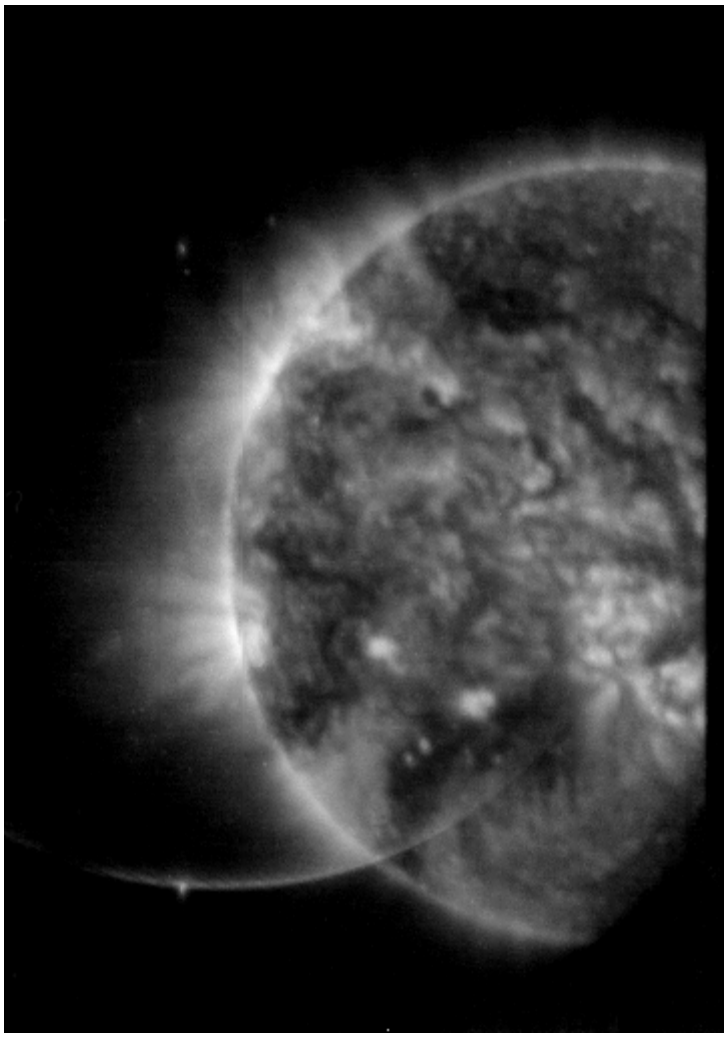

Figure 54. Image from the 150 Å Ritchey-Chrétien telescope.

150 Å Ritchey-Chrétien

This telescope shows the worst misalignment of any of the MSSTA images; the mediocre resolution, analysis of its interferograms, and the fact that the solar disk is significantly off-center and cut by the edge of the film frame all indicate that the primary is tipped in its cell. The limited range of adjustment in the design of the Ritchey-Chrétien optical tubes prevented us from fixing this misalignment. There is also a bright ring of scattered light indicating inadequate baffling of the telescope. Nevertheless, despite these flaws and the confusion about the exact shape of the bandpass, this image is extremely interesting: it is the first image of the solar atmosphere at this wavelength, and the first detailed large-scale view of the solar atmosphere in a line whose peak formation temperature is ~700,000 K.

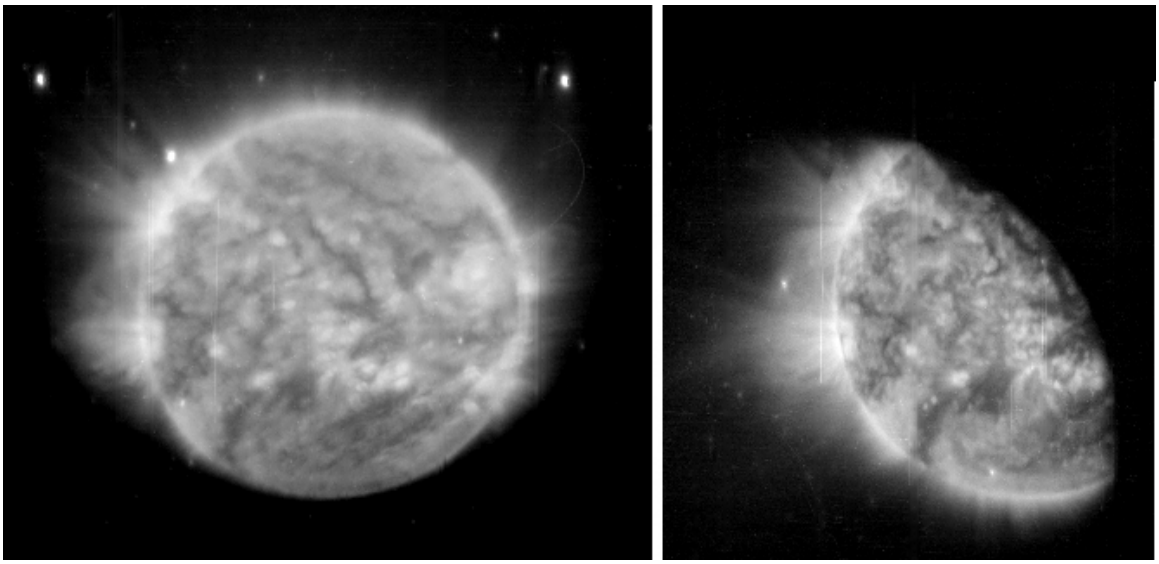

Figure 55. Images from the small Ritchey-Chrétien telescopes at 171 Å (*left)* and 180 Å *(right)*.

171 Å Small Ritchey-Chrétien

This telescope had the worst image resolution of any of the telescopes that recorded images due to the stress on its secondary mirror; however, it produced extremely high contrast, and provided full-disk views in 14 different exposures. It is useful for cross-calibration with TRACE and EIT. There is mild vignetting by the baffle tube at the bottom (south) edge of the disk.

180 Å Small Ritchey-Chrétien

The good (film-limited) resolution performance of this telescope was somewhat offset by the misalignment of its baffle tube, which obscures roughly 40% of the area of the disk. The bandpass is interesting as a bridge between the 171 Å and 195 Å bandpasses; it is another wavelength at which this MSSTA image is the best ever taken.

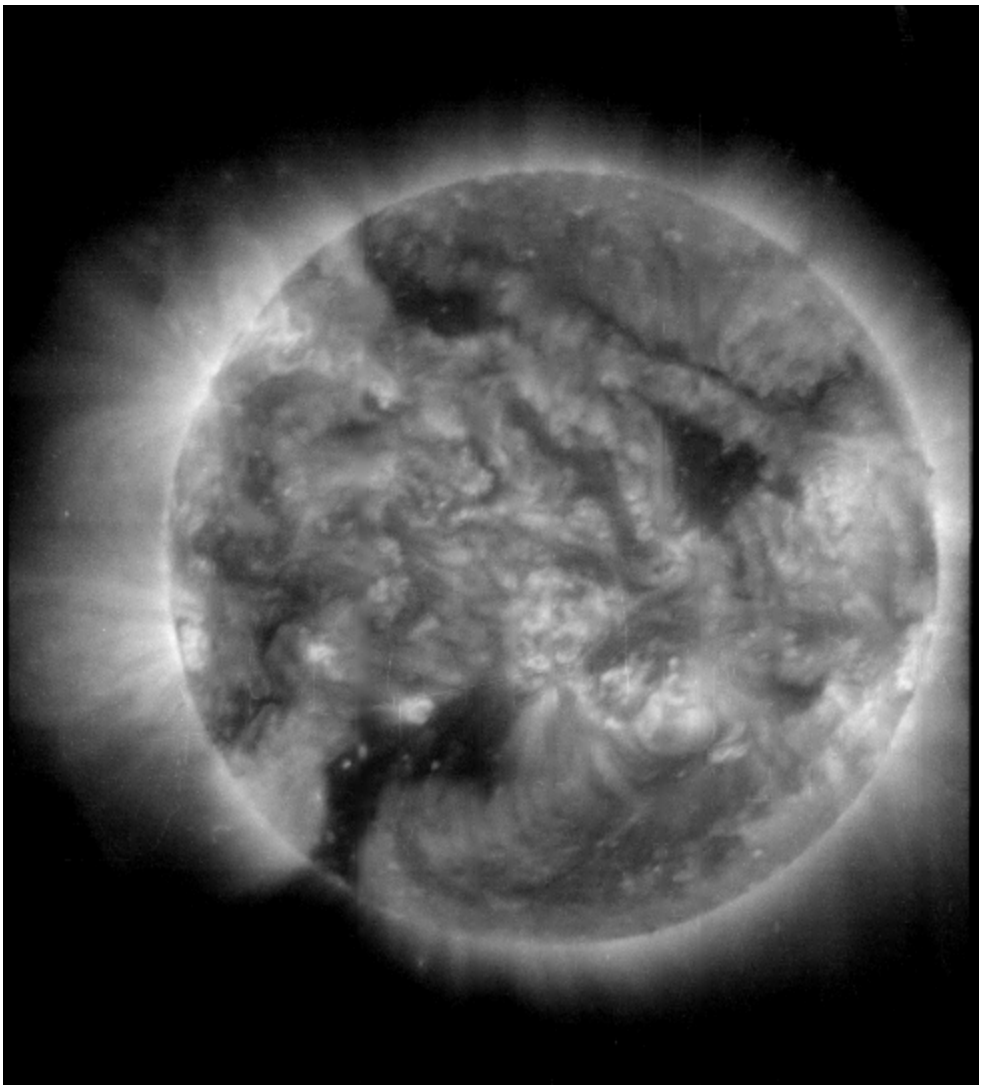

Figure 56. Image from the 195 Å Large Ritchey-Chrétien telescope.

195 Å Ritchey-Chrétien

This telescope provided excellent film-limited resolution and full-disk coverage comparable to the EIT 195 Å telescope. It recorded 14 images, including several short 5-10 second exposures shortly after the opening of the payload's shutter door. This bandpass was used as the reference during image co-alignment and sub-region extraction.

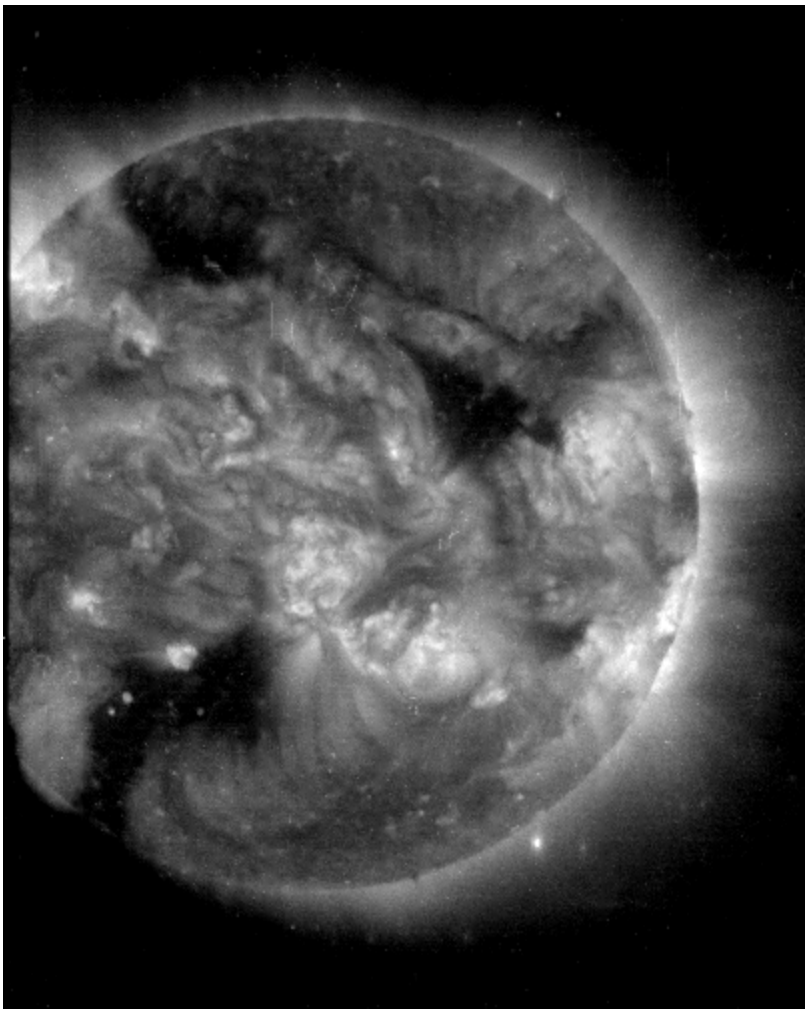

Figure 57. Image from the 211 Å Ritchey-Chrétien telescope.

211 Å Ritchey-Chrétien

The 211 Å telescope had the best resolution of any of the MSSTA EUV telescopes during pre-flight testing, and its images are comparable in sharpness to the 195 Å images. This bandpass, centered on a strong Fe XIV line and serving as a good temperature bridge between the 195 Å and 284 Å bandpasses used by TRACE and EIT, has been flown before (Sakao, Tsuneta et al. 1999), but the MSSTA III image is the highest-resolution 211 Å image ever recorded.

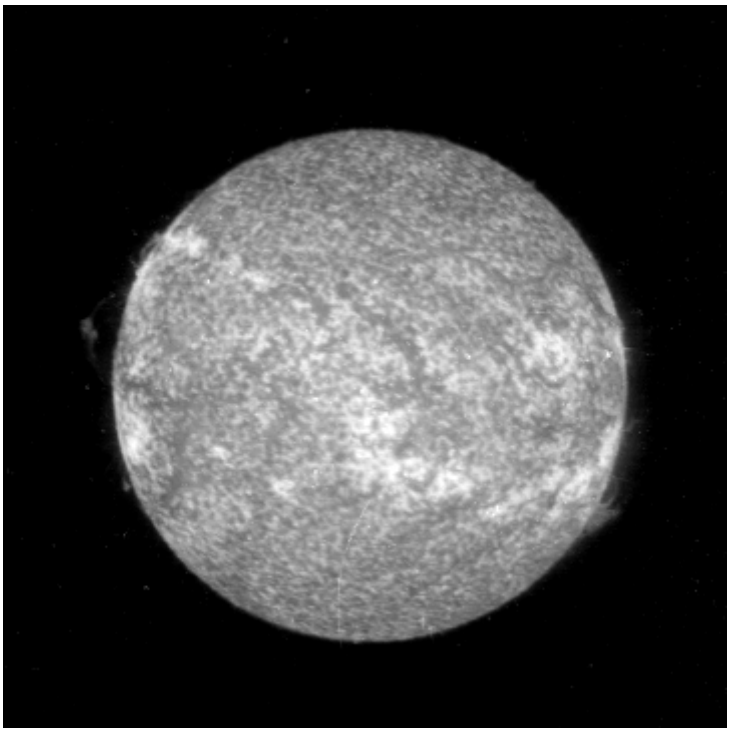

Figure 58. Image from the 1216 Å Ritchey-Chrétien telescope.

1216 Å Ritchey-Chrétien

The short Ritchey-Chrétien Lyman α telescope produced 10 very detailed images, thanks to the extremely fine-grained S-649 emulsion used in its camera. These images show a number of intriguing off-disk loops, and offer the potential for some interesting work. They could be used to explore the connection between coronal and chromospheric structures, and to cross-calibrate the TRACE 1216 Å bandpass.

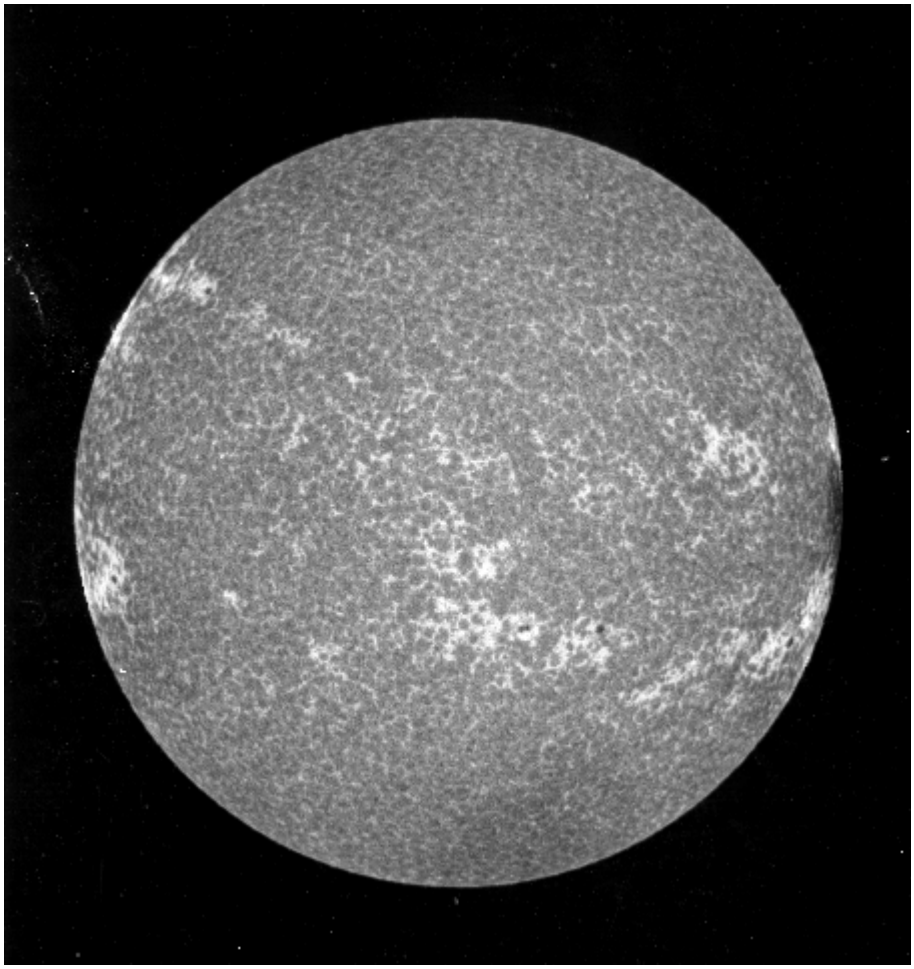

Figure 59. Image from the 1550 Å Ritchey-Chrétien telescope.

1550 Å Ritchey-Chrétien

The resolution in this bandpass is the best of any of the MSSTA telescopes, close to 1 arc-second. The image shows a detailed map of the supergranular network, as well as some bright emission in active regions coming from C IV at 100,000 K. Images in this bandpass or similar ones flown on TRACE are frequently used as proxies for the magnetic network; however, quantitative analysis of such images is difficult because of the strong continuum component in their throughput.

3.3 Post-Flight Calibration

3.3.1 ATMOSPHERIC ABSORPTION

Solar EUV emission is absorbed in the Earth's thermosphere (by atomic and molecular oxygen and ozone, and to a lesser extent by nitrogen), the atmospheric layer that extends from about 90 to 500 km in altitude. At its apogee of 270 km, the MSSTA is well above the point at which most of the absorption takes place. Nevertheless, absorption of ~200 Å radiation begins at altitudes of 400 km, and can be significant at the altitude of the MSSTA. Previous MSSTA flights have not corrected their data for atmospheric absorption. However, because of our concern with precise calibration, and because of the availability of new data and models of the thermosphere, we did attempt to correct the MSSTA III data.

Column densities of the absorbing particles in the atmosphere were computed using the MSIS90 atmospheric model (Hedin 1991), via an IDL interface designed by Don Woodraska of LASP. The model uses the solar 10.7 cm flux as a proxy for overall levels of EUV emission in describing the state of the thermosphere. From the column densities, the absorption coefficient $\mu(\lambda, h)$ of the atmosphere was tabulated as a function of wavelength and altitude over the range explored by the MSSTA.

We determined the altitude of the payload as a function of time *h(t)* based on the known time and altitude at apogee and on the assumption that the payload followed a ballistic trajectory (this assumption is validated by the flight event log in the appendix). Then, for each exposure *j*, the overall atmospheric correction coefficient was found by integrating the atmospheric absorption at the central wavelength of the bandpass from the start time of the exposure to the time the shutter closed:

(Equation 18)
$$\mu_{\lambda,j} = {}^{1}\!\!\diagup\!\!{}_{\Delta t_j} \int_{t_0}^{t_0+\Delta t_j} \mu(\lambda, h(t))\mathrm{d}t$$

Correction factors were of order 5-10% for most of the MSSTA EUV exposures, implying that this is a crucial step if we hope to achieve reliable results. The accuracy of the MSIS90 model is estimated to be ~20-30%; as this factor is primarily associated with the neutral density of the thermosphere, it should show appear as a constant scaling factor in all wavelengths. Thus, the correction introduces a systematic error of a few percent into the absolute accuracy of the MSSTA observations, with a lower error in their relative accuracy.

3.3.2 COMPARISON WITH PREVIOUS EXPERIMENTS

To this day, the only full-disk absolutely-calibrated spectrum of the sun in the 50-300 Å region with sufficient spectral resolution to resolve individual emission lines is the one measured by (Malinovsky and Heroux 1973) in 1969. Therefore, we will use their results as a sanity check on the MSSTA observations. It is worth noting the Malinovsky *et al.* did not correct their spectra for atmospheric absorption; their observations were recorded at around 240 km in altitude, so absorption is likely to be significant at about the 10% level. However, before adjusting the measurements of Malinovsky *et al.*, we note that the 2800 MHz radio flux, often used as a proxy for overall EUV emission (Rugge and Walker 1974), was approximately 11% higher on the day their spectrum was recorded than on the day of the MSSTA flight. These two effects should essentially cancel each other out to within the errors of the observations.

It is possible to check Malinovsky *et al.*'s spectrum against the contemporary measurements from the TIMED-SEE satellite (Woods, Rodgers et al. 1999), which records total irradiance in 10 Å spectral bins. Summing the spectrum of Malinovsky *et al.* to the same bins, adding a small offset for the EUV continuum and lines not included in their line list, and comparing with the TIMED results gives us Table 14. TIMED-SEE measures a solar EUV flux that is notably higher than that reported by Malinovsky *et al.*; the variations among the bins are due to omissions in the line list, or to variations in the detailed shape of the spectra.

Center of 10 Å wavelength bin [Å]	M&H line fluxes plus continuum [10^{-2} ergs cm^{-2} s^{-1}]	Ratio TIMED-SEE/ M&H
145	5.13	1.14
155	5.96	0.76
165	5.42	1.75
175	18.85	2.32
185	19.31	1.30
195	16.54	1.09
205	7.41	2.39
215	9.26	0.93
225	5.73	1.58

Table 14. Comparsion of the full-disk spectrum of (Malinovsky and Heroux 1973) with that measured on the day of flight by TIMED-SEE.

The spectrum of Malinovsky *et al.* was then folded through the bandpass of each of the MSSTA instruments in order to predict the energy that would have been deposited at the instrument's film plane had it observed the full solar disk emitting the measured spectrum. The predictions were compared to the energy summed over all the pixels in each MSSTA image. Because the scanning, alignment and calibration of the MSSTA images is a laborious process, only ~4 different exposures from each bandpass were included in this analysis. The results are summarized in Table 15. The noise estimates based on repeated sampling in the MSSTA images are not too discouraging; most of the observed variation is probably due to scratches in the film or turn-on at extremely low pixel values which are not observed by the shorter exposures, but overall the variance is in line with our expected calibration accuracy. However, it is immediately obvious that the MSSTA observations contain substantially less flux than we would have predicted based on spectral observations; indeed, they are low by factors ranging from 6 to 25!

Central Wavelength [Å]	Number of Measurements	ΔE/E	Ratio MSSTA/M&H
150	4	0.07	0.12
171	3	0.29	0.14
180	4	0.14	0.17
195	5	0.23	0.04
211	4	0.36	0.09

Table 15. Full-disk fluxes observed by the MSSTA telescopes compared with those predicted based on the spectrum of (Malinovsky and Heroux 1973).

3.3.3 COMPARISON WITH THEORETICAL PREDICTIONS

Clearly, this is unacceptable. It is difficult to reconcile these results with the exacting calibration work described in Chapter 2. While it is conceivable that there are large errors in the observations of (Malinovsky and Heroux 1973), it is not possible that they are so far off. They have been qualitatively verified by comparison with TIMED-SEE and numerous other measurements since their publication. The bulk of the discrepancy must come from improper calibration of the MSSTA. The most likely culprit is the film calibration, perhaps during the development time correction phase (see Section 2.5.4). However, re-examination of the calibration film did not eliminate the discrepancy.

We can get a better idea of where the MSSTA observations are diverging from the predictions, and to what extent, by looking at subregions on the disk. For this purpose, the MSSTA images were co-aligned with a set of full-disk EIT images taken roughly 45 minutes earlier. I then identified a sub-region of the EIT images containing an active region whose average flux in the EIT bandpasses agreed with the flux predicted based on the CHIANTI active region DEM (which is itself based on the spectral observations of (Vernazza and Reeves 1978); thus, the chosen sub-region should have a very similar temperature structure to those they observed). The same was done for a quiet-sun region. Then the pixel values in the MSSTA images were averaged over those same sub-regions, using the technique described in Section 4.2.2. The results are shown in Table 16.

Central Wavelength [Å]	Quiet Sun ΔE/E	Quiet Sun Ratio Observations/ Predictions	Active Region ΔE/E	Active Region Ratio Observations/ Predictions
MSSTA				
150	0.19	0.78	0.08	0.55
171	0.30	0.19	0.25	0.16
180	0.18	0.16	0.20	0.17
195	0.24	0.12	0.20	0.10
211	0.18	0.14	0.18	0.10
EIT				
171		1.01		1.01
195		1.02		1.02
284		1.06		1.02

Table 16. MSSTA observations of a quiet-sun region and an active region are compared with predictions based on the CHIANTI DEMs extracted from the spectra of (Vernazza and Reeves 1978). In order to ensure that the selected sub-regions were well-represented by those DEMs, their extent was defined in order to produce good agreement with the predicted EIT observations.

Again, the noise level in the MSSTA images is acceptable, but the overall scale factor is certainly not. It is clear that a correction must be applied to the MSSTA observations in order to bring them into line with the existing body of larger data. This is a bitter blow; one of the major goals of the MSSTA was to offer independently calibration measurements of the solar EUV emission, and to have to renormalize its data to produce agreement with EIT and older spectral observations defeats that purpose. Furthermore, the fact that it is not clear why this correction is necessary is worrisome, and suggests that, even after the MSSTA data have been corrected, their reliability is suspect. What is clear is that the correction is not entirely due to errors in CHIANTI, since the same procedure was used to generate the EIT temperature kernels that offer such good agreement with the predictions. In order to renormalize the MSSTA data in a sensible manner and reassure ourselves of its validity, we must make some assumptions about where this error comes from.

Systematic Renormalization

If indeed the film calibration is to blame, then it is equally to blame in all the MSSTA EUV bandpasses. That is, if we decide to generate a new film calibration transfer function in order to bring the MSSTA observations into line with those from EIT, it must be applied to all MSSTA images. This is the preferred method of renormalization. In order to define the correction to the film calibration, we regridded the EIT images to the same pixel scale as the MSSTA observations. We then examined the ratio of the MSSTA 171 Å images to the EIT 171 Å images, and MSSTA 195 Å to EIT 195 Å, on a pixel by pixel basis.

The procedure is identical to the development time and wavelength corrections described in Section 2.5.4. A fourth order polynomial function, like Equation 15, was fit to optimize the agreement between the MSSTA and EIT pixels in the 171 and 195 Å bandpass. This polynomial was then applied to every MSSTA image in every bandpass during film calibration. It results in an increase in the observed pixel values by an average factor of 8.21.

Arbitrary Renormalization

Alternately, we can simply give up on identifying the source of the error, and simply do the best we can to bring the images in line with our expectations by applying an *ad hoc* scale factor to each image based on the comparisons in Table 16. The easiest way to do this is to simply average the ratios in the active and quiet regions for each bandpass and divide all the images in that bandpass by the average ratio (thus scaling the MSSTA images by a factor ranging from 5, in the case of the 150 Å telescope, to 9 for the 195 Å). This produces the best agreement with the CHIANTI standard DEMs, of course, but it is the most troubling from a theoretical standpoint. In particular, it suggests that we are manipulating our data in order to achieve the outcome we desire.

If we consider the CHIANTI DEMs accurate representations of the conditions in the plasma used for the renormalization, and if we believe that the CHIANTI data used to generate the MSSTA temperature kernels is reliable, then perhaps such a manipulation can be excused. However, particularly in the case of the 150 Å telescope, those assumptions questionable, and if we make them we lose the ability to identify fundamental flaws in the DEM extraction technique. It may be reasonable to enforce agreement between the MSSTA 171 Å and 195 Å bandpasses and the EIT versions of those same telescopes; but then taking the next step and forcing the MSSTA 150 Å telescope to agree with predicted observations without similar experimental verification is more difficult to justify.

Some examinations were made using arbitrarily renormalized data; however, the bulk of the analytical work described in the following chapter is based on data renormalized with the film calibration correction explained above.

4 Data Analysis

4.1 Techniques of DEM Recovery

New data demand new analysis techniques. The MSSTA is exciting because it produces a dataset fundamentally unlike any other currently available: a set of 5 calibrated narrowband EUV spectroheliograms. However, the novelty of the data makes interpreting these results challenging. The DEM extraction techniques we employ on the MSSTA data cannot be tested on a well-studied dataset because no dataset suitable for such an investigation exists. There have been efforts to extract spatially-resolved DEMs from CDS observations (Schmelz, Scopes et al. 2001); however, the rastered-slit spectrograms produced by CDS are fundamentally quite different from the narrowband full-disk images obtained by the MSSTA. The inability of TRACE and EIT observations alone to constrain a DEM is discussed at length in Section 1.3.2.

4.1.1 SIMULATING OBSERVATIONS

Therefore, in order to refine the DEM extraction technique and establish realistic expectations for its performance, we must begin by producing artificial datasets consisting of simulated observations based on a realistic instrument model and a reasonable assumption about the state of the corona. Running our analysis algorithm on these synthetic observations and comparing the extracted DEM to the input DEM will accomplish some important goals:

- First, working with simulated observations will establish whether DEM extraction is possible at all with the kind of data we have obtained.

- Assuming the basic concept is viable, we can test a number of approaches to DEM recovery and determine which works best. The detailed parameters of that approach can be fine-tuned in order to speed up its execution, enhance its reliability or improve its flexibility.

- We will be able to test the sensitivity of the analysis to unexpected problems in the data set – calibration errors, gaps in the coverage of one or more bandpasses, etc. Conversely, we can explore how improving the data by more accurate calibration or additional bandpasses might improve the breadth and accuracy of the results.

- Most important of all, we will be able to see whether the results of our analysis are trustworthy. Simply putting error bars on the recovered DEM is not enough; we need to get an intuitive sense for whether DEMs obtained in this way are stable, consistent, and realistic descriptions of the conditions underlying our dataset.

Ideally, an artificial dataset would consist of synthetic images in each of our multilayer bandpasses of a region of the corona, based on a three-dimensional model of the temperature structure of that region (Weber, DeLuca et al. 2004). However, the complexity involved in generating such a model is substantial, and in fact such an artificial dataset would not give us any more information about our ability to recover DEMs from a set of pixel values than we can gain from a much simpler approach. Instead, we start by assuming a single pixel. Without fully enumerating the distribution of plasma within the column-of-sight defined by that pixel, we characterize that pixel with an ideal DEM. (As noted in section 1.3.4, a fundamental conceit of analyzing multilayer images is that the DEM contains all the information about the state of the plasma along a line of sight that is needed to calculate the intensity of EUV emission from that plasma.) Using the assumed DEM, we calculate the pixel value found at that point in each of the images in the MSSTA dataset. This artificial dataset can then be fed into a variety of candidate DEM extraction algorithms to produce a recovered DEM. The recovered DEM is compared to the input DEM to test the accuracy of the algorithm.

A number of different input DEMs were chosen in order to reproduce the range of possible observed pixel values expected from the flight dataset. Most tests were run using one of three

standard DEMs (active region, bright quiet-sun network, and coronal hole) from the CHIANTI package, derived from the observations of (Vernazza and Reeves 1978). These are all broad, multithermal temperature distributions based on spectrograms averaged over large areas on the solar disk; all have been used extensively in the solar literature and are widely accepted as being characteristic of solar plasma in a general class of feature. In addition to these three broad DEMs, a number of artificial datasets were generated using sharply-peaked DEMs, in order to evaluate the algorithms' response to an image of an isothermal plasma. Since the question of whether broad or narrow DEMs are the norm for coronal loops is one of the central problems that we hope to solve using high-resolution multi-spectral observations, it is important to be sure that the DEM extraction technique is capable of reproducing an input distribution with any shape.

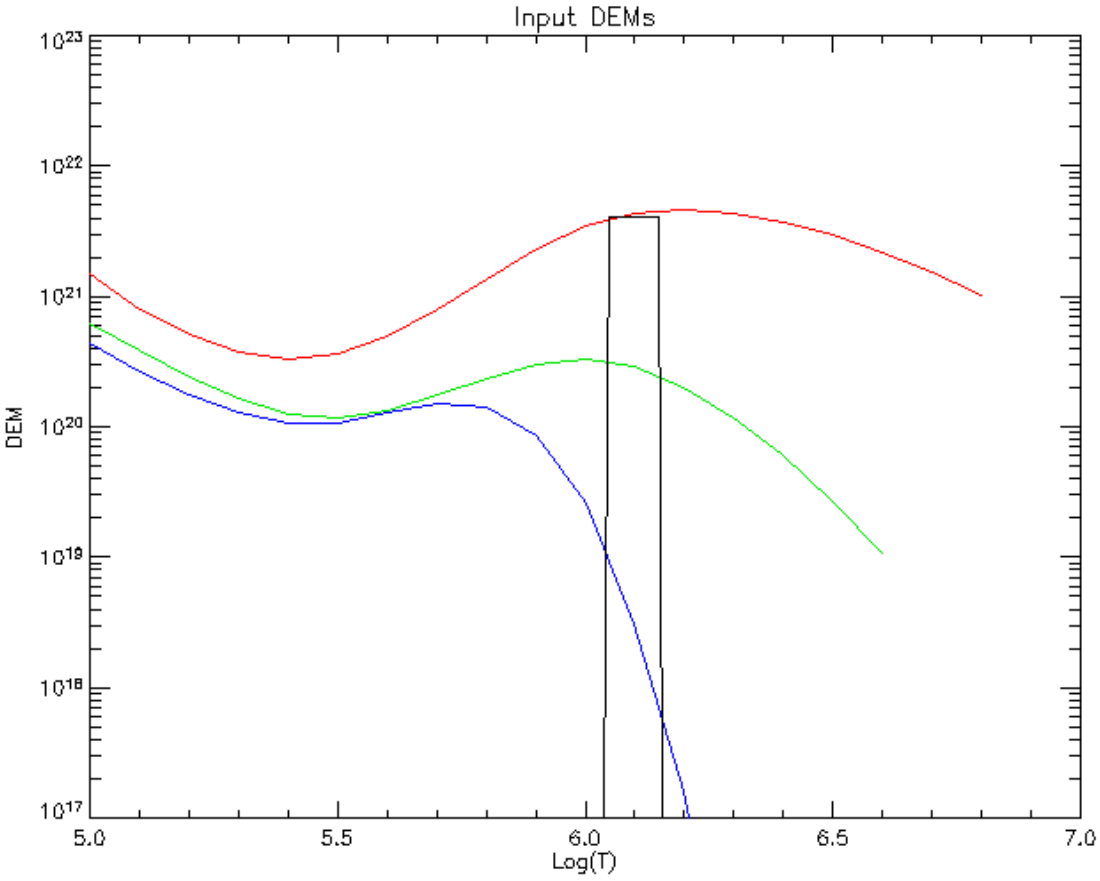

Figure 60. The DEMs used to simulate observations in order to test the data analysis techniques. The colored curves represent standard averaged active region (red), bright quiet sun (green) or coronal hole (blue) type emission. The black curve represents an isothermal coronal loop based on loop 1 from (Aschwanden, Newmark et al. 1999). Its DEM is centered at 1.25 MK; the width of the peak is 0.1 in Log(T), corresponding with the temperature precision of the line contribution functions that go into the DEM. Similar isothermal DEMs at other temperatures were occasionally used to ensure that the algorithm didn't have substantial "blind spots" in temperature space.

Of course, the exact shape of the isothermal DEM is somewhat arbitrary; a truly isothermal plasma would have a delta-function DEM, but asking a general DEM-fitting routine to recover such a function is unrealistic. The temperature precision of the DEM is only 0.1 in Log(T); that is the step size at which the atomic data in CHIANTI is tabulated. Interpolating to a finer temperature grid does not increase the accuracy of the extracted function. Thus, when we generated isothermal input DEMs, we used box functions with a width of 0.1 in Log(T), normalized to a reasonable isothermal emission measure. The "isothermal" DEM shown in Figure 60, chosen to reproduce the observations of (Aschwanden, Newmark et al. 1999), is centered at Log(T) = 6.1 and normalized to an emission measure of $\sim 5 \times 10^{27}$ cm^{-5}.

The observations expected from a pixel with each of these input DEMs are listed in Table 17. For the 9 MSSTA EUV telescopes, the predicted observations are in units of ergs cm^{-2} s^{-1}, the flux units of MSSTA pixels after film calibration has been applied to the image. For the EIT observations, the units are in DN (counts) per second. Comparing these predictions with those based on the pre-flight calibration of the EIT made in Table XV of (Dere, Moses et al. 2000) reveals discrepancies of up to a factor of 2. These differences are due to different assumptions made in computing the instrument temperature kernels; I recalculated the EIT kernels using a lower assumed pressure, and updated abundances, ionization equilibria, and line strengths thanks to enhancements to the CHIANTI database (Young, Del Zanna et al. 2003). As a result, the EIT observations predicted in Table 17 offer somewhat better agreement with actual EIT data[3] (including the 1996 and 1998 observations mentioned in Dere et al.'s Table XV) than the predictions of (Dere, Moses et al. 2000). This should serve as a reminder of the sensitivity to detailed atomic physics that underlies any analysis of EUV emission by coronal plasmas; such a reminder is needed, since the original temperature kernels presented in (Dere, Moses et al. 2000) are still widely used in the literature.

[3] The exception is the 304 Å bandpass, which is not entirely susceptible to temperature kernel analysis. It is included here for completeness; Dere et al. used an *ad hoc* modification to the 304 Å temperature kernel for their predictions.

Bandpass Central Wavelength [Ångstroms]	Active Region	Quiet Sun	Coronal Hole	Isothermal Loop
MSSTA Telescopes	Predicted Pixel Value (10^{-2} ergs cm^{-2} s^{-1})			
150	6.0	0.3	0.1	0.6
171	254.0	28.1	8.1	47.0
180	165.1	12.3	1.3	61.5
195	180.5	9.7	0.4	55.6
211	65.8	2.8	0.1	9.9
131	238.3	18.8	9.5	13.1
98	27.1	2.0	0.5	4.2
58	3.6	0.1	0.0	0.7
256	1.7	0.1	0.0	0.3
EIT Telescopes	Predicted Pixel Value (DN s^{-1})			
171	464.9	47.0	11.3	106.9
195	358.4	21.6	1.7	119.1
284	10.1	0.4	0.1	0.5
304	13.3	0.9	0.3	1.7

Table 17. Predicted pixel values based on the input DEMs shown in Figure 60. These simulated observations were used to test DEM reconstruction techniques.

Extracting a DEM from a perfectly clean set of synthetic observations like those in Table 17 is not difficult; the real test is handling noisy observations. I simulated a noisy dataset using a Monte Carlo technique: a random number was added to each of the predicted pixel values before they were passed to the DEM extraction procedure. The random number was chosen from a Gaussian distribution centered at zero, with a FWHM set by the overall noise level times the predicted pixel value. (Thus, when simulating observations with 25% error, most of the pixel values in the synthetic dataset would be within about ±25% of their true predicted value.) In most cases, several hundred different noisy datasets were created for each true dataset, and the DEMs extracted from all of these Monte Carlo realizations were compared.

While straightforward, a Gaussian description of noise and error is not entirely accurate. As described in Section 2.6.2, the overall error on the MSSTA observations is 25-35%, but much of this error comes from systematics. Only a small part is due to sources that might be accurately modeled by a Gaussian distribution centered at 0 (although film grain and some aspects of development chemistry can add what looks like Gaussian noise to a small, pixel-sized sample of a

negative). The same is true for EIT. Systematic errors in calibration and in underlying atomic physics generally predominate over the statistical noise found in EUV spectroheliograms. Unfortunately, modeling systematic error is tricky. One approach is to add an offset to each pixel value before generating the randomized noisy datasets. However, the number of Monte Carlo realizations needed to fully explore the effect of systematic errors in this way is unreasonably large. For the most part, the simulated datasets included only Gaussian noise at a realistic overall level, while the effect of treating that noise as systematic error instead was briefly studied after the fact.

4.1.2 MATRIX INVERSION

With a goal (the input DEM) and a few hundred sets of simulated, noisy observations in hand, we can now test our ability to reconstruct a DEM from MSSTA data. We begin by re-examining Equation 7 from Section 1.3.3:

(Equation 7) $$p_i(\mathbf{x}) = \int_0^\infty K_i(T) DEM(T, \mathbf{x}) \mathrm{d}T \qquad [\text{counts s}^{-1}]$$

This is really a set of N equations, where N is the number of telescopes contributing to the dataset. For each telescope i (i = 1, …, N), the pixel value is found by integrating the temperature kernel of the ith telescope times the DEM over temperature. In order to solve this set of equations for the DEM, the most obvious approach is to discretize the problem in temperature. We define a set of temperatures T_j (for simplicity, we choose j = 1, …, N), changing the DEM from a continuous function of temperature to a set of tabulated values. The set of temperature kernels now becomes an N x N temperature response *matrix* describing the sensitivity of the entire instrument package, and the pixel values are determined by summing over temperature, rather than integrating:

(Equation 19) $$p_i(\mathbf{x}) = \sum_{j=1}^{N} K_{ij} DEM_j(\mathbf{x}) \qquad [\text{counts s}^{-1}]$$

Inverting such a simple system of linear equations is tantalizingly easy. We invert the square temperature response matrix by Gaussian elimination (using IDL's INVERT routine) to obtain the inverse matrix K_{ij}^{-1}, such that

(Equation 20) $$DEM_j(\mathbf{x}) = \sum_{i=1}^{N} K_{ij}^{-1} p_i(\mathbf{x}) \qquad [\mathrm{cm}^{-5}\ \mathrm{K}^{-1}]$$

Thus, in principle, any set of observations can be turned into a DEM almost instantaneously, with a simple matrix multiplication.

A quick test of this method using noise-free simulated data gave very promising results. Since the MSSTA dataset consists of images in 5 EUV bandpasses, we defined a discrete temperature grid with 5 points T_j such that $\mathrm{Log}(T_j) = 5.35 + 0.2 \times j$. The instrument response matrix K_{ij} was generated by sampling the temperature kernel of each instrument i at all temperatures j. This matrix was then inverted, and a set of simulated MSSTA observations generated using the CHIANTI active region DEM was multiplied by the inverse matrix to yield DEM values at each of the temperature grid points. This output DEM was compared to the input active region DEM; the results, shown in Figure 61, are accurate to about 10%. Similar agreement was found with quiet region and coronal hole DEMs; even isothermal DEMs were recovered fairly well, although those results were quite sensitive to the spacing of the temperature grid.

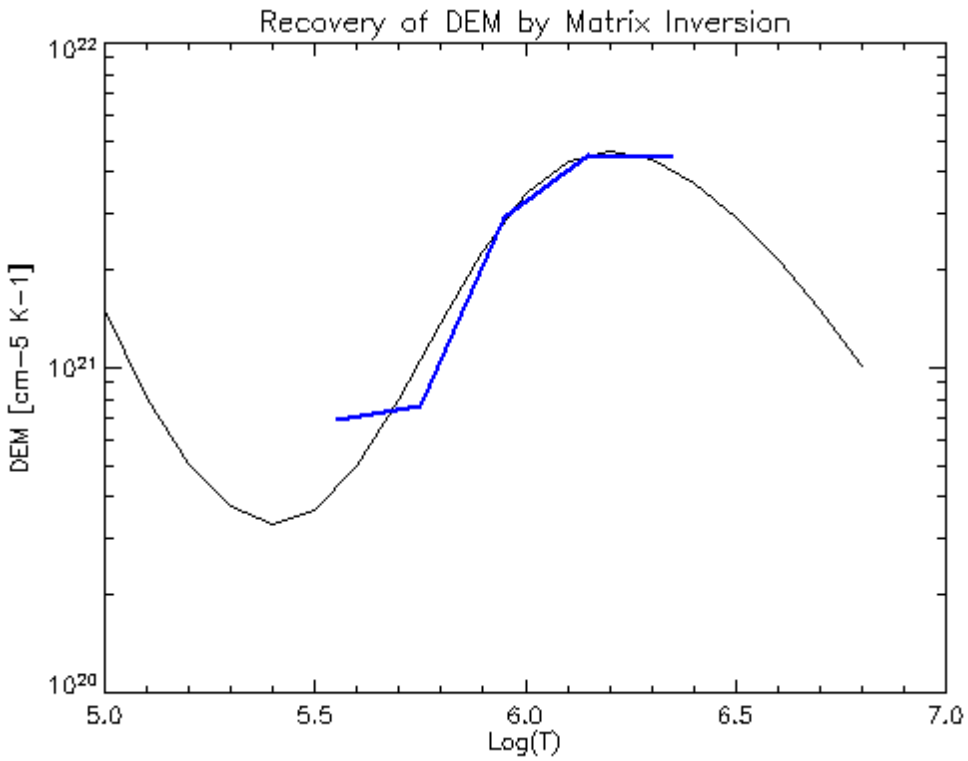

Figure 61. An active region DEM (black curve) was used to generate noise-free simulated observations in the 5 MSSTA EUV channels; these simulated observations were then multiplied by the inverse temperature kernel matrix to give a recovered DEM. The result agrees with the input DEM to ±10% over the temperature range sampled by the MSSTA.

However, the agreement quickly deteriorates when we add noise to the observations. As shown in Figure 62, even a very small amount of noise (5%) results in a recovered DEM that is generally only close to the input DEM at one or two temperature points; with more realistic noise levels (25%), the solution becomes wildly oscillatory, and utterly unreliable. Typically, the recovered DEM takes on unphysical negative values at one or more points. Including additional bandpasses (like the EIT instruments, or the temperature kernels of the MSSTA telescopes whose filters failed on flight) in the kernel matrix does not help; indeed, a large number of bandpasses forces us to use a finer temperature grid (or extend it over a broader temperature space), which tends to increase the instability of the solution.

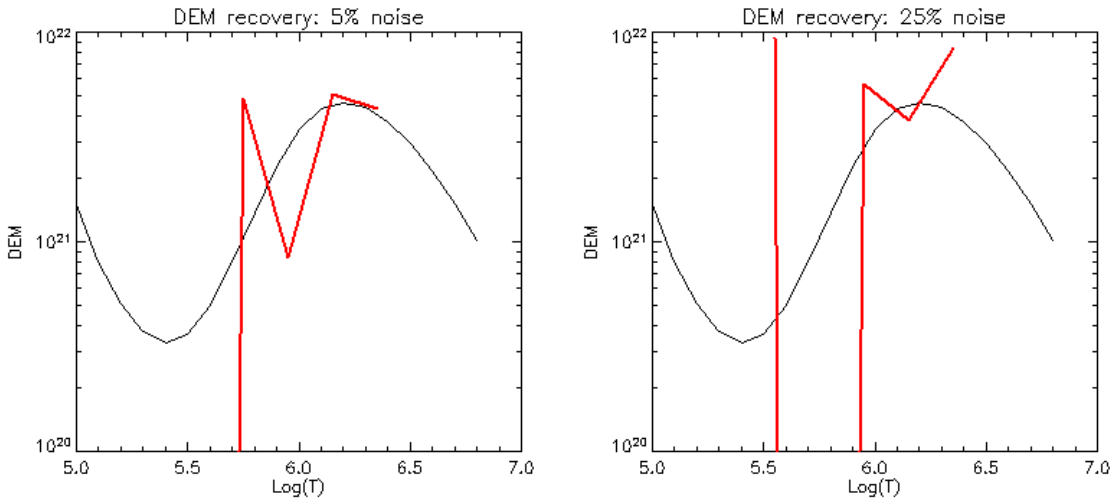

Figure 62. Adding noise to the simulated observations before inverting them quickly destroys the accuracy of the recovered DEM. The result (shown in red) is unstable under even a small amount of Gaussian noise (left), frequently going negative as the noise level increases (right).

The problem is that the temperature response matrix K is very badly-conditioned. We can quantify this ill-conditioning, and gain some insight into what it means and how to deal with it, by looking at the singular value decomposition (SVD) of the matrix. Following the derivation by (Hansen 1998), we define the SVD as

$$K = U\Sigma V^T = \sum_{i=1}^{N} \mathbf{u}_i \sigma_i \mathbf{v}_i^T$$

where $U = (\mathbf{u}_1, \ldots, \mathbf{u}_N)$ and $V = (\mathbf{v}_i, \ldots, \mathbf{v}_N)$ are matrices of orthonormal columns and $\Sigma = \mathrm{diag}(\sigma_1, \ldots, \sigma_N)$. The SVD is similar to an eigenvalue decomposition of the matrix KK^T; it has the following general properties that are useful for our case:

- The σ_i are the singular values of the matrix; they decrease gradually and monotonically to 0 with increasing i. The condition number of the matrix σ_i / σ_N is generally quite large; increasing the dimension of the matrix tends to increase the number of small singular values.

- The $\mathbf{u}_i$ and $\mathbf{v}_i$ are the singular vectors of the matrix; they can be thought of as a set of basis observations and basis DEMs, onto which the actual or simulated observations and measured DEM are projected. They tend to have more sign changes as i increases, becoming highly oscillatory at large i.

If we now consider Equation 19 as a mapping of a vector of observations **p** onto a DEM vector **d** (leaving out the indices from Equation 19, which serve only to make the matrix operations explicit; note that the index *i* now refers to a particular singular value, rather than a particular instrument), we can write

$$\mathbf{p} = K\mathbf{d} = \sum_{i=1}^{N} \sigma_i (\mathbf{v}_i^T \mathbf{d}) \mathbf{u}_i$$

It is clear that the high-frequency components of the DEM vector **d** are damped out by multiplication with the small singular values; thus the observations are relatively insensitive to small fluctuations in DEM. However, when the problem is inverted, any high-frequency oscillations in the data **p**, such as those introduced by small-scale noise, are hugely amplified, more so as the condition number of the kernel matrix (the smallness of the high-order singular values) increases.

The singular values of the MSSTA temperature kernel matrix are plotted in Figure 63. The effect of choosing different combinations of instruments, and different temperature grids, is illustrated by the four different curves. The blue curves, based on the 5 successful MSSTA EUV telescopes, show that substantially better results are obtained when the discretization is defined over a fairly narrow range of temperatures; spreading the 5 bandpasses over a broad temperature range leaves only one large singular value, indicating that the information content of the resulting response matrix is quite small. The black curves include three extra bandpasses, but do not generally produce many more large singular values; most of the additional singular values are small, and thus only contribute to noise in the inversion. However, it is clear that, with more bandpasses, it is advantageous to consider a broader temperature range.

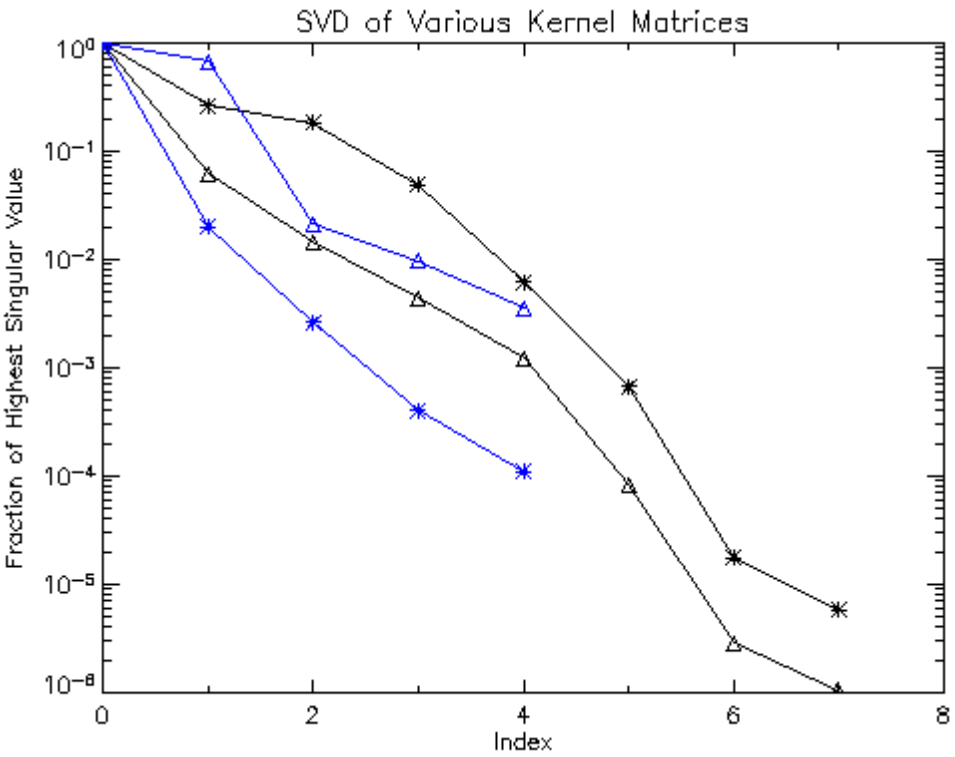

Figure 63. The SVD of the kernel matrix is sensitive to the temperature range and number of bandpasses used. Blue lines are for matrices that include the MSSTA 150 Å, 171 Å, 180 Å, 195 Å and 211 Å telescopes; black lines include these bandpasses as well as EIT's 171 Å, 195 Å and 284 Å telescopes. Triangles indicate kernels that use a temperature grid from Log(T) = 5.55 – 6.75; stars indicate kernels that were gridded over Log(T) = 5.35 – 7.15.

The SVD serves several important functions. First, simply examining plots like Figure 63 provides invaluable insight into the information content of the instrument response matrix. It enables us to fine-tune the temperature-discretization process in order to maximize the usefulness of our results, and it indicates the relevance of including various bandpasses. Studying the singular vectors $\mathbf{u}_i$ and $\mathbf{v}_i$ corresponding to large singular values can help us understand what sorts of DEMs an instrument is actually capable of discriminating. Such information could be used to optimize the design of future EUV instruments (indeed, it would have been helpful to look at the SVD during the selection of bandpasses for the MSSTA), and to constrain any analysis programs that use their data.

Furthermore, the SVD can serve as the stepping stone to a regularized solution to Equation 20, one that is still a unique inverse solution but that reduces some of the extreme noise-sensitivity illustrated by Figure 62 (Larsen, Kosovichev et al. 2004). A simple truncated SVD approach,

where the observations are projected onto the singular vectors $\mathbf{u}_i$ with large singular values (i =1, …, M, $M < N$) and a solution is constructed from the corresponding superposition of singular vectors $\mathbf{v}_i$, is certainly possible; slightly more complex schemes like Tikhonov regularization (Tikhonov and Arsenin 1977) can provide better approximations to the exact solution while minimizing unphysical oscillations in the DEM. Regularization of ill-conditioned matrices is a vast and richly-studied field (see (Hansen 1998) for an overview); however, while a regularized linear solution has been discussed by (Judge, Hubeny et al. 1997), among others, as a possible method for analyzing spectral data from SERTS or SUMER, most of the literature of coronal EUV observations relies on forward fitting techniques similar to the approach described in the following section.

My own efforts to construct a regularized solution to the problem of obtaining a DEM by inverting MSSTA observations are preliminary at best. The approach is certainly interesting, but enforcing the requirement that the singular vectors, or at least the resulting DEM, be non-negative has proven to be a considerable obstacle (though perhaps not an insurmountable one). The extracted DEMs are generally either trivial or completely unphysical, and thus uninteresting from a solar physics standpoint. I will continue to study the linear inversion approach, but for now will move on to discuss a more typical forward-modeling procedure that consistently generates believable solutions. This technique lacks some of the rigor of the linear inversion method, and does not guarantee a unique solution, but it will enable us to determine whether any solutions to the DEM problem can be found, and provide a glimpse of what those solutions might look like.

4.1.3 FORWARD FITTING

The forward approach to solving Equation 7 does not require that we discretize the problem in temperature and invert the equation to solve for DEM(T). Instead, we begin by examining our observations $p_i(\mathbf{x})$ and making a guess about the shape of the DEM that produced them. The guessed DEM is plugged into Equation 7 to predict a set of observations $p_i'(\mathbf{x})$, and the predicted observations are compared to the actual observations. Then the guessed DEM is iteratively modified to obtain the best possible agreement between the predicted and the observed pixel values.

In order to implement a forward-fitting solution, it is necessary to define a metric describing the agreement between predicted and observed pixel values. I used a standard χ^2:

$$\chi^2 = \sum_i \frac{(p_i' - p_i)^2}{p_i'}$$

An additional penalty function was applied to the χ^2 when the DEM became excessively oscillatory; however, the penalty function was not generally a factor in the analysis. It is also necessary to parameterize the DEM so that it can be modified in a systematic way. That is, we must model the DEM as a function of some set of parameters π_i (i = 1, …, N). Any particular combination of parameters then specifies a particular DEM, and thus a particular set of predicted observations, which lead to a value of χ^2. The fitting algorithm (I used the downhill simplex method as implemented in IDL's built-in AMOEBA function) then searches the N-dimensional space for the set of parameters that leads to the minimum value of χ^2. Defining the functional dependence of the DEM on the π_i is a subtle procedure; the choice of the number of parameters, and the functional form that turns those parameters into a DEM, has a strong effect on the ability of the fitting algorithm to find stable and unique solutions.

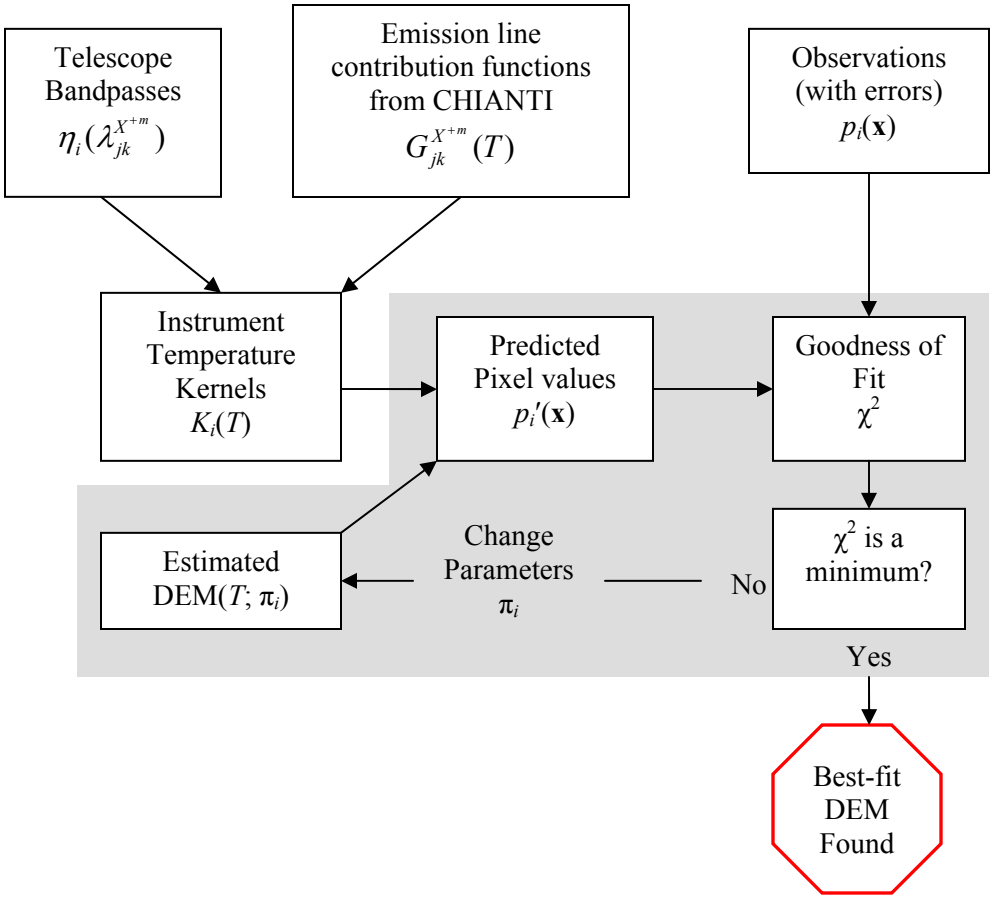

Figure 64. The forward-fitting procedure. Diagram modeled after one in (Golub, DeLuca et al. 2004).

After experimenting with polynomial and Fourier-series functions, I settled on defining the DEM with a cubic spline, where the parameters specified the DEM at temperature points equally spaced over the range of sensitivity of the MSSTA instruments. The spline is intuitive and flexible enough to reproduce almost any shape of curve, given enough grid points. The number of grid points specifies the dimension of the solution space. While it is tempting to use a number equal to or just less than the number of observations (see, *e.g.*, (Weber, DeLuca et al. 2004), who used N-1 spline points), it is important to remember the lessons about the poor conditioning of the instrument's temperature response that we learned by looking at the SVD of the kernel matrix. As noted in (Craig and Brown 1976), the contribution functions of EUV lines (and thus the temperature kernels of narrowband EUV instruments) are fundamentally broad in temperature, and thus the line intensity is relatively insensitive to small fluctuations in DEM. (Craig and Brown 1976) found that using more than 3-4 spline points was not justified by even the best

spectral observations. My testing of multi-point spline DEMs supports that conclusion; while a DEM based on 5 or 6 temperature grid points was better able to match a variety of input DEMs in the absence of noise, its performance quickly deteriorated under even small perturbations to the simulated observations.

Therefore, three-point splines were used to construct the model DEMs during the fitting procedure. I fine-tuned the DEM parameterization by generating simulated observations with a range of input DEMs and testing the ability of the model DEMs to reproduce these observations. At this stage, the location of the spline points and the domain over which the model DEM was defined were varied by hand until a good compromise between breadth and stability was found. The fitting algorithm was disturbingly sensitive to the location of the spline points; however, a good compromise was found by defining the model DEM over the interval Log(T) = 5.3 – 6.8, with spline points at Log(T) = 5.6, 6.0 and 6.4. The endpoints (*i.e.* the DEM values at Log(T) = 5.3 and 6.8) were forced to be lower than the adjacent spline points in order to prevent the model from diverging to a high value outside of the range over which the MSSTA instruments were sensitive. The results are shown in Figure 65. Clearly, this model is quite capable of matching any reasonable input DEM, including isothermal DEMs, over the range of Log(T) = 5.7 – 6.4. That such good agreement can be achieved with only three free parameters is quite encouraging; the fitting algorithm's sensitivity to noise increases greatly with the number of free parameters, so adding an extra spline point just to improve the fit at the low-temperature end of the range would defeat the purpose.

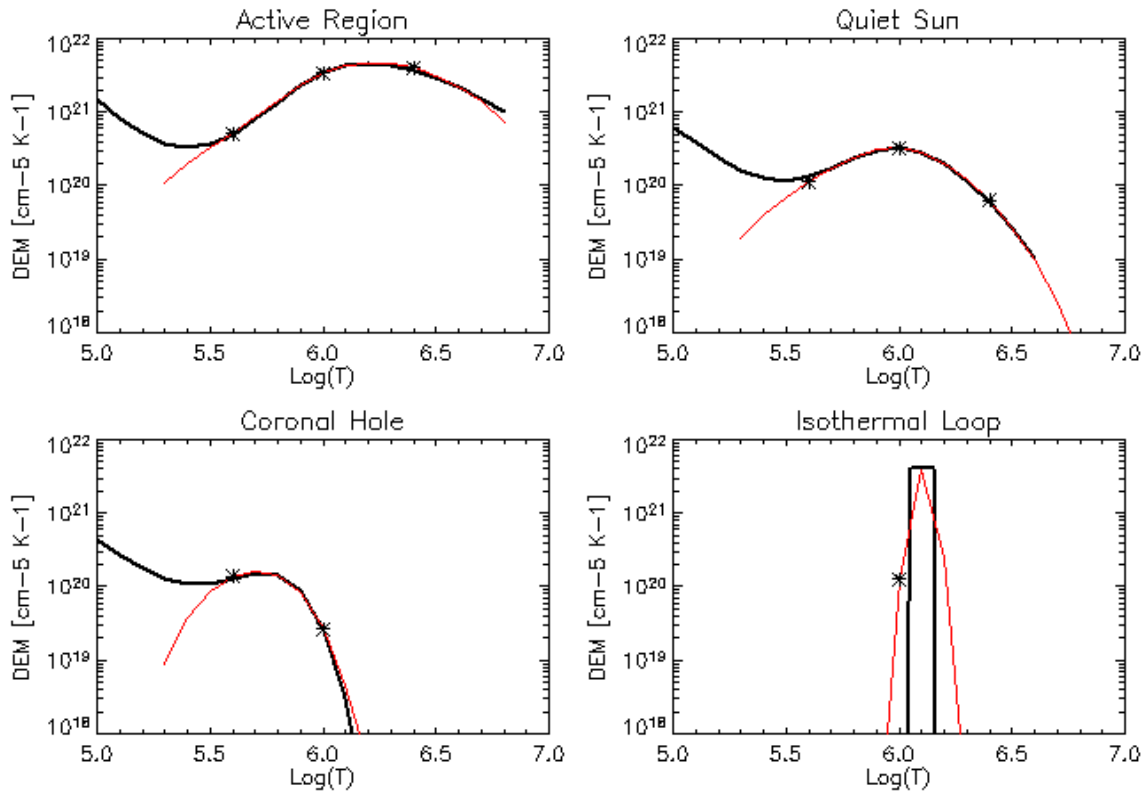

Figure 65. The red curves show the best-fit DEMs found by forward fitting to noise-free simulated observations. The input DEMs used to generate the simulated observations are shown by the heavy black lines. The stars mark the location of the spline points. Three-point splines provided adequate flexibility to match a wide range of possible input DEMs, including very sharp isothermal DEMs like the one shown in the lower right panel. Plots such as these were used to fine-tune the temperature range, temperature grid, and boundary conditions of the DEM splines.

There remains the danger that the location of the spline points will bias our results. This concern is somewhat alleviated by the chosen grid's success in recovering many different DEMs, including a number of isothermal DEMs at various temperatures not plotted in Figure 65. However, while simplicity demands that we chose a single temperature grid and apply it to all observations, it is important to double-check the resulting DEM by periodically attempting to fit a set of observations with DEMs defined on different temperature grids and making sure that they converge to the same function. I made some effort to introduce a fourth free parameter dictating the location of the spline points, but this did not produce reliable results.

Another potential source of bias is the initial guess at the DEM. The starting point for each set of observations was a flat DEM, whose value was determined by normalizing to the MSSTA 195 Å pixel value. Different initial guesses appeared to have little effect on the final result; the algorithm

spent a little more time hunting for a minimum if the starting point was chosen without reference to the data, but tended to converge to the same solution.

A variety of simulated datasets were fed into the forward fitting algorithm to test its response to noise and its dependence on the number of different bandpasses. A summary of the results is shown in Figure 66. For each panel, the CHIANTI active region DEM was used to generate 100 randomized datasets, as described in Section 4.1.1. The upper left panel shows the result of simulations using a realistic low-end estimate of 25% noise on the temperature kernels of the 5 MSSTA EUV telescopes that succeeded in flight: the 150 Å, 171 Å, 180Å, 195 Å and 211 Å instruments. The 1-σ accuracy of the recovered DEM is about ±50% over the interval from Log(T) = 6.0 – 6.3; the results are substantially worse at the edges of the temperature interval.

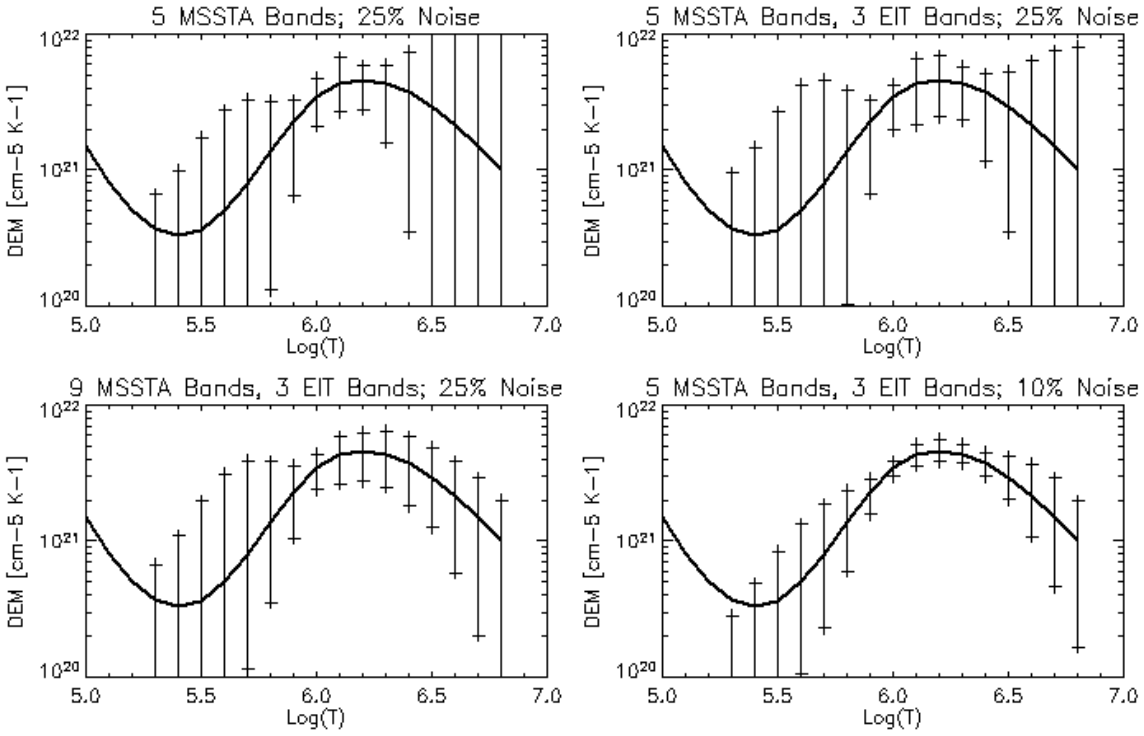

Figure 66. Reconstruction of DEM from simulated datasets. The simulated data sets consisted of 100 randomized observations of CHIANTI's active region DEM (dark black line). Clockwise from upper left: observations using the MSSTA 150 Å, 171 Å, 180Å, 195 Å and 211 Å bandpasses, with 25% noise; the previous bandpasses, plus EIT's 171 Å, 195 Å and 284 Å bandpasses, also with 25% noise; the same 8 bands, with only 10% noise; and those 8 bands, plus the MSSTA 58 Å, 98 Å, 131 Å and 256 Å bands, all with 25% noise. Error bars show 10%-90% solutions (>1σ).

Increasing the number of bandpasses does not substantially improve the accuracy in the center of the curve, but it does extend the range over which the reconstruction is valid. The upper right panel shows the effect of adding the 3 EIT EUV bandpasses to the analysis, still with a 25% error on all observations. (These conditions most closely resemble the expected state of the data obtained from the MSSTA flight and supporting observations). The 1-σ errors are now about ±35% over the 1-2 MK region (Log(T) = 6.0 – 6.3). In the bottom left panel, we examine how our capabilities could have improved had the other four MSSTA EUV telescopes (at 58 Å, 98 Å, 131 Å and 256 Å) recorded usable images. In this instance, the performance of the reconstruction improves notably at the high temperature end of the range; but, somewhat surprisingly, it does not look much better at temperatures below 10^6 K, and the accuracy near the peak of the DEM curve is not noticeably better.

The accuracy of the reconstructed DEM depends strongly on the amount of error in the observations. In the bottom right panel of Figure 66, we see the effect of assigning only 10% error to the temperature kernels obtained on the day of flight. These results are quite encouraging: the 1-σ errors are down to ±20% over the range Log(T) = 5.9 – 6.4. The persistent poor performance of the fit at temperatures below Log(T) = 5.8 can be attributed in part to the fact that the active-region DEM plotted here is dominated by a peak around Log(T) = 6.1; similar analyses using the quiet region and coronal hole DEMs show better agreement at lower temperatures. However, in no case is the algorithm successful at temperatures below about Log(T) = 5.7; the instruments are simply not tuned to transition region material.

Clearly, both the level of error in the observations and the exact nature of that error are critical to interpreting the results of a DEM recovery. Considerable effort went into pinning down the sources of error in the MSSTA observations; however, it is important to reiterate that this error is not necessarily well-modeled by the Monte Carlo process used in the above simulations. While the simulations introduce noise by adding uncorrelated random numbers to the true value to each observation, the actual error associated with each pixel value consists of several components:

- There is some statistical noise (photon counting or film grain statistics) in every pixel. This component, which does behave in the same way as the noise in the simulations, is probably only at the level of a few percent;

- Each instrument has some intrinsic systematic error (for example, the difference between the true reflectivity of its multilayer mirrors and the efficiency curves used to generate its temperature kernel). Generally at the level of ~10%, this error will not be centered on 0 in a set of 100 Monte Carlo realizations, and thus will distort the shape of the recovered DEM (or render DEM recovery impossible).

- Uncertainties and inaccuracies associated with the calculation of the EUV emission line contribution functions were not measured, but they certainly exist. Abundance, ionization equilibria and atomic physics of the emitting ions are probably uncertain at about the 10% level. This adds to the systematic error of each bandpass.

- Some systematic errors are common to one or more instruments. For example, most of the bandpasses used in the analysis are dominated by emission from ionized iron, so errors in the assumed iron abundance affect all instruments similarly. The uncertain calibration of the MSSTA photographic film also has similar (though not identical) effects on all the MSSTA images.

Sadly, the net result of all this uncertainty, and uncertainty about the uncertainty, is that there is no obvious answer to the question of how reliable our results might be. That the largest component of the error in the MSSTA observations – the film calibration – is shared by all the MSSTA bandpasses suggests that the relative error on the MSSTA observations may be only about 10%, while the absolute error is up around 25%-35%. In that case, we might hope to recover the *shape* of the DEM curve quite accurately, though the overall normalization of the DEM might be off. However, a more pessimistic reading of the above caveats would emphasize the fact that all the bandpasses contain substantial uncorrelated systematic errors, and that therefore even the [somewhat underwhelming] results shown in the "realistic" simulation in the upper right panel of Figure 66 are not achievable with the data in hand.

The data themselves will provide some insight into these questions. Keep in mind that one of the central advantages of using a DEM-recovery approach to analyzing narrowband EUV images,

instead of filter ratios or direct physical modeling, is the possibility that no DEM will be found that reproduces the observations to within their error bars. Obviously, the simulations assume that a true DEM exists; nevertheless, they can provide a glimpse of the diagnostic power of unsuccessful DEM recovery. Figure 67 shows one instance of the DEM reconstruction using 12-band simulated data with 25% noise (similar to the ones plotted in the lower left panel of Figure 66). This instance was selected for its rather poor fit. The left panel shows a recovered DEM that bears little resemblance to the true DEM used to generate the observations. At right, we see that the recovered DEM reproduced the noisy observations to within their 25% error bars in 8 of the 12 bandpasses. To the eye, the agreement seen here is fairly typical of simulations with 25% noise; however, the χ^2 of this iteration was about 50% higher than the median for the run of 100 iterations. The high error statistic could serve as a clue that the recovered DEM was not as reliable as most of the others found in the run. Still, it is a fairly subtle clue, and would be unlikely to set off any alarms if these results were obtained on flight data. The fact that the observations were reproduced so well by a DEM so different from the true target simply reinforces the point that line fluxes are not the sensitive indicators of small fluctuations in temperature structure that we might like them to be.

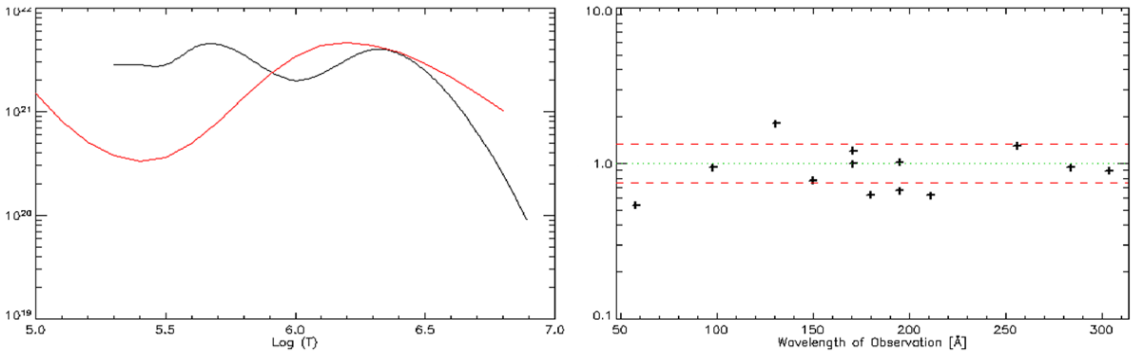

Figure 67. A rather poor DEM recovery in the presence of 25% noise. On the left is the recovered DEM in black with the input active region DEM in red. On the right is the ratio of noisy observations to observations predicted by the recovered DEM. Note that the observations agree fairly well with the predictions.

Thus the final word on the simulations is a cautionary one. Realistic error estimates limit the accuracy of any DEM recovery attempted with MSSTA and EIT data to about ±35% over the range Log(T) = 5.9 – 6.3. While there is some hope that correlations in the systematic errors might allow us to do better, at least as far as the shape of the DEM is concerned, it is also possible that systematic errors not accounted for may make our answers even worse. Furthermore, the χ^2

statistic will only alert us to fairly serious failings of our recovered DEM. This picture of what we might hope to accomplish is notably bleaker than the one painted by (Golub, DeLuca et al. 2004) using simulated data from the AIA; however, their investigation assumed primarily random noise at or below 10%, and did not consider uncertainties in the atomic physics parameters.

Even so, as long as our eyes are open to its shortcomings, the forward-fitting DEM recovery technique is well worth applying to real data. Indeed, it is an essential step if we are ever to extract meaningful quantitative information about the thermal structure of the corona from the beautiful and plentiful EUV spectroheliograms that make up such an important segment of the data currently available to solar physicists. As noted in Section 1.3.4. the limitations that apply to DEM extraction apply to any analysis of narrowband images; the DEM extraction technique just serves to highlight those limitations. With that in mind, we will now turn that technique on the images from the MSSTA III.

4.2 Extracting DEMs from the MSSTA data

The calibration of the MSSTA data is described at length in Chapters 2 and 3. As noted there, calibrated images consist of pixel values giving flux density (ergs cm^{-2} s^{-1}) at the film plane averaged over the area of the pixel. Thus, averaging pixel values over any region in the image and feeding those pixel values to the reconstruction algorithm will produce a line-of-sight DEM averaged over a region of the corona. For the purpose of the analysis, I also included the EIT 171 Å, 195 Å and 284 Å images; the MSSTA images were co-aligned and cross-calibrated with EIT as described in Section 3.3.

The images were then passed to an interactive sub-region extraction program (PB_INTERACT_DEM; the IDL code is in the Appendix) based on Dominic Zarro's image mapping software. There are some concerns that this software does not perfectly conserve energy when used to regrid images on different pixel scales (De Forest 2004), but perfunctory testing with MSSTA and EIT images suggested that any such distortions were below the 5% level. The program prompts the user to crop a region from the MSSTA 195 A image and select the MSSTA and EIT images to be included in the analysis; it then identifies the pixels in each selected image that correspond to the selected sub-region, averages them, and passes the resulting list of pixel values to one of the DEM-extraction routines tested in Section 4.1.3.

4.2.1 FULL-DISK

I began by examining the full-disk average pixel values; that is, the "sub-region" was a square 2000 arc-seconds on a side, centered on the solar disc (including the full solar disc, out to at least 10 Megameters above the limb on all sides). Gaps in the MSSTA (due to vignetting or misalignment of the telescopes) and EIT (due to dropped blocks within the images) data were ignored. The resulting average pixel values allow comparison with calibrated full-disk spectra such as those observed by [(Malinovsky and Heroux 1973), (Woods, Rodgers et al. 1999)], and are a valid test of the principle of analyzing flight data, although any results obtained from these

full-disk averages should probably not be considered for any in-depth analysis due to the data gaps and the non-rigorous square shape of the sub region.

Central λ [Å]	Exposure Time [s]	Full-Disk Average Pixel Value
MSSTA		
150	15	9.95
	20	10.33
	40	11.57
	100	11.26
171	15	74.51
	40	82.59
	100	66.03
180	3	61.76
	30	60.12
	40	61.99
	100	45.10
EIT		
171	8	133.54
195	13	114.24
284	123	7.98

Central λ [Å]	Exposure Time [s]	Full-Disk Average Pixel Value
MSSTA		
195	20	46.39
	30	47.31
	40	32.09
	100	29.29
211	65	30.26
	15	20.27
	30	24.07
	40	18.83
	100	38.93

MSSTA Units: 10^{-2} ergs cm^{-2} s^{-1}

EIT Units: DN s^{-1}

Table 18. Full-disk observations used to generate disk-averaged DEMs. All corrections described in Section 3.3 have been applied to these data.

The results, shown in Table 18, were then used to generate DEMs with the three-point temperature spline method. The output was extremely sensitive to the width of the temperature region and the placement of the pivot points – much more so than all but the noisiest simulations (done with 50% random error). This sensitivity immediately suggests that the data contain errors larger than the nominal 25%. Nevertheless, it was possible to find reasonable-looking DEM solutions that provided good agreement with the observations. The best results came from extending the temperature range from Log(T) = 4.5 – 7.5 (this is more of a way of tricking the spline method into lowering its endpoints than a statement about the physical insight provided by the instruments). The outcome is shown over the standard quiet sun DEM of (Vernazza and Reeves 1978), which is often used as a proxy for a full-disk average DEM, in Figure 68.

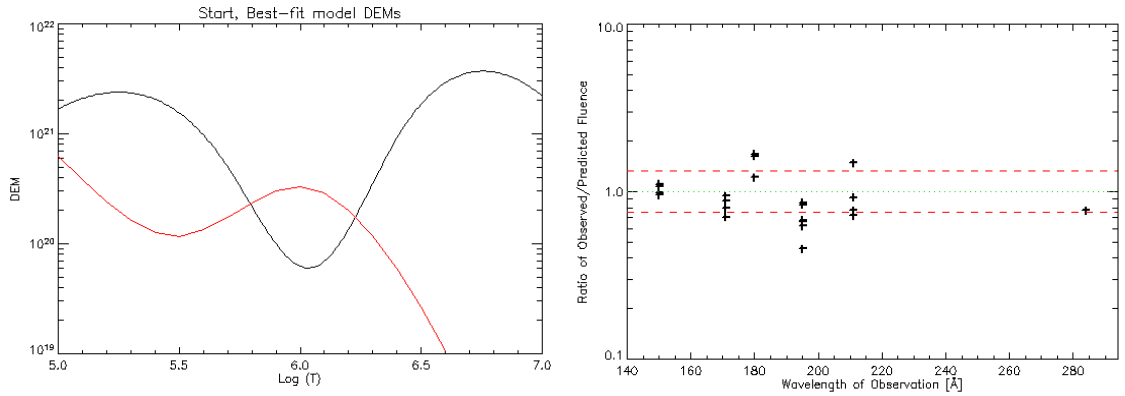

Figure 68. The best-fit three-point spline to the full-disk average pixel values shown in Table 18. At left, the recovered DEM (black) is plotted over the standard quiet-sun DEM (red). At right, the ratio of observed pixel values to those predicted by the recovered DEM are plotted; the red lines indicate ±25% error. The majority of the observations are well-reproduced by the recovered DEM.

Most striking about the recovered DEM is the dip at Log(T) = 6.0 – 6.1, precisely the temperature range at which the MSSTA and EIT instruments are most sensitive (and the temperature at which the standard DEM has its peak). This is a qualitatively persistent feature regardless of the placement of the spline points. Indeed, relaxing the conditions on the DEM reconstruction tends to make the dip even more pronounced. Figure 69 shows the effect of removing some of the constraints on the spline; the depletion of material at 1 MK becomes even more extreme, and the fit to the data becomes (slightly) better. Contrast these results with the ones shown in Figure 70, which uses the fluxes predicted by a flat DEM and the quiet sun DEM (with an overall normalization to optimize the fit). It is immediately apparent that the dip at 10^6 K improves the agreement between the model and the observations; in particular, it makes it possible to match the instruments at the cool (MSSTA 150 Å) and hot (EIT 284 Å) extremes of the overall kernel matrix. The slope of the observations at 171 Å, 180 Å, 195 Å and 211 Å (with increasing temperature of peak sensitivity) in Figure 70 indicates that the million-degree peak in the quiet-sun DEM is probably too hot; the cooler lobe of the recovered DEMs in peak is Figure 69 accounts for most of the emission seen in these bandpasses, and flattens out that slope.

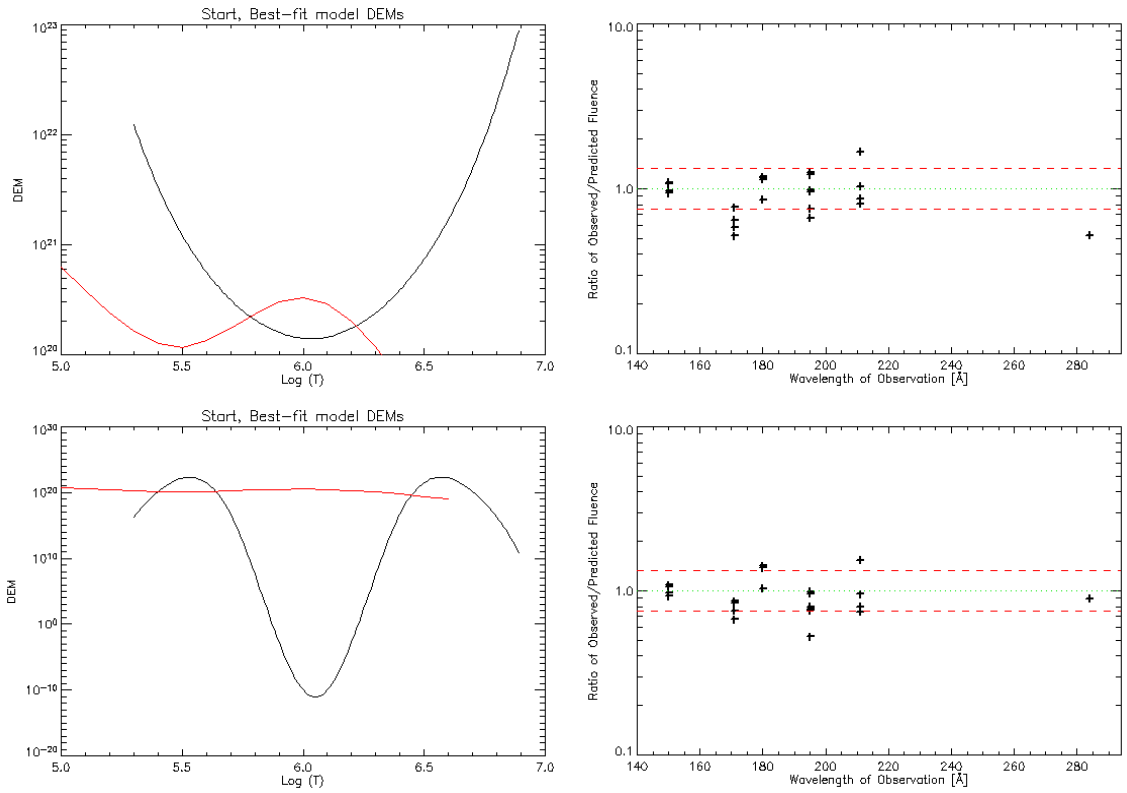

Figure 69. Relaxing the conditions on the spline only enhances the dip at 10^6 K. At top, the range was truncated at Log(T) = 5.3 – 6.9, and the endpoints allowed to float; at bottom, the endpoints were forced to go low, and the penalty function for excessively oscillatory DEMs was removed. Both result in slightly better fits to the observations, though qualitatively the DEMs and the reproduced observations are fairly similar to those shown in Figure 68.

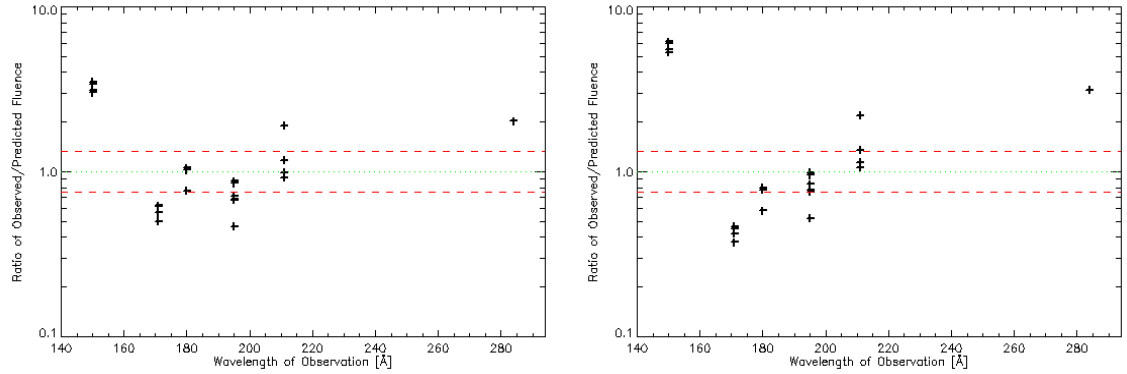

Figure 70. On the left, ratios of full-disk observations to those predicted by an optimized flat DEM of 3.1×10^{20} cm^{-5} K^{-1}; on the right ratios based on a scaled version of the standard quiet sun DEM. Both show noticeably worse agreement than that obtained from the distributions with little or no material at 10^6 K; the flat distribution is slightly preferred, although neither is entirely excluded by the data, given the possibility of systematic errors in the observations and temperature kernels.

The two-part plots in Figure 68 and Figure 69 are a rather unconventional view of observations fit by splined DEMs. Generally, a set of observations is plotted over the extracted DEM as error bars; for each bandpass (or emission line), the temperature at which the product of the temperature kernel (or contribution function) and DEM is a maximum is used as the x-coordinate of the point, and the ratio of observed to predicted pixel value times the predicted DEM is used as the y-coordinate (see, e.g., (Brosius, Davila et al. 1996)). The best-fit full-disk DEM is plotted in this fashion in Figure 71. This technique leads to confusion in terms of interpreting both the recovered DEM and interpreting multilayer observations in general, as it implies that each bandpass provides a measurement of the emission measure of plasma at a particular temperature, so that the DEM can be found simply by drawing a line through those points. In fact, both the x and y coordinates of the points shifts as the DEM is varied. However, this plot does verify that the best-fit DEM implies that the MSSTA is seeing very little million-degree material.

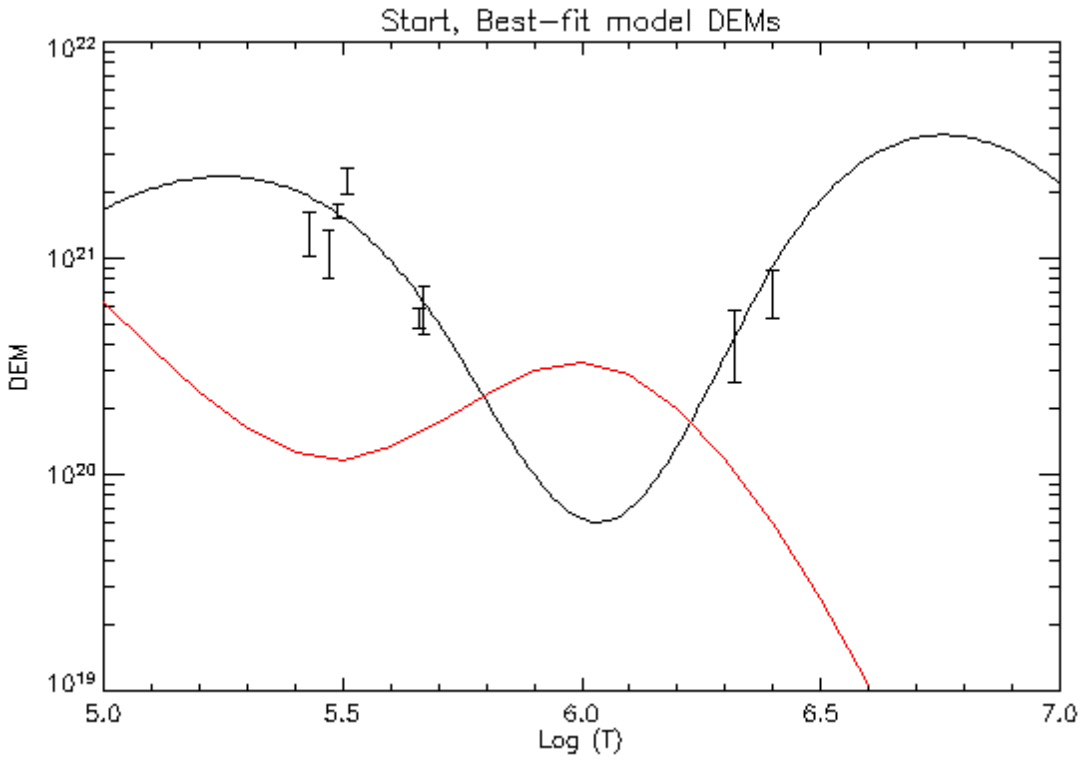

Figure 71. The best-fit full-disk DEM shown in Figure 68 is replotted. For each MSSTA and EIT bandpass, error bars are placed at the temperature at which the contribution in that bandpass is maximum. The size of the error bars is based on the scatter of multiple observations in each bandpass, and is not an estimate of systematic error. Plotting error bars in this way is somewhat misleading.

4.2.2 AREA-RESOLVED

Looking at averages over sub-regions of the solar disk has a number of advantages over treating the full-disk flux. We can avoid data gaps, ensuring that the measured average pixel values reflect the same lines of sight in each image. Furthermore, the extracted DEMs are easier to interpret; attempting to construct a model that reproduces an active-region DEM is more likely to put useful constraints on interesting physical parameters like heating rate and energy conductivity than trying to model a full-disk DEM. Ultimately, of course, we would like to extract DEMs for sub-regions of one arc-second or smaller, but the first step is to examine selected areas of a particular characteristic type of solar "terrain," and see what their recovered DEMs look like.

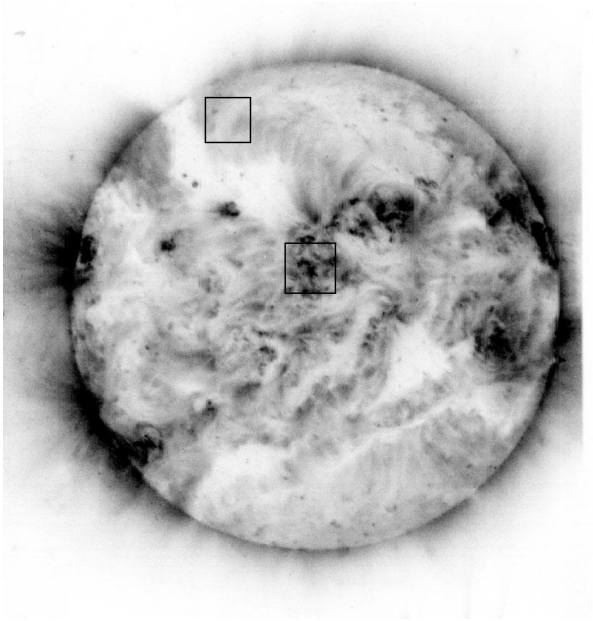

Figure 72. The active region and quiet region analyzed below were selected because of their placement on the disk, the fact that they were found in images in all 5 MSSTA and 3 EIT bandpasses, and because each is a fairly typical representative of a variety of solar feature. Here the selected sub frames are shown in boxes superimposed on an image from the MSSTA 195 Å telescope.

In Figure 72, the selected sub-regions are shown. These selections were made with reference to the MSSTA 195 Å telescope's 20-second exposure; pixels from the corresponding regions in the other MSSTA and EIT images were then identified and averaged by the DEM recovery routine. The results of the sub-region extraction are shown in Figure 73, with heliographic coordinates superimposed. The accuracy of the MSSTA-to-EIT co-alignment is somewhat problematic for the quiet region; however, any offset is unlikely to be a leading source of error.

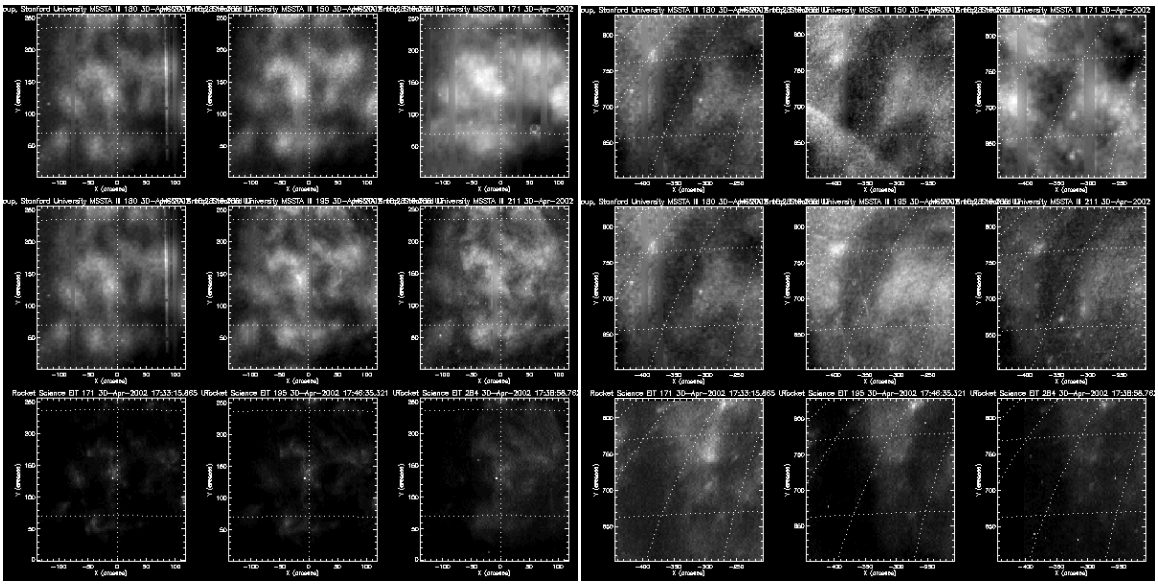

Figure 73. Sub-regions analyzed from the MSSTA III dataset. The left half of the frame shows a crop from an active region; the right half shows a region of diffuse quiet sun emission. Each sub-region is shown in 9 images. From left to right: (*top row*) MSSTA 180 Å, 150 Å, 171 Å; (*middle row*) MSSTA 180 A, 195 A and 211 A; (*bottom row*) EIT 171 Å, 195 A and 284 A. The 284 A quiet-region subframe contains a partial data gap, and was not used in the analysis.

Again, DEM recovery displayed great sensitivity to the definition of the temperature grid over which the spline was performed, casting the uniqueness of the solution into doubt. Figure 74 shows the results. Both recovered DEMs show depressed emission measure at 10^6 K, with most of the flux in all the bandpasses other than the 284 Å coming from cool material (T = 250,000 – 500,000K). However, despite the presence of the error bars plotted exclusively on the cool temperature lobe, the high-temperature lobe of the recovered DEM does contribute to the emission seen in the images and cannot be changed without affecting the fit. The agreement with observation is not especially good; the quiet region in particular is of by a factor of 2 on the 171 Å flux, and reproduces only two of the 5 wavelengths to within their nominal error bars. Still, the agreement is not unreasonable given the potential systematic errors associated with the images. The recovered DEMs provide substantially better agreement than either scaled versions of the relevant CHIANTI standard DEMs or optimized flat DEMs.

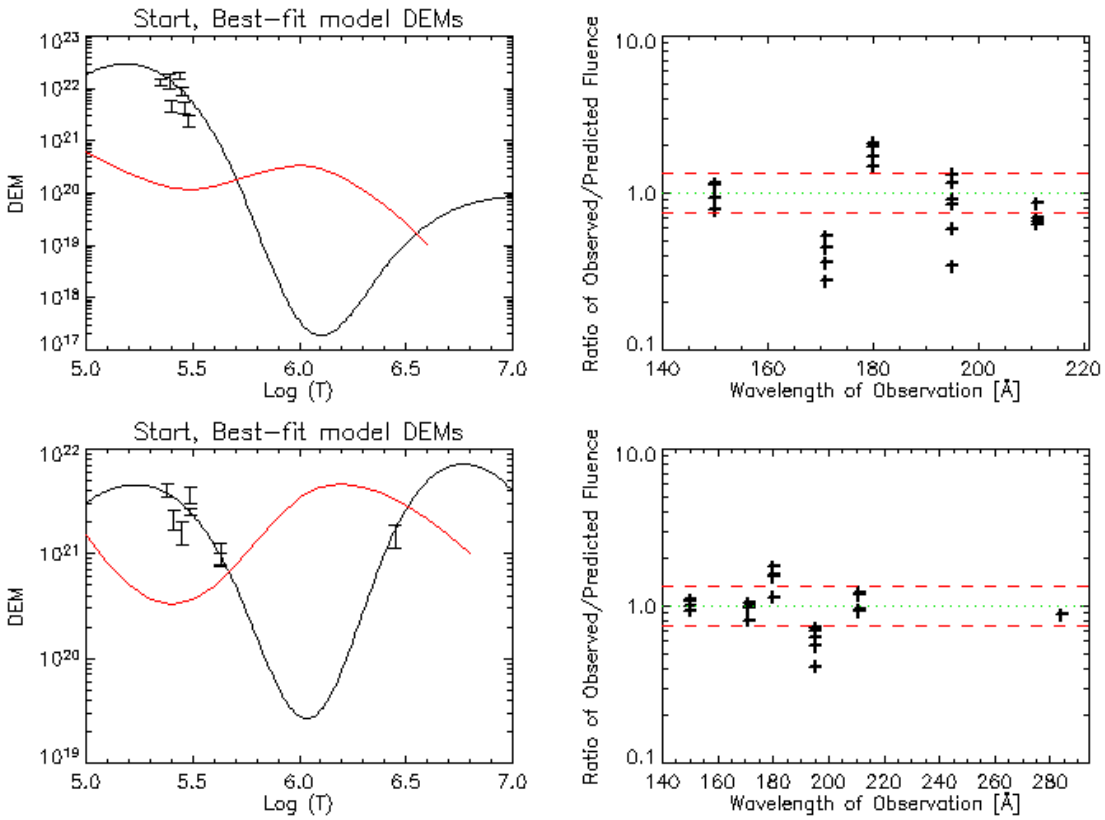

Figure 74. Results of sub-region DEM extraction. On top are the results from the quiet-sun region; the lower pair of frames are from the active region.

Carrying the sub-region DEM extraction to smaller spatial scales is certainly possible, but perhaps not as illuminating as might be hoped. Due to the imprecise co-alignment and marginal spatial resolution and signal-to-noise of some of the images, the smallest sub-region that can reliably be measured in multiple frames is about 30 arc-seconds across (so that the number of resolution elements on the full solar disk is of order 1000). Because of the alignment problems of the MSSTA 150 Å and 180 Å images, and data gaps in the EIT images, as many as half of these pixels will contain subsets of the full dataset. 30 arc-second-wide columns of sight through the corona are guaranteed to contain many unrelated structures, and thus the DEMs extracted from observations on this scale must be treated as ensemble averages or descriptions of global conditions in much the same way that the larger sub-regions discussed above were. Only by measuring multiple independent bandpasses at spatial scales of 1 arc-second or less will we have any hope of constraining plasma conditions in a single coronal loop (and, as discussed in Section 1.3, even if we could achieve a spatial resolution of 0.1 arc-second or smaller the problem of line-of-sight confusion in an optically thin plasma cannot be entirely avoided).

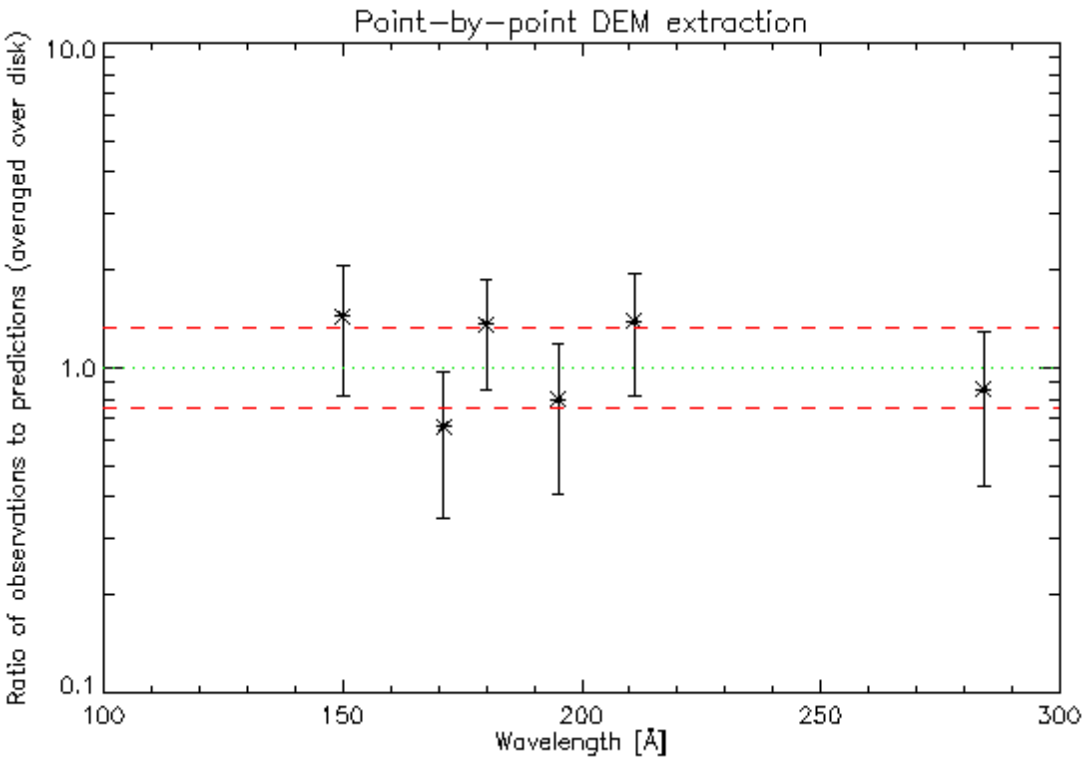

Figure 75. Pixel values predicted by DEM extraction on 30 arc-second square sub-regions compared with observations from those sub-regions (mean and RMS error over the full disk).

Nevertheless, a preliminary point-by-point DEM extraction was performed by mapping all the images to a regular 30-arcsecond grid and feeding the fluences for those points in the grid with full wavelength coverage to the DEM-fitting algorithm. The behavior of the fit under different splining procedures was not studied in detail; the run time of the algorithm for a single set of observations is of order 10 seconds, so extracting DEMs for the full disk takes several hours of computation. The overall agreement between observations and the predictions of the best-fit DEM is somewhat worse for the small pixels than for the more global regions, as might be expected. Figure 75 demonstrates this; for each bandpass, the RMS of the ratio of observations to predictions for all pixels and all exposures in that bandpass is plotted for the 8 EUV instruments included. The results are noticeably worse than what was found for the full-disk average DEM, and outside the nominal calibration error of most of the instruments. It is likely that these results could be improved by a more thorough optimization of the DEM modeling technique. In general, however, the pixel-sized DEMs display the same suppression of 10^6 degree material seen in the averaged regions.

4.2.3 RELIABILITY OF RESULTS

The first explanation for this phenomenon must be based on consideration of instrumental effects, particularly those effects that are not well-described by the calibration measurements listed in Chapter 2. For example, it is obvious from a cursory examination of the images that they contain significant scattered light (see, for example, the broad arcs of reflection from the Ritchey-Chrétien baffle tube overlying the disk in Figure 54), which our piecemeal approach to calibration does not account for. A white-light contribution to the flux observed in each pixel and each wave band would tend to suppress the expected peak in the DEM around one million degrees.

However, the general bimodal shape of our DEM results suggests that a pixel-by-pixel two-temperature model, like the one constructed by (Zhang, White et al. 1999) using just the three EIT bandpasses, could be made to fit the observations over the full disk. Constructing such a model based on the 8 bandpasses we observed would, in principle, be more reliable, less dependent on assumptions and initial conditions, and easier to interpret. However, before we conduct any analysis using the extracted DEMs, it is important to understand their limitations.

Re-examining Figure 69, we note that there is little to help us decide between the two recovered DEMs on the basis of their agreement with observations (that is, the right panels of the top and bottom rows, and the χ^2 of the fits, are difficult to distinguish). However, the DEMs bear only the most superficial qualitative resemblance to each other in that they are two-peaked, and have little emission measure at Log(T) = 6.0.

The problem is that the cubic spline tends to find solutions by driving the emission measure out to the edges of the region of sensitivity of the instrument temperature kernels; the χ^2 changes more smoothly in this regime, making it easier to find a solution. However, if good solutions without the dip at 10^6 K were to be found, they would have been uncovered; the fits were performed over a number of different combinations of end points and spline points, and always wound up with a two-temperature solution. Inspecting the error surface in parameter space confirms that more conventional-looking solutions like the CHIANTI standard DEMs consistently produce higher χ^2

values than the best-fit results. However, a wide variety of possible DEMs – including the two-temperature recovered solutions, the CHIANTI DEMs, and even flat multithermal plateaus such as those found by (Schmelz, Saba et al. 1999) – predict pixel values that are within a factor of 2 of all the observations in the MSSTA dataset, and thus none of these possibilities can be ruled out under the most pessimistic interpretation of the errors involved in the calibration of the instrument and the assumptions underlying the analysis.

4.3 Solar Physics Implications

Thus, my efforts at DEM recovery lead to two general conclusions: first, that the MSSTA observations are best fit by a model of the solar atmosphere that includes very little material at 10^6 K; and second, that neither the DEMs I found by analyzing the MSSTA observations, nor other DEMs obtained from similar analysis of similar observations, constitute compelling descriptions of the state of the solar plasma.

4.3.1 THE 1 MK DIP

If we believe the suggestion that there is very little million-degree material in the solar atmosphere, and that most of what is seen in the MSSTA images is much cooler plasma, we are forced to question a large body of observational evidence and an even larger body of received wisdom to the contrary. That images in the 171 Å bandpass depict the distribution of million-degree plasma is virtually gospel; the vast majority of studies of EUV spectroheliograms conclude that the plasma being observed is around $1 - 2 \times 10^6$ K (see, *e.g.*, (Lenz, DeLuca et al. 1999), (Aschwanden, Newmark et al. 1999) and numerous other works cited in Section 1.3). However, it has already been argued that any temperature measurements based on EUV filter ratios or forward modeling of plasma conditions are non-unique and thus highly suspect. More difficult to dismiss are the independent measures of coronal temperature obtained from microwave observations(White 1999), or spectral observations, including temperature sensitive emission line ratios (Feldman, Doschek et al. 1999); still, there are ambiguities in these observations, including discrepancies of a factor of two or more between microwave brightness temperatures and temperatures measured from EUV observations (Landi and Chiuderi Drago 2003).

It is interesting to note how much work is conducted by starting from the assumption that all plasma seen in a narrowband image is at the temperature at which the sensitivity of that imager peaks (in addition to the sources cited previously, see, *e.g.,* (Nightingale, Aschwanden et al.

1999), (Reale, Peres et al. 2000)). One of the central theoretical pillars of this sort of analysis of EUV images is the Unresolved Fine Structure model proposed by (Feldman 1983; Feldman, Widing et al. 1999) based on spectral observations. The UFS model states that the distribution of plasma at any temperature T_e in the solar atmosphere is dominated by nearly-isothermal structures that hold their peak temperature T_e along most of their lengths. Thus, while the heating source of structures at different temperatures may be the same, those structures are essentially unrelated to each other.

The UFS model discounts the importance of conduction in heating the lower corona and transition region, and holds that, in general, hot structures do not have visible footpoints at cooler temperatures. Evidence for this picture is provided by the observations of (Vourlidas, Klimchuk et al. 2001), who found that Hydrogen Lyman α emission is much too strong for back-heating from the corona (which they assumed to be isothermal, with temperature and density based on TRACE filter ratios) to account for more than a tiny fraction; and (Aschwanden, Schrijver et al. 2001), whose forward models of EUV-emitting loops included negligible conductive flux. In general, the assumption that narrowband multilayer images show isothermal, million-degree plasma leads to assumptions that favor isothermal models of coronal structures, which in turn imply little connectivity between the various temperature layers of the solar atmosphere. As noted in Section 1.3.4, this unified picture of the solar atmosphere also has implications for the location and nature of the coronal heating function.

However, it is possible to lose track of which results of the UFS model are based on observations and which are based on assumptions. There is some evidence of the importance of conduction from hot material to cool material: for example, (Berger, De Pontieu et al. 1999) found that the "moss" observed in TRACE 171 Å images was in fact composed of the roots of very hot structures seen as large coronal loops in Yohkoh SXT. Using forward modeling on MSSTA II data, (Martínez-Galarce, Walker et al. 2003) discovered a class of coronal funnels that could account for 171 Å and 1550 Å observations; these funnel models included solutions with peak temperatures ~500,000 K and strong emission in the 171 Å bandpass, in qualitative agreement with the two-temperature best-fit solutions presented in the previous section. As discussed in (Oluseyi, Walker et al. 1999)'s overview of solutions to the general quasistatic loop equation of (Vesecky, Antiochos et al. 1979), coronal loops with relatively low peak temperature can account for much of the observed diffuse EUV emission when ambipolar diffusion is taken into account;

these models imply substantially higher downward conduction than more conventional loop models.

Therefore, the fact that the MSSTA and EIT data can be reproduced by DEMs that consist of very little million-degree material, suggesting that most of the EUV flux is coming from cooler plasma, with contributions from a high-temperature component, is intriguing. In order to make this conclusion more quantitative, we would like to better-constrain the cool temperature component. As noted previously, it should be possible to construct a two-component DEM model for each pixel in the MSSTA/EIT dataset. Such a model would use four parameters (temperature and emission measure of the hot and cool components), similar to the models presented by (Zhang, White et al. 1999), but with the advantage of not being nearly as underconstrained. An effort to fit such a model to the points on a 30-arc-second grid is underway.

However, it is doubtful that such models will prove useful in the long run. They are not motivated by any compelling physical intuition: despite the fact that the corona is optically thin, and thus any line of sight will likely sample multiple different structures, there is no reason to believe that, in any large region, the solar atmosphere is well-described as a distribution of plasma at exactly two well-separated temperatures. Furthermore, the interpretation of the results is difficult (see the full-disk maps of the four model parameters in (Zhang, White et al. 1999), which cannot be said to provide much more insight into the state of the corona than the raw images). They are interesting primarily as an empirical result; that is, they are interesting because they can reproduce the observations.

4.3.2 DEM INDETERMINACY

The most important conclusion we are forced to draw, however, is that there are a lot of possible DEMs that can reproduce the observations. It would be absurd to state that the MSSTA and EIT data prove that there is no million-degree plasma in the solar atmosphere, and presumptuous to state even that they strongly suggest the absence of million-degree material. What we can say is that it is possible to account for MSSTA and EIT observations with a DEM that includes little or no million-degree material. Indeed, given the potential errors associated with the MSSTA and

EIT, it is impossible to rule out a two-temperature DEM, or a flat plateau, or even a modest peak at around 10^6 K. While the suite of narrowband images is not entirely useless as a constraint on the DEM – the overall level is fairly well-specified, and vast regions of DEM-space can be excluded for each pixel – it is not nearly as useful as might be hoped, or as is frequently assumed.

What can be done to improve the reliability of the results? First, it is possible in principle to extend the dataset by adding more multilayer bandpasses or including spectral observations. Ideally, we would like more bandpasses to constrain the behavior of the DEM at lower and higher temperatures, in order to exclude spline solutions with unrealistically high values at these temperatures. For example, the recovered quiet-sun DEM shown in Figure 74 includes a very high emission measure at T < 500,000K; the MSSTA observations are not sensitive enough to half-million degree material to reject this solution, but the large value of the DEM at Log(T) = 5.4 is inconsistent with the results of (Dupree 1972) and other spectral measurements of lines formed at transition region temperatures. From a practical standpoint, the set of data that could be used to extend the analysis of the MSSTA images is limited. TRACE images were taken simultaneously with the MSSTA flight, and these could be added to the fitting algorithm; but TRACE includes essentially the same 171 Å, 195 Å and 284 Å bandpasses as EIT, so its usefulness would be more as a cross-check than as an extension. Spectra from SUMER and CDS are available, but they cover such a small spatial region of the sun as to be largely inapplicable to the full-disk MSSTA and EIT images, and are offset in time by several hours. Ground-based observations in H α or Ca K are taken every day, but those lines are not optically thin and thus not susceptible to temperature kernel analysis. The same is true of the MSSTA 1550 Å and 1216 Å telescopes. Full-disk spectra from TIMED-SEE might be valuable in setting boundary conditions on the spline, but lack the spatial and spectral resolution to be included in the extraction routine.

However, as demonstrated in Figure 66, broader temperature coverage is less important than more accurate observations. We could certainly impose more constraints on the lower temperature ends of the DEM, or exclude some of solutions returned by the algorithm, on the basis of physical insight; that is an essential part of forward modeling. But the fact that such a wide range of diverse DEM distributions are capable of fitting the data means that it is there is no clear point at which we can draw the line between providing intelligent feedback to the fit and simply specifying the DEM *a priori*. As long as our measurements contain errors of 25% or more, there is little hope of identifying unique, well-constrained DEM distributions. We need to get the

error down to about 10% before we can begin to make definitive statements about the shape of the DEM. That 10% limit must include not only photon counting statistics, but systematic errors in the instrument calibration, imprecision and inaccuracies in the atomic physics of the emitting ions, and breakdowns or incorrect choices in the assumptions underlying a DEM analysis. The implications of this requirement for future missions are discussed in the final chapter.

5 Conclusions

5.1 Summary of the MSSTA III data

The MSSTA III obtained 84 spectroheliograms in 5 EUV (150 Å, 171 Å, 180 Å, 195 Å, 211 Å) and 2 FUV (1216 Å and 1550 Å) bandpasses. Several of these bands that are well-studied, but some (the 150 Å and 211 Å) have never before been imaged at high resolution. Four of the MSSTA telescopes failed to record images; in three of the four cases, this was due to the failure of their Zirconium visible-light rejection filters under the concentrated solar flux. These failures limited our ability to study upper transition region plasma. The resolution of the EUV images is limited to about 10 arc-seconds by the graininess of the film used to record their images. Furthermore, the 150 Å and 180 Å telescopes were slightly misaligned, and thus include just over half the area of the solar disk in their images. The FUV images are full-disk, and are noticeably sharper than the EUV.

Extensive work was done to ensure accurate photometric calibration of the MSSTA telescopes. Prior to flight, we estimated the calibration accuracy at 25-35%, with the largest component of the error coming from the film response curve. Unfortunately, there are indications that the calibration of the EUV images is off by up to a factor of 8. While the overall statistical noise in the MSSTA measurements is of roughly the expected size, the large systematic errors are extremely troubling, particularly in light of our findings regarding the sensitivity of DEM extraction to error. The images were renormalized to bring them into agreement with the photometric calibration of EIT by adjusting the film calibration after flight.

Nevertheless, the MSSTA images constitute a unique and powerful dataset. In combination with observations from EIT and TRACE, they can be used to probe the thermal structure of the solar atmosphere in the range 300,000 K < T < 3,000,000 with unprecedented breadth and accuracy.

They offer a badly-needed remedy to the problem of underconstraint that has plagued past quantitative analyses based on multilayer images.

5.2 Summary of the DEM reconstruction results

Any dataset consisting of measurements of EUV line intensities (or, in the case of narrowband imagers, some combination of EUV line intensities) can be used to place constraints on the differential emission measure of the emitting plasma. By making some simplifying assumptions, we can see that the DEM contains all the information about the configuration and conditions of the observed material that can possibly be derived from such observations. Therefore, extracting DEMs from multilayer observations, and understanding the precision of those DEMs is an essential step in realizing the diagnostic power of multilayer telescopes.

I explored the problem of characterizing the thermodynamic state of an emitting plasma based on narrowband observations, and found that conventional techniques like the filter-ratio method and two-bandpass forward modeling do not generally lead to reliable and unique solutions. However, a suite of simultaneous, co-aligned images in at least five distinct bandpasses can be used to extract full and accurate DEMs. Treating the extraction as an inverse problem leads to the conclusion that the transformation is ill-conditioned due to the broad temperature response of the line contribution functions. Therefore, the inversion is extremely sensitive to noise and error.

Taking a forward approach to the problem allows us to test the performance of the DEM extraction with simulated data. We find that, while additional bandpasses are useful in extending the applicable range of the recovered DEM, the amount of error in the dataset is absolutely critical to the success of the DEM extraction. At 10%, the DEM can be obtained quite reliably; at 25%, the recovery has some value but is suspect, and errors much larger than that render the recovery process almost completely untrustworthy. The precise nature of the error must be understood: while random errors were most thoroughly studied, systematic errors can be much more damaging. Systematic errors that effect all bands equally, on the other hand, lead to an overall normalization error in the best-fit DEM, but do not distort its shape.

Using the re-normalized MSSTA images and EIT images taken shortly before, I was able to find DEM functions describing the full solar disk, a characteristic active region and a quiet region, and smaller-scale DEMs describing 30 arc-second square subregions on the disk. The recovered DEMs generally reproduced more than half the observations to within 25%, and virtually all to within 50%. The most noteworthy, persistent feature of the recovered DEMs was a dip at 10^6 K, suggesting that most of the emission seen in the MSSTA images comes from either cooler or hotter plasma. This finding is not in agreement with the prevailing view of the temperature structure of the solar atmosphere.

It may be possible to account for this result with theoretical arguments based on reconsidering the amount of conductive heating between the corona and the chromosphere. However, it is more likely an indication of the inability of the selected multilayer observations to provide firm constraints on the shape of the coronal DEM. In light of this difficulty, further quantitative analysis of those observations (or similar ones) must be considered highly suspect.

5.3 Future Prospects

From the beginning, the MSSTA project has been a two-pronged effort to extract precise quantitative information about the state of the corona by obtaining a novel data set and applying innovative analysis techniques. The primary result of this work has been, not a new understanding of the physics of the sun, but a deeper awareness of the limitations of existing datasets and of the challenges involved in constraining models of the corona. While a certain amount of disappointment is inevitable, that does not mean that this result is not useful or interesting; its implications for our understanding of coronal structures are potentially quite broad. Many of the conclusions presented in the solar literature of the last several years must be re-examined based on a full appreciation of the extent and effect of uncertainty in multilayer images.

Furthermore, the data obtained by the MSSTA III and the procedures developed after its flight have not exhausted their utility yet. The fact that the data are insufficient to constrain a DEM implies that the types of analyses performed on past MSSTA data sets, such as physical modeling of x-ray bright points or funnels, are inappropriate, but the data set is varied and flexible enough that it could be used in a number of other ways. In addition, the DEM extraction procedure may prove extremely valuable when combined with the observations of instruments now in their planning stages. In this section, I will briefly discuss some future applications that might make use of the MSSTA results.

5.3.1 APPLICATIONS OF MSSTA III DATA

The best way to improve the analysis of any given set of data is to incorporate more data. The stability of the quantitative analysis of the MSSTA EUV images could be improved by using other data sets to add more constraints to the recovered DEM. There are no candidates for inclusion in such an analysis that would not require some sacrifices; the three EUV channels on EIT are the only observations that can be easily combined with the MSSTA images without loss of spatial coverage, resolution or ease of execution.

However, vast amounts of solar data taken around the time of the MSSTA III launch could be used with some care. Full-disk calibrated spectra from TIMED-SEE have already been brought in to re-calibrate the MSSTA images, but these spectra can be used to derive a full-disk DEM which would constitute a valuable additional constraint on the spatially-resolved DEMs obtained by the MSSTA. CDS and SUMER observations could similarly provide reference DEMs for subsets of the MSSTA field of view. Though it is not optically thin, EIT's 304 Å bandpass could give an approximate constraint on the low-temperature end of the DEM curve, and help eliminate the suspiciously large peak of cool material suggested by some of the MSSTA results.

The MSSTA III data could of course be studied in the way that data from its predecessors was generally used: to constrain physical models of coronal structures. The problems of uniqueness and noise sensitivity that arise from using multilayer images in this manner could be somewhat alleviated by incorporating magnetograms or FUV or visible-wavelength observations in the same forward models.

The FUV data of the MSSTA III have not been used at all, which seems wasteful considering their excellent spatial resolution (especially for the 1550 Å telescope) and spectral purity (especially for the 1216 Å telescope). These images could certainly prove valuable for forward modeling of physical structures; in particular, Lyman α emission has been used as a proxy for conductive flux at the base of the transition region (Kankelborg, Walker et al. 1996). More recent observations have suggested that back-conduction is insufficient to account for the bulk of the disk Lyman α emission (Vourlidas, Klimchuk et al. 2001), but even if only a handful of bright footpoint-type structures seen in the MSSTA 1216 Å image can be fit by tweaking the coronal loop models of (Aschwanden, Schrijver et al. 2001) and applying them to the corresponding structures seen in the MSSTA EUV images, the implications for the debate on the interconnectivity of the various layers of the solar atmosphere would be significant.

An intriguing possible application of the MSSTA data was suggested during the attempt to correct the images for the effects of atmospheric absorption (see Section 3.3.1). Existing atmospheric models like the MSIS model have uncertainties of 20-50% in the parameters that determine the EUV absorption cross-section as a function of altitude. The MSSTA provides a

wonderfully uncomplicated set of soundings of the EUV absorption characteristics of the Earth's atmosphere in the range of 150 – 270 km, if we treat the sun as a back-light of roughly constant intensity (which it is, over the duration of the flight, at sufficiently large spatial scales). While the calibration uncertainties in the MSSTA data may render them useless for this application, only relative calibration accuracy is necessary; and state-of-the-art atmospheric models are based on analysis of substantially less applicable data (Zhitnik, Boyarchuk et al. 2003).

5.3.2 APPLICATIONS OF THE DEM RECONSTRUCTION TECHNIQUE

The success of the last generation of multilayer instruments, from the MSSTA I and II through EIT and TRACE to the MSSTA III, has made high-resolution EUV images an increasingly essential part of our understanding of the corona. As a result, most large-scale solar missions planned for the coming decade rely to some extent, directly or indirectly, on multilayer imagers. Improvements in detectors, deposition processes and spacecraft systems will pave the way for increasingly powerful versions of these highly successful instruments.

The next generation of narrowband multilayer telescopes is typified by the Atmospheric Imaging Assembly on the Solar Dynamics Observatory, scheduled for launch in 2008. The AIA design combines the advantages of TRACE (high cadence and spatial resolution) and EIT (continuous, long-term full-disk coverage) with an essentially MSSTA-like approach to multilayer imaging, emphasizing the importance of simultaneous, full-disk images in six EUV bandpasses using an array of telescopes. Its dataset is expected to have the following properties:

- It will consist of images in EUV bandpasses centered on strong iron emission lines at 94 Å, 133 Å, 171 Å, 195 Å, 211 Å, and 335 Å;
- White-light and FUV images at the same scale will be obtained concurrently;
- Each EUV channel will record continuous image sequences with a cadence of ~ 10-15 seconds (using four telescopes, with two channels on each telescope, and alternating between the channels);
- Each image will be 16 Megapixels, covering the full solar disk with ~1 arc-second pixel-limited spatial resolution;

- Near-continuous coverage throughout the mission is possible thanks to the inclined geosynchronous orbit of the SDO (which does result in eclipse seasons twice per year).

The AIA represents the best chance yet at grasping the holy grail described in Chapter 1: DEM functions obtained for lines of sight all over the solar disk with high cadence and high spatial resolution. Indeed, DEM extraction is one of the primary science goals of the AIA, and simulated AIA data have already been used to test a variety of DEM-recovery algorithms similar to those presented in Chapter 4 (Weber, DeLuca et al. 2004). (A related group is pursuing a more sophisticated, but much less efficient, Markov-Chain Monte-Carlo approach to DEM reconstruction (Lin, Kashyap et al. 2004) that can incorporate broad-band imagers; they are testing their algorithm against simulated data from the planned Solar-B mission.)

Discussions and code-exchanges with Weber *et al.* have confirmed that their forward-fitting algorithm is essentially identical to the one I used on the MSSTA images. How, then, to explain their finding that AIA observations will be sufficient to constrain DEMs over the range Log(T) = 5.5 – 7.5 with a temperature resolution of ~ 0.2 in Log(T) and an accuracy of ~ 5%? The results of Chapter 4 suggest that MSSTA and EIT, with a similar number of bandpasses, cannot constrain the DEM at three temperatures from 5.8 – 6.4 to better than ~ 50%. Certainly the AIA channels are well-chosen, providing broader temperature coverage and less overlap than the combined MSSTA and EIT dataset. However, most of the discrepancy is due to different treatment of error and uncertainty in the two sets of simulations. Weber *et al.* simulate ~ 3% uncorrelated statistical error on each bandpass; their simulations do not explicitly consider the effect of systematic errors, although they estimate (based on a separate analysis) that systematic errors in a single channel are tolerable up to ~ 15%.

While it is true that the approximation I have made in treating systematic errors as random errors uncorrelated between the various bandpasses is a crude one, it cannot be denied that systematic errors are present and will continue to be present in all the EUV bandpasses of even an extremely well-calibrated instrument at levels greater than 20%. Moreover, the correlations that exist between these systematic errors cannot be reliably assumed to be perfect, so there is no justification for assuming that these uncertainties will result in an overall normalization error rather than a distortion in the shape of the recovered DEM. Indeed, the distortion of the DEM

result is amplified in proportion to the temperature resolution used by the recovery algorithm, so the more ambitious a DEM-extraction routine becomes, the more sensitive it becomes to systematic errors. The implications of these considerations, and a more subtle approach to modeling the effect of uncertainty on AIA data, are under discussion with Weber *et al.*

The AIA is certainly not the last word on coronal DEM-measuring instruments; payloads with still more bandpasses, telescopes with still better spatial, temporal and spectral resolution, instruments and databases with ever more reliable calibration can be designed and built. As we work towards such instruments, the lessons learned in the analysis of the MSSTA data will be worth revisiting once more. A careful selection of EUV bandpasses based on the narrowness and separation of the individual channels' temperature responses (expressed quantitatively through the SVD of the kernel matrix) should be the starting point of any instrument design. Algorithms that balance accuracy with suppression of noise should be developed and tested on simulated data before the instrument is built. And finally, an understanding of the nature and effect of uncertainty on the analysis of the results is absolutely critical if multilayers are to be used to improve our still-vague quantitative understanding of the corona.

EUV multilayers are powerful tools that have already revolutionized solar physics, and have the potential to provide final answers to some of the most puzzling problems in the field. But the fact is that the current generation of multilayer instruments is limited by large uncertainties in instrument calibration and knowledge of atomic processes. Even if these practical challenges can be overcome, future multilayer imagers will still face fundamental limitations due to the line-of-sight confusion inherent in observations of an optically thin plasma, and to the broad temperature range over which EUV emission lines are radiated. Multilayers are not magic mirrors; they do not tell us the whole story; they do not render other types of instruments, and physical intuition, obsolete; and, no matter how advanced the telescopes and the analysis routines become, they never will.

5.4 The ATSSI

It is unlikely that the MSSTA experiment will be flown again. At best, if the instrument could be reconfigured with new filters and multilayers and upgraded with CCD detectors as described in the previous chapter, it might return a dataset with more images, superior resolution, and better coverage of the upper transition region than we achieved with the MSSTA III. However, the generation of solar observatories scheduled for launch in the next three years (including Solar-B, STEREO, and especially the AIA instrument on SDO) will return enough high-quality data to render even an improved MSSTA IV obsolete.

Nevertheless, sounding rockets can still play an important role in the development of our understanding of the corona. In particular, they offer a relatively low-cost, high-speed platform for assessing the viability of novel observational techniques. In this chapter, I describe a proposed design for the Advanced Technology Solar Spectroscopic Imager (ATSSI) – a sounding rocket experiment using the MSSTA truss that will test the suitability of several promising new technologies for coronal observations. The chapter is adapted from (Boerner, Martínez-Galarce et al. 2004), which was presented at the LTD-10 conference in Genoa, Italy in July 2003.

5.4.1 ABSTRACT

The Advanced Technology Solar Spectroscopic Imager (ATSSI) is a sounding rocket-borne experiment that will employ a Transition-Edge Sensor (TES) placed at the focus of a Wolter-I mirror to study large active region loops in the solar corona. The TES instrument will operate in the ~ 500 – 1500 eV EUV/soft X-ray bandpass, obtaining ~ 3 eV energy-resolved spectra at ~ 6.25 arc-second image resolution with a count rate of ~ 1000 photons/sec/pixel. Over a typical observation period of ~360 sec, we will raster scan over a 0.6 x 0.6 arc minute field of view to obtain a 6 x 6 pixel image containing true EUV/soft X-ray spectroheliograms of a solar active region. Using these observations, we can directly determine composition, electron density and thermal differential emission measure of large active region loops in order to constrain models of

heating mechanisms and accurately measure the thermal morphology of these structures. In the current analysis, we present an initial instrument concept and discuss some of the mission science goals.

5.4.2 INTRODUCTION

The Advanced Technology Solar Spectroscopic Imager (ATSSI) (Wamba, Walker et al. 2000) is a sounding-rocket borne observatory that will debut the use of a Transition-Edge Sensor (TES) and replicated grazing-incidence optic to measure the solar corona in the 500–1500 eV EUV/soft X-ray spectral range with ~3 eV resolution.

Obtaining high-energy spectral observations in conjunction with high spatial resolution imaging is imperative to understanding the temporal, spatial and thermal morphology of the solar atmosphere. Armed with highly resolved spectra at every imaged point, we will be able to further constrain models of coronal structures (e.g. small and large loops, funnels, bright points, spicules, etc.). Such highly detailed information regarding dynamics, magnetic morphology and elemental abundance will give us further clues toward understanding the complex nature of the sun. In the present analysis we briefly discuss the ATSSI instrument and present a representative active region solar spectrum we could expect to observe using a TES.

5.4.3 ATSSI SYSTEM CONCEPT

The ATSSI will be built on the truss structure of the Multi-Spectral Solar Telescope Array (MSSTA) rocket payload, which has successfully flown three times. ATSSI will fly a single TES pixel at the focus of a Wolter I mirror. The TES instrument will be pointed at an active region on the sun, and, using the rocket's Attitude Control System, we will raster scan a 6 x 6 pixel image array. The dwell time of ~10 seconds at each 6.25 arc-second pixel should be short enough to avoid distortion in the image caused by motion of small-scale coronal sources. (This deviates from the original concept of flying an 8x8 array that has proven more complex and costly.(Boerner, Martínez-Galarce et al. 2004))

The primary technical challenge of the mission will be to maintain the TES detector at its operating temperature of ~80 mK throughout the mission (particularly during launch). The cryostat will be an adiabatic demagnetization refrigerator (ADR), based on the one that was launched three times by McCammon et al. beginning in 1996 (McCammon, Almy et al. 2002). This system will be modified by introducing a combination of active and passive magnetic shielding in order to isolate the TES and SQUID amplifiers from the cryostat's strong magnetic field.

The detector itself will be a superconducting bilayer TES developed at NIST (Wollman, Nam et al. 2000). The detectors are fabricated as Mo/Cu bilayers on a Si_3N_4 membrane with a base Si substrate. Because of the steepness of the superconducting transition, the measurement of the photon energy is very accurate ($\Delta \lambda \sim 3$ eV at 1.5 keV for ATSSI), resulting in a highly efficient, high resolution detector. Although better energy resolution has been achieved (~2.0 eV (Wollman, Nam et al. 2000)), we expect to suffer some degradation in resolution from pileup caused by the high solar flux.

In the present design, the Wolter telescope that feeds the detector will have an aperture of 125 mm and a focal length of 1820 mm. The geometrical collecting area of the optic is approximately 7 cm^2. The mandrels for the paraboloidal and hyperboloidal mirror sections will be precision diamond turned and flow-polished to the desired shape, and inspected for roughness and figure errors using optical interferometry and atomic force microscopy. The mirrors will then be constructed using a replication technique against the mandrels. Precisely controlled build-up of a ruthenium shell results in a finished internal paraboloid and hyperboloid, each 100mm long, with a grazing angle of 1° on each segment. Because the ATSSI uses a single-pixel detector, off-axis aberrations are not a significant concern.

It is important to keep out-of-band photons from reaching the detector, and to make sure that the count rate of in-band photons does not saturate the detector. The size and efficiency of the Wolter mirror are such that the unfiltered x-ray flux is several orders of magnitude higher than the detector is capable of counting. However, we have flexibility in filtering the flux and can use an assortment of different filter materials so that their absorption edges define a narrow energy

window. The proposed filter stack uses a series of 5 filters, each consisting of a 4000 Å polyimide film with a 1500 Å aluminum coating on one side. The first filter will be placed at the telescope's entrance aperture to reject most of the visible and infrared light before it reaches the Wolter mirror shell, ensuring that the optic will not heat up and deform and that the filter will not be damaged by the concentrated solar flux. The rest of the filter stack will be placed between the optic and the detector. Those closest to the detector will need to be cooled in stages (130, 30 and 2K) in order to reduce infrared emission from the filters themselves. (In a separate analysis, we intend to more precisely determine the cooled filter stack and the impinging thermal load and infrared photon count rate.) The filters will be fabricated by Luxel Corp., who has built filters for the MSSTA missions, as well as TRACE and other extreme ultraviolet/soft x-ray observatories.

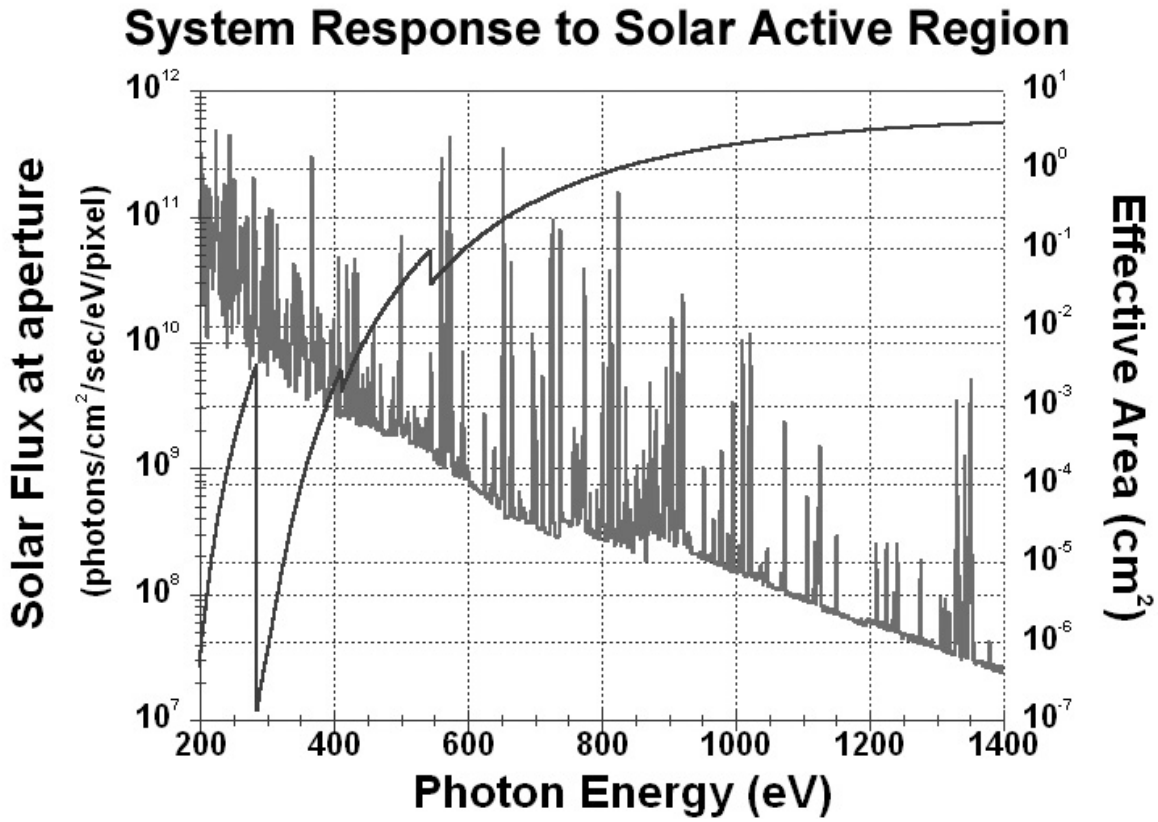

Figure 76. Effective area (collecting area times efficiency) of the ATSSI telescope and filters, superimposed on a simulated spectrum from a solar active region at the aperture of the ATSSI.

Figure 76 shows the effective area of the ATSSI instrument. Its response is dominated by the transmission of the filter stack, which strongly attenuates flux from EUV lines and continuum below 400 eV, as well as rejecting visible and infrared light. The mirror material and grazing

angle were chosen so that throughput from the optic is essentially constant over the energy range of interest (500-1500 eV). The mirror reflectivity begins to drop very sharply at about 2500 eV, and defines the upper end of the ATSSI's energy window (solar active regions, however, do not emit strong lines beyond 1500 eV).

5.4.4 AN ACTIVE REGION IN THE X-RAY

Superimposed on the throughput in Figure 1 is the expected emission over the energy range of the ATSSI bandpass from a solar active region. It was calculated using the CHIANTI database (Dere, Landi et al. 1997). The spectrum contains a continuum component that is strongest at low energies; at higher energies, it is characterized by strong, well-isolated emission lines from highly ionized iron, oxygen and other elements.

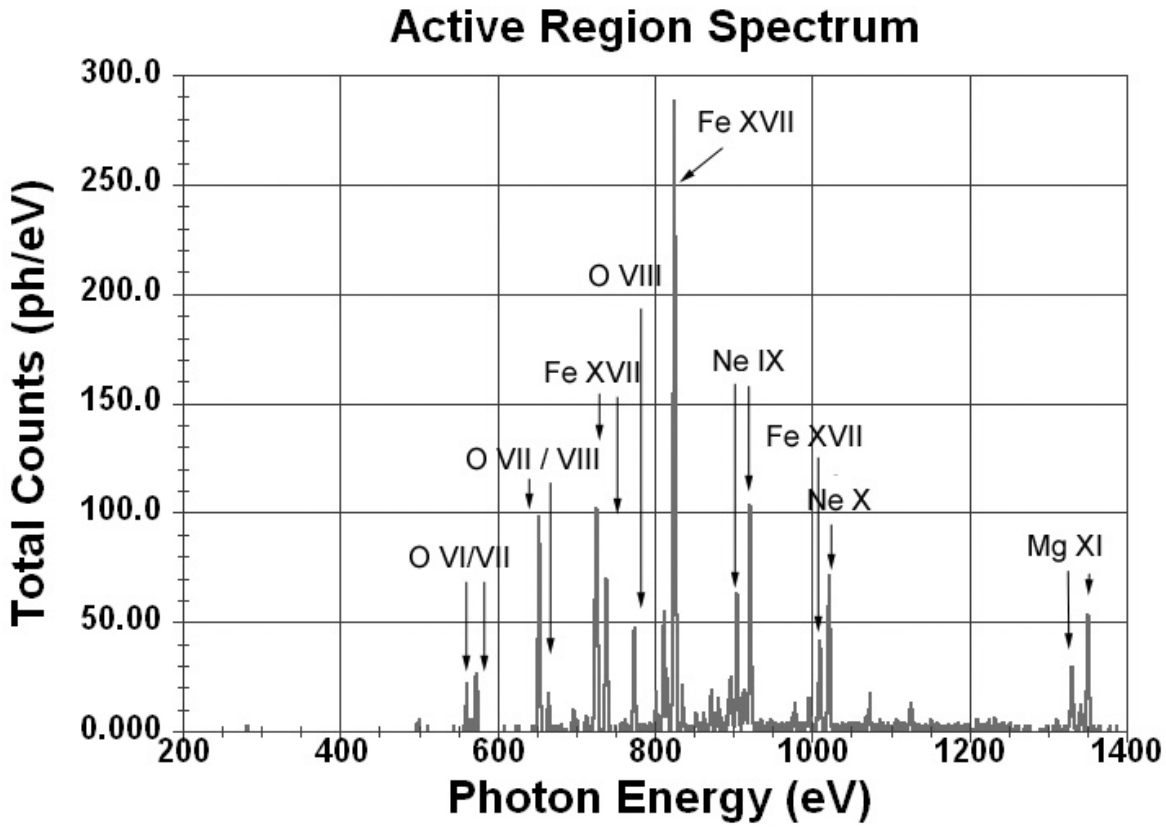

Figure 77. Simulated result of a 10-sec, single pixel (~6.25 arcsec), observation of an active region by ATSSI.

Figure 77 contains the results of a simulation of what the ATSSI data might look like given the solar spectrum and instrument response of Figure 76. Because the TES counts individual photons, the number of photons from a particular emission line which reach the detector was chosen based on Poisson statistics. The effect of the instrument's 3 eV resolution was simulated by assigning each photon to an energy bin chosen from a Gaussian distribution with FWHM of 3 eV. The continuum was also included in the simulation; however, few continuum photons contribute to the final spectrum.

A total of 16 emission lines are detected at a signal-to-noise ratio of at least 10:1. The energy resolution of the detector is not sufficient to detect Doppler shifts from any but the fastest plasma flows (~few hundred km/s). However, simply measuring fluxes in these lines provides a wealth of diagnostic information about the condition of the coronal plasma. The contribution functions for

the lines in the ATSSI bandpass span the temperature range $T = 10^6 – 10^7$, thereby constraining the thermal differential emission measure over that range. This knowledge of the temperature and density distribution of material can be used to generate models of the structures responsible for this emission and to test theoretical coronal heating functions. Temperature-sensitive line ratios of O VII and Fe XVII can be measured as a further diagnostic tool. This observational technique will yield a wealth of important clues about the corona.

Bibliography

Allen, M. J., H. M. Oluseyi, A. B. C. Walker*, et al.* (1997). "Chromospheric and coronal structure of polar plumes. I. Magnetic structure and radiative energy balance." *Solar Physics* **174**: 367-401.

Allen, M. J., T. D. Willis, C. C. Kankelborg*, et al.* (1991). "Calibration of the Multi-Spectral Solar Telescope Array Multilayer Mirrors and XUV Filters." Proceedings of the SPIE, San Diego, CA, USA.

Arnaud, M. and J. Raymond (1992). "Iron Ionization and Recombination Rates and Ionization Equilibrium." *Astrophysical Journal* **398**(1): 394-406.

Arnaud, M. and R. Rothenflug (1985). "An updated evaluation of recombination and ionization rates." *Astronomy and Astrophysics Supplement Series* **60**: 425-457.

Aschwanden, M. J. (2002). "The Differential Emission Measure Distribution in the Multiloop Corona." *Astrophysical Journal* **580**: L79-L83.

Aschwanden, M. J., D. Alexander, N. Hurlburt*, et al.* (2000). "Three-dimensional Stereoscopic Analysis of Solar Active Region Loops. II. SOHO/EIT Observations at Temperatures of 1.5-2.5 MK." *Astrophysical Journal* **531**: 1129-1149.

Aschwanden, M. J., J. S. Newmark, J. P. Delaboudiniére*, et al.* (1999). "Three-dimensional Stereoscopic Analysis of Solar Active Region Loops. I. SOHO/EIT Observations at Temperatures of (1.0-1.5) X 10^6 K." *Astrophysical Journal* **515**: 842-867.

Aschwanden, M. J., C. J. Schrijver and D. Alexander (2001). "Modeling of Coronal EUV Loops Observed with TRACE. I. Hydrostatic Solutions with Nonuniform Heating." *Astrophysical Journal* **550**: 1036-1050.

Barbee, T. W. and D. L. Keith (1978). Synthetic Structures Layered on the Atomic Scale. Stanford, CA, Stanford Synchrotron Radiation Laboratory.

Berger, T. E., B. De Pontieu, L. Fletcher*, et al.* (1999). "What is Moss?" *Solar Physics* **190**: 409-418.

Boerner, P., D. S. Martínez-Galarce, K. Wamba*, et al.* (2004). "The Advanced Technology Solar Spectroscopic Imager - a novel experiment employing a transition-edge sensor to probe the soft X-ray solar corona." *Nuclear Instruments & Methods in Physics Research Section a-Accelerators Spectrometers Detectors and Associated Equipment* **520**(1-3): 372-375.

Boerner, P. F. X., A. B. C. Walker, II, R. B. Hoover*, et al.* (1999). "Chromospheric/Coronal Spectroheliograph." Proceedings of the SPIE, Denver, CO, USA.

Brosius, J. W., J. M. Davila and R. J. Thomas (1998). "Solar active region and quiet-Sun extreme-ultraviolet spectra from SERTS-95." *Astrophysical Journal Supplement Series* **119**: 255-276.

Brosius, J. W., J. M. Davila, R. J. Thomas*, et al.* (1996). "Measuring active and quiet-Sun coronal plasma properties with extreme-ultraviolet spectra from SERTS." *Astrophysical Journal Supplement Series* **106**: 143-164.

Callahan, G. P. and B. K. Flint (1999). "Characteristics of deep-UV optics at 193 nm and 157 nm." Laser-Induced Damage in Optical Materials: 1998, Boulder, CO, USA, SPIE.

Cargill, P. J. and J. A. Klimchuk (2004). "Nanoflare Heating of the Corona Revisited." *Astrophysical Journal* **605**: 911-920.

Craig, I. J. D. and J. C. Brown (1976). "Fundamental Limitations of X-Ray-Spectra as Diagnostics of Plasma Temperature Structure." *Astronomy and Astrophysics* **49**(2): 239-250.

Curdt, W., P. Brekke, U. Feldman*, et al.* (2001). "The SUMER spectral atlas of solar-disk features." *Astronomy and Astrophysics* **375**: 591-613.

Dancy, C. C. and M. V. Buckley, Eds. (1987). *Scientific Imaging with Kodak Films and Plates (P-315)*. Rochester, NY, Eastman Kodak Co.

De Forest, C. D. (2004).

De Pontieu, B., T. E. Berger, C. J. Schrijver*, et al.* (1999). "Dynamics of Transition Region `Moss' at high time resolution." *Solar Physics* **190**: 419-435.

Del Zanna, G. and H. E. Mason (2003). "Solar active regions: SOHO/CDS and TRACE observations of quiescent coronal loops." *Astronomy and Astrophysics* **406**: 1089-1103.

Dere, K. P., E. Landi, H. E. Mason*, et al.* (1997). "CHIANTI - an atomic database for emission lines." *Astronomy and Astrophysics Supplement Series* **125**: 149-173.

Dere, K. P., E. Landi, H. E. Mason*, et al.* (1997). "CHIANTI: An atomic database for emission lines. I. Wavelengths greater than 50 AA." *Astronomy and Astrophysics Supplement Series* **125**: 149-173.

Dere, K. P., J. D. Moses, J.-P. Delaboudiniére*, et al.* (2000). "The Preflight Photometric Calibration of the Extreme-Ultraviolet Imaging Telescope EIT." *Solar Physics* **195**: 13-44.

Dupree, A. K. (1972). "Analysis of the Extreme-Ultraviolet Quiet Solar Spectrum." *Astrophysical Journal* **178**: 527-542.

Edlén, B. (1945). "The identification of the coronal lines." *Monthly Notices of the Royal Astronomical Society* **105**: 323.

Feldman, U. (1983). "On the unresolved fine structures of the solar atmosphere in the 3e4 - 2e5 K temperature region." *Astrophysical Journal* **275**: 367-373.

Feldman, U. (1992). "Elemental abundances in the upper solar atmosphere." *Physica Scripta Volume T* **46**: 202-220.

Feldman, U., G. A. Doschek, U. Schuhle*, et al.* (1999). "Properties of quiet-Sun coronal plasmas at distances of 1.03 <= R_solar <= 1.50 along the solar equatorial plane." *Astrophysical Journal* **518**(1): 500-507.

Feldman, U., P. Mandelbaum, J. F. Seely*, et al.* (1992). "The Potential for Plasma Diagnostics from Stellar Extreme-Ultraviolet Observations." *Astrophysical Journal Supplement Series* **81**(1): 387.

Feldman, U., K. G. Widing and H. P. Warren (1999). "Morphology of the Quiet Solar Upper Atmosphere in the 4x10^4 < T_e < 1.4x10^6 K Temperature Regime." *Astrophysical Journal* **522**: 1133-1147.

Foing, B., R. M. Bonnet and M. Bruner (1986). "New high-resolution rocket-ultraviolet filtergrams of the solar disc." *Astronomy and Astrophysics* **162**: 292-306.

Golub, L. (1989). "A Normal Incidence X-ray Telescope (NIXT) sounding rocket payload." Smithsonian Astrophysical Observatory Report.

Golub, L., E. DeLuca, M. Weber*, et al.* (2004). "DEM Reconstruction with the AIA." Living with a Star Workshop, Boulder, CO.

Golub, L., G. Nystrom, M. Herant*, et al.* (1990). "Sub-arcsecond observations of the solar X-ray corona." *Nature* **344**: 842-844.

Golub, L. and J. M. Pasachoff (2001). *Nearest star : the surprising science of our sun*. Cambridge, Mass., Harvard University Press.

Green, A. E. S. and R. D. Mcpeters (1975). "New Analytic Expressions of Photographic Characteristic Curves." *Applied Optics* **14**(2): 271-272.

Grevesse, N. and A. J. Sauval (1998). "Standard solar composition." *Space Science Reviews* **85**(1-2): 161-174.

Gullikson, E. M., S. Mrowka and B. B. Kaufmann (2001). "Recent developments in EUV reflectometry at the Advanced Light Source." Emerging Lithographic Technologies V, Santa Clara, CA, USA, SPIE.

Handy, B. N., L. W. Acton, C. C. Kankelborg*, et al.* (1999). "The transition region and coronal explorer." *Solar Physics* **187**: 229-260.

Handy, B. N., M. E. Bruner, T. D. Tarbell*, et al.* (1998). "UV Observations with the Transition Region and Coronal Explorer." *Solar Physics* **183**: 29-43.

Handy, B. N., T. D. Tarbell, C. J. Wolfson*, et al.* (1999). "Calibrated H I Lyman €€alpha; Observations with TRACE." *Solar Physics* **190**: 351-361.

Hansen, P. C. (1998). *Rank Deficient and Discrete Ill-Posed Problems*. Philadelphia, PA, Society for Industrial and Applied Mathematics.

Harrison, R. A., E. C. Sawyer, M. K. Carter*, et al.* (1995). "The Coronal Diagnostic Spectrometer for the Solar and Heliospheric Observatory." *Solar Physics* **162**: 233-290.

Hedin, A. E. (1991). "Extension of the Msis Thermosphere Model into the Middle and Lower Atmosphere." *Journal of Geophysical Research-Space Physics* **96**(A2): 1159-1172.

Henke, B. L., E. M. Gullikson and J. C. Davis (1993). "X-Ray Interactions - Photoabsorption, Scattering, Transmission, and Reflection at E=50-30,000 Ev, Z=1-92." *Atomic Data and Nuclear Data Tables* **54**(2): 181-342.

Hoover, R. B., A. B. Walker, C. D. De Forest*, et al.* (1990). "Performance of the Multi-Spectral Solar Telescope Array VI. Performance and Characteristics of the Photographic Films, SPIE.

Hoover, R. B., A. B. Walker, C. D. De Forest*, et al.* (1991). "Photographic Films for the Multi-Spectral Solar Telescope Array." Multilayer and Grazing Incidence X-Ray/EUV Optics, SPIE.

Hoover, R. B., A. B. C. Walker, C. E. DeForest, *et al.* (1994). "X-ray/EUV/FUV calibration of photographic films for solar research." Multilayer and Grazing Incidence X-Ray/EUV Optics II, San Diego, CA, USA, SPIE.

Hoover, R. B., A. B. C. Walker, C. E. DeForest, *et al.* (1991). "Ultrahigh Resolution Photographic Films for X-Ray/EUV/FUV Astronomy." Proceedings of the SPIE.

Hoover, R. B., A. B. C. Walker, Jr., C. E. DeForest, *et al.* (1991). "EUV/FUV response characteristics of photographic films for the Multi-Spectral Solar Telescope Array." *Optical Engineering* **30**: 1116-1124.

Hoover, R. B., A. B. C. Walker, Jr., J. F. Lindblom, *et al.* (1992). "Solar Observations with the Multi-Spectral Solar Telescope Array." Proceedings of the SPIE, San Diego, CA, USA.

Judge, D. L., D. R. McMullin and H. S. Ogawa (1999). "Absolute solar 30.4 nm flux from sounding rocket observations during the solar cycle, 23 minimum." *Journal of Geophysical Research* **104**: 28321.

Judge, P. G., V. Hubeny and J. C. Brown (1997). "Fundamental Limitations of Emission-Line Spectra as Diagnostics of Plasma Temperature and Density Structure." *Astrophysical Journal* **475**: 275.

Kankelborg, C. C. (1996). Multi-spectral Observations of Coronal X-ray Bright Points. *Physics*. Stanford, CA, Stanford University.

Kankelborg, C. C., A. B. C. Walker, II and R. B. Hoover (1997). "Observation and modeling of soft X-ray bright points. II. Determination of temperature and energy balance." *Astrophysical Journal*.

Kankelborg, C. C., A. B. C. Walker, II, R. B. Hoover, *et al.* (1996). "Observation and modeling of soft X-ray bright points. I. Initial results." *Astrophysical Journal* **466**: 529-536.

Landi, E. and F. Chiuderi Drago (2003). "Solving the Discrepancy between the Extreme-Ultraviolet and Microwave Observations of the Quiet Sun." *Astrophysical Journal* **589**: 1054-1061.

Landi, E., U. Feldman and K. P. Dere (2002). "CHIANTI-An Atomic Database for Emission Lines. V. Comparison with an Isothermal Spectrum Observed with SUMER." *Astrophysical Journal Supplement Series* **139**: 281-296.

Landi, E., U. Feldman and K. P. Dere (2002). "A Comparison between Coronal Emission Lines from an Isothermal Spectrum Observed with the Coronal Diagnostic Spectrometer and CHIANTI Emissivities." *Astrophysical Journal* **574**: 495-503.

Landini, M. and B. C. M. Fossi (1991). "Ion equilibrium for minor components in a thin plasma." *Astronomy and Astrophysics Supplement Series* **91**: 183-196.

Larsen, R. M., A. G. Kosovichev, J. Zhao, *et al.* (2004). Stanford, CA.

Lenz, D. D., E. E. DeLuca, L. Golub, *et al.* (1999). "Long-lived Coronal Loop Profiles from TRACE." *Solar Physics* **190**: 131-138.

Lin, L., V. L. Kashyap, J. J. Drake, *et al.* (2004). "The Nearest Star: Emission Structure of the Sun's Corona." American Astronomical Society, Denver, CO.

Malinovsky, L. and M. Heroux (1973). "An Analysis of the Solar Extreme Ultraviolet between 50 and 300 Å." *Astrophysical Journal* **181**: 1009-1030.

Malory, T. and H. Cooper (1998). *Le Morte D'Arthur : the Winchester Manuscript*. New York, Oxford University Press.

Martens, P. C. H., J. W. Cirtain and J. T. Schmelz (2002). "The Inadequacy of Temperature Measurements in the Solar Corona through Narrowband Filter and Line Ratios." *Astrophysical Journal* **577**: L115-L117.

Martínez-Galarce, D. S. (2000). The Solar Transition Region: High Resolution FUV-EUV Imaging and Modeling of Unresolved Coronal Funnels as Observed With the Multi-Spectral Solar Telescope Array, II -- MSSTA II, the Second Flight. *Physics*. Stanford, CA, Stanford University**:** 220.

Martínez-Galarce, D. S., A. B. C. Walker, D. B. Gore*, et al.* (2000). "High resolution imaging with multilayer telescopes: resolution performance of the MSSTA II telescopes." *Optical Engineering* **39**(4): 1063-1079.

Martínez-Galarce, D. S., A. B. C. Walker, II , T. W. Barbee, II *, et al.* (2003). "The Solar Chromosphere/Corona Interface. I. Far-Ultraviolet to Extreme-Ultraviolet Observations and Modeling of Unresolved Coronal Funnels." *Astrophysical Journal* **585**: 1095-1113.

McCammon, D., R. Almy, E. Apodaca*, et al.* (2002). "A High Spectral Resolution Observation of the Soft X-Ray Diffuse Background with Thermal Detectors." *Astrophysical Journal* **576**: 188-203.

Mouchel, P. (1966). "Photographic Processing with 1-Time Use of Solutions." *Journal of Photographic Science* **14**(4): 209-&.

NASROC (2002). 36.194 Flight Performance Report. Wallops Island, VA.

Neupert, W. M., G. L. Epstein, R. J. Thomas*, et al.* (1992). "An EUV imaging spectrograph for high-resolution observations of the solar corona." *Solar Physics* **137**: 87-104.

Neupert, W. M., J. Newmark, J. P. Delaboudiniére*, et al.* (1998). "Observations of Coronal Structures Above an Active Region by EIT and Implications for Coronal Energy Deposition." *Solar Physics* **183**: 305-321.

Nightingale, R. W., M. J. Aschwanden and N. E. Hurlburt (1999). "Time Variability of EUV Brightenings in Coronal Loops Observed with TRACE." *Solar Physics* **190**: 249-265.

Oluseyi, H. M., A. B. C. Walker, II, J. G. Porter*, et al.* (1999). "Observation and Modeling of the Solar Transition Region: I. Multi-spectral solar telescope array observations." *Astrophysical Journal* **524**: 1105-1121.

Palik, E. D., Ed. (1985). *Handbook of Optical Constants of Solids*. San Diego, CA, Academic.

Palik, E. D., Ed. (1991). *Handbook of Optical Constants of Solids II*. San Diego, CA, Academic.

Parker, E. N. (1988). "Nanoflares and the Solar-X-Ray Corona." *Astrophysical Journal* **330**(1): 474-479.

Plummer, J. E., C. E. DeForest, D. S. Martinez-Galarce*, et al.* (1994). "Design and Performance of Thin Foil XUV Filters for the Multi-Spectral Solar Telescope Array II." Proceedings of the SPIE, San Diego, CA, USA.

Pottasch, S. R. (1963). "The Lower Solar Corona: Interpretation of the Ultraviolet Spectrum." *Astrophysical Journal* **137**: 945.

Powell, F. R. and J. Fox (1994). "Transmittance measurements for a variety of x-ray/EUV filter materials and pinhole leak measurements utilizing a new visible light photometer system." Multilayer and Grazing Incidence X-Ray/EUV Optics II, San Diego, CA, USA, SPIE.

Reale, F., G. Peres, S. Serio*, et al.* (2000). "A Brightening Coronal Loop Observed by TRACE. I. Morphology and Evolution." *Astrophysical Journal* **535**: 412-422.

Rottman, G. J., T. N. Woods and T. P. Sparn (1993). "Solar-Stellar Irradiance Comparison Experiment 1. I - Instrument design and operation." *Journal of Geophysical Research* **98**: 10667.

Rugge, H. R. and A. B. C. Walker, Jr. (1974). "Relative intensities of the Lyman lines of hydrogen-like oxygen, magnesium, and silicon in the solar corona." *Astronomy and Astrophysics* **33**: 367-371.

Sakao, T., S. Tsuneta, H. Hara*, et al.* (1999). "The XUV Doppler Telescope (XDT)." *Solar Physics* **187**(2): 303-333.

Schmelz, J. T., J. E. Beene, K. Nasraoui*, et al.* (2003). "The Effect of Background Subtraction on the Temperature of EIT Coronal Loops." *Astrophysical Journal* **599**: 604-614.

Schmelz, J. T., J. L. R. Saba, K. T. Strong*, et al.* (1999). "Emission Measure Distribution for an Active Region Using Coordinated SERTS and YOHKOH SXT Observations." *Astrophysical Journal* **523**: 432-443.

Schmelz, J. T., R. T. Scopes, J. W. Cirtain*, et al.* (2001). "Observational Constraints on Coronal Heating Models Using Coronal Diagnostics Spectrometer and Soft X-Ray Telescope Data." *Astrophysical Journal* **556**: 896-904.

Schrijver, C. J., M. J. Aschwanden and A. M. Title (2002). "Transverse oscillations in coronal loops observed with TRACE - I. An Overview of Events, Movies, and a Discussion of Common Properties and Required Conditions." *Solar Physics* **206**: 69-98.

Smith, A. G., H. W. Schrader and Richards.Ww (1971). "Response of Type IIIa-J Kodak Spectroscopic Plates to Baking in Various Controlled Atmospheres." *Applied Optics* **10**(7): 1597.

Spiller, E. (1972). "Low-Loss Reflection Coatings Using Absorbing Materials." *Applied Physics Letters* **20**(9): 365-&.

Spiller, E. A., T. W. Barbee, Jr.*, et al.* (1994). "Results from the recent flights of the IBM/SAO x-ray telescopes." Multilayer and Grazing Incidence X-Ray/EUV Optics II, San Diego, CA, USA, SPIE.

Sylwester, J., J. Schrijver and R. Mewe (1980). "Multitemperature analysis of solar X-ray line emission." *Solar Physics* **67**: 285-309.

Testa, P., G. Peres, F. Reale*, et al.* (2002). "Temperature and Density Structure of Hot and Cool Loops Derived from the Analysis of TRACE Data." *Astrophysical Journal* **580**: 1159-1171.

Thomas, R. J. and W. M. Neupert (1994). "Extreme ultraviolet spectrum of a solar active region from SERTS." *Astrophysical Journal Supplement Series* **91**: 461-482.

Tikhonov, A. N. and V. Y. Arsenin (1977). *Solutions of Ill-Posed Problems*. Washington, D. C., Winston & Sons.

Tirsell, K. G. and V. P. Karpenko (1990). "A General-Purpose Sub-Kev X-Ray Facility at the Stanford-Synchrotron-Radiation-Laboratory." *Nuclear Instruments & Methods in Physics Research Section a-Accelerators Spectrometers Detectors and Associated Equipment* **291**(1-2): 511-517.

Underwood, J. H., E. M. Gullikson, M. Koike*, et al.* (1996). "Calibration and standards beamline 6.3.2 at the Advanced Light Source." The 9th National conference on synchrotron radiation instrumentation, Argonne, Illinois (USA), AIP.

Vernazza, J. E. and E. M. Reeves (1978). "Extreme ultraviolet composite spectra of representative solar features." *Astrophysical Journal Supplement Series* **37**: 485-513.

Vesecky, J. F., S. K. Antiochos and J. H. Underwood (1979). "Numerical modeling of quasi-static coronal loops. I. Uniform energy input." *Astrophysical Journal* **233**: 987-997.

Vourlidas, A., J. A. Klimchuk, C. M. Korendyke*, et al.* (2001). "On the Correlation between Coronal and Lower Transition Region Structures at Arcsecond Scales." *Astrophysical Journal* **563**: 374-380.

Walker, A. B. C., Jr. , J. F. Lindblom, T. W. Barbee, Jr. *, et al.* (1988). "Soft X-ray images of the solar corona with a normal-incidence Cassegrain multilayer telescope." *Science* **241**: 1781-1787.

Walker, A. B. C., Jr., J. F. Lindblom, R. H. O'Neal*, et al.* (1990). "Multi-Spectral Solar Telescope Array." *Optical Engineering* **29**: 581-591.

Wamba, K. D., A. B. Walker, D. S. Martinez-Galarce*, et al.* (2000). "Sounding rocket mission to study the solar soft x-ray and EUV emission using transition-edge sensor technology." Proc. SPIE Vol. 4140, p. 384-396, X-Ray and Gamma-Ray Instrumentation for Astronomy XI, Kathryn A. Flanagan; Oswald H. Siegmund; Eds.

Warburton, W. K. and P. Pianetta (1990). "A Novel Differential Pump for Synchrotron Beamlines - Tests, Models and Applications." *Nuclear Instruments & Methods in Physics Research Section a-Accelerators Spectrometers Detectors and Associated Equipment* **291**(1-2): 350-356.

Weber, M. A., E. E. DeLuca, L. Golub*, et al.* (2004). "Differential Emission Measure Reconstruction with the Atmospheric Imaging Assembly." Living With a Star Workshop, Boulder, CO.

Wheatland, M. S., P. A. Sturrock and L. W. Acton (1997). "Coronal Heating and the Vertical Temperature Structure of the Quiet Corona." *Astrophysical Journal* **482**: 510.

White, S. M. (1999). "Radio Versus EUV/X-Ray Observations of the Solar Atmosphere." *Solar Physics* **190**: 309-330.

Wilhelm, K., W. Curdt, E. Marsch*, et al.* (1995). "SUMER - Solar Ultraviolet Measurements of Emitted Radiation." *Solar Physics* **162**: 189-231.

Withbroe, G. L. (1975). "The analysis of XUV emission lines." *Solar Physics* **45**: 301-317.

Wollman, D. A., S. W. Nam, D. E. Newbury*, et al.* (2000). "Superconducting transition-edge-microcalorimeter X-ray spectrometer with 2 eV energy resolution at 1.5 keV." *Nuclear Instruments & Methods in Physics Research Section a-Accelerators Spectrometers Detectors and Associated Equipment* **444**(1-2): 145-150.

Woods, T. N., E. Rodgers, S. M. Bailey*, et al.* (1999). "TIMED Solar EUV Experiment: pre-flight calibration results for the XUV photometer system." Proceedings of the SPIE, SPIE.

Young, P. R., G. Del Zanna, E. Landi*, et al.* (2003). "CHIANTI-An Atomic Database for Emission Lines. VI. Proton Rates and Other Improvements." *Astrophysical Journal Supplement Series* **144**: 135-152.

Zhang, J., S. M. White and M. R. Kundu (1999). "Two-Temperature Coronal Models from SOHO/EIT Observations." *Astrophysical Journal* **527**: 977-991.

Zhitnik, A., K. A. Boyarchuk, O. I. Bugaenko*, et al.* (2003). "Effects of the Absorption of Solar XUV Radiation by the Earth's Upper Atmosphere at Altitudes of 100 - 500 km in the X-ray Solar Images Obtained Onboard the Coronas-I (TEREK Telescope) and Coronas-F (SPIRIT X-ray Complex) Satellites." *Solar System Research* **37**(4): 296-301.